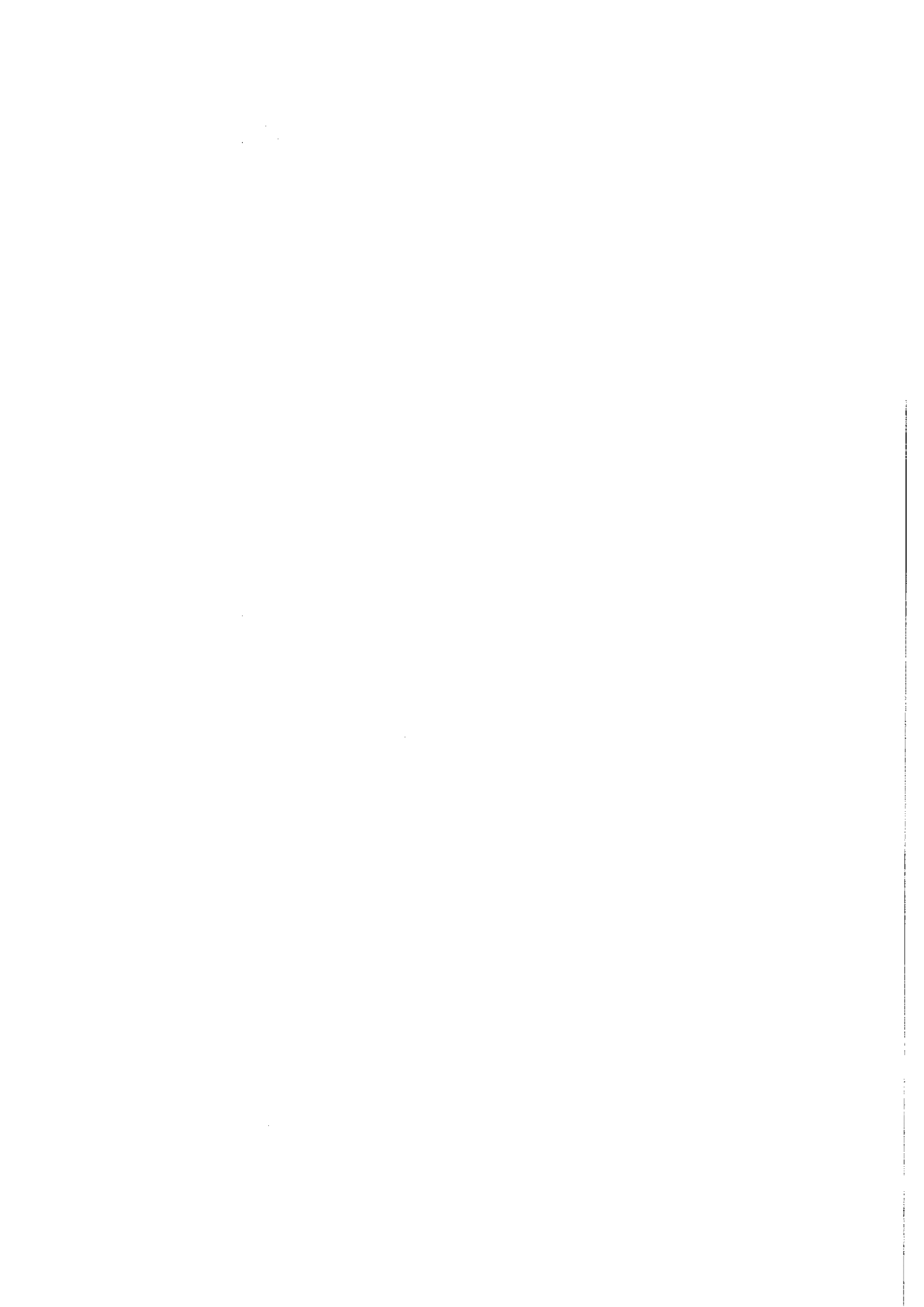# SATURN-FS 1
A Computer Code for Thermo-mechanical Fuel Rod Analysis

H. J. Ritzhaupt-Kleissl, M. Heck
Institut für Materialforschung
Projekt Nukleare Sicherheitsforschung

Kernforschungszentrum Karlsruhe

KERNFORSCHUNGSZENTRUM KARLSRUHE

SATURN-FS 1

A Computer Code for Thermo-mechanical Fuel Rod Analysis

H.J. Ritzhaupt-Kleissl, M. Heck

Abstract

The SATURN-FS code was written as a general revision of the SATURN-2 code. SATURN-FS is capable to perform a complete thermomechanical analysis of a fuel pin, with all thermal, mechanical and irradiation-based effects.

Analysis is possible for LWR and for LMFBR fuel pins.

The thermal analysis consists of calculations of the temperature profile in fuel, gap and in the cladding. Pore migration, stoichiometry change of oxide fuel, gas release and diffusion effects are taken into account. The mechanical modeling allows the non steady-state analysis of elastic and nonelastic fuel pin behaviour, such as creep, strain hardening, recovery and stress relaxation. Fuel cracking and healing is taken into account as well as contact and friction between fuel and cladding. The modeling of the irradiation effects comprises swelling and fission gas production, Pu-migration and irradiation induced creep.

The code structure, the models and the requirements for running the code are described in the report. Recommendations for the application are given.

Program runs for verification and typical examples of application are given in the last part of this report.

Zusammenfassung

SATURN-FS 1: Ein Rechenprogramm zur thermomechanischen Brennstabanalyse (Benutzerhandbuch)

SATURN-FS stellt eine Weiterentwicklung des Brennstabrechenprogramms SATURN-2 dar. Es erlaubt eine umfassende thermomechanische Brennstabanalyse unter Berücksichtigung aller thermischer, mechanischer und bestrahlungsbedingter Effekte.

Es können sowohl LWR- als auch LMFBR-Brennstäbe analysiert werden.

Die thermische Analyse umfaßt die Berechnung der Temperaturprofile in Brennstoff, Spalt und Hülle sowie die Betrachtung von Porenwanderung, der Änderung des Sauerstoff- zu Metall-Verhältnisses im Oxidbrennstoff, von Gasfreisetzung und bestrahlungsbedingten Diffusions-Effekten. Die mechanische Modellierung erlaubt die instationäre Analyse des elastischen und nichtelastischen Brennstabverhaltens wie Kriechen, Verfestigung, Materialerholung, Spannungsrelaxation. Aufreißen und Ausheilen des Brennstoffs sowie Kontakt- und Reibungseffekte zwischen Hülle und Brennstoff werden beschrieben. Die Modellierung der Bestrahlungseffekte umfaßt Schwellen, Spaltgasproduktion und -freisetzung sowie bestrahlungsbedingtes Kriechen.

Dieser Bericht beinhaltet die Beschreibung der verwendeten mathematischen Modelle, der Programmstruktur und eine Benutzeranleitung zum Gebrauch des Programms.

Programmläufe zur Absicherung und typische Anwendungsbeispiele sind im letzten Teil dieses Handbuchs enthalten.

CONTENTS

Part 2

Part 1

Modelling the Fuel Rod Behavior

A. Introduction

The computer code SATURN-FS was developed during the last years in order to meet new requirements in the field of fuel element modeling and designing. SATURN-FS is a successor of the SATURN-2 code which was also developed in the "Institut für Materialforschung" (IMF III) at the Kernforschungszentrum Karlsruhe (KfK). The abbreviations FS in the name of the code mean that

- the code uses a Finite element structure of the fuel rod and

- the code calculates fuel rods within their operational limits ("Steady state").

Conditions beyond the safety limits, such as fuel melting, LOCA considerations or accidental transients are not modeled.

Great emphasis was laid on an improved description of the fuel rod mechanics and here especially in the field of modeling the nonelastic behaviour, such as plastic deformation, creep and stress relaxation. By the consistent consideration of the time-dependent derivatives of stress and strain, i.e. their "rates" it was possible to introduce a transient mechanical modeling of a fuel rod. This possibility is especially advantageous for the analyses of fast operational or design transients.

The general code structure is modular. There is a strict separation between structure models describing material behaviour.

The code is written for general applicability, i.e. for any types of fuel rod or fuel/cladding combinations. For simplification two standard combinations can be called by user's option: LWR with UO_2 fuel and Zry cladding and FBR with $(U,Pu)O_2$ fuel and stainless steel cladding.

The SATURN-FS code was thoroughly tested and verified by recalculating various experiments and comparing the code calculations with the experimental data. The results of some interesting verification calculations are given within this report. Furthermore, design calculations for anticipated irradiation experiments have been performed, especially in the field of FBR-fuel development.

This report as a user's manual wants to give a comprehensive survey on the code structure, the used models, the required input information and the calculated output.

It so enables the user to run SATURN-FS calculation without major complications.

B. The Structure of the Computer Program

The advanced version FS1 of the SATURN fuel rod computer program is intended to model the fuel rod by means of the Finite Element Method (FEM). Severe accicental transient behaviour with fuel melting and total destruction of the fuel rod is left out of consideration by the program. So, the fuel rod behaviour during steady state operation and operational transiensts is the subject modelling. Axial variations are also left out of consideration in the present version.

SATURN - FS1.

Generally speaking,the computer program in its present version has three characteristic features:

* Use of the Finite Element Method (FEM) to solve the mechanical problem. Assuming axial-symmetric fuel rod geometry, ring elements with rectangular cross-sections have been chosen, i. e., description of shear stresses and sliding has been dispensed with. Neglecting these phenomena does not produce a major error source because both our own investigations with two-dimensional FEM programs and analytical considerations [B1] have shown that shear stresses are normally by about one order of magnitude smaller than normal stresses.

* In general, a structure has been described which consists of the fuel as a heat generating ceramic cylinder which may crack and whose cracks can heal again. This cylinder is surrounded by another metallic hollow tube -the cladding-, which transfers the produced heat to a cooling medium, and is separated from the fuel by an annular gap filled with a transfer medium (gas, liquid metal). The physical relationship described here applies to any material combinations and it is not necessary for the user to make any modifications to this inner part of the program.

* All variables needed to solve the thermomechanical problems involving forces, displacements, stresses, strains and sometimes temperatures, are substituted during one computer time-step by their derivatives with respect to time, i. e. their rates. These rates are assumed to remain constant during the time-step. At the end of this time-step the variables proper are calculated by integration over the time-step interval.

Reference:

[B1] K. Keller:
Elastizitätstheorie zur Brennstabmechanik von Reaktorbrennstäben bei schnellen Brennstab-Leistungsänderungen, KfK 3176, March 1982

C. Calculation of Temperature

The most important cladding material and fuel properties as well as the effects occurring in the fuel rod during operation are heavily dependent on the temperature. Therefore, the precise determination of the temperature distribution in the fuel rod is of particular importance in analyzing the fuel rod behaviour. With the computer program described here, the radial temperature distribution in the fuel rod is continuously calculated from outside to inside. The starting point is the coolant temperature which is assumed to be known. Using the cladding/coolant heat transfer coefficient, the external cladding temperature T_{Ha} can be calculated. This gives the temperature course along the cladding cross-section by use of the rod power Q_O (W/cm) and the thermal conductivity of the cladding $\lambda_H(T)$ as

$$T(r) = T_{Ha} + \frac{Q_0}{2\pi \cdot \lambda_H(T)} \cdot \ell n\left(\frac{R_{Ha}}{r}\right) \tag{C-1}$$

The temperature dependence of the thermal conductivity needs an iterative solution. When the internal cladding temperature has been calculated, the computation of the heat transfer in the gap between the fuel and the cladding can start. This will not be treated in more detail here because the known GAPRS module [C1] is used to calculate the heat transfer in the gap; see Section E.1. GAPRS yields the surface temperature of the fuel This is the value used to start computation of the radial fuel temperature field which will be briefly described in the next section. The method of computation presented here is similar to that of the CYGRO-4 computer program [C 2].

Let us assume a ring having the dimensions $r_1 \leq r \leq r_n$. The volumetric heat production rate in the ring is assumed to be Q_v [W/cm³] so that the total heat production rate in the ring per unit length is obtained as

$$q \ (W/cm) = \pi \cdot Q_v (r_n^2 - r_1^2) \tag{C-2}$$

With an optional additional heat source located in the centre of the ring which contributes q_0, a total heat production per unit length for the radius $0 \leq r \leq r_n$ of

$$\bar{q} \ (W/cm) = q_0 + q \tag{C-3}$$

is obtained.

Computation of the temperature distribution requires the knowledge of the power distribution. It is postulated that the relative radial power distribution p(r) meets the following conditions:

$$\lim_{r \to r_i; \; r < r_i} p(r) = p_i^{(-)} \tag{C-4}$$

$$\lim_{r \to r_i; \; r >, r_i} p(r) = p_i^{(+)} \tag{C-5}$$

With these prerequisites fulfilled, the heat production rate in a ring element having the dimension $r_k \le r \le r_{k+1}$ can be described approximately, i. e. by linear approximation, as

$$Q(r) \; (W/cm^3) \simeq \frac{p_k^{(+)} \cdot (r_{k+1} - r) + p_k^{(-)} (r - r_k)}{(r_{k+1} - r_k)} \cdot R \cdot Q_v \tag{C-6}$$

where R is a proportionality factor which will be discussed later. The heat produced in any ring element

$$r_k \le r \le r_{k+1}; \qquad k = 1 \ldots (n-1)$$

is obtained as

$$q_k \; (W/cm) = \int_0^{2\pi} \int_{r_k}^{r_{k+1}} Q(r) \cdot r \, dr \, d\phi \tag{C-7}$$

This corresponds to

$$q_k = \pi \cdot R \cdot Q_v (B_k \cdot p_k^{(+)} + A_{k+1} \cdot p_{k+1}^{(-)} \tag{C-8}$$

with A_k and B_k calculated by the formulae

$$A_k = \frac{1}{3} (r_k - r_{k-1}) \cdot (r_{k-1} + 2r_k) \tag{C-9}$$

$$B_k = \frac{1}{3} (r_{k+1} - r_k) \cdot (2r_k + r_{k+1}) \tag{C-10}$$

Moreover, the following equation holds true:

$$A_1 = B_n = 0 \tag{C-11}$$

By this formula the heat produced in the entire cylinder, i. e. in the range $r_1 \le r \le r_n$, can be expressed as

$$q\ (W/cm) = \sum_{k=1}^{n-1} q_k = \text{u} \cdot R \cdot Q_v \cdot \sum_{k=1}^{n} \left(A_k \cdot p_k^{(-)} + B_k \cdot p_k^{(+)} \right) \tag{C-12}$$

Using equation (C-12) the variable R can be determined as a function of r_k, $p_k^{(+)}$ and $p_k^{(-)}$. Actually, it follows from (C-12) that the known heat production rate Q_v, as averaged over the radius and multiplied by the volume of the cylinder, must equal the total heat production rate in the cylinder. This automatically yields the factor R to read

$$R = \frac{r_n^2 - r_1^2}{\sum\limits_{k=1}^{n} (A_k \cdot p_k^{(-)} + B_k \cdot p_k^{(+)})} \tag{C-13}$$

Introducing (C-13) into (C-12), one obtains

$$q\ (W/cm) = \text{u} \cdot Q_v \cdot (r_n^2 - r_1^2) \tag{C-14}$$

The temperature at a given radius r can under steady-state conditions be described by the equation of thermal conduction:

$$- \lambda(T) \cdot \frac{\partial T}{\partial r} = \frac{1}{2\text{u}} \cdot q(r) \tag{C-15}$$

where $\lambda(T)$ is the temperature dependent thermal conductivity on the and $q(r)$ is the heat flux per unit length, which passes through the cylinder surface at radius r.

Assuming that the temperature T(r) in the interval $r_k \le r \le r_{k+1}$ is linearly dependent on the radius, we obtain:

$$T(r) = \frac{T_k (r_{k+1} - r) + T_{k+1} (r - r_k)}{(r_{k+1} - r_k)} \quad ; r_k \le r \le r_{k+1} \tag{C-16}$$

Writing

$$r = \frac{r_k + r_{k+1}}{2} \quad and \quad T(r) = \frac{T_k + T_{k+1}}{2} \ resp.$$

equation (C-15) can be expressed by means of the derivative of equation (C-16) instead of the partial derivative in (C-15) as follows:

$$\lambda \left(\frac{T_k + T_{k+1}}{2} \right) \cdot \frac{(T_{k+1} - T_k)}{(r_{k+1} - r_k)} = - \frac{q \left(\frac{r_k + r_{k+1}}{2} \right)}{\text{u} \cdot (r_k + r_{k+1})} \tag{C-17}$$

Transposing the terms of equation (C-17) we get:

$$T_k = T_{k+1} + D_k \; \frac{q \left| \frac{1}{2} (r_k + r_{k+1}) \right|}{n \cdot \lambda \left| \frac{1}{2} (T_k + T_{k+1}) \right|} \tag{C-18}$$

with

$$D_k = \frac{r_{k+1} - r_k}{r_{k+1} + r_k} \tag{C-19}$$

Using equation (C-18) and assuming the temperature at the fuel surface to be known, the temperatures at given radii of the ring elements can be calculated. However, due to the temperature dependence of the thermal conductivity, this calculation can again be made only iteratively.

The heat production term $q(\frac{1}{2}(r_k + r_{k+1}))$ on the right-hand side of equation (C-18) can be expressed as

$$q \left| \frac{1}{2} (r_k + r_{k+1}) \right| = q_0 + \int_0^{2\pi} \int_0^{\frac{1}{2}(r_k + r_{k+1})} Q(r) \cdot r \; dr \; d\phi \tag{C-20}$$

Inserting equation (C-6) in equation (C-20) yields

$$q \left| \frac{1}{2} (r_k + r_{k+1}) \right| = \pi \cdot Q_0 \cdot R \left\{ \sum_{j=1}^{k-1} (A_j \cdot p_j^{(-)} + B_j \cdot p_j^{(+)} + A_k \cdot p_k^{(-)} + \right.$$

$$\left. + \frac{r_{k+1} - r_k}{12} \left| p_k^{(+)} \cdot (7 r_k + 2 r_{k+1}) + p_{k+1}^{(-)} \cdot (2 r_k + r_{k+1}) \right| \right\} + q_0 \tag{C-21}$$

Introducing two geometry factors, namely

$$F_k = \frac{1}{12} \frac{(7 r_k + 2 r_{k+1}) (r_{k+1} - r_k)^2}{r_{k+1} + r_k} \tag{C-22}$$

$$G_k = \frac{1}{12} \frac{(2 r_k + r_{k+1}) (r_{k+1} - r_k)^2}{r_{k+1} + r_k} \tag{C-23}$$

one can write equation (C-18) as follows

$$T_k = T_{k+1} + \frac{D_k \cdot Q_v}{\lambda \left(\frac{1}{2} \left| T_k + T_{k+1} \right| \right)} \cdot \left[q_0 + \sum_{j=1}^{k-1} (A_j \cdot R \cdot p_j^{(-)} + B_j \cdot R \cdot p_j^{(+)}) + A_k \cdot R \cdot p_k^{(-)} \right]$$

$$+ \frac{R_k \cdot Q_v}{\lambda \left(\frac{1}{2} \left| T_k + T_{k+1} \right| \right)} \cdot (F_k \cdot p_k^{(+)} + G_k \cdot p_k^{(-)}) \tag{C-24}$$

Generally, and leaving aside possible discontinuities in the fuel, the following relation holds for the coefficients of the radial flow distribution: $p_k^{(+)} = p_k^{(-)}$.

Procedure in the Computer Program:

In order to compute the temperature, the RADIAL subroutine is called by the MAIN program. It calculates the radial power distribution in the fuel and calls in turn the GEOFAK subroutine for calculating the factors A_k, B_k, D_k, F_k and G_k. The MAIN program then calls the TEMPER subroutine which performs the temperature calculation properly.

TEMPER calculates the temperature both of the cladding and of the fuel (provided that the computation is performed for a rod with fuel and cladding). In that case, TEMPER calls GAPRS before it calculates the fuel temperatures. If only the fuel or only the cladding is to be analyzed, the proper parts of the sub-routine are selected by different. With increasing burn-up the radial power profile changes. The program calculates new radial power factors (p_k) for each element and so new radial power distributions which are then used as starting values for the calculation in the new time step. This calculation is performed at the end or each time step in the PRBDIF routine and at the beeinning of the new time step in QPROF.

References:

[C1]   M. Heck, H. Steiner:
        Internal Note, September 1977.

[C2]   J.B. Newman, J.F. Giovengo, L.P. Comden:
        The CYGRO-4 Fuel Rod Analysis Computer Program,
        WAPD-TM-1300, July 1977.

D. Fuel Rod Mechanics

D1. Loadings of the Fuel Rod

When modelling the behavior of a nuclear reactor fuel rod, the various loadings must be described to which the fuel rod is exposed during its service life. These loadings may result from the large radial temperature gradients in the fuel of several 100 K/mm, on the one hand, or from forces generated on the contact areas between the fuel and the cladding after the initial gas gap has closed. These contact forces may act both radially and in an axial direction; in the latter case as friction forces. The loadings further include the gas pressure inside the fuel rod, the pressure of the coolant acting from outside on the fuel rod, and last but not least, the generally high level of temperatures to which the fuel rod components are exposed. For example, in a typical fast breeder fuel rod the average cladding temperature is about 600 °C and average fuel temperatures are about 1600 °C.

These high loadings, but also variations in local power to which the fuel rods are subjected during operation, imply that a time independent computation in terms of elasticity and elastoplasticity will not be sufficient for a comprehensive fuel rod analysis. Time dependent material phenomena such as creep, stress relaxation and material recovery in the existing temperature and stress fields also play an important role and should not be neglected.

The idealized structure of a fuel rod together with the actual loadings have been represented in Fig. D1-1. The structure consists of a heat-producing inner cylinder, with or without a central bore, surrounded by a hollow cylinder which transfers the produced heat to a coolant medium.
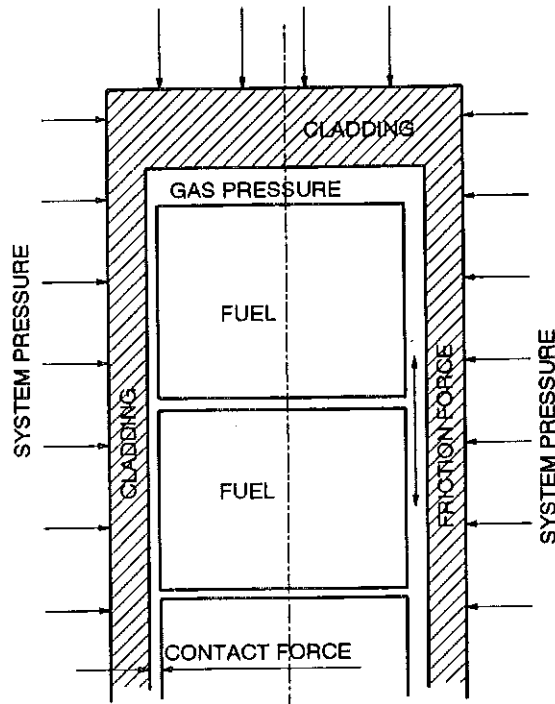
Fig. D1-1: Fuel pin model

D2. Method of Solution

The mechanical problem, i. e. computation of the stress and strain fields in the individual fuel rod components, is solved by use of the Finite Element Method (FEM). This method generally operates by dividing a structure with a complex geometry into a number of well defined finite elements. In most cases, these elements are simple, regular geometric elements such as triangular and rectangular elements for plane structures or toroidal elements with triangular or square cross-sections for axial-symmetric structures such as the fuel rod to be considered here. With this "idealization" made, the structure is practically no longer a solid continuum, but a system of individual elements, which are interlinked at their nodal points. The equations for description of the equilibrium and the continuity at the nodes of the elements together with the stress-strain relations make up a system of linear equations. This system of equations can be solved using given boundary conditions so that the displacements of each individual node and the stress acting in each element can be determined.

D3. Idealization of the Structure, Choice of the Elements

The fuel rod model represented in Fig. D.1-1 will now be idealized according the FEM requirements.

The real fuel rod, consisting mainly of breeder material/fuel, plenum, gas gap and cladding, is divided into a finite number of axial segments. These axial segments are characterized by the fact that no axial changes of the external forces, pressures and temperatures occur within them. Consequently, analysis of the fuel rod is made consecutively and separately for each axial segment. As the computations are the same for each segment, all the following considerations will be restricted to analyzing one segment which will be representative of the fuel rod.

The axial segment of the fuel rod to be analyzed is divided into finite elements as shown in Fig. D3-1: i.e. the structure is idealized. In the case under scrutiny the procedure is that both the cladding and the fuel are represented as concentric rings. The external forces acting on the fuel and the cladding are also schematically represented and shown in Fig. D3-1.

The separate representation of the chosen type of finite element, namely a torus with rectangular cross-section, is evident from Fig. D3-2.

Figure D3-3 shows the position of the element within the structure and the designation of the nodal points. The nodal point coordinates for the i-th element are:

> node 1: (r_1, z_1)
> node 2: (r_2, z_2)
> node 3: (r_3, z_3)
> node 4: (r_4, z_4)

It is agreed that in order to further simplify the element loads the description of shear stresses and slidings will be dispensed with. This means that the orthogonality of the elements is always maintained.

The simplification implies that all components of the four nodal point coordinates are no longer needed to define the ring element above, only four of them, namely r_1, r_2, z_1, z_3. Consequently, the element coordinates become:

> node 1: (r_1, z_1)
> node 2: (r_2, z_1)
> node 3: (r_2, z_3)
> node 4: (r_1, z_3)

Moreover, in the analysis of an axial segment or - in FEM terms - in a system of local coordinates the axial coordinate z_1 can be set $z_1 = 0$ without any restriction of the general validity so that the element is finally defined by:

node 1: $(r_1, 0)$

node 2: $(r_2, 0)$

node 3: (r_2, z_3)

node 4: (r_1, z_3)

Again, this definition is equivalent to describing a torus with rectangular cross-section by specification of its inner radius, outer radius and axial height. Therefore, in the following description the terms "element node," "structural node" etc., (as currently used in the literature on FEM), will no longer be used. Instead, reference will be made in a more illustrative way to elemental radii, etc.
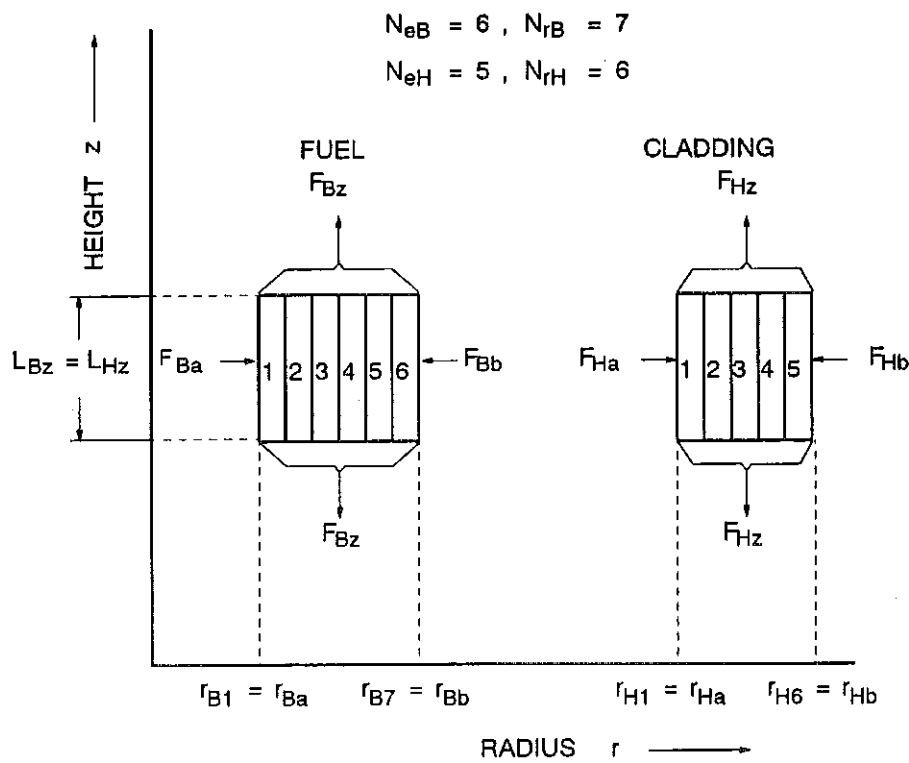
Fig. D3-1: Idealization of one axial node of a fuel pin structure
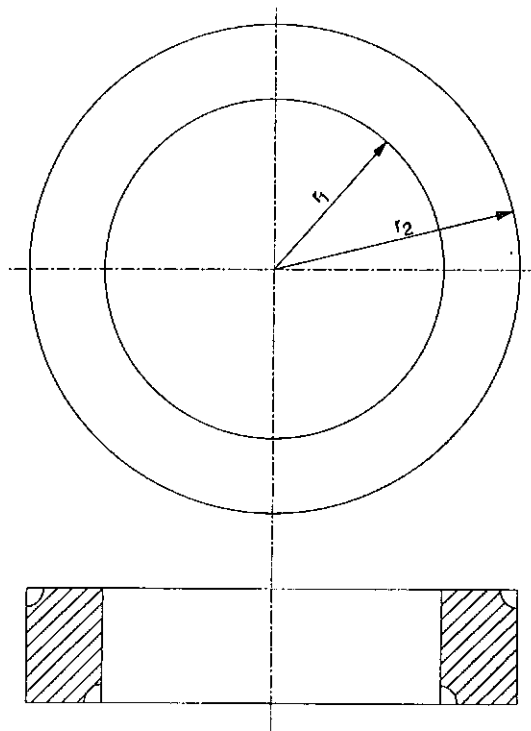
Fig. D3-2: Ring element with rectangular cross section
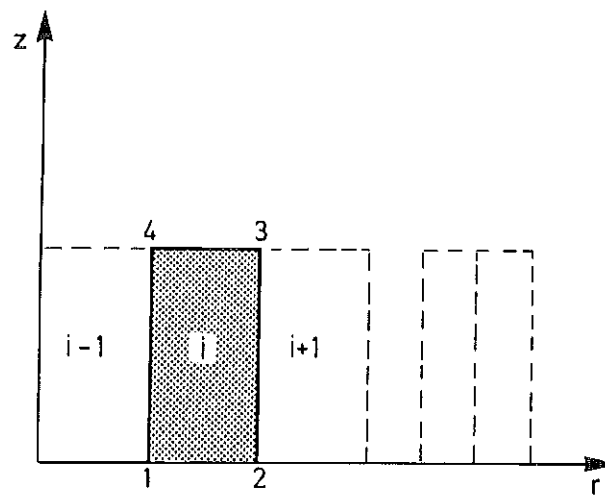
Fig. D3-3: Position of the i-th element within the structure

D4. Element Mechanics - From the Displacement Equations to the Matrix of the Shape Functions

This section describes one of the essential features of the Finite Element Method, i.e. the derivation of the shape functions from the general element displacements. The results will be the strain/displacement notations for cylindrycally shaped bodies, i.e. familiar equations. The procedure used by FEM is a general approach which leads to the above result. The approach has universal applicability beyond the scope of this report

The element position and shape is changed by thermal influence or external forces which means that each point within the element undergoes displacement. This displacement of a general element point is represented in the FEM notation as a function of the displacement of the defined nodal points.

Let us set up the shape functions for the selected element which has a nodal point at each of the four corners. If two degrees of freedom of the translation, namely in the r and z directions, are assumed for each element point, then displacements in r and z directions can be described by the following displacement equations:

$$u_r(r,z) = b_1 + b_2 \cdot r + b_3 \cdot z + b_4 \cdot r \cdot z \tag{D4-1}$$

$$u_z(r,z) = b_5 + b_6 \cdot r + b_7 \cdot z + b_8 \cdot r \cdot z \tag{D4-2}$$

This approach yields for the nodal points:

$$u_{1r} = b_1 + b_2 \cdot r_1 + b_3 \cdot z_1 + b_4 \cdot r_1 \cdot z_1$$

$$u_{2r} = b_1 + b_2 \cdot r_2 + b_3 \cdot z_2 + b_4 \cdot r_2 \cdot z_2$$

$$u_{3r} = b_1 + b_2 \cdot r_3 + b_3 \cdot z_3 + b_4 \cdot r_3 \cdot z_3$$

$$u_{4r} = b_1 + b_2 \cdot r_4 + b_3 \cdot z_4 + b_4 \cdot r_4 \cdot z_4$$

$$u_{1z} = b_5 + b_6 \cdot r_1 + b_7 \cdot z_1 + b_8 \cdot r_1 \cdot z_1 \tag{D4-3}$$

$$u_{2z} = b_5 + b_6 \cdot r_2 + b_7 \cdot z_2 + b_8 \cdot r_2 \cdot z_2$$

$$u_{3z} = b_5 + b_6 \cdot r_3 + b_7 \cdot z_3 + b_8 \cdot r_3 \cdot z_3$$

$$u_{4z} = b_5 + b_6 \cdot r_4 + b_7 \cdot z_4 + b_8 \cdot r_4 \cdot z_4$$

and written as a matrix

$$\{u\} = |A| \cdot \{b\} \tag{D4-4}$$

Now the system of equations (D4-4) must be solved with respect to the vector $\{b\}$ which means that b_1 through b_8 have to be determined as

$$\{b\} = |A^{-1}| \cdot \{u\} \tag{D4-5}$$

The solutions b_1 through b_4 for the general approach read:

$$b_4 = \frac{1}{N_4} \left| u_{1r}(z_4 - z_3) - u_{3r}(z_4 - z_1) + u_{4r}(z_3 - z_1) \right| \tag{D4-6}$$

with

$$N_4 = (r_3 z_3 - r_1 z_1)(z_4 - z_1) - (r_4 z_4 - r_1 z_1)(z_3 - z_4)$$

$$b_3 = \frac{1}{N_3} \left\{ (r_2 - r_3)u_{1r} - |(r_2 - r_3) + (r_1 - r_2)|u_{2r} + (r_1 - r_2) \cdot u_{3r} \right\} \tag{D4-7}$$

with

$$N_3 = (z_1 - z_2)(r_2 - r_3) + (z_2 - z_3)(r_1 - r_2)$$

$$b_2 = \frac{1}{N_2} \left\{ |N_3 - (r_1 - r_3)(z_1 - z_2)| \cdot u_{1r} - |N_3 + (z_1 - z_2)(r_1 - r_3)| \cdot u_{2r} + \right.$$
$$\left. + (z_1 - z_2)(r_1 - r_2) \cdot u_{3r} \right\} \tag{D4-8}$$

with

$$N_2 = N_3 \cdot (r_1 - r_2)$$

$$b_1 = u_{1r} - b_2 \cdot r_1 - b_3 \cdot z_1 - b_4 \cdot r_1 z_1 \tag{D4-9}$$

The solutions for b_5 through b_8 correspond to those for b_1 through b_4.

If the general validity of the approach written above is restricted such that no general square element, but a rectangular element is defined which is characterized by

- the element sides always being parallel to the axis,
- the four right-angles being maintained,
- the z-coordinates of the first two nodes being $z_1 = z_2 = 0$,

the following simplifications are obtained; see Fig. D3-3:

$$r_4 = r_1$$
$$r_3 = r_2$$
$$u_{1z} = u_{2z} = 0$$
$$u_{4r} = u_{1r}$$
$$u_{4z} = u_{3z}$$
$$u_{3r} = u_{2r}$$

(D4-10)

Thus, the first four equations of the system (D4-3) can be written:

$$u_{1r} = b_1 + b_2 \cdot r_1 + b_3 \cdot 0 + b_4 \cdot 0$$
$$u_{2r} = b_1 + b_2 \cdot r_2 + b_3 \cdot 0 + b_4 \cdot 0$$
$$u_{3r} = b_1 + b_2 \cdot r_3 + b_3 \cdot z_3 + b_4 \cdot r_3 \cdot z_3$$
$$u_{4r} = b_1 + b_2 \cdot r_4 + b_3 \cdot z_4 + b_4 \cdot r_4 \cdot z_4$$

(D4-11)

and

$$\{u_r\} = \begin{bmatrix} 1 & r_1 & 0 & 0 \\ 1 & r_2 & 0 & 0 \\ 1 & r_2 & z_3 & r_2 z_3 \\ 1 & r_1 & z_3 & r_1 z_3 \end{bmatrix} \cdot \{b\}$$

(D4-12)

resp.

This system of equations can be solved with respect to:

$$\{b\}_r = \frac{1}{z_3 (r_2 - r_1)} \cdot \begin{bmatrix} r_2 z_3 & -r_1 z_3 & 0 & 0 \\ -z_2 & z_2 & 0 & 0 \\ -r_2 & r_1 & -r_1 & r_2 \\ 1 & -1 & 1 & -1 \end{bmatrix} \cdot \{u_r\}$$

(D4-13)

Thus, the displacement of any point (r,z) of the element in radial direction can be described as follows:

$$u_r (r,z) = \frac{1}{N} \cdot \Big| u_{1r} \ (r_2 z_3 - r \cdot z_3 - z \cdot r_2 + r \cdot z) +$$

$$+ u_{2r} \ (-r_1 z_3 + r \cdot z_3 + z \cdot r_1 - r \cdot z) +$$

(D4-14)

$$+ u_{3r} \ (-z \cdot r_1 + r \cdot z) + u_{4r} (z \cdot r_2 - r \cdot z) \Big|$$

with $\quad N = z_3 (r_2 - r_1)$

The system of equations describing the displacements in z-direction yields a result corresponding to (D4-13):

$$\{b\}_z = \frac{1}{N} \cdot \begin{bmatrix} r_2 z_3 & -r_1 z_3 & 0 & 0 \\ -z_3 & z_3 & 0 & 0 \\ -r_2 & r_1 & -r_1 & r_2 \\ 1 & -1 & 1 & -1 \end{bmatrix} \cdot \{u_z\} \qquad \text{(D4-15)}$$

Using the rest of boundary conditions from (D4-10), we finally obtain:

$$\{b\}_z = \frac{1}{N} \cdot \begin{bmatrix} 0 & 0 & 0 & 0 \\ 0 & z_2 & 0 & 0 \\ 0 & (r_2 - r_1) & 0 & 0 \\ 0 & 0 & 0 & 0 \end{bmatrix} \cdot \{u_z\} \qquad \text{(D4-16)}$$

For any point in the element the equation describing the displacement in z-direction according to (D4-2) now reads in explicit terms:

$$u_z(r,z) = \frac{u_{3z}}{z_3} \cdot z \qquad \text{(D4-17)}$$

Thus, the displacement vector reads:

$$\{u(r,z)\} = \begin{bmatrix} \dfrac{r_2 - r}{r_2 - r_1} & \dfrac{r - r_1}{r_2 - r_1} & 0 \\ \\ 0 & 0 & \dfrac{z}{z_3} \end{bmatrix} \cdot \left\{ \begin{array}{c} u_{1r} \\ u_{2r} \\ u_{3z} \end{array} \right\} \qquad \text{(D4-18)}$$

The following familiar relationships apply between displacements and strains:

$$\varepsilon_r = \frac{\partial u_r}{\partial r}$$

$$\varepsilon_t = \frac{u_r}{r}$$

$$\varepsilon_z = \frac{\partial u_z}{\partial z} \qquad \text{(D4-19)}$$

$$\varepsilon_{rz} = \frac{\partial u_r}{\partial z} + \frac{\partial u_z}{\partial r}$$

Thus, an equation system (D4-18) is obtained which provides the relationship existing between strains and displacements of the nodal points:

$$\varepsilon_r = \frac{1}{r_2 - r_1} \cdot (u_{2r} - u_{1r}) \tag{D4-20}$$

$$\varepsilon_t = \frac{1}{r_1 - r_2} \cdot (u_{1r} - u_{2r}) \tag{D4-21}$$

$$\varepsilon_z = \frac{u_{3z}}{z_3} \tag{D4-22}$$

$$\varepsilon_{rz} = 0 \tag{D4-23}$$

Equation (D4-23) implies once more that no sliding is taken into consideration. This was assumed already in defining the rectangular element.

For simplification, new subscripts will be introduced in the subsequent considerations. The following definitions will hold:

r_a, r_b: inner and outer radii, resp., of the element

u_{ra}, u_{rb}:   displacements on the inner and outer boundary, resp., of the element

ℓ_z: axial length of the element

u_z: axial displacement

Thus, the system of equations for the elemental strains reads:

$$\{\varepsilon\} = \left\{ \begin{array}{c} \varepsilon_r \\ \varepsilon_t \\ \varepsilon_z \end{array} \right\} = \begin{bmatrix} \dfrac{1}{r_a - r_b} & \dfrac{-1}{r_a + r_b} & 0 \\ \dfrac{1}{r_a + r_b} & \dfrac{1}{r_a + r_b} & 0 \\ 0 & 0 & \dfrac{1}{\ell_z} \end{bmatrix} \cdot \left\{ \begin{array}{c} u_{ra} \\ u_{rb} \\ u_{ra} \end{array} \right\} \tag{D4-24}$$

Formally, equation (D4-24) can be written as follows:

$$\{\varepsilon\} = |C| \cdot \{u\} \tag{D4-25}$$

with the matrix [C] as the matrix of the shape functions; see equations (D4-3), (D4-13) and (D4-14). It actually interlinks strains in the element, represented by the strain vector $\{\varepsilon\}$, with the displacements of the element nodal points described by the vector $\{u\}$.

It was stated at the beginning of this section that familiar strain/displacement relations would be obtained at the end of it. These relations are shown in equation (D4-24) after multiplication of the right side and substitution of the derived function for the difference quotient. Then, one obtains:

$$\varepsilon_{rr} = \frac{u_{rb} - u_{ra}}{r_b - r_a} = \frac{\Delta u}{\Delta r} \approx \frac{\partial u_r}{\partial r} \tag{D4-26}$$

$$\varepsilon_{tt} = \frac{u_{ra} - u_{rb}}{r_a + r_b} = \frac{\frac{1}{2}(u_{ra} + u_{rb})}{\frac{1}{2}(r_a + r_b)} \approx \frac{\bar{u}}{\bar{r}} = \frac{u}{r} \tag{D4-27}$$

$$\varepsilon_{zz} = \frac{u_z}{\ell_z} = \frac{u_z - u_{z0}}{\ell_z - 0} = \frac{\Delta u_z}{\Delta z} \approx \frac{\partial u_z}{\partial z} \tag{D4-28}$$

D5. Description of the Material Behavior

D5.1 General Remarks

It has been demonstrated in the preceding section how the element strains can be calculated using the displacements of the nodal points. The strains will be now discussed in more detail. Various types of strain will be described in this section which finally can all be grouped into two categories, socalled "stress associated" and "thermal" strains. The following types of strain will be investigated in detail here:

- elastic strain,
- non-elastic strain,
- thermal strain,
- irradiation induced strain.

All these individual strain components make up the total strain which, as has been shown in the preceding section, can be determined from the nodal displacements.

If one examines the mechanical characteristics - stresses and strains - of a fuel rod in operation, it will be seen that these two variables undergo permanent variation.

However, the usually standard description of the material behavior always relate to a state in which at least one of these variables is constant.

The approach adopted here takes into account the transient mechanical behavior. As main characteristic the derivatives w.r.t. time (i.e. rates) are taken and not the basic variables of strain, stress and force. These are calculated by integration at desired points in time.

D5.2 Elastic Strain

The elastic strain rate is described by differentation of Hooke's law with respect to time:

$$\{\dot{\varepsilon}_{e\ell}\} = \frac{d}{dt}\{\varepsilon_{e\ell}\} = [A_{e\ell}] \cdot \{\frac{\partial \sigma}{\partial t}\} + \frac{\partial}{\partial t}([A_{e\ell}]) \cdot \{\sigma\} \tag{D5-1}$$

explicitly represented for the adopted cylinder geometry:

$$\{\dot{\varepsilon}_{e\ell}\} = \frac{1}{E}
\begin{bmatrix}
1 & -\nu & -\nu \\
-\nu & 1 & -\nu \\
-\nu & -\nu & 1
\end{bmatrix}
\cdot
\begin{Bmatrix}
\dot{\sigma}_r \\
\dot{\sigma}_t \\
\dot{\sigma}_z
\end{Bmatrix}
\tag{D5-2}$$

Formally, the relationship between the vector of the stress rates and the vector of the strain rates reads:

$$\{\dot{\varepsilon}_{e\ell}\} = [A_{e\ell}] \cdot \{\dot{\sigma}\} \tag{D5-3}$$

Regarding the formulation of equations (D5-1) through (D5-3), it should be added that the strain and stress rates treated here as vectors are evidently to be described as tensors in the general representation. With the assumptions postulated in the preceding section that e.g. no shear strains and no shear stresses will be taken into account, only the positions of the main diagonals are still occupied by elements different from zero for the corresponding tensors. These elements will be represented as column vectors for the sake of simplicity and clarity.

The matrix $[A_{e\ell}]$ is termed the compliance or flexibility matrix of the elastic strains. This term is self evident as the expression $[A_{e\ell}]$ becomes smaller with an increase in the Young's modulus term in the denominator, and vice versa. The Young's modulus of course describes the rigidity or stiffness of a system. It will be

shown later on how the element or structural stiffness is calculated by inversion of the flexibility matrices.

D5.3 Non-elastic Material Behaviour

D5.3.1 General Assumptions

For the description of the non-elastic material behavior the hypothesis of the equivalent stress according to the Von Mises and Prandtl-Reuss equations will be used to describe the relationship existing between the stress and the plastic strain increment [D5-1]:

$$\left(\frac{\partial \varepsilon_i}{\partial \varepsilon_v}\right)_{plast} = \left(\frac{\partial \sigma_v}{\partial \sigma_i}\right) \tag{D5-4}$$

where

ε_i: components of the strain vector

ε_v: strain in uniaxial equivalent coordinates

σ_v: Von Mises equivalent stress

σ_i: components of the stress vector

Equation (D5-4) can be re-formulated to read:

$$\dot{\varepsilon}_{i_{ne}} = \frac{\partial \sigma_v}{\partial \sigma_i} \cdot \dot{\varepsilon}_v \tag{D5-5}$$

and written as a matrix:

$$\{\dot{\varepsilon}_{ne}\} = |A_{ne}| \cdot \dot{\varepsilon}_v \tag{D5-6}$$

Now any material law having the form

$$\dot{\varepsilon}_v = f_{ev}(\sigma, \varepsilon, ...) \tag{D5-6a}$$

can be expressed according to equation (D5-6) for the description of non-elastic strain.

The time-dependent nonelastic material behaviour is described in the SATURN-FS code by means of a viscoplastic approach. This approach is based on a model of Gittus [D5-2, D5-3, D5-4], modified by Duncombe et al. [D5-5, D5-6] for the

CYGRO fuel pin behaviour code. An own version [D5-7, D5-8] was written for SATURN-FS.

The derivation of these equations and their usefulness in analyzing structures under transient loads have been described in detail [D5-7]. Only a summarizing survey will be presented here.

The approach is very similar to the strain-hardening method. But the total non-elastic strain is divided into two parts, a "hardening" and a "non-hardening" or recovery portion. The model is based on time-independent characteristics:

- The creep rate in the secondary range, represented as

$$\dot{\varepsilon}_S = u \cdot \sigma^v \tag{D5-7}$$

- The non-elastic strain associated with material hardening, (strain hardening strain) represented as

$$\varepsilon_{SHO} = x \cdot \sigma^y \tag{D5-8}$$

which means that any material, for example under a constant tensile stress, finally shows even after a time a rate of deformation which satisfies equation (D5-7) and a strain hardening strain according to equation (D5-8). At any earlier in time, the rate of deformation is greater than $\dot{\varepsilon}_S$, namely $\dot{\varepsilon}_v$. The actual hardening strain is smaller than ε_{SHO} and will be termed ε_{SH} thereafter. Thus, the following relationship can be derived:

$$\dot{\varepsilon}_v = \dot{\varepsilon}_S \cdot \left(\frac{\varepsilon_{SH}}{\varepsilon_{SHO}} \right)^{v3} \tag{D5-9}$$

The quotient $(\varepsilon_{SH}/\varepsilon_{SHO})$ can also be termed degree of hardening.

The parameters x, y, u, v and v3, which can be derived either from materials' laws or from experiment have to be read in into the code input in the form of tabulated values for predefined temperatures, burnups and fissioning rates. This means a rather great flexibility for the user. It is possible to take into account any material, only by changeing the input parameters. But with this approach it was not yet possible to describe the viscoplastic material behaviour in SATURN-FS in a closed form by one expression as a function of stresses, temperatures and fission rates or neutron fluxes. So, the actual values were calculated by interpolations of tabulated values. These again must have been determined at defined boundary conditions by experimental data.

This disadvantage has been compensated. The interpolation of the tabulated values can be omitted by user´s option.

D5.3.2 Derivation of the Materials Equations

D5.3.2.1 Fuel

- Secondary creep rate:

The secondary creep portion with its constant rate is described in SATURN-FS by the FCREEP subroutine.

For FBR-mixed oxide fuel this is performed by the Interatom creep formula [D5-9] based on investigations of J.T.A. Roberts et al. [D5-10].

- Thermal creep

$$\dot{\varepsilon}_T = (1 + 1250 \cdot P^2) \cdot 2,67 \cdot 10^7 e^{-45000/T} \cdot sinh\,(1,5\,\frac{\sigma_v}{T \cdot d^2} \cdot e^{-10320/T}) \tag{D5-10}$$

with:

$\dot{\varepsilon}_T$	=	secondary thermal creep rate	[h^{-1}]
P	=	actual fuel porosity	[-]
T	=	fuel temperature	[K]
σ_v	=	equivalent stress	[N / cm^2]
d	=	grain diameter	[cm]

- Irradiation creep:

$$\dot{\varepsilon}_B = (5,366 \cdot 10^{-25}) + 2,84 \cdot 10^{-21} e^{-6895/T}) \cdot \dot{\phi} \cdot \sigma_v \tag{D5-11}$$

With:

$\dot{\varepsilon}_B$	=	irradiation creep rate	[h^{-1}]
T	=	fuel temperature	[K]
σ_v	=	equivalent stress	[N / cm^2]
$\dot{\phi}$	=	fission rate	[fiss / cm$^2 \cdot$ s]

- Total creep rate:

$$\dot{\varepsilon}_{S,ges} = \dot{\varepsilon}_T + \dot{\varepsilon}_B \tag{D5-12a}$$

The description of UO$_2$ secondary creep is done according to MATPRO-11 [D5-11]

$$\dot{\varepsilon}_S [h^{-1}] = (\frac{1,411 \cdot 10^{-3}}{(\rho - 0,877) \cdot d^2} + 1,131 \cdot 10^{-20} \phi \cdot e^{-4103/T} + 1,349 \cdot 10^{-23} \dot{\phi}) \cdot \sigma$$

$$+ \frac{7,285 \cdot 10^{-6}}{\rho - 0,905} \cdot e^{-6600/T} \cdot \sigma_v^{4,5} \tag{D5-12b}$$

with

$\dot{\varepsilon}_s$ = secondary thermal creep rate [h^{-1}]

ρ = relative fuel density   [-]

$\dot{\phi}$ = fission rate   [fiss / (cm$^3 \cdot$ s)]

σ_v = equivalent stress   [N/cm^2]

d = grain diameter   [cm]

- Strain hardening and recovery, primary creep

According to the materials date and correlations, collected by Steinmetz and Fenneker [D5-9], fuel creep is modeled by adding a time-independent portion of deformation to the secondary creep $\dot{\varepsilon}_S$. This is done by the method of the so-called "pre-run time".

This pre-run time, multiplied by the steady state creep rate results in an instantaneous portion of the creep strain, or in a plastic strain, resp.

This portion of strain equals the limit of the strain hardening strain ε_{SHO} as described above.

$$\varepsilon_{SHO} = 2{,}5 \cdot 10^{-5} \cdot \dot{\varepsilon}_S \cdot e^{12000/TK} \qquad \text{(D5-13)}$$

The strain hardening strain as a function of time may be described as follows:

$$\varepsilon_{SH}(t) = \varepsilon_{SHO} (1 - e^{k' \cdot t}) \qquad \text{(D5-14)}$$

Sometimes, in the literature a strain hardening factor h is defined:

$$h = \frac{\varepsilon_{SH}}{\varepsilon_{SHO}} \qquad \text{(D5-15a)}$$

or

$$h(t) = 1 - e^{-k't} \qquad \text{(D5-15b)}$$

The strain hardening rate is the time-derivative of Eq. (D5-14):

$$\dot{\varepsilon}_{SH}(t) = k' \cdot \varepsilon_{SHO} \cdot e^{-k't} \qquad \text{(D5-16)}$$

The following boundary conditions are valid:

for t = 0: $\dot{\varepsilon}_{SH}(0) = k' \cdot \dot{\varepsilon}_{SHO}$ (D5-17a)

where $\dot{\varepsilon}_{SH}(0) \gg \dot{\varepsilon}_{S}$ (D5-17b)

or $\dot{\varepsilon}_{SH}(0) = k \cdot \dot{\varepsilon}_{S}$ (D5-17c)

Setting equal Eq. (D5-17a) and Eq. (D5-17c), one gets

$$k' \cdot \dot{\varepsilon}_{SHO} = k \cdot \dot{\varepsilon}_{S}$$

$$k' = k \cdot \frac{\dot{\varepsilon}_{S}}{\dot{\varepsilon}_{SHO}} \qquad (D5\text{-}18)$$

The expression for k' in Eq. (D5-18) can be inserted into Eqs.(D5-14, -15, and -16) :

$$\varepsilon_{SH}(t) = \varepsilon_{SHO}\,(1 - e^{-k \cdot \frac{\dot{\varepsilon}_{S}}{\dot{\varepsilon}_{SHO}} t}\,) \qquad (D5\text{-}19a)$$

$$\dot{\varepsilon}_{SH}(t) = k \cdot \dot{\varepsilon}_{S} \cdot e^{-k \cdot \frac{\dot{\varepsilon}_{S}}{\dot{\varepsilon}_{SHO}} t} \qquad (D5\text{-}19b)$$

The time t as the independent variable in Eqs. (D5-19a and -19b) can be replaced and the equations can be rearranged:

$$t = - \frac{\varepsilon_{SHO}}{k \cdot \dot{\varepsilon}_{S}} \cdot \ell n \,(\frac{\dot{\varepsilon}_{SH}}{k \cdot \dot{\varepsilon}_{S}}) \qquad (D5\text{-}20)$$

$$\dot{\varepsilon}_{SH}\,(\varepsilon_{SH}) = k \cdot \dot{\varepsilon}_{S}\,(1 - \frac{\varepsilon_{SH}}{\varepsilon_{SHO}}) \qquad (D5\text{-}21)$$

$$\varepsilon_{SH} = \varepsilon_{SHO}\,(1 - \frac{\dot{\varepsilon}_{SH}}{k \cdot \dot{\varepsilon}_{S}}) \qquad (D5\text{-}22)$$

The time-dependent recovery taking place in a material under consideration can be described by a "recovery strain" or its rate $\dot{\varepsilon}_{R}$ (see also (D5-4, -5, -7)).

$$\dot{\varepsilon}_{R} = h \cdot \dot{\varepsilon}_{S} \qquad (D5\text{-}23a)$$

or

$$\dot{\varepsilon}_R = \frac{\varepsilon_{SH}}{\varepsilon_{SH0}} \cdot \dot{\varepsilon}_S \qquad \text{(D5-23b)}$$

It can be seen from Eq. (D5-23b), that at the beginning of the deformation, when $\varepsilon_{SH} = 0$, the recovery strain rate $\dot{\varepsilon}_R = 0$. At this time, the main mechanism is strain hardening. But when h = 1 ($\varepsilon_{SH} = \varepsilon_{SH0}$), i.e. the material has reached its final strain hardening under the existing conditions the recovery strain rate is $\dot{\varepsilon}_R = \dot{\varepsilon}_S$, which is the rate of steady state creep. The nonelastic deformation behaviour shall be described so, that the total nonelastic strain is composed from a "hardening" and a "softening" term.

$$\varepsilon_v = \varepsilon_{SH} + \varepsilon_R \qquad \text{(D5-24a)}$$

or

$$\dot{\varepsilon}_v = \dot{\varepsilon}_{SH} + \dot{\varepsilon}_R \qquad \text{(D5-24b)}$$

Regarding Eqs. (D5-21) and (D5-23), the total deformation rate is:

$$\dot{\varepsilon}_v = k \cdot \dot{\varepsilon}_S (1 - \frac{\varepsilon_{SH}}{\varepsilon_{SH0}}) + \dot{\varepsilon}_S \cdot \frac{\varepsilon_{SH}}{\varepsilon_{SH0}} \qquad \text{(D5-25)}$$

Rearrangement results in:

$$\dot{\varepsilon}_v = \dot{\varepsilon}_S [k - \frac{\varepsilon_{SH}}{\varepsilon_{SH0}} (k - 1)] \qquad \text{(D5-26)}$$

Eq. (D5-26) can be interpreted as follows:

for t = 0, i.e. for $\varepsilon_{SH} = 0$ the total deformation rate is only consisting of the hardening portion

$$\dot{\varepsilon}_v(0) = \dot{\varepsilon}_S \cdot k \overset{\wedge}{=} \dot{\varepsilon}_{SH}(0) \qquad \text{(D5-27)}$$

The steady state will be reached for $\varepsilon_{SH} \to \varepsilon_{SH0}$. This state is described by Eq. (D5-26) as:

$$\dot{\varepsilon}_v(\varepsilon_{SH} = \varepsilon_{SH0}) = \dot{\varepsilon}_S \qquad \text{(D5-28)}$$

So the complete description of viscoplastic fuel behaviour is possible.

D5.3.2.2 Cladding Material

- **Zircaloy**

When evaluating cladding creep test results with respect to the secondary creep region (D5-12, -13, -14, -15) can be well interpreted by the quasi-theoretical approach according to Dorn [D5-16]. It reads:

$$\frac{\dot{\varepsilon}_S \cdot k \cdot T}{D \cdot E \cdot b} = c_1 \cdot e^{c_2 \cdot \sigma/E} \tag{D5-29}$$

With

$\dot{\varepsilon}_S$	=	secondary creeprate
k	=	Boltzmann-constant $= 1{,}38020 \cdot 10^{-23}$ J/K
T	=	temperature in K
D	=	$D_0 \cdot e^{-Q/RT}$ with $D_0 = 5 \cdot 10^{-4}$ m^2/s
Q	=	activation energy $= 2{,}594 \cdot 10^{-5}$ J/mol
R	=	universal gas constant $= 8{,}314$ J / (mol $\cdot$ K)
E	=	Youngs modulus
b	=	burgersvector (lattice parameter) $= 3{,}232 \cdot 10^{-10}$ m
c_1, c_2	=	empirical factors
c_2	=	2620
c_1	=	dimension factor $= 4{,}60 \cdot 10^{-5}$, if E is given in N/m^2 and $\dot{\varepsilon}_s$ in h^{-1}

Eq. (D5-29) can be solved for $\dot{\varepsilon}_s$:

$$\dot{\varepsilon}_s \,[h^{-1}] = 5{,}381 \cdot 10^9 \; E/T \cdot e^{c_2 \cdot \sigma/E - Q/RT} \tag{D5-30}$$

As usually in SATURN-FS, the required input dimension for E is N/cm^2. The numeric values in the formula given above are only valid for a special type of Zircaloy, the factors must be adjusted to the material.

The maximum portion of hardening can be determined in the same way as for the fuel.

$$\dot{\varepsilon}_{SH0} = a_1 \cdot \dot{\varepsilon}_S \cdot e^{a_2/T} \tag{D5-31}$$

with $a_1 = 4{,}16 \cdot 10^{-6}$

$a_2 = 12500$

T = temperature in K

$\dot{\varepsilon}_s$ = secondary creep rate in h^{-1}

ε_{SH0} = limit of the strain hardening strain

As for the fuel, the irradiation creep term is added:

$$\dot{\varepsilon}_s = \dot{\varepsilon}_{s_{th}} + \dot{\varepsilon}_{s_{irr}} \qquad \text{(D5-32)}$$

with

$$\dot{\varepsilon}_{s_{irr}} = 4{,}35 \cdot 10^{-25} \cdot \sigma \cdot \dot{\phi} \qquad \text{(D5-33)}$$

with

$\dot{\phi}$ = fast flux in n/(cm^2 · s)

σ = stress in N/cm^2

The term $k = \dot{\varepsilon}_V / \dot{\varepsilon}_S$ for t = 0 has to be determined. For the Zircaloy under consideration it was determined according to Murty et al. [D5-13, -14] to

$$k = 8{,}5 \qquad \text{(D5-34)}$$

So a complete description of the viscoplastic behaviour of Zircaloy is also possible.

* Austenitic stainless steel for FBR fuel pins

Only secondary cladding creep was so far taken into accont in FBR analyses. No hardening or recovery models were used. This is justified by the fact, that the in-pile creep of stainless steel cladding tubes is dominated by irradiation creep. This results in a time-independent constant creep rate, which can be regarded as a part of the secondary creep rate. Hardeining effects are of less importance but they can be modeled for completeness. For this purpose creep tests with the stainless steel, material no. 1.4970 were evaluated. From these tests the strain hardening limit could be determined:

$$\varepsilon_{SH0} = 2{,}05 \cdot 10^{-5} \cdot \dot{\varepsilon}_S [h^{-1}] \cdot e^{13400/T} \qquad \text{(D5-35)}$$

with T in [K].

D5.3.3 Anisotropic Material Behaviour

The Von Mises equivalent stress σ_v as used in equations (D5-4) and (D5-5) will be applied here in its generalized form in order to take into account anisotropic effects in the material, according to [D5-5]:

$$\sigma_v = \frac{1}{\sqrt{RP+P}} \sqrt{R(\sigma_r - \sigma_t)^2 + RP(\sigma_t - \sigma_z)^2 + P(\sigma_z - \sigma_r)^2} \qquad (D5\text{-}36)$$

The normalization factor $\sqrt{RP+P}$ is introduced so that the value of generalized stress σ_v is equal to the axial stress σ_z when σ_r and σ_t are zero.

With $R = P = 1$, the above formula describes isotropic material behaviour.

For a thin-walled tube the constants P and R can be determined from the following special cases of loading:

- Uniaxial tensile test in z-direction:

  where: $\sigma_v = \sigma_z, \sigma_r = \sigma_t = 0$.

On the basis of the Prandtl-Reuss equations, see eqs. (D5-4) and (D5-5), the following relationship holds (see [D5-20] and [D5-21]):

$$\begin{Bmatrix} \Delta\varepsilon_r \\ \Delta\varepsilon_t \\ \Delta\varepsilon_z \end{Bmatrix} = \frac{\Delta\varepsilon_v}{\sigma_v} \frac{1}{P(R+1)} \begin{bmatrix} R+P & -R & -P \\ -R & R(P+1) & -RP \\ -P & -RP & P(R+1) \end{bmatrix} \begin{Bmatrix} \sigma_r \\ \sigma_t \\ \sigma_z \end{Bmatrix} \qquad (D5\text{-}37)$$

Thus, for uniaxial loading the following relation is valid:

$$R = \frac{\Delta\varepsilon_t}{\Delta\varepsilon_R} \qquad (D5\text{-}38a)$$

- Biaxial stress state:

In the case of thin-walled tubes under internal pressure there is approximataly a biaxial stress state ($\sigma_r \approx 0$) so that the following expression can be derived from equation (D5-37):

$$\frac{\Delta\varepsilon_t}{\Delta\varepsilon_z} = \frac{\frac{P+1}{P} \cdot \alpha - 1}{\frac{R+1}{R} - \alpha} \qquad with \quad \alpha = \frac{\sigma_t}{\sigma_z} \qquad (D5\text{-}38b)$$

For the special case of the thin-walled tube exposed to internal pressure and $\alpha = 2$, we obtain:

$$\frac{\Delta \varepsilon_t}{\Delta \varepsilon_z} = \frac{R(P+2)}{P(1-R)}$$

(D5-38c)

Using equations (D5-37) through (D5-38c) we can determine quite conveniently the anisotropic factors R and P for thin-walled tubes in tensile and internal pressure tests.

The description of the anisotropic behavior and calculation of an equivalent stress according to the procedure described here by introduction of two parameters R and P constitutes a useful approach in so far as familiar equations, such as the equation for the Von Mises equivalent stress, are used. However, the derivation explained here contains the restriction that the R and P values are the same for tension and compression.

Using equation (D5-36), equation (D5-6) can be written explicitly

$$\{\dot{\varepsilon}_{ne}\} = \frac{1}{(RP+P) \cdot \sigma_v} \begin{bmatrix} (R+P)\sigma_r & -R\sigma_t & -P\sigma z \\ -R\sigma_r + & (R+RP)\sigma_t & -RP\sigma z \\ -P\sigma_r - & RP\sigma_t & +(RP+P)\sigma z \end{bmatrix} \cdot \dot{\varepsilon}_v$$

(D5-39a)

and

$$\{\dot{\varepsilon}_{ne}\} = \frac{1}{(RP+P) \cdot \sigma_v} \begin{bmatrix} R+P & -R & -P \\ -R & R+RP & -RP \\ -P - RP & RP+P \end{bmatrix} \cdot \begin{Bmatrix} \sigma_r \\ \sigma_t \\ \sigma_z \end{Bmatrix} \cdot \dot{\varepsilon}_v$$

(D5-39b)

D5.3.4 Implementation into the SATURN-FS Code

In SATURN-FS the nonelastic deformation rate is described by a linear vector equation.

with $\{\dot{\varepsilon}_{ne}\} = \{A_{1ne}\} + |A_{2ne}| \cdot \{\dot{\sigma}\}$ (D5-40)

$\{\dot{\varepsilon}_{ne}\}$:   vector of the non elastic deformation rate

$\{\dot{\sigma}\}$:   vector of the stress rate

$\{A_{1ne}\}$:   vector of the non stress-related (thermal) portion of the nonelastic flexibility

$|A_{2ne}|$:   matrix of the stress-related portion of the noneleastic flexibility

The equations derived in section 2 can be transferred to the form required by SATURN-FS in the following way.

Eqs. (D5-21), (D5-23), and (D5-26) can be written formally:

Eq. (D5-26), where *fev* corresponds to $\dot{\varepsilon}_v$:

$$fev = fev\,(\varepsilon_{SH}, \sigma) \qquad\qquad\text{(D5-41)}$$

Eq. (D5-21), where *fesh* equals $\dot{\varepsilon}_{SH}$:

$$fesh = fesh\,(\varepsilon_{SH}, \sigma) \qquad\qquad\text{(D5-42)}$$

and Eq (D5-23) where *fer* equals $\dot{\varepsilon}_R$:

$$fer = fer\,(\varepsilon_{SH}, \sigma) \qquad\qquad\text{(D5-43)}$$

For the development of a Taylor series the total differentials $d\,fev$, $d\,fesh$ and $d\,fer$ has to be set up, with the additional condition:

$$fev = fesh + fer \qquad\qquad\text{(D5-44)}$$

The total differentials read:

$$d\,fesh = \frac{\partial\,fesh}{\partial\,\varepsilon_{SH}}\,fesh_0 \cdot dt + \frac{\partial\,fesh}{\partial\,\dot{\varepsilon}_S} \cdot \frac{\partial\,\dot{\varepsilon}_S}{\partial\,\sigma_v} \cdot \sigma_v\,dt \qquad\qquad\text{(D5-45)}$$

$$d\,fer = \frac{\partial\,fer}{\partial\,\varepsilon_{SH}}\,fesh_0 \cdot dt + \frac{\partial\,fer}{\partial\,\dot{\varepsilon}_S} \cdot \frac{\partial\,\dot{\varepsilon}_S}{\partial\,\sigma_v} \cdot \sigma_v\,dt \qquad\qquad\text{(D5-46)}$$

so $d\,fev$ is

$$d\,fev = \left(\frac{\partial\,fesh}{\partial\,\varepsilon_{SH}} + \frac{\partial\,fer}{\partial\,\varepsilon_{SH}} \right) \cdot fesh_0 \cdot dt + \left(\frac{\partial\,fesh}{\partial\,\dot{\varepsilon}_S} + \frac{\partial\,fer}{\partial\,\dot{\varepsilon}_S} \right) \cdot \frac{\partial\,\dot{\varepsilon}_S}{\partial\,\sigma_v} \cdot \sigma_v\,dt \qquad\text{(D5-47)}$$

The total nonelastic strain rate is now described by the Taylor series and reads:

$$fev\,(t) = fev\,(t_0) + d\,fev \qquad\qquad\text{(D5-48)}$$

with $d\,fev$ according to Eq. (D5-47).

With the von Mises flow rate and the Prandtl-Reuß equations the vector of the nonealstic deformations can be written:

$$\{\dot{\varepsilon}_{ne}\} = \{A_{ne}\} \cdot fev \qquad \text{(D5-49a)}$$

From this and from Eqs. (D5-47) and (D5-48) one derives:

$$\{\dot{\varepsilon}_{ne}\} = \{A_{ne}\} \cdot fev_0 + \{A_{ne}\} \cdot \left(\frac{\partial fesh}{\partial \varepsilon_{SH}} + \frac{\partial fer}{\partial \varepsilon_{SH}} \right) fesh_0 \cdot dt +$$

$$+ \{A_{ne}\} \cdot \left(\frac{\partial fesh}{\partial \dot{\varepsilon}_S} + \frac{\partial fer}{\partial \dot{\varepsilon}_S} \right) \cdot \frac{\partial \dot{\varepsilon}_S}{\partial \sigma_v} \cdot \dot{\sigma}_v \, dt \qquad \text{(D5-49b)}$$

With

$$\dot{\sigma}_v = \{A_{ne}\}^T \cdot \{\dot{\sigma}\} \qquad \text{(D5-50)}$$

it can be written

$$\{\dot{\varepsilon}_{ne}\} = \{A_{ne}\} \cdot \left(fev_0 + \frac{\partial fesh + \partial fer}{\partial \varepsilon_{SH}} \cdot fesh_0 \cdot dt \right) +$$

$$+ \{A_{ne}\} \cdot \{A_{ne}\}^T \cdot \frac{\partial fesh + \partial fer}{\partial \dot{\varepsilon}_S} \cdot \frac{\partial \dot{\varepsilon}_S}{\partial \sigma_v} \cdot \{\dot{\sigma}\} \cdot dt \qquad \text{(D5-51)}$$

or with $\partial fer + \partial fesh = \partial fev$ one derives

$$\{A1_{ne}\} = \{A_{ne}\} \cdot \left(fev_0 + \frac{\partial fev}{\partial \varepsilon_{SH}} \cdot fesh_0 \cdot dt \right)$$

$$\{A2_{ne}\} = \{A_{ne}\} \cdot \{A_{ne}\}^T \cdot \frac{\partial fev}{\partial \dot{\varepsilon}_S} \cdot \frac{\partial \dot{\varepsilon}_S}{\partial \sigma_v} \cdot dt$$

and finally $\qquad\qquad\qquad\qquad\qquad\qquad\qquad\qquad\qquad$ (D5-52)

$$\{\dot{\varepsilon}_{ne}\} = \{A1_{ne}\} + \{A2_{ne}\} \cdot \{\dot{\sigma}\}$$

The differentials used in Eqs. (D5-45) to (D5-52) can be written explicitly in the following way:

$$\frac{\partial fesh}{\partial \varepsilon_{SH}} = -k \cdot \frac{\dot{\varepsilon}_S}{\varepsilon_{SHO}}$$ (D5-53a)

$$\frac{\partial fesh}{\partial \sigma_v} = \frac{\partial fesh}{\partial \dot{\varepsilon}_S} \cdot \frac{\partial \dot{\varepsilon}_S}{\partial \sigma_v} = k \left(1 - \frac{\varepsilon_{SH}}{\varepsilon_{SHO}}\right) \cdot \frac{\partial \dot{\varepsilon}_S}{\partial \sigma_v}$$ (D5-53b)

$$\frac{\partial fer}{\partial \varepsilon_{SH}} = \frac{\dot{\varepsilon}_S}{\varepsilon_{SHO}}$$ (D5-53c)

$$\frac{\partial fer}{\partial \sigma_v} = \frac{\partial fer}{\partial \dot{\varepsilon}_S} \cdot \frac{\partial \dot{\varepsilon}_S}{\partial \sigma_v} = \frac{\varepsilon_{SH}}{\varepsilon_{SHO}} \cdot \frac{\partial \dot{\varepsilon}_S}{\partial \sigma_v}$$ (D5-53d)

$$\frac{\partial fev}{\partial \varepsilon_{SH}} = \frac{\partial fesh + \partial fer}{\partial \varepsilon_{SH}} = \frac{\dot{\varepsilon}_S}{\varepsilon_{SHO}} (1 - k)$$ (D5-53e)

$$\frac{\partial fev}{\partial \sigma_v} = \frac{\partial fesh + \partial fer}{\partial \dot{\varepsilon}_S} \cdot \frac{\partial \dot{\varepsilon}_S}{\partial \sigma_v} = \left| k + \frac{\varepsilon_{SH}}{\varepsilon_{SHO}} (1 - k) \right| \cdot \frac{\partial \dot{\varepsilon}_S}{\partial \sigma_v}$$ (D5-53f)

All these values are known from creep equations or from the evaluation of creep tests.

D5.4   The Thermal Strain Rate

For the thermal strain rate of a ring element the following relationship holds:

$$\{\dot{\varepsilon}_{th}\} = \left\{ \begin{array}{c} R_{ar} \\ R_{at} \\ R_{az} \end{array} \right\} \cdot \alpha \cdot \dot{T}_v \qquad and \{\dot{\varepsilon}_{th}\} = \{A_{th}\}, resp.$$

(D5-54)

where $R\alpha_r$, $R\alpha_t$ and $R\alpha_z$ are weight factors for a potential anisotropy of the thermal strain in radial, circumferential and axial directions. For the isotropic case it holds that $R\alpha_r = R\alpha_t = R\alpha_z = 1$.

The factor α is the coefficient of linear thermal expansion and $\dot{T}_e$ describes the time dependent change of the element temperature (i.e. temperature rate).

D5.5 Consideration of the Pellet Void Volume and of Fuel Swelling

D5.5.1 General Remarks:

The following section shows how the local, time dependent and volumetric distribution of the fuel void volume is treated. Some of the representations and derivatives used are based on a similar treatment in the CYGRO computer programs [D5-5, D5-6, D5-17].

The following consideration are now dealt with; matrix swelling of the fuel and the behaviour of pores and gas bubbles in the fuel, i.e. gas bubble swelling and pore compaction as a function of the external pressure and of the hydrostatic pressure in the pores.

As in the preceding considerations, a pellet is assumed here to be been divided into Ne ring elements. Each of these elements with the volume V corresponding to 100% consists of the matrix volume V_F and the region of void volume V_L. The area of the void volume can be divided into an area of true porosity (net porosity) = V_{LL} and a matrix portion where porosity may occur and which is directly influenced by the pores = V_{LF}, resp.

For each category of void volumes i defined in the ring element (termed pore category below) with i ranging from 0 to Np, the following definitions apply;

V_{Li}: volume of the i-th range of void volumes, related to the total pore volume of the ring element (cf. V_L):

$$V_{Li} = V_{LLi} + V_{LFi} \qquad (cf.\ V_L = V_{LL} + V_{LF}) \qquad \text{(D5-55)}$$

V_{LLi}: volume of the i-th category of net porosity, related to the initial volume of the ring element

V_{LFi}:   matrix volume directly influenced by the porosity of the i-th pore category (cf. V_{LF})

i :   integer variable for pore categories; $i = 1, 2 \dots Np$

On the basis of the definitions above the following relationships are obtained:

$$V_L = \sum_{i=1}^{Np} V_{Li} \qquad (D5\text{-}56)$$

$$V_{LL} = \sum_{i=1}^{Np} V_{LLi} \qquad (D5\text{-}57)$$

$$V_{LF} = \sum_{i=1}^{Np} V_{LFi} \qquad (D5\text{-}58)$$

$$V_L = \sum_{i=1}^{Np} V_{LLi} + \sum_{i=1}^{Np} V_{LFi} \qquad (D5\text{-}59)$$

For a further representation of the defined variables see Fig. D5-1.

D5.5.2   Radiation Induced Volumetric Change in Volume of the Solid Volume (Swelling)

First Possibility:

Definition: $\dot{V}_{F0}(t;\Phi)[s^{-1}]$ = reference value of fuel swelling at reference temperature and pressure, e.g. room temperature and 1 bar.

Using the variable $\dot{V}_{F0}$, a real swelling rate can be represented as:

$$\dot{V}_F / s^{-1} / = f_{PT} (\bar{p}, T) \cdot \dot{V}_{F0} \qquad (D5\text{-}60)$$

where f_{PT} is a tabular function of the mean ring temperature and of the mean hydrostatic pressure in the ring element.

The hydrostatic pressure p is calculated as:

$$\bar{p} = -\{R_v\}^T \cdot \{\sigma\}$$

$$\bar{p} = -\left\{\begin{array}{c} R_{vr} \\ R_{vt} \\ R_{vz} \end{array}\right\}^T \cdot \left\{\begin{array}{c} \sigma_r \\ \sigma_t \\ \sigma_z \end{array}\right\} \tag{D5-61}$$

$$\bar{p} = -\{R_{vr} \cdot \sigma_r + R_{vt} \cdot \sigma_t + R_{vz} \sigma_z\}$$

For isotropic behavior it holds:

$$R_{vr} = R_{vt} = R_{vz} = \frac{1}{3} \tag{D5-62}$$

and hence

$$\bar{p} = -\frac{1}{3}(\sigma_r + \sigma_t + \sigma_z) \tag{D5-63}$$

Second Possibility:

Determination of $\dot{V}_F$ using any swelling formula from the literature.

D5.5.3 Consideration of the Fuel Void Volume

The following expression applies to the pore type i (i = 1,2 ... Np):

$$\dot{V}_{LFi} = 0 , \tag{D5-64}$$

i.e. of the solid part of the pore zone is constant implying that in that zone only plasticity and creep occur, while elastic deformation is neglected.

(Incompressibility of the plastic and creep zones).

With

$$V_{Li} = V_{LLi} + V_{LFi}$$

$$\dot{V}_{Li} = \dot{V}_{LLi} + \dot{V}_{LFi} \tag{D5-65}$$

we obtain

$$\dot{V}_{Li} = \dot{V}_{LLi}$$ (D5-66)

<u>Def.:</u>

$$V_{LLi} = f_{VLL}(V_{Li})$$ (D5-67)

$$f_{VLL}(V_{Li}) = V_{Li} - V_{LFi}$$ (D5-68)

$$(\text{or} \quad V_{LLi} = V_{Li} - V_{LFi})$$

Definition:

N_{Li} = number of the pores in the volume fraction V_{Li}

N_{Li} depends on the temperature and on the time (and burnup, resp.)

Control of N_{Li}:

The number of the pores of type i is controlled by means of two auxiliary functions. The starting basis is a reference value N_{Li} (ref) indicating the number of the pores, related to the entire element volume, under initial conditions (time t = 0).

Moreover, the parameter M_{NLi} is supposed to be a control variable which may adopt the three values +1, -1 and 0. This leads to the following relationship;

$M_{NLi} = 0$: $N_{Li} = N_{Li}(ref)$ = independent of time and temperature

$M_{NLi} = +1$: $N_{Li} = N_{Li}(ref) \cdot f_{gas}(\dot{T})$
  where $f_{gas}(\dot{T})$ is a tabular function of the mean ring temperature $\dot{T}$

$M_{NLi} = -1$: $N_{Li} = min(N_{Li}, N_{Li}(ref) \cdot f_{gas}(\dot{T}))$

Using the function N_{Li}, restructuring and thermal densification can e.g. be modelled.

Moreover, it holds that

R_{ai} = radius of the pore type i in the volume fraction V_{LLi} and hence:

$$V_{LLi} = \frac{4}{3} \pi \cdot R_{ai}^3 \cdot N_{Li} = f_{VLL}(V_{Li})$$ (D5-69)

This is the absolute void volume of the i-th pore category in the ring. The radius of the i-th pore category in the element can, consequently, be determined as:

$$R_{ai} = f_{ra}(V_{Li}) = \left(\frac{3 \cdot f_{VLL}(V_{Li})}{4 \pi \cdot N_{Li}} \right)^{\frac{1}{3}}$$

(D5-70)

Definition:

- $R_c =$ radius of the creep area of a pore in the volume portion V_{Li}

- $V_c =$ volume within the radius R_c of all N_{Li} pores

Consequently:

$$V_c = \frac{4}{3} \pi R_c^3 N_{Li}$$

(D5-71)

$$\dot{V}_c = 4 \pi \cdot R_c^2 \cdot N_{Li} \cdot \dot{R}_c$$

(D5-72)

$$\frac{\dot{R}_c}{R_c} = \frac{1}{3} \frac{\dot{V}_c}{V_c}$$

(D5-73)

Since $\dot{V}_{LFi} = 0$ (see equation (D5-64)),it holds:

$$\dot{V}_c = \dot{V}_{Li} \quad for \quad V_{LLi} \leq V_c \leq V_{Li}$$

(D5-74)

and

$$\frac{\dot{R}_c}{R_c} = \frac{\dot{V}_{Li}}{3 V_c}$$

(D5-75)

resp.

Equation (D5-75) describes a strain rate in two directions normal to the radius R_c.

Assuming constant volume of plastic strain this yields for the strain rate in radial direction:

$$0 = \dot{\varepsilon}_{ri} + \frac{\dot{R}_c}{R_c} + \frac{\dot{R}_c}{R_c}$$

(D5-76)

and with (D5-75):

$$\dot{\varepsilon}_{ri} = - \frac{2\,\dot{V}_{Li}}{3\,V_c} \qquad (D5\text{-}77)$$

resp.

Accordingly, a rate of "plastic equivalent strain" can be defined as:

$$\dot{\varepsilon}^P_{Vi} = \left\{ \frac{2}{3} \left(\dot{\varepsilon}^2_{ri} + (\frac{\dot{R}_c}{R_c})^2 + (\frac{\dot{R}_c}{R_c})^2 \right) \right\}^{\frac{1}{2}} \qquad (D5\text{-}78)$$

and

$$\dot{\varepsilon}^P_{Vi} = \left| \frac{2\,\dot{V}_{Li}}{3\,V_c} \right| \qquad (D5\text{-}79)$$

resp., or

$$\dot{\varepsilon}^P_{Vi} = \frac{S_i \cdot 2 \cdot \dot{V}_{Li}}{3\,V_c} \qquad (D5\text{-}80)$$

where S_i is the sign of V_{Li}.

D5.5.4 Change of the Void Volume - Fission Gas Release

Fission gas balance:

Definition: Mg_i is the number of the gas moles in the volume V_{LLi}. This number is increased by the fission gas generation and is decreased by fission gas release. The balance can be described by the following differential equation:

$$\dot{Mg}_i = A \cdot \dot{\phi} - B \cdot Mg_i \cdot D_{\phi T}(\phi T) \qquad (D5\text{-}81)$$

where

A :   coeffcient of gas production (moles/fission)

$\dot{\phi}$:   fission rate (fiss/cm³·s)

ϕ :   burnup

B :   coefficient of gas release

$D_{\Phi T}$ is a tabular function of temperature and burnup.

However, the second part of the equation can optionally be described by a release equation taken from the literature.

The gas moles left in the various pore types of the fuel have to be attributed to a given pressure pg_i for each pore type, namely

$$pg_i = \frac{Mg_i \cdot R \cdot T}{V_{LLi}} \tag{D5-82}$$

Def.: $$pg_i = f_{pg}(V_{Li}, t) \tag{D5-83}$$

$$f_{pg}(V_{Li}, t) = \frac{Mg_i(t) \cdot R \cdot T}{V_{LLi}} \tag{D5-84}$$

With equation (D5-68) we obtain:

$$f_{pg}(V_{Li}, t) = \frac{Mg_i(t) \cdot R \cdot T}{f_{V_{LL}}(V_{Li})} \tag{D5-85}$$

Exception:

For porosity generated during manufacture the expression holds: $f_{pg}(V_{Li}, t) = 0$,

because: $Mg_i(t) = 0$.

For $Mg_i(t) \geq 0$ the volume V_{LLi} is restricted by the fact that the following equation must always hold:

$$p_{gi} \geq 0 \tag{D5-86}$$

Equilibrium between internal pore pressure and surface tension

Definition: $R_{ai} =$ inner radius of the creep zone around the pore and outer radius, resp., of the net pore

$p_{ai} =$ interface pressure at radius R_{ai}

$\gamma =$ surface tension

This allows the following equation to be written:

$$\pi R_{ai}^2 (p_{gi} - p_{ai}) = 2\pi R_{ai} \cdot \gamma \tag{D5-87}$$

and

$$\Delta p = \frac{2\gamma}{R_{ai}} \tag{D5-88}$$

resp.

Using the relationship

$$R_{ai} = f_{ra}(V_{Li}) \tag{D5-89}$$

and reformulating equation (D5-87) with the help of equation (D5-83) to read

$$p_{ai} = f_{pa}(V_{Li}, t) = f_{pg}(V_{Li}, t) - \frac{2\gamma}{f_{ra}(V_{Li})} \tag{D5-90}$$

we can represent the interface pressure P_{ai} as the function

$$p_{ai} = f_{pa}(V_{Li}, t) \tag{D5-91}$$

D5.5.5 Pore Densification and Gas Bubble Swelling

The problem of describing densification and swelling rests in the representation of

$$\left.\begin{array}{l} \text{pore growth} \\ \text{pore shrinkage} \end{array}\right\} \triangleq V_L$$

as a linear function of the pressure rate $\dot{p}$.

Proposed solution: Writing a relation for description of the reference strain rate $\dot{\varepsilon}_V$ as a function of the load rate $\dot{\sigma}$.

The rate of the deformation energy in the i-th ring element can be represented as

$$\dot{W}_i = \int_{V_{LLi}}^{V_{Li}} \sigma_{Vi} \dot{\varepsilon}_{Vi} \, dV_c \tag{D5-92}$$

or by

$$\dot{\varepsilon}_{Vi} = \left| \frac{2 V_{Li}}{3 V_c} \right| \tag{D5-78}$$

$$\dot{W}_i = \left| \frac{2\,\dot{V}_{Li}}{3} \right| \cdot \int_{V_{LLi}}^{V_{Li}} \frac{{}^o\sigma_{Vi}}{V_c}\, dV_c \tag{D5-93}$$

$$\dot{W}_i = \left| \frac{2\,V_{Li}}{3} \right| \cdot {}^o\sigma_{Vi} \cdot \ell n \cdot \frac{V_{Li}}{V_{LLi}} \tag{D5-94}$$

This inner deformation energy must be equal to the work exerted by the external (pressure) forces:

$$\dot{W} = p_{ai} \cdot \dot{V}_{LLi} - \bar{p} \cdot \dot{V}_{Li} \tag{D5-95}$$

With

$$p_{ai} = f_{pa}(V_{Li}, t) \tag{D5-91}$$

and

$$\bar{p} = - \{R_v\}^T \cdot \{\sigma\} \tag{D5-61}$$

or, since $\quad \dot{V}_{LLi} = \dot{V}_{Li}$ $\hfill$ (D5-66)

we obtain:

$$\dot{W}_i = (p_{ai} - \bar{p}) \cdot \dot{V}_{Li} \tag{D5-96}$$

Setting equal the internal and the external work yields

$$p_{ai} - \bar{p} = \frac{2\,Si}{3} \int_{V_{LLi}}^{V_{Li}} \frac{{}^o\sigma_{Vi}}{V_c}\, dV_c \tag{D5-97}$$

and

$$p_{ai} - \bar{p} = \frac{2\,{}^o\sigma_V}{3} \cdot \ell n \left(\frac{V_{Li}}{V_{LLi}} \right) \cdot Si \tag{D5-98}$$

resp.,

with S_i = sign of the difference $p_{ai} - \bar{p}$.

Solving for $\bar{\sigma}_V$ yields:

$$\bar{\sigma}_V = \frac{3 \cdot Si \, (p_{ai} - \bar{p})}{2 \cdot \ell n \left(\dfrac{V_{Li}}{V_{LLi}}\right)} \qquad \text{(D5-99)}$$

and

$$\bar{\sigma}_V = \left| \frac{3 \, (p_{ai} - \bar{p})}{2 \cdot \ell n \left(\dfrac{V_{Li}}{V_{LLi}}\right)} \right| \qquad \text{(D5-100)}$$

resp.

The stress-strain behavior of a material in the plastic zone can be described by:

$$\sigma = K \cdot \varepsilon_p^{\eta} \qquad \text{(D5-101)}$$

and

$$\varepsilon_p = x \cdot \sigma^y \qquad \text{(D5-102)}$$

resp.

Likewise, secondary creep can be described as:

$$\dot{\varepsilon}_S = u \cdot \sigma^v \qquad \text{(D5-103)}$$

The stress at the yield point, e.g. $\varepsilon_p = 2 \times 10^{-3}$ - can according to equation (D5-102) be determined as:

$$2 \cdot 10^{-3} = x \cdot \sigma_y^y$$

and

$$\sigma_y = \left(\frac{2 \cdot 10^{-3}}{x}\right)^{\frac{1}{y}} \qquad \text{(D5-104)}$$

resp.

Non-elastic deformation can now be divided simply into two zones, a creep zone and a zone of ideally plastic behavior. This division is evident from Fig. D5-2.

The following variables are defined:

Definition:

σ_p = stress limit; corresponds to a maximum stress to be accommodated by the material

$$\sigma_p = R_{sp} \cdot \sigma_y \qquad \text{(D5-105)}$$

R_{sp} = empirical factor

$\dot{\varepsilon}_y$ = creep rate at the yield point $\dot{\varepsilon}_y = u \cdot \sigma_y^V$

$$S_c = \tan \alpha = \frac{R_{sc} \cdot \sigma_y}{\dot{\varepsilon}_y} \quad : \text{slope of the creep curve for } \sigma < \sigma_p$$

R_{sc} = empirical factor

Representation of deformation in the creep zone:

$$\sigma_V = S_c \cdot \dot{\varepsilon}_V \qquad \text{(D5-106)}$$

and

$$\dot{\varepsilon}_V = \frac{1}{S_c} \cdot \sigma_V \qquad \text{(D5-107)}$$

$$\dot{\varepsilon}_V = \frac{\dot{\varepsilon}_y}{R_{sc} \cdot \sigma_p} \cdot \sigma_V \qquad \text{(D5-108)}$$

resp.

Using equations (D5-105) and (D5-106), the following relationships can be indicated between σ_V and $\dot{\varepsilon}_V$:

$$\sigma_V = \begin{cases} \sigma_p & \text{for} \quad \sigma_p \leq S_c \cdot \dot{\varepsilon}_V \\ & \text{and} \\ & \text{for} \quad \sigma_V > \sigma_p, \quad \text{resp.} \\ S_c \cdot \dot{\varepsilon}_V & \text{for} \quad \sigma_p > S_c \cdot \dot{\varepsilon}_V \\ & \text{and} \\ & \text{for} \quad \sigma_V \leq \sigma_p, \quad \text{resp.} \end{cases} \qquad \text{(D5-109)}$$

and using equation (D5-80), resp., namely

$$\dot{\varepsilon}^p_{Vi} = \frac{S_i \cdot 2 \cdot \dot{V}_{Li}}{3 \, V_c}$$

$$\sigma_V = \begin{cases} \sigma_p & \text{for} & \sigma_p \leq \dfrac{2 \cdot S_c \cdot S_i \cdot \dot{V}_{Li}}{3 \, V_c} \\[4mm] \dfrac{2 \cdot S_c \cdot S_i \cdot \dot{V}_{Li}}{3 \, V_c} & \text{for} & \sigma_p > \dfrac{2 \cdot S_c \cdot S_i \cdot \dot{V}_{Li}}{3 \, V_c} \end{cases}$$

(D5-110)

Equation (D5-110), extended by V_c/σ_p, yields:

$$\sigma_V = \begin{cases} \sigma_p & \text{for} & \dfrac{\sigma_p \cdot V_c}{\sigma_p} \leq \dfrac{2 \cdot S_c \cdot S_i \cdot \dot{V}_{Li} \cdot V_c}{3 \, V_c \cdot \sigma_p} \\[4mm] \dfrac{2 \cdot S_c \cdot S_i \cdot \dot{V}_{Li}}{3 \, V_c} & \text{for} & \dfrac{\sigma_p \cdot V_c}{\sigma_p} > \dfrac{2 \cdot S_c \cdot S_i \cdot \dot{V}_{Li} \cdot V_c}{3 \, V_c \cdot \sigma_p} \end{cases}$$

(D5-111)

<u>Def.:</u>
$$V_{pc} = \frac{2 \cdot S_c \cdot S_i \cdot \dot{V}_{Li}}{3 \, \sigma_p}$$

(D5-112)

Using equation (D5-112), (D5-111) can be written as:

$$\sigma_V = \begin{cases} \sigma_p & \text{for} & V_c \leq V_{pc} \\[4mm] \sigma_p \cdot \dfrac{V_{pc}}{V_c} & \text{for} & V_c > V_{pc} \end{cases}$$

(D5-113)

With the following definition:

<u>Definition:</u> $\sigma_v = f_{sv}(V_c, \dot{V}_{Li})$

<div align="center">one obtains:</div>

$$f_{sv}(V_c, \dot{V}_{Li}) = \begin{cases} \sigma_p & \text{for} \quad V_c \leq \dfrac{2 \cdot S_c \cdot S_i \cdot \dot{V}_{Li}}{3 \cdot \sigma_p} \\[3em] \dfrac{2 \cdot S_c \cdot S_i \cdot \dot{V}_{Li}}{3 \, V_c} & \text{for} \quad V_c > \dfrac{2 \cdot S_c \cdot S_i \cdot \dot{V}_{Li}}{3 \, \sigma_p} \end{cases} \qquad \text{(D5-114)}$$

D5.5.6 Growth and Shrinkage of the Pores

The growth rate $\dot{V}_{Li}$ will be represented now as a linear function of the pressure rate $\dot{p}$.

<u>Def.:</u> $\bar{\dot{p}} = f_p(V_{Li}, \dot{V}_{Li}, t)$ (D5-115)

If one uses equations (D5-67), (D5-91), (D5-114) and (D5-115), it results from equation (D5-97):

$$f_p(V_{Li}, \dot{V}_{Li}, t) = f_{pu}(V_{Li}, t) - \frac{2 S_i}{3} \int_{f_{V_{LL}}(V_{Li})}^{V_{Li}} \left[f_{sv}(\dot{V}_{Li}, V_c) \cdot \frac{1}{V_c} \right] dV_c \qquad \text{(D5-116)}$$

Extending equation (D5-115) while taking into account constant pressure rates during the time step Δt yields:

$$\bar{\dot{p}} + \bar{\ddot{p}} \, \Delta t = f_p(V_{Li} + \dot{V}_{Li}\Delta t, \dot{V}_{Li}, t + \Delta t) \qquad \text{(D5-117)}$$

$$\bar{\dot{p}} = f_p(V_{Li} + \dot{V}_{Li}'\Delta t, \dot{V}_{Li}', t + \Delta t) = f_p'(\dot{V}_{Li}') \qquad \text{(D5-118)}$$

The development of a Taylor series of equation (D5-117) by $\dot{V}_{Li}'$ gives:

$$\bar{\dot{p}} + \bar{\ddot{p}} \, \Delta t = \bar{\dot{p}} + (\dot{V}_{Li} - \dot{V}_{Li}') \cdot \frac{df_p'}{d\dot{V}_{Li}} \qquad , \qquad \text{(D5-119)}$$

solved for $\dot{V}_{Li}$:

$$\dot{V}_{Li} = \dot{V}_{Li}' + \left(\frac{\Delta t}{df_p'/d\dot{V}_{Li}'} \right) \cdot \dot{\bar{p}}$$, (D5-120)

formally:

$$\dot{V}_{Li} = f_{VLi} + f_{Vpi} \cdot \dot{\bar{p}}$$ (D5-121)

Summation of all pore categories yields

$$\dot{V}_L = f_{VL} + f_{Vp} \cdot \dot{\bar{p}}$$ (D5-122)

An alternative possibility is offered e.g. by the hot press model according to Murray, Livey & Williams [D5-18]:

$$\dot{V}_{LLi} = \frac{3 V_{LLi}}{2\eta} \left| \frac{\gamma}{2 R_{ai}} + \frac{\bar{p}}{2} \right| + \frac{3\sqrt{2}}{4} \cdot \frac{\sigma y}{\eta} \cdot V_{LLi} \cdot \ell n \left(\frac{1}{V_{LLi}} \right)$$ (D5-123)

with

$$\frac{1}{\eta} = \frac{\dot{\delta\epsilon}}{\delta\sigma}$$ results the following expression

$$\dot{\epsilon} = u \cdot \sigma^v + A\phi \cdot \sigma$$ (D5-124)

(see equation (D5-103))

in $$\frac{\dot{\delta\epsilon}}{\delta\sigma} = u \cdot v \cdot \sigma^{v-1} + A\phi$$ (D5-125)

and

$$\frac{1}{\eta} = \frac{1}{R_{sc}} (u \cdot v |\bar{p}|^{v-1} + A\phi)$$ (D5-126)

resp.

This yields for η

$$\eta = \frac{R_{sc}}{u \cdot v |\bar{p}|^{v-1} + A\phi}$$

(D5-127)

According to the hot press model the total irradiation induced volume change is obtained as:

$$\dot{V} = R_{V_p}(\bar{p},T) \cdot \dot{V}_{Fo} + \dot{V}_{LLi}$$

(D5-128)

formally:

$$\dot{V} = f_{V_l} + f_{V_p} \cdot \dot{\bar{p}}$$

(D5-129)

$$\dot{V}_{LLi} = \frac{3}{4} \cdot \frac{V_{LLi}}{\eta} \cdot \frac{\gamma}{R_{ai}} + \frac{3}{4} \cdot \frac{V_{LLi}}{\eta} \cdot \{R_V\}^T\{\dot{\sigma}\} + \frac{3\sqrt{2}}{4} \frac{\sigma y}{\eta} V_{LLi} \cdot \ell n(\frac{1}{V_{LLi}})$$

(D5-130)

$$\{\dot{V}_l\} = \frac{3}{4} \cdot \frac{V_{LLi}}{\eta} \frac{\gamma}{R_{ai}} + \frac{3\sqrt{2}}{4} \frac{\sigma y}{\eta} V_{LLi} \cdot \ell n(\frac{1}{V_{LLi}}) + \frac{3}{4} \cdot \frac{V_{LLi}}{\eta} \cdot \{-R_V\}^T \cdot \{\dot{\sigma}\}$$
$$+ \dot{V}_{Fo} \cdot \{-R_V\}^T \cdot \{\dot{\sigma}\}$$

(D5-131)

Formal representation:

$$\{\dot{V}\} = |A_{1V}| + |A_{2V}| \cdot \{\dot{\sigma}\}$$

(D5-132)

This implies the description of fuel densification due to hot press effects using a linear matrix equation.

D5.5.7 Joining Matrix Swelling and Gas Bubble Swelling/Pore Shrinkage after Originally Separate Analysis

According to equation (D5-59) it applies:

$$\dot{V} = \dot{V}_L + \dot{V}_F \tag{D5-133}$$

or, in a different representation:

$$\dot{V} = f_{Vl} + f_{Vp} \cdot \dot{\bar{p}} \tag{D5-134}$$

where:

<u>Def.:</u> $f_{Vl} = \dot{V}_F + f_{VL}$ $\qquad$ (D5-135)

According to equation (D6-61) it applies:

$$\dot{\bar{p}} = \{-R_V\}^T \cdot \{\dot{\sigma}\} \tag{D5-136}$$

Hence:

$$\dot{V} = f_{Vl} - f_{Vp} \cdot |\{R_V\}^T \cdot \{\dot{\sigma}\}| \tag{D5-137}$$

with definition of irradiation induced strain rate as:

<u>Def.:</u> $\{\dot{\varepsilon}_{irr}\} = \{R_V\} \cdot \dot{V}$ $\qquad$ (D5-138)

it can be written formally:

$$\{\dot{\varepsilon}_{irr}\} = \{A_{1_{irr}}\} + |A_{2_{irr}}| \cdot \{\dot{\sigma}\} \tag{D5-139}$$

and hence a linear matrix equation applies, with

$$\{A_{1_{irr}}\} = \{R_V\} \cdot f_{Vl} \tag{D5-140}$$

$$[A_{2_{irr}}] = -\{R_V\} \cdot f_{Vp} \cdot \{R_V\}^T \tag{D5-141}$$

D5.5.8 Pore Migration

At time t, the volume of a fuel ring according to equation (D5-59) is composed of the matrix and void volumes:

$$V_i = V_{Li} + V_{Fi} \; .$$

The gross void volume is made up of the net porosity V_{LLi} and the zones of creep and plastic deformation of the pores, (V_{LFi}). Now, additionally matrix swelling, ε_{VF} shall be introduced into the considerations. Considering the i-th porosity category for a ring element, its portions are composed as follows:

$$V_{TOT} = V_{LLi} + V_{LFi} + \varepsilon_{VF} \; . \tag{D5-142}$$

All these variables are related variables so that it holds e.g.:

$$V_{LLi} + V_{LFi} = 1 \; . \tag{D5-143}$$

Consequently, equation (D5-142) becomes:

$$V_{TOT} = 1 + \varepsilon_{VF} \tag{D5-144}$$

To consider pore migration, V_{TOT} is used as a reference variable so that it can now be defined:

$$V_{LLr} = \frac{V_{LLi}}{V_{TOT}} \tag{D5-145}$$

Example: Porosity in the initial volume of the fuel at time t = 0:

$$V_{LLi/relative_1} = \frac{V_{LLi}}{V_0} = 5 \cdot 10^{-2} \; (density = 95\,\%)$$

Swelling causes a change in the volume V_0 to become $V_0 + \varepsilon_{VF} = V_{TOT}$.

This gives a new $V_{LLi/relative}$:

$$V_{LLi/relative_2} = \frac{V_{LLi}}{V_0} \cdot \frac{V_0}{V_{TOT}} = \frac{V_{LLi}}{V_{TOT}}$$

Accordingly, the following expression holds for porosity in a fuel ring at time t:

$$V_{LLr} = \frac{V_{LLi}}{V_{TOT}} \cdot \text{n}(r_j^2 - r_i^2) = V_{LLi} \cdot K \qquad (\text{D5-146})$$

where

r_j: external radius of the fuel ring

r_i: internal radius of the fuel ring

To differentiate the indices of the ring elements i, the pore categories will be marked KG below, where $KG = 1 \ldots NP$. Thus, for the creep and plastic portions of porosity, now summed up over each porosity category, it holds that

$$V_{LFr} = \sum_{KG=1}^{Np} \left(V_{LFi}(KG) + v_{VF} \right) \cdot \frac{\text{n}(r_j^2 - r_i^2)}{V_{TOT}} = \sum_{KG=1}^{Np} \left(V_{LFi}(KG) + v_{VF} \right) \cdot K \qquad (\text{D5-147})$$

At the end of each time step the void volume leaving the ring is subtracted from V_{LLr} and the void volume coming from the ring adjoining outside is added.

The matrix volume V_{LFr} is considered to be constant and gives so the basis to determine each new ring radius.

The new porosity distribution and the new ring radii are determined as follows: we imagine a fuel ring with an inner radius i and an outer radius j.

After a time dt the portion of porosity of a given category which has left the ring towards the center can be determined according to equation (D5-146):

$$d(V_{LLr})_i = \frac{V_{LLi}}{V_{TOTi}} \cdot \rho_i \cdot dt \cdot 2 \text{n} r_i \qquad , \qquad (\text{D5-148})$$

where ρ_i is the migration rate of the specific pore category considered under the conditions of the relevant fuel ring.

Accordingly, the porosity which came from the next outer ring can be written as:

$$d(V_{LLr})_j = \frac{V_{LLj}}{V_{TOTj}} \cdot \rho_j \cdot dt \cdot 2 \text{n} r_j \qquad (\text{D5-149})$$

For V_{LLr} at time $t + dt$ it consequently holds:

$$V_{LLr}(t+dt) = \frac{V_{LLi}}{V_{TOTi}} \text{n}(r_j^2 - r_i^2) - \frac{V_{LLi}}{V_{TOTi}} \rho_i \, dt \, 2 \text{n} r_i + \frac{V_{LLj}}{V_{TOTj}} \rho_j \, dt \, 2 \text{n} r_j \qquad (\text{D5-150})$$

The volume V_{LF_r} keeps to be determined by equation (D5-147). Now V_{LLr} will be re-normalized again because all expressions for V can be interpreted only in the correct relation to each other. Re-normalization shall be made in such a way that the new value of V_{LLi} and hence the new ring radii are chosen so that the new value of

$$\sum_{KG=1}^{Np} (V_{LFi}(KG)+\varepsilon_{VF}) \qquad \text{is equal to the old value.}$$

This is done by division of equation (D5-150) by the expression K of equation (D5-146).

This gives:

$$V_{LLi}(t+dt) = V_{LLi}(t)\left(1 - \frac{\rho_i \cdot dt \cdot 2r_i}{r_j^2 - r_i^2}\right) - \frac{V_{TOTi}(t)}{V_{TOTj}(t)} \cdot V_{LLj}(t) \cdot \rho_j\, dt\, \frac{2\,r_j}{r_j^2 - r_i^2} \qquad \text{(D5-151)}$$

V_{TOTi} is obtained as:

$$V_{TOTi}(t+dt) = \left(\sum_{KG=1}^{Np} V_{LFi}(KG)\right) + \varepsilon_{VF} + V_{LLi}(t+dt) \qquad \text{(D5-152)}$$

To determine the new ring radii a relationship is established between $V_{TOTi}(t)$ and $V_{TOTi}(t+dt)$:

$$\frac{V_{TOTi}(t+dt)}{|r_j(t+dt)|^2 - |r_i(t+dt)|^2} = \frac{V_{TOTi}(t)}{|r_j(t)|^2 - |r_i(t)|^2} \qquad \text{(D5-153)}$$

With the help of equation (D5-153), $r_i(t+dt)$ can be calculated recursively because the outer radius of the outermost ring element does not undergo changes due to pore migration.

Moreover, the following restriction applies regarding the time step control: To guarantee that the porosity migrates in each case to the adjoining ring only, the computer time step Δt must be chosen to be so small that the pores can migrate at maximum a path corresponding to half the distance to the next inner radius. This can be expressed by the following formula:

$$\rho_i \cdot \Delta t \le 0.5\,(r_i - r_{i-1}) \qquad \text{(D5-154)}$$

Procedure in the computer program

Swelling of the fuel matrix is computed in the SWELLB subroutine from which various models taken from the literature can be called.

The fuel void volume is computed in the PORMECH, PORMIG and PORCOM subroutines.

PORMECH computes the behavior of pores and gas bubbles, i.e. pore swelling and densification, as a function of the external pressure and the internal pore pressure.

Moreover, the partial element flexibilities $\{A1_{irr}\}$ and $[A2_{irr}]$ describing the influence of swelling and pore migration on the element stiffness are calculated in these subroutine.

PORMIG describes a pore migration procedure, with special emphasis on the consideration of the change in the pellet geometry. Despite the redistribution of void volumes, the number of the ring elements remains constant in the model developed here; only the radii undergo variations. This change in the element radii is computed in PORMIG. PORMIG calls the WANDER subroutine. The latter is a model taken from the literature, e.g. from [D5-19] which determines the pore migration velocity.

The PORCOM subroutine computes the integration of the rates of pore migration and swelling over time and determines at the end of each time step the number of the gas moles released, both per pore category and in total. Furthermore, the gas pressure in the fission gas bubbles is determined, the resulting pressure is calculated from the gas pressure and the surface tension, and the radius is determined for each pore category.

D5.6   Swelling of the Cladding

The swelling rate of the cladding can be described as a function of the local cladding temperature and the neutron dose.

Besides this general possibility of describing cladding swelling, the Interatom swelling formula will be applied to describe cladding swelling for materials 1.4970 kv and kv.a.

D5.7 Addition of the Strain Rates

The strain rates derived in the preceding sections can be added and represented formally by the following equation:

$$\{ \dot{\varepsilon}_{tot} \} = \{ A_1 \} + | A_2 | \bullet \{ \dot{\sigma} \}$$

(D5-155)

where the matrices $\{A_1\}$ and $| A_2 |$ are composed each of:

$$\{ A_1 \} = \{ A_{1ne} \} + \{ A_{th} \} + \{ A_{1irr} \}$$

(D5-156)

$\{A_1\}$ being the not stress related or thermal flexibility matrix resp.

$$| A_2 | = | A_{e\ell} | + | A_{2ne} | + | A_{2irr} |$$

(D5-157)

The matrix $[A_2]$ is defined as the stress related flexibility matrix.

Finally, the stiffness calculation is done, by inversion of the flexibility matrix as already mentioned at the beginning of this section. This results in

$$\{ \dot{\sigma} \} = \{ B_1 \} + | B_2 | \cdot \{ \dot{\varepsilon} \}$$

(D5-158)

with

$$| B_2 | = | A_2 |^{-1}$$

(D5-159)

and

$$\{ B_1 \} = - | B_2 | \bullet \{ A_1 \}$$

(D5-160)

References:

[D5-1]   R. Hill:
           The Mathematical Theory of Plasticity,
           Oxford University Press, London, 1960

[D5-2]   J. Gittus
           A Model of Creep Embodying Dislocations whose Movements Produce
           Work Hardening and Recovery, Phil. Mag. 21, 1970, S. 495.

[D5-3]   J. Gittus
           Strain, Recovery and Work Hardening during Creep due to Disloca-
           tions, Phil. Mag. 23, No. 186, Juni 1971, S. 1281.

[D5-4]   J. Gittus
           The Mechanical Equation of States: Dislocation Creep due to Stresses
           Varying in Magnitude and Direction, Phil. Mag. 24, No. 192, Dez.
           1971, S. 1423.

[D5-5]   E. Duncombe, C.M. Friedrich. J.K. Fischer:
           WAPD-TM-961, 1970

[D5-6]   E. Duncombe, C.M. Friedrich, W.H. Guilinger
           An Analytic Model for the Prediction of In-Pile Behaviour of Oxide
           Fuel Rods, Nucl. Technology 12, 1971, S. 195.

[D5-7]   H.-J. Ritzhaupt-Kleissl, W. Ernst:
           KfK 3145, April 1981

[D5-8]   H.-J. Ritzhaupt-Kleissl, M. Heck
           J. Nucl. Eng. & Design 101 (1987).

[D5-9]   B. Steinmetz, K. Fenneker
           Internal Note, 1982

[D5-10]   J.T.A. Roberts et al.
           ANL-8028, Juli 1973.

[D5-11]   D.L. Hagrmann, G.A. Reymann Eds.
           MATPRO-Version 11, NUREG/CR 0497, TREE-1280, 1979.

[D5-12]   K.L. Murty
           Scripta Met. 13, No. 4, 1979, S. 299.

[D5-13]   K.L. Murty et al.
           Trans. 4th. Int. Conf. on SMIRT, Aug. 1977, Paper C3/4.

[D5-14]   K.L. Murty, K.K. Yoon
           Trans. 4th. Int. Conf. on SMIRT, Aug. 1977, Paper C3/6.

[D5-15]   M. Mayuzumi, T. Onchi
           J. Nucl. Mat. 171, 1990, S. 381-388.

[D5-16]   J.E. Bird, A.K. Mukherjee, J.E. Dorn
           Correlations between High-Temperature Creep Behaviour and
           Structure, Proceedings of an International Conference on Quantitative
           Relations between Properties and Microstructure, Haifa, 1969, Ed.:
           D.G. Brandon, A. Rosen, Israel University Press, 1969.

[D5-17]   J.B. Newman, J.F. Giovengo, L.B. Comden:
          WAPD-TM-1300, 1977

[D5-18]   P. Murray, D.T. Livey, and J. Williams:
          The Hot Pressing of Ceramics, in Ceramic Fabrication Processes, W.D.
          Kingery, Ed. pp. 147-171, John Wiley and Sons, Inc., New York, 1958

[D5-19]   H. Hoffmann:
          Crack Formation, Crack Healing and Porosity Redistribution During
          Irradiation of UO_2 and $(U,Pu)O_2$,
          Journal of Nucl. Mat. V. 54 (1974), pp. 9-23

[D5-20]   W.A. Backofen, W.F. Hosford, J.J. Burke:
          Transactions of the ASM 55 No. 1, 1962

[D5-21]   C.R. Woods (Hrsg.):
          Properties of Zircaloy-4 Cladding,
          WAPD-TM-585, 1966
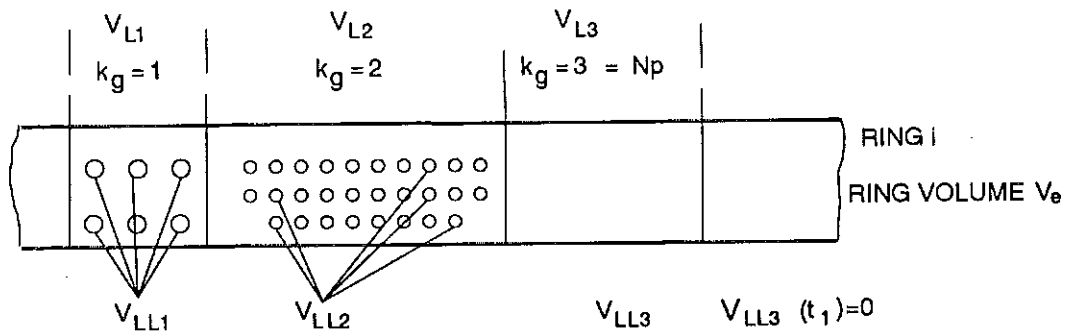
V_{L1}, V_{L2}, V_{L3} fraction of the area of void volume of category k_g in the ring
volume V_e ,related to the initial volume of the ring i

> Example: The pore zone of category $k_g = 1$ (V_{L1}) takes 20%
> of the original volume of the ring i, namely: $V_{L1} = 0.2$.

$V_{LL1}, V_{LL2}, V_{LL3}$ fraction of the true void volume (net porosity) of category k_g in
the volumes V_{L1}, V_{L2}, V_{L3} , related to the initial volume of the
ring i.

> Example: In the ring i, the pore distribution is as follows at
> time t_1 :
> total porosity: 5%
> porosity of category $k_g = 1$: 2% ⟶ $V_{LL1} = 0.02$
> porosity of category $k_g = 2$: 3% ⟶ $V_{LL2} = 0.03$
> porosity of category $k_g = 3$: 0% ⟶ $V_{LL3} = 0$

Fig. D5-1: Modeling the fuel porosity in the i-th ring element (Consideration at
time $t = t_1$)
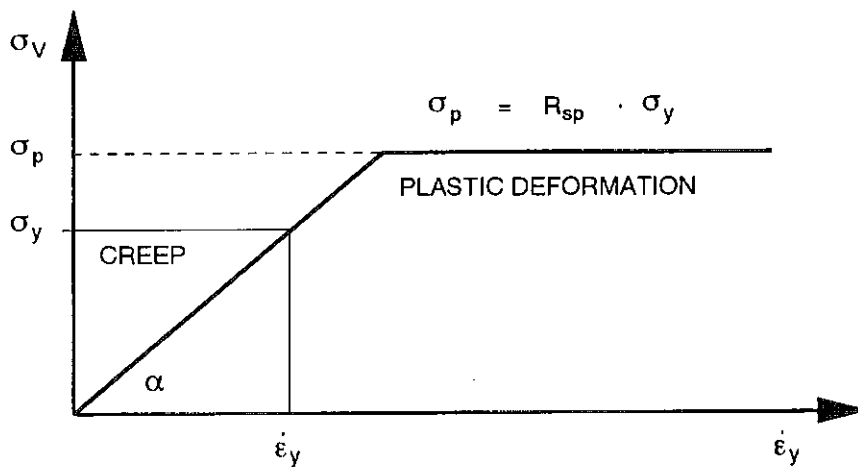
Fig. D5-2: Modeling creep and plasticity in the pore regions

D6. Establishing the Equilibrium of Forces at the Element

Work done by the external forces

For the work done by the external forces acting at the element, the following relationship holds:

$$W_{ext} = \sum_{i=1}^{n} \{F_e\}^T \cdot \{u^+\} + \int_A \{F_A\}^T \{u^+\} dA + \int_V \{FV\}^T \cdot \{u^+\} dV \qquad \text{(D6-1)}$$

where

$\quad$ n $\quad$ = number of element nodes

$\quad$ u$^+$ $\quad$ = virtual displacement

$$\{F_e\} = \{^{F_{er}}_{F_{ez}}\} \quad \textit{vector of the external nodal forces}$$

$$\{F_A\} = \{^{F_{ar}}_{F_{az}}\} \quad \textit{vector of the distributed surface forces}$$

$$\{F_V\} = \{^{F_{Vr}}_{F_{Vz}}\} \quad \textit{vector of the volume forces}$$

For the rectangular element with four nodes chosen here, eight nodal forces are obtained ; cf. also Fig. D6-1:

$$\{F_e\} = \begin{Bmatrix} F_{e1r} \\ F_{e1z} \\ F_{e2r} \\ F_{e2z} \\ F_{e3r} \\ F_{e3z} \\ F_{e4r} \\ F_{e4z} \end{Bmatrix} \qquad \text{(D6-2)}$$

A simplification can be made because for this rectangular element, the surface and nodal forces can be combined as shown in Fig. D6-2:

$$F_{e1r} + F_{e4r} + F_{ara} = F_{ea}$$

$$F_{e2r} + F_{e3r} + F_{arb} = F_{eb}$$

$$F_{e1z} + F_{e2z} + F_{e3z} + F_{e4z} + F_{az} = F_{ez}$$

hence $\qquad \{F_e\} = \left\{ \begin{array}{c} F_{ea} \\ F_{eb} \\ F_{ez} \end{array} \right\}$ (D6-3)

Furthermore, it applies: $\qquad \{F_A\} = \{F_V\} = 0$ (D6-4)

For the work done by the external forces the relationship holds:

$$\dot{W}_e = \{F_e\}^T \cdot \{\dot{u}\}$$ (D6-5)

Equation (D6-5), expressed in explicit terms, reads:

$$\dot{W}_e = \left\{ \begin{array}{c} F_{ea} \\ F_{eb} \\ F_{ez} \end{array} \right\}^T \cdot \left\{ \begin{array}{c} \dot{R}_a \\ \dot{R}_b \\ \dot{u}_z \end{array} \right\}$$ (D6-6)

Work done by the internal element forces

Generally, the work done by the internal element forces can be expressed as:

$$W_i = \int_V \{\sigma\}^T \cdot \{\varepsilon\} dV$$ (D6-7)

If the volume V_0, normalized after each time step, is assumed to be the element volume, one can write:

$$\dot{W}_i = V_0 \{\sigma\}^T \cdot \{\dot{\varepsilon}\}$$ (D6-8)

and

$$\dot{W}_i = V_0 \{\sigma\}^T \cdot |C| \cdot \{\dot{u}\}$$ (D6-9)

resp.

Setting equal the work done by the internal element forces with that done by the external forces

If the work of the external forces resp. their rates as described by equation (D6-5), is set equal to the work or the rates of the inner element forces represented by equation (D6-9), one obtains:

$$\dot{W}_i = \dot{W}_e \tag{D6-10}$$

$$\{F_e\}^T \cdot \{\dot{u}\} = V_0 \{\sigma\}^T \cdot |C| \cdot \{\dot{u}\} \tag{D6-11}$$

$$\{F_e\}^T = V_0 \{\sigma\}^T \cdot |C| \tag{D6-12}$$

$$\{F_e\} = V_0 \cdot |C|^T \cdot \{\sigma\} \tag{D6-13}$$

The description of the element forces according to equation (D6-13) will now be modified according to that for stresses, displacements and strains. This will lead to the description of the force rates. For this to be done, equation (D6-13) must be differentiated with respect to time:

In a formal derivation, equation (D6-13) reads:

$$\{\dot{F}_e\} = V_0 [\dot{C}]^T \cdot \{\sigma\} + V_0 |C|^T \cdot \{\dot{\sigma}\} \tag{D6-14}$$

The matrix [C]^T is obtained from equation (D4-24) as

$$|C|^T = \begin{bmatrix} \dfrac{1}{r_a - r_b} & \dfrac{1}{r_a + r_b} & 0 \\[2ex] \dfrac{-1}{r_a + r_b} & \dfrac{1}{r_a + r_b} & 0 \\[2ex] 0 & 0 & \dfrac{1}{\ell_z} \end{bmatrix} \tag{D6-15}$$

$$
[\dot{C}]^T =
\begin{bmatrix}
\dfrac{-1}{(r_a-r_b)^2} \cdot \dfrac{\partial(r_a-r_b)}{\partial t} & \dfrac{-1}{(r_a+r_b)^2} \cdot \dfrac{\partial(r_a+r_b)}{\partial t} & 0 \\[3ex]
\dfrac{+1}{(r_a-r_b)^2} \cdot \dfrac{\partial(r_a-r_b)}{\partial t} & \dfrac{-1}{(r_a+r_b)^2} \cdot \dfrac{\partial(r_a+r_b)}{\partial t} & 0 \\[3ex]
0 & 0 & \dfrac{1}{\ell_z^2} \cdot \dfrac{\partial \ell_z}{\partial t}
\end{bmatrix}
$$

(D6-16)

With

$$
\frac{\partial r_a}{\partial t} = \dot{R}_a \qquad \frac{\partial \ell_z}{\partial t} = \dot{u}_z
$$

$$
\frac{\partial r_b}{\partial t} = \dot{R}_b
$$

the product $[\dot{C}]^T \cdot \{o\}$ is obtained as follows:

$$
[\dot{C}]^T \cdot \{o\} =
\begin{bmatrix}
\dfrac{-o_r}{(r_a-r_b)^2} \dot{R}_a + \dfrac{o_r}{(r_a-r_b)^2} \dot{R}_b & \dfrac{-o_t}{(r_a+r_b)^2} \dot{R}_a - \dfrac{o_t}{(r_a+r_b)^2} \dot{R}_b & 0 \\[3ex]
\dfrac{+o_r}{(r_a-r_b)^2} \dot{R}_a - \dfrac{o_r}{(r_a-r_b)^2} \dot{R}_b & \dfrac{-o_t}{(r_a+r_b)^2} \dot{R}_a - \dfrac{o_t}{(r_a+r_b)^2} \dot{R}_b & 0 \\[3ex]
0 & 0 & \dfrac{o_z}{\ell_z^2} \dot{u}_z
\end{bmatrix}
$$

(D6-17)

A new matrix $[C_{ce}]$ can be introduced so that the following relationship holds:

$$
[\dot{C}]^T \cdot \{o\} = [C_{ce}] \cdot \{\dot{u}\}
$$

(D6-18)

Consequently, equation (D6-18) can be formulated as follows:

$$
\dot{|C|}^T \cdot \{\sigma\} = \begin{bmatrix} \dfrac{-\sigma_r}{(r_a - r_b)^2} & - & \dfrac{\sigma_t}{(r_a + r_b)^2} & \dfrac{\sigma_r}{(r_a - r_b)^2} & - & \dfrac{\sigma_t}{(r_a + r_b)^2} & 0 \\[3ex] \dfrac{\sigma_r}{(r_a - r_b)^2} & - & \dfrac{\sigma_t}{(r_a + r_b)^2} & \dfrac{-\sigma_r}{(r_a - r_b)^2} & - & \dfrac{\sigma_t}{(r_a + r_b)^2} & 0 \\[3ex] & 0 & & & 0 & & \dfrac{\sigma_z}{\ell_z^2} \end{bmatrix} \cdot \begin{Bmatrix} \dot{R}_a \\[2ex] \dot{R}_b \\[2ex] \dot{u}_z \end{Bmatrix}
$$

(D6-19)

With

$$
C_1 = \frac{\sigma_r}{(r_a - r_b)^2} \qquad \text{and} \qquad C_2 = \frac{\sigma_t}{(r_a + r_b)^2} \qquad \text{we obtain}
$$

$$
\dot{|C|}^T \cdot \{\sigma\} = \begin{bmatrix} -C_1 - C_2 & C_1 - C_2 & 0 \\[2ex] C_1 - C_2 & -C_1 - C_2 & 0 \\[2ex] 0 & 0 & \dfrac{\sigma_z}{\ell_z^2} \end{bmatrix} \cdot \begin{Bmatrix} \dot{R}_a \\[2ex] \dot{R}_b \\[2ex] \dot{u}_z \end{Bmatrix}
$$

(D6-20)

Thus, equation (D6-14) reads:

$$
\{\dot{F}_e\} = V_0 |C|^T \cdot \{\dot{\sigma}\} + V_0 |C_{ee}| \cdot \{\dot{u}\}
$$

(D6-21)
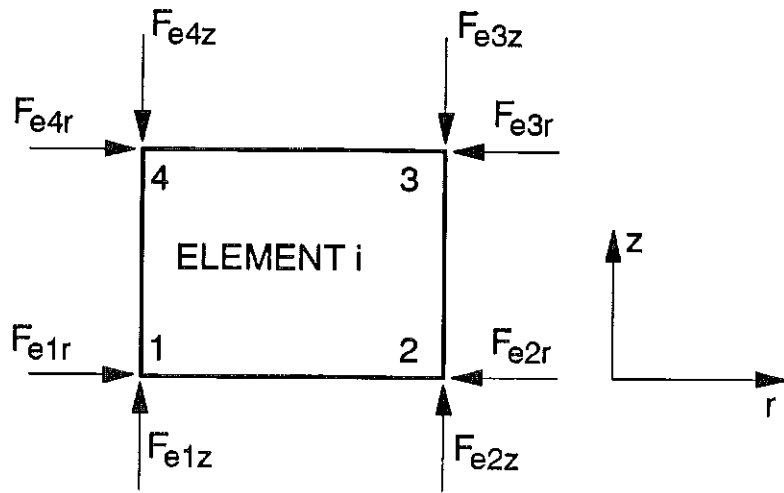
Fig. D6-1:   Nodal forces acting on the element
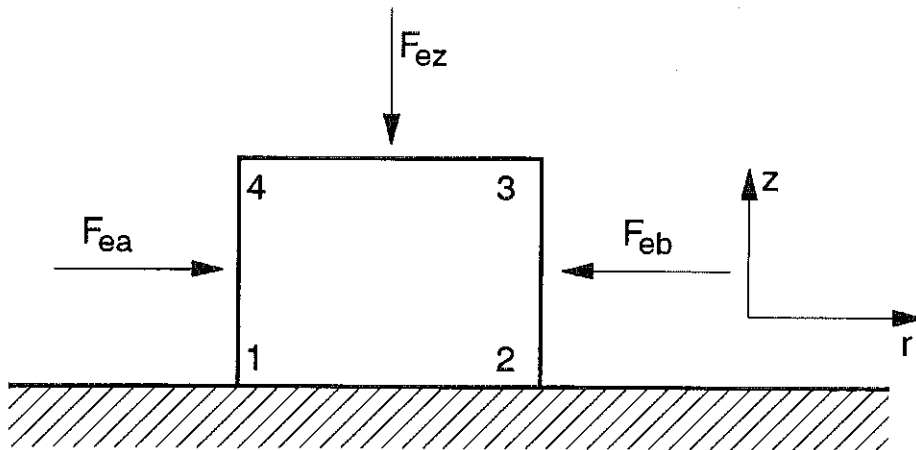
Fig. D6-2:   Combination of surface and nodal forces acting on a rectangular element

D7. The Element Stiffness Matrix

Introducing equation (D5-158), which represents the vector of the stress rates as a function of the displacements of the nodal points, into equation (D6-21), one obtains:

$$\{\dot{F}_e\} = V_0 [C]^T \left(\{B_1\} + [B_2] \cdot [C] \cdot \{\dot{u}\} \right) + V_0 \cdot [C_{ee}] \cdot \{\dot{u}\} \tag{D7-1}$$

Re-formulation yields:

$$\{\dot{F}_e\} = V_0 [C]^T \{B_1\} + \left(V_0 [C]^T [B_2] [C] + V_0 [C_{ee}] \right) \cdot \{\dot{u}\} \tag{D7-2}$$

Equation (D7-2) can be formally written as:

$$\{\dot{F}_e\} = \{B_{et}\} + [B_{es}] \cdot \{\dot{u}\} \tag{D7-3}$$

with

$$\{B_{et}\} = V_0 \cdot [C]^T \{B_1\} \tag{D7-4}$$

$$[B_{es}] = V_0 \cdot \left([C]^T [B_2] [C] + [C_{ee}] \right) \tag{D7-5}$$

where the matrix [B$_{es}$] is the stiffness matrix of the ring element. The matrix {B$_{et}$} is that of the so-called "thermal" element loadings.

As the matrices [B$_2$] and [C$_{ee}$] are symmetric, the element stiffness matrix [B$_{es}$] is also symmetric.

The matrix [C$_{ee}$] has been derived from the large deformation theory [D7-1]. In the problems to be analyzed here it is not essential to take it into account. For this reason, the user of the program can optionally activate or skip the matrix [C$_{ee}$].

Setting up the element stiffness matrices (equations (D7-4) and (D7-5)) terminates the consideration of the element mechanics. The element stiffness matrices describe the behavior of one element by defined material characteristics under thermal and mechanical loads. These stiffness matrices are consecutively set up for all elements, both of the fuel and the cladding.

Procedure in the computer program

The result of Section D4, the matrix of the shape functions, is calculated in the SHAPE subroutine. This subroutine is called for each element.

The matrix $[C_{ee}]$ is likewise calculated for each element in the CMAT 1 subroutine. In the MATH and MATB subroutines the Young's modulus, the Poisson ratio and the thermal strain are calculated for the cladding and the fuel.

The material laws and the flexibility matrices, resp., described in Section D5 are calculated in the subroutines;

ATH	for	$[A_{th}]$
ELAS	for	$[A_{el}]$
ANE	for	$[A_{ne}]$ and
PLAST	for	$[A1_{ne}]$ and $[A2_{ne}]$
PORMECH	for	$[A1_{irr}]$ and $[A2_{irr}]$

The element stiffness matrix for each element is determined in the STIME subroutine.

Reference:

[D7-1]   O.C. Zienkiewicz:
          Methode der finiten Elemente,
          Hanser-Verlag, 1975.

D8. Assembly of the Elements to the Complete Structure

After the stiffness has been determined for each element, all elements of the fuel and cladding are combined so that the total stiffness of the fuel and the cladding is obtained.

Starting from the consideration of any element, the assembly will be described here.

The element displacement rates and the external forces acting at the k-th element can be written as follows, e.g. for the fuel:

$$\{\dot{u}\}^k = \left\{ \begin{array}{c} \dot{R}_{ka} \\ \dot{R}_{kb} \\ \dot{u}_z \end{array} \right\} \tag{D8-1}$$

$$\{F_e\}^k = \left\{ \begin{array}{c} F_{ka} \\ F_{kb} \\ F_{kz} \end{array} \right\} \tag{D8-2}$$

With a number of N-1 elements, i.e. for N radii, N-1 systems of equations of the type of equation (D7-3) are obtained:

$$\{F_e\}^k = \{B_{el}\}^k + [B_{es}]_k \cdot \{u\}^k \tag{D8-3}$$

with: k = 1.2...(N-1).

For the rates of the total external forces acting at the structure the following relations hold:

$$\dot{F}_{1a} = \dot{F}_{Ba} \tag{D8-4}$$

$$\dot{F}_{(N-1)b} = \dot{F}_{Bb} \tag{D8-5}$$

$$\sum_{k=1}^{N-1} \dot{F}_{kz} = \dot{F}_z \tag{D8-6}$$

Moreover, the following equilibrium of forces at the interfaces of the ring elements apply:

$$F_{ka} = -F_{(k-1)b} \qquad \text{(N-2 equations)} \qquad \text{(D8-7)}$$

Furthermore, the rates of displacement of the external fuel contours can be written as follows:

$$\dot{R}_{1a} = \dot{R}_{Ba} \qquad \text{(D8-8)}$$

$$\dot{R}_{(N-1)b} = \dot{R}_{Bb} \qquad \text{(D8-9)}$$

and the following condition of continuity holds:

$$\dot{R}_{ka} = \dot{R}_{(k-1)b} \qquad \text{(N-2 equations)} \qquad \text{(D8-10)}$$

The number of equations available for determination of the overall equilibrium is 5N-2 using equations (D8-3) through (D8-10).

Using these equations, three stiffness equations of the following type will now be written for the fuel:

$$\{\dot{F}_B\} = \{B_{Bt}\} + [B_{Bb}] \{\dot{u}_B\} \qquad \text{(D8-11)}$$

$$\{\dot{F}_B\} = \left\{ \begin{array}{c} \dot{F}_{Ba} \\ \dot{F}_{Bb} \\ \dot{F}_{Bz} \end{array} \right\}$$

$$\{\dot{u}_B\} = \left\{ \begin{array}{c} \dot{R}_{Ba} \\ \dot{R}_{Bb} \\ u_{Bz} \end{array} \right\}$$

Based on the assumption that the assembly for the first k-1 elements has already been completed, this leads to the following equations:

$$\{\dot{F}_{k-1}\} = \{B_{(k-1)t}\} + [B_{(k-1)(k-1)}] \cdot \{\dot{u}_{(k-1)}\} \qquad \text{(D8-12)}$$

with $\{\dot{F}_{k-1}\} = \left\{ \begin{array}{c} \dot{F}_{Ba} \\ \dot{F}_{(k-1)b} \\ F_{1(k-1)z} \end{array} \right\}$

and $\{\dot{u}_{(k-1)}\} = \left\{ \begin{array}{c} \dot{R}_{Ba} \\ \dot{R}_{(k-1)b} \\ u_{Bz} \end{array} \right\}$

The equation describing the element stiffness of the k-th ring reads:

$$\{\dot{F}_e^{(k)}\} = \{B_{el}^{(k)}\} + [B_{es}^{(k)}] \cdot \{\dot{u}^{(k)}\} \tag{D8-13}$$

The rate of work done by the external forces on the structure of the first k-1 elements is obtained as follows:

$$\dot{W}_{1(k-1)} = \{F_{k-1}\}^T \cdot \{\dot{u}_{1(k-1)}\} \tag{D8-14}$$

For the k-th element the following relation is obtained:

$$\dot{W}_k = \{F_e^{(k)}\}^T \cdot \{\dot{u}^{(k)}\} \tag{D8-15}$$

Sum of the equations (D8-14) and (D8-15):

$$\dot{W}_{1k} = \{F_{k-1}\}^T \cdot \{\dot{u}_{1(k-1)}\} + \{F_e^{(k)}\}^T \cdot \{\dot{u}^{(k)}\} \tag{D8-16}$$

or

$$\dot{W}_{1k} = \{F_{(k-1)k}\}^T \cdot \{\dot{u}_{(k-1)k}\} \tag{D8-17}$$

with the dimensions:

$$\{D_{(k-1)k}\} = \left\{ \begin{array}{c} R_{ba} \\ R_{kb} \\ L_{Bz} \\ R_{(k-1)b} \end{array} \right\} \tag{D8-18}$$

and with the forces

$$\{F_{(k-1)k}\} = \begin{Bmatrix} F_{Ba} \\ F_{kb} \\ F_{1(k-1)z} \\ F_{(k-1)b} + F_{ka} \end{Bmatrix}$$

(D8-19)

Since

$$\frac{\partial \{D\}}{\partial t} = \{\dot{u}\}$$

(D8-20)

one can write:

$$\{\dot{u}_{k-1}\} = |C_{k-1}| \{\dot{u}_{(k-1)k}\}$$

(D8-21)

$$\{\dot{u}\}^{(k)} = |C_e| \{\dot{u}_{(k-1)k}\}$$

(D8-22)

with

$$\begin{Bmatrix} \dot{R}_{Ba} \\ \dot{R}_{(k-1)b} \\ \dot{u}_{Bz} \end{Bmatrix} = \underbrace{\begin{bmatrix} 1 & 0 & 0 & 0 \\ 0 & 0 & 0 & 1 \\ 0 & 0 & 1 & 0 \end{bmatrix}}_{[C_{k-1}]} \cdot \begin{Bmatrix} \dot{R}_{Ba} \\ \dot{R}_{kb} \\ \dot{u}_{Bz} \\ \dot{R}_{(k-1)b} \end{Bmatrix}$$

(D8-23)

$$\begin{Bmatrix} \dot{R}_{ka} \\ \dot{R}_{kb} \\ \dot{u}_{Bz} \end{Bmatrix} = \underbrace{\begin{bmatrix} 0 & 0 & 0 & 1 \\ 0 & 1 & 0 & 0 \\ 0 & 0 & 1 & 0 \end{bmatrix}}_{[C_e]} \cdot \begin{Bmatrix} \dot{R}_{Ba} \\ \dot{R}_{kb} \\ \dot{u}_{Bz} \\ \dot{R}_{(k-1)b} \end{Bmatrix}$$

(D8-24)

Hence:

$$\dot{W}_{1k} = \left(\{F_{k-1}\}^T \cdot |C_{k-1}| + \{F_e^{(k)}\}^T \cdot |C_e| \right) \cdot \{\dot{u}_{(k-1)k}\} \tag{D8-25}$$

and

$$\{F_{(k-1)k}\}^T = \{F_{k-1}\}^T \cdot |C_{k-1}| + \{F_e^k\}^T \cdot [C_e] \tag{D8-26}$$

resp.

or

$$\{F_{(k-1)k}\} = |C_{k-1}|^T \cdot \{F_{k-1}\} + |C_e|^T \cdot \{F_e^k\} \tag{D8-27}$$

Differentiating with respect to time yields the following

$$\{\dot{F}_{(k-1)k}\} = |C_{k-1}|^T \cdot \{\dot{F}_{k-1}\} + |C_e|^T \cdot \{\dot{F}_e^k\} \tag{D8-28}$$

Equation (D8-28) can now be written formally so that the force-displacement relations can be described, provided that the k-th element is attached to the k-1 elements previously assembled:

$$\{\dot{F}_{(k-1)k}\} = \{B_{(k-1)kt}\} + |B_{(k-1)k}| \cdot \{\dot{u}_{(k-1)k}\} \tag{D8-29}$$

Thus, equation (D8-29) describes the stiffness of the structure from element 1 through element k in the case considered here.

The two matrix expressions in equation (D8-29) read in detail:

$$\{B_{(k-1)kt}\} = |C_{k-1}|^T \cdot \{B_{(k-1)t}\} + |C_e|^T \cdot \{B_{et}\}^{(k)} \tag{D8-30}$$

(see equation (D8-13))

$$|B_{(k-1)k}| = |C_{k-1}|^T \cdot |B_{(k-1)(k-1)}| \cdot |C_{k-1}| + |C_e|^T \cdot |B_{es}^{(k)}||C_e| \tag{D8-31}$$

(see equation (D8-13))

As the matrix $|B_{(k-1)k}|$ is positive definite, it can be inverted so that equation (D8-29) can be solved for $\{\dot{u}_{(k-1)k}\}$:

$$\{\dot{u}_{(k-1)k}\} = \{A_{(k-1)kt}\} + |A_{(k-1)k}| \cdot \{\dot{F}_{(k-1)k}\} \cdot \{\dot{F}_{(k-1)k}\} \tag{D8-32}$$

with $\qquad \{A_{(k-1)kl}\} = -[B_{(k-1)k}]^{-1} \cdot \{B_{(k-1)kl}\}$

and $\qquad [A_{(k-1)k}] = -[B_{(k-1)k}]^{-1}$

As there must be an equilibrium of the forces at the interface of two ring elements when they are assembled, the fourth component of the vector $\{F_{(k-1)k}\}$ in equation (D8-19) reads as follows:

$$F_{(k-1)b} + F_{ka} = 0 \qquad \text{(D8-33)}$$

Consequently, the fourth component of the vector $\{\dot{F}_{(k-1)k}\}$ in equations (D8-29) and (D8-32) also becomes

$$\dot{F}_{(k-1)b} + \dot{F}_{ka} = 0 \qquad \text{(D8-34)}$$

Thus, the first three lines of equation (D8-32) can be formulated as follows:

$$\{\dot{u}_k\} = \{A_{kl}\} + [A_{kk}] \cdot \{\dot{F}_k\} \qquad \text{(D8-35)}$$

where A_{kl} consists of the first three elements of $\{A_{(k-1)kl}\}$ and A_{kk} of the first three lines and three columns of the matrix $[A_{(k-1)k}]$. As $[A_{(k-1)k}]$ is positive definite, equation (D8-35) can be solved for the vector of the force rates:

$$\{\dot{F}_k\} = \{B_{kl}\} + [B_{kk}] \cdot \{\dot{u}_k\} \qquad \text{(D8-36)}$$

with

$$\{B_{kl}\} = -[A_{kk}]^{-1} \cdot \{A_{kl}\}$$

$$[B_{kk}] = [A_{kk}]^{-1}$$

Equation (D8-36) is the required equation for description of the stiffness of the structure of the first k-elements.

Special case:

For $k = 1$ it holds:

$$\{B_{1l}\} = \{B_{el}\}^{(1)}$$

$$[B_{11}] = [B_{es}]^{(1)}$$

For $k = N\text{-}1$ it holds, e.g. for the fuel, subscript B:

$$\{B_{Bt}\} = \{B_{(N-1)t}\} \qquad\qquad |B_{BB}| = |B_{(N-1)(N-1)}|$$

and hence:

$$\{F_B\} = \{B_{Bt}\} + |B_{BB}| \cdot \{u_B\} \qquad\qquad \text{(D8-36a)}$$

The procedure is similar in assembling the elements of the cladding. According to equation (D8-36a) with the subscript H meaning cladding, we obtain:

$$\{\dot{F}_H\} = \{B_{Ht}\} + |B_{HH}| \cdot \{\dot{u}_H\} \qquad\qquad \text{(D8-37)}$$

with

$$\{\dot{F}_H\} = \left\{ \begin{array}{c} \dot{F}_{Ha} \\ \dot{F}_{Hb} \\ F_{Hz} \end{array} \right\}$$

and

$$\{\dot{u}_H\} = \left\{ \begin{array}{c} R_{Ha} \\ R_{Hb} \\ u_{Hz} \end{array} \right\}$$

With equations (D8-36) and (D8-37) available, a general solution is now at hand for the description of the relationship existing between the forces or their rates resp. acting on the structure, and the resulting displacements and displacement rates, resp., of the structure.

Procedure in the computer program:

The assembly of the elements of the fuel and cladding and the generation of the structure stiffnesses are performed in the ASSEM subroutine. The matrices $[C_e]$ and $[C_{k\,1}]$ are get up by the CMAT subroutine.

D9. External Forces Acting on the Fuel Rod

D9.1 Pressure Forces and Contact Forces

The external forces in the fuel/cladding system are pressure and contact as well as friction forces, as represented in Fig.D9-1.

Assuming the axial length normalized to unity, the following relationship holds:

$$L_{Bz}(t) = L_{Hz}(t) = 1 \tag{D9-1}$$

The pressure forces exerted by the fission gas pressure p_{gap} are:

$$F_{pBa} = 2\pi R_{Ba} \cdot L_{Bz} \cdot p_{gap}$$

$$F_{pBb} = 2\pi R_{Bb} \cdot L_{Bz} \cdot p_{gap} \tag{D9-2}$$

$$F_{pBz} = 2\pi (R_{Bb}^2 - R_{Ba}^2) \cdot p_{gap}$$

Equations (D9-2), differentiated with respect to time, read:

$$\{\dot{F}_{pB}\} = \pi \cdot \begin{bmatrix} 2R_{Ba} \cdot L_{Bz} \\ 2R_{Bb} \cdot L_{Bz} \\ (R_{Bb}^2 - R_{Ba}^2) \end{bmatrix} \cdot \dot{p}_{gap} \tag{D9-3}$$

Accordingly, the following expression applies to the cladding:

$$\{\dot{F}_{pH}\} = \pi \cdot \begin{bmatrix} 2R_{Ha} \cdot L_{Hz} \cdot \dot{p}_{gap} \\ 2R_{Hb} \cdot L_{Hz} \cdot \dot{p}_{gap} \\ (R_{Hb}^2 \cdot \dot{p}_k - R_{Ha}^2 \cdot \dot{p}_{gap}) \end{bmatrix} \tag{D9-4}$$

where p_k stands for coolant pressure.

The total loads on the fuel and cladding system can be separated into pressure forces and contact forces:

For the fuel:

$$F_{Ba} = F_{pBa}$$

$$F_{Bb} = - F_{pBb} - F_{2con} \tag{D9-5}$$

$$F_{Bz} = - F_{pBz} - F_{3con}$$

and for the cladding

$$F_{Ha} = + F_{pHa} + F_{2con}$$

$$F_{Hb} = - F_{pHb}$$

$$F_{Hz} = - F_{pHz} + F_{3con}$$

(D9-6)

resp.

The systems of equations (D9-5) and (D9-6) can be differentiated and written as matrices:

For the fuel

$$\{\dot{F}_B\} = [C_B] \cdot \{\dot{F}_{pB}\} + [C_B] \cdot \{\dot{F}_{con}\}$$

(D9-7)

For the cladding

$$\{\dot{F}_H\} = [C_B] \cdot \{\dot{F}_{pH}\} + [C_H] \cdot \{\dot{F}_{con}\}$$

(D9-8)

with

$$[C_B] = \begin{bmatrix} 1 & 0 & 0 \\ 0 & -1 & 0 \\ 0 & 0 & -1 \end{bmatrix}$$

(D9-9)

$$[C_H] = \begin{bmatrix} 0 & 1 & 0 \\ 0 & 0 & 0 \\ 0 & 0 & 1 \end{bmatrix}$$

(D9-10)

The vectors $\{F_{pB}\}$ and $\{F_{pH}\}$ are known; $\{F_{con}\}$ must be determined using the boundary conditions. The first component of $\{F_{con}\}$ is $\dot{F}_1 = 0$, since there is no contact pressure from the central channel to the pellet. The second component $\dot{F}_2$ is the rate of the radial contact force normalized to the axial length

$$\dot{F}_2 = \dot{F}_R$$

(D9-11)

The third component $\dot{F}_3$ is the rate of the contact force which is transmitted by friction and which acts in axial direction.

$$\dot{F}_3 = \dot{F}_Z$$

(D9-12)

D9.2 Friction Between the Pellet and the Cladding

Radial and axial displacement take place after closure of the gap between the fuel and the cladding. This is due to the forces whitch are evaluated above. There is also possible relative displacement between the fuel and the cladding due to sliding friction. These effects are now analysed.

For the axial friction force the following expression holds:

$$F_z \le \int_0^\ell \mu \cdot F_R \, d\ell \tag{D9-13}$$

where ℓ is the contact length.

In the case considered here, equation (D9-13) will be simplified by introducing a mean friction coefficient which is independent of the contact length so that we obtain in an approximation:

$$F_z \le \overline{\mu} \cdot F_R \tag{D9-14}$$

The equations used to describe the forces and relative displacements at the contact surfaces between the pellet and the cladding are supposed to take the form:

$$\Delta\varepsilon_z = a + b\Delta t + c\Delta F_R + d\Delta F_z \tag{D9-15}$$

$$\Delta(r_{Ha} - r_{Hb}) = f + g\Delta t + h\Delta F_R + k\Delta F_z \tag{D9-16}$$

where

$\Delta\varepsilon_z =$ axial relative strain between the pellet and the cladding

$r_{Ha} =$ inner radius of the cladding

$r_{Bb} =$ outer radius of the pellets

In case the fuel and the cladding do not contact each other, $\Delta(r_{Ha} - r_{Bb}) > 0$, $F_R = F_Z = 0$.

The rates of the external forces acting on the fuel and the cladding are given by equations (D9-7) and (D9-8); the vector for describing the spacing between the fuel and the cladding reads:

$$\{D\} = \left\{ \begin{array}{c} R_{Ba} \\ R_{Ha} - R_{Bb} \\ \varepsilon_{Hz} - \varepsilon_{Bz} \end{array} \right\} \tag{D9-17}$$

Differentiating with respect to time, the relative rates of displacement between the fuel and the cladding are obtained

$$\{\dot{D}\} = \left\{ \begin{array}{c} \dot{R}_{Ba} \\ \dot{R}_{Ha} - \dot{R}_{Bb} \\ \dot{\varepsilon}_{Hz} - \dot{\varepsilon}_{Bz} \end{array} \right\} \tag{D9-18}$$

or

$$\{\dot{D}\} = \underbrace{\begin{bmatrix} 1 & 0 & 0 \\ 0 & -1 & 0 \\ 0 & 0 & -1 \end{bmatrix}}_{[C_B] = [CB]^T} \cdot \left\{ \begin{array}{c} \dot{R}_{Ba} \\ \dot{R}_{Bb} \\ \dot{\varepsilon}_{Bz} \end{array} \right\} + \underbrace{\begin{bmatrix} 0 & 0 & 0 \\ 1 & 0 & 0 \\ 0 & 0 & 1 \end{bmatrix}}_{[C_H]^T} \cdot \left\{ \begin{array}{c} \dot{R}_{Ha} \\ \dot{R}_{Hb} \\ \dot{\varepsilon}_{Hz} \end{array} \right\} \tag{D9-19}$$

Consequently, the expression reads:

$$\{\dot{D}\} = [C_B]^T \cdot \{\dot{u}_B\} + [C_H]^T \cdot \{\dot{u}_H\} \tag{D9-20}$$

The stiffness equations for the fuel and the cladding yield: (cf. equation (D8-35):

$$\{\dot{u}_B\} = \{A_{Bt}\} + [A_{BB}] \cdot \{\dot{F}_B\} \tag{D9-21}$$

with

$$\{A_{Bt}\} = -[B_{BB}]^{-1} \cdot \{B_{Bt}\}$$

$$[A_{BB}] = [B_{BB}]^{-1} \tag{D9-22}$$

$$\{\dot{u}_H\} = \{A_{Ht}\} + [A_{HH}] \cdot \{\dot{F}_H\}$$

with

$$\{A_{Ht}\} = -[B_{HH}]^{-1} \cdot \{B_{Ht}\}$$

$$[A_{HH}] = [B_{HH}]^{-1}$$

Introduction into (D9-20) yields:

$$\{\dot{D}\} = |C_B|^T \cdot \{\dot{A}_{Bt}\} + |C_B|^T \cdot |A_{BB}| \cdot \{\dot{F}_B\} + |C_H|^T \cdot \{\dot{A}_{Ht}\} + |C_H|^T \cdot |A_{HH}| \cdot \{\dot{F}_H\}$$

$$(D9\text{-}23)$$

Rearrangement, we get:

$$\{\dot{D}\} = |C_B|^T \cdot \{\dot{A}_{Bt}\} + |C_H|^T \cdot \{\dot{A}_{Ht}\} + |C_B|^T \cdot |A_{BB}| \cdot \{\dot{F}_B\} + |C_H|^T \cdot |A_{HH}| \cdot \{\dot{F}_H\}$$

with $$(D9\text{-}24)$$

$$\{\dot{F}_B\} = |C_B|\{\dot{F}_{pB}\} + |C_B|\{\dot{F}_{con}\} \qquad \text{(s. equation (D9-7))}$$

and

$$\{\dot{F}_H\} = |C_B|\{\dot{F}_{pH}\} + |C_H|\{\dot{F}_{con}\} \qquad \text{(s. equation (D9-8))}$$

one finally obtains:

$$\boxed{\{\dot{D}\} = \{A_t\} + |A| \cdot \{\dot{F}_{con}\}} \qquad (D9\text{-}25)$$

with

$$\{A_t\} = |C_B|^T \cdot \{\dot{A}_{Bt}\} + |C_H|^T \cdot \{\dot{A}_{Ht}\} + |C_B|^T \cdot |A_{BB}| \cdot |C_B| \cdot \{\dot{F}_{pB}\} +$$

$$+ |C_H|^T \cdot |A_{HH}| \cdot |C_B| \cdot \{\dot{F}_{pH}\}$$

and with

$$|A| = |C_B|^T \cdot |A_{BB}| \cdot |C_B| + |C_H|^T \cdot |A_{HH}| \cdot |C_H|$$

In explicit terms, the vector $\{\dot{D}\}$ can be written by its components as follows:

$$\dot{D}_1 = A_{1t} + A_{11} \ \dot{F}_1 + A_{12} \ \dot{F}_r + A_{13} \ \dot{F}_z$$

$$\dot{D}_2 = A_{2t} + A_{21} \ \dot{F}_1 + A_{22} \ \dot{F}_r + A_{23} \ \dot{F}_z \qquad (D9\text{-}26)$$

$$\dot{D}_3 = A_{3t} + A_{31} \ \dot{F}_1 + A_{32} \ \dot{F}_r + A_{33} \ \dot{F}_z$$

Since $F_1 = 0$, one obtains:

$$\dot{D}_1 = \dot{R}_{Ba}$$

$$\dot{D}_2 = A_{2t} + A_{22} \ \dot{F}_r + A_{23} \ \dot{F}_z \qquad (D9\text{-}27)$$

$$\dot{D}_3 = A_{3t} + A_{32} \ \dot{F}_r + A_{33} \ \dot{F}_z$$

Now several cases can be distinguished.

1st case: There is no contact between the fuel and the cladding. In that case, contact forces are neither acting, i.e. $\dot{F}_r = \dot{F}_z = 0$, and

$$\dot{D}_2 = A_{2t} \qquad\qquad \dot{D}_3 = A_{3t} \qquad\qquad \text{(D9-28)}$$

2nd case: There is contact between the fuel and the cladding. In that case, the general expression $\dot{D}_2 = 0$ holds which means that the radial displacements of the fuel and the cladding on the contact surface are identical.

Now, there are two possibilities of axial relative displacement: adhesion or slip. The case of adhesion will first of all be investigated. In that case it applies:

$$\dot{D}_3 = 0$$

This yields the axial and radial contact force rates from equation (D9-27) as:

$$\dot{F}_z = \frac{A_{3t} \cdot A_{22} - A_{2t} \cdot A_{32}}{A_{23} \cdot A_{32} - A_{22} \cdot A_{33}} \qquad\qquad \text{(D9-29)}$$

$$\dot{F}_r = \frac{A_{2t} \cdot A_{33} - A_{3t} \cdot A_{23}}{A_{23} \cdot A_{32} - A_{22} \cdot A_{33}} \qquad\qquad \text{(D9-30)}$$

The question is asked whether the condition of adhesion is fulfilled; in that case, the following expression must be satisfied:

$$F_z + \dot{F}_z \cdot \Delta t \leq \mu (F_r + \dot{F}_r \cdot \Delta t) \qquad\qquad \text{(D9-31)}$$

where F_z and F_r are the axial and radial contact forces, resp., at the end of the last time step and μ is the friction coefficient.

If equation (D9-31) is fulfilled, then expressions (D9-29) and (D9-30) are the axial and radial contact and friction forces, resp.

However, if condition (D9-31) is not fulfilled, i.e.

$$F_z + \Delta F_z > \mu (F_r + \Delta F_r) \qquad\qquad \text{(D9-32)}$$

the second assumption will apply which describes slipping of the pellet and cladding against each other. The maximum force rates which can be transmitted are calculated as:

$$\dot{F}_z \quad \frac{\mu \, (F_r + \Delta F_r) - F_z}{\Delta t} \qquad\qquad\qquad \text{(D9-33)}$$

$$\dot{F}_r \quad \frac{A_{23}\,(F_z - \mu \cdot F_r) - A_{2t} \cdot \Delta t}{(A_{22} + \mu \cdot A_{23}) \cdot \Delta t} \qquad\qquad \text{(D9-34)}$$

In this way, all elements of equation (D9-7) and (D9-8) have been determined and the overall equilibrium of the structure can be calculated.

Procedure in the computer program

The pressure and the total forces acting on the fuel and the cladding and likewise the free displacements of fuel and cladding are calculated in the FORCES subroutine. The FORCES subroutine also queries whether the fuel and the cladding are in contact. If so, FORCES calls the CONTAC subroutine which computes the rates of the radial and axial contact forces. The matrices [CB] and [CH] are called from the CMAT subroutine; the friction coefficient μ is made available via the input. The time interval Δt is the result of a time step calculation which is done in the DTIME, DTTEMP and DTPOR subroutines. This will be reported elsewhere.
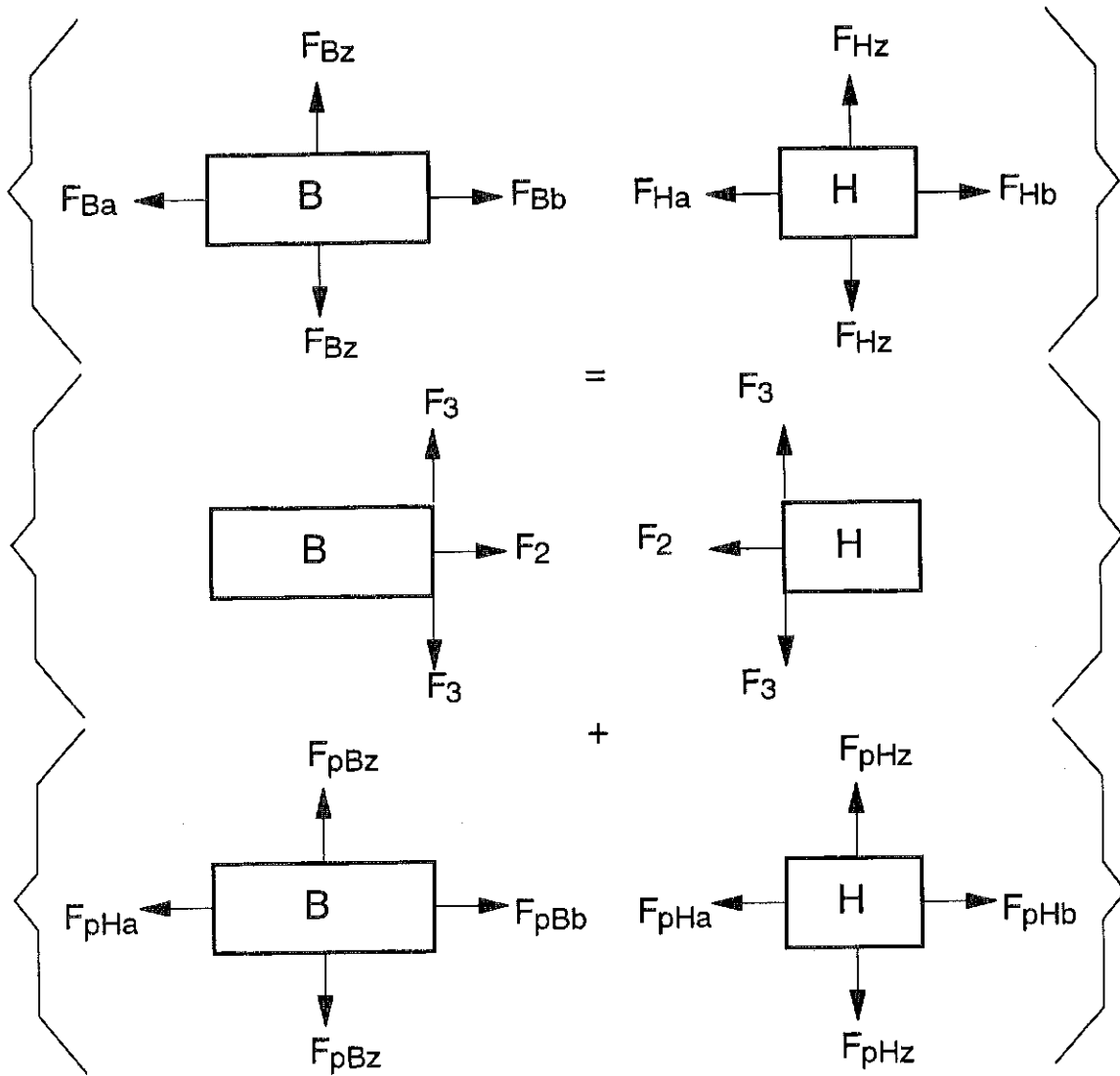
Fig. D9-1: External forces as the sum of pressure loads and contact forces

D10. Computation of the Stress and Strain Rates of the Elements

The forces acting on the entire structure have now been determined. What now remains is to use this information, together with the calculated stiffness, to determine the displacement, strain and stress rates of the individual elements. Starting with a general force-displacement approach for the structure, the computation proceeds in reverse fashion to the assembly of the elements.

The procedure of computation for the fuel is as follows :

for $k = N_e$ it applies

$$\{\dot{F}_k\} = \{\dot{F}_B\} \tag{D10-1}$$

and

$$\{\dot{F}_{k-1,k}\} = \left\{ \begin{array}{c} \dot{F}_{B1} \\ \dot{F}_{B2} \\ \dot{F}_{B3} \\ 0 \end{array} \right\} \tag{D10-2}$$

This yields

$$\{\dot{u}_{(k-1)k}\} = \{A_{t(k-1)k}\} + |A_{(k-1)k}| \cdot \{\dot{F}_{(k-1)k}\} \tag{D10-3}$$

because when beginning computations for the k-th ring, the first three components of the vector $\{\dot{F}_{(k-1)k}\}$ (see equation (D8-19)) are known. The fourth component is found to be zero which means that it is also known (see equation (D8-19): $F_{(k-1)b} = F_{ka}$). Consequently, the fourth line of equation (D8-32) yields the displacement rate $\dot{R}_{ka}$ which is identical with $\dot{R}_{(k-1)b}$, so that all components of the displacement vector $\{\dot{u}_{(k-1)k}\}$ are known.

The displacement vector of the k-th element can be calculated from this as:

$$\{\dot{u}_e\}^k = |CE| \cdot \{\dot{u}_{(k-1)k}\} \tag{D10-4}$$

The force rates at the k-th element are obtained as

$$\{\dot{F}_e\}^k = \{B_{et}\}^k + |B_{es}|^k \cdot \{\dot{u}_e\}^k \tag{D10-5}$$

For a general k, i.e. for k < N_e, it follows:

However, all these components of the vector are known, namely:

$$\{\dot{F}_{(k-1)\,k}\} = \left\{ \begin{array}{c} \dot{F}_{B1} \\ -\dot{F}_{e1}^{k} \\ \dot{F}_{k(k+1)\,3} - \dot{F}_{e3}^{k} \\ 0 \end{array} \right\} \tag{D10-6}$$

- $\dot{F}_{B1}$ is the radial force on the inner edge of the pellet.

- $-\dot{F}_{e1}$ is the negative 1st component and $\dot{F}_{e3}{}^{k}$ is the 3rd component of the vector of the force rates of the k-th element, i.e. the element calculated last.

One can calculate from this:

$$\{\ddot{u}_{(k-1)\,k}\}$$
$$\{\ddot{u}_{e}\}^{k}$$
$$\{\dot{F}_{e}\}^{k} \quad \text{etc.}$$

The procedure is similar for the cladding.

The strain rates of the individual elements can then simply be calculated from the displacement rates using the matrix of the shape functions

$$\{\dot{\varepsilon}\}_{k} = |C|_{k} \cdot \{\dot{u}_{e}\}^{k} \tag{D10-7}$$

and the stress rates

$$\{\dot{\sigma}\}_{k} = \{B1\}_{k} + |B2|_{k} \cdot \{\dot{\varepsilon}\}^{k} \tag{D10-8}$$

Splitting the strain rates into individual parts:

elastic strain rate:

$$\{\dot{\varepsilon}_{el}\}_{k} = |A_{el}|_{k} \cdot \{\dot{\sigma}\}_{k} \tag{D10-9}$$

non-elastic portion:

$$\{\dot{\varepsilon}_{ne}\}_{k} = \{A1_{ne}\}_{k} + |A2_{ne}|_{k} \cdot \{\dot{\sigma}\}_{k} \tag{D10-10}$$

Strain rate caused by swelling, densification, fission gas bubbles, porosity:

$$\{\dot{\varepsilon}_{irr}\}_k = \{A1_{irr}\}_k + | A2_{irr}|_k \cdot \{\dot{\sigma}\}_k \tag{D10-11}$$

Computation of the equivalent stress rate:

$$\{\dot{\sigma}_v\}_k = \{(A_{ne})_k\}^T + \{\dot{\sigma}\}_k \tag{D10-12}$$

Procedure in the computer program

Dividing the entire structure into single elements and computation of force, displacement, strain and stress rates are all performed in the STDIS subroutine.

D11. Fuel Cracking Relocation and Crack Healing

D11.1 General Remarks

The complete modeling of a fuel pin, and especially of a fuel stack needs the knowledge and the detailed description of the thermomechanical behaviour. This means not only the description of a ceramic, heat generating cylinder, the shape in which the fuel pellet originally exists.

Still the detailed and sophisticated modeling of a cylindrical fuel pellet during reactor operation is not quite easy, the description of a pellet which undergoes cracking, relocation and crack healing is far more complicated and subject to further uncertainties, because of the following reasons:

- The cracking of a ceramic pellet in an axisymmetric, parabolic temperature field is a randomly occuring effect, which cannot be modeled in a deterministic way, as all the other phenomena in the field of fuel modeling.

- Pellet cracking during startup ramps causes a radial displacement of the fragments, the pellet relocation. This relocation, reducing the radial gap between pellet and cladding, has a direct influence on the gap conductance and so on the temperature profile in the fuel.

- By cracking the stiffness of the fuel is reduced. This effect has an influence on the mechnical behaviour when the radial gap between fuel and cladding closes - and it will close earlier because of the relocation. So the mechanical interaction between pellet and cladding (PCI) will look different, based on changed mechanical fuel properties.

- During operation crack healing will occur, dependent on the fields of local temperature and hydrostatic pressure.

- During shutdown, further cracking will occur, partly resulting in crack surfaces perpendicular to the radial direction.

D11.2 Mechanisms of Fuel Cracking and Relocation

A fuel pellet cracks because of the high thermal stresses which cannot be accomodated in the brittle ceramic material. Linear powers of only a few Watts/cm are sufficient to cause stresses in the peripheric zones of the pellet, exceeding the cracking stress and so leading to cracks.

Stress patterns of an uncracked pellet and of those with different crack configurations have been published by Laßmann and Blank [D11-1], based on investigations by G. Mezzi [D11-2], see Fig. D11-1. The calculations were performed with a two-dimensional (r- $\varnothing$ plane), Finite-Element code, giving an impression on the local stresses in the fragments of a cracked pellet. One of the most important things which can be seen from this figure is the fact, that the stress field in a cracked pellet or in the pellet fragments cannot really be modeled by the commonly used axisymmetric fuel pin behaviour codes. Most of these codes assume that still after cracking the pellet will behave like a continuum and that the distribution of the residual stresses is still axisymmetric. But the reality shows that after cracking the continuum of the pellet is severely damaged or even has been split into fragments. The fragments show a thermomechanical behaviour, which is more or less independent of the characteristic of the fuel compound and which cannot be described by the characteristical data of a fuel pellet. One aspect of this behaviour is the radial outward migration of pellet fragments and of the wedge-shaped cracks, thus leading to an increase of the crack volume in the fuel and to a reduction of the fuel-cladding gap with the resulting consequences. Among these the improvement of the heat transfer between fuel and cladding and the earlier onset of the mechanical interaction between fuel and cladding are most important.

The objective of all crack models is to quantify these crack- and relocation phenomena and to describe the resulting consequences.

D11.3 Review on some Crack- and Relocation Models

An overview on some of the most known relocation models is given by Laßmann and Blank [D11-1]. The authors mention 7 different models, among which are still three different models in use within the FRAP-code family [D11-8, 10]. The simplest models, which are reviewed, define a relocation either by a spontaneous jump of the outer pellet radius towards the cladding, immediately after the first startup power [D11-7, 9, 10] or they show a second relocation step at a certain burnup threshold [D11-11, 12]. Some models define relocation functions which are dependent on burnup, power or on the contact pressure [D11-9, 13, 14, 15, 16]. More sophisticated interdependencies are modeled by Walton and Matheson [D11-17] for the FUMAC-code. But they need several empirically derived constants, which are not published in the open literature.

D11.4 Derivation of the SATURN-FS Model

D11.4.1 Objectives and Assumptions

Efforts were made to develop a new model, which should be based as far as possible on the stress pattern in the fuel. Cracking and relocation should be described using the theory of elasticity and the crack volume should be brought in by consideration of the differences in stiffness between the cracked and the uncracked fuel regions as well as by modeling a "crack portion" in the material. So, the overall objectives of the model are:

To describe

- Cracking of the pellet and the resulting mechanical consequences.

- Radial relocation of the fuel, i.e. reduction of the gap between fuel and cladding.

- Crack healing during irradiation and the resulting mechanical consequences.

The assumed boundary conditions are:

For every element - uncracked or cracked - the following expression is calculated:

$$CRAF = 1 + ICRACK \cdot \frac{V_{crack}}{V_{crack,0}} \qquad (D11\text{-}1)$$

$ICRACK$ = number of cracks

V_{crack} = actual crack volume

$V_{crack,0}$ = crack volume just after cracking

It can be seen, that $CRAF = 1$ for the uncracked element and $CRAF > 1$ for the cracked fuel. $CRAF$ will be used for the mechanical consequences of the cracking.

Before cracking, there is a stress pattern in the fuel, showing tensile, circumferential and axial stresses in the outer part of the fuel, and compressive stresses in the center.

D11.4.2 Mechanical Treatment of Cracking

D11.4.2.1 Introduction of a Crack Volume

If a threshold stress is reached within a certain ring element, this element shall crack. The transition from the uncracked to the cracked state is treated as follows:

- the stresses are reduced to zero
- the elastic strains are reduced to zero (like a broken spring)
- the disappearing elastic strains are converted into a crack volume:

$$V_{crack} = V_{ele} \cdot \Sigma \varepsilon_{el} \qquad (D11\text{-}2)$$

So, after cracking, there is a composite material, consisting of matrix material and crack volume.

D11.4.2.2   Changeing the Stiffness of the Cracked Element

The elastic partial flexibilities of the matrix, the crack volume and the composite material may be formally given as follows:

For the matrix:

$$A_{matrix_{el}} = \frac{1}{E} \cdot \begin{bmatrix} 1 & -v & -v \\ -v & 1 & -v \\ -v & -v & 1 \end{bmatrix} \qquad \text{(D11-3)}$$

$$E = \text{Young's modulus}$$
$$v = \text{Poisson's ratio.}$$

The elastic behaviour of the crack portion is characterized by the fact that the Poisson's ratio is zero.

So, it can be formulated:

$$A_{crack_{el}} = y \cdot \begin{bmatrix} 1 & 0 & 0 \\ 0 & 1 & 0 \\ 0 & 0 & 1 \end{bmatrix} \qquad \text{(D11-4)}$$

Hereby 1/y represents an unknown "elastic modulus".
The composite material shall be described as follows:

$$A_{comp_{el}} = \frac{CRAF}{E} \cdot \begin{bmatrix} 1 & x & x \\ x & 1 & x \\ x & x & 1 \end{bmatrix} \qquad \text{(D11-5)}$$

The unknown value x has to be determined.

An additional condition is:

$$A_{comp_{el}} = A_{matrix_{el}} + A_{crack_{el}} \qquad \text{(D11-6)}$$

This formal condition, together with equations (D11-3), (D11-4) and (D11-5) gives again two equations to determine the unknows x and y:

$$\frac{1}{E} + y = \frac{CRAF}{E} \qquad\qquad \frac{-v}{E} = \frac{x \cdot CRAF}{E}$$

and

$$x = \frac{-v}{CRAF} \qquad\qquad y = \frac{1}{E} \cdot (CRAF - 1)$$

This results in the elastic behaviour of the composite.

$$A_{comp_{el}} = \frac{1}{E} \cdot \begin{bmatrix} CRAF & -v & -v \\ -v & CRAF & -v \\ -v & -v & CRAF \end{bmatrix} \qquad\qquad \text{(D11-7)}$$

and for the crack portion:

$$A_{crack_{el}} = \frac{CRAF - 1}{E} \cdot \begin{bmatrix} 1 & 0 & 0 \\ 0 & 1 & 0 \\ 0 & 0 & 1 \end{bmatrix} \qquad\qquad \text{(D11-8)}$$

The mechanical model, described here, allows the description of the fuel's stiffness dependent on the amount of crack volume in the fuel. The stiffness is decreased with an increase of void volume in the fuel. On the other hand, any radial expansion of the pellet is accompanied by a further increase of void volume, which again causes a further decrease of the stiffness in the cracked regions.

So, the radial expansion of the pellet is governed more and more by the thermal expansion of the hot inner portion of the pellet, which is still under - even low - compressive stress. This mechanism causes a larger radial expansion of the pellet than the classical treatment. Additionally, void volume is packed into the fuel, which later on is used to build the central hole and gives a contribution to the pore and crack pattern.

D11.4.3 Cracking Modes

D11.4.3.1 General Overview

An overview over the model describing cracking and relocation is given as a flow sheet in Fig. D11.3. From this figure the different cases can be seen, which may occur. Furthermore, the treatment of these cases - or modes - becomes more obvious.

The modes, mentioned here, take the following cases into consideration:

D11.4.3.2 Cracking from the uncracked State

If cracking occurs from the uncracked state, the model does the following:

$$ICRACK = 1$$

$$V_{crack} = V_{ele} \cdot \sum \varepsilon_{el}$$

$$V_{crack, 0} = V_{crack}$$

$$CRAF = 1 + ICRACK$$

Also, stresses and elastic strains are set to zero.

D11.4.3.3 Cracking from a cracked State

The increase of the crack volume is calculated:

$$\Delta V_{crack} = \frac{CRAF - 1}{CRAF - 2v} \cdot \Delta V_{element} \tag{D11-9}$$

$$V_{crack} = V_{crack, old} \cdot \Delta V_{crack} \tag{D11-10}$$

$$CRAF = 1 + ICRACK \cdot \frac{V_{crack}}{V_{crack, 0}} \tag{D11-11}$$

Whenever the threshold cracking strees is reached in an already cracked element, the calculation proceeds as follows:

$$ICRACK = 2 \cdot ICRACK \tag{D11-12}$$

and stresses and elastic strains are set to zero.

D11.4.3.4 Crack Healing

When the local temperature is higher than a threshold temperature, the fuel ring is treated as healed. The residual crack volume is converted into porosity.

Also, if there is a certain compressive stress in the element, this ring is described as healed.

D11.4.3.5   Cracking of the whole Pellet

The model, as it is described so far, is not capable to describe a totally cracked through pellet. To take into account this case, the following is done:

If more than half of the elements are cracked during ramp up, the total pellet will crack through. When this occurs, an additional crack roughness is introduced, modeling the mismatch of the fuel fragments and causing some more relocation.

Procedure in the computer program

The fuel crack and relocation model is described in the subroutine Riss. The flow sheet in Fig. D11-3 gives an impression of the modeling of fuel cracking, healing and relocation.

References:

[D11-1]   K. Laßmann, H. Blank:
           Nucl. Eng. and Desgn 106 (1988), 291-313

[D11-2]   G.P. Mezzi at al.:
           Nucl. Eng. and Design 73 (1983), 83-93

[D11-3]   E. Duncombe:
           WAPD-TM-794 (1968)

[D11-4]   E. Duncombe, C.M. Friedrich, J.K. Fischer:
           WAPD-TM-961 (1970)

[D11-5]   J.B. Newmann, J.F. Giovengo,L.O. Comden:
           WAPD-TM-1300 (1977)

[D11-6]   M. Ichikawa:
           IAEA Specialist Meeting on Water Reactor Fuel Element Perfor-
           mance Computer Modeling, Blackpool, UK (1980)

[D11-7]   K. Ito et al.:
           Nucl. Eng. and Design 76 (1983), 3-11

[D11-8]   H.-J. Ritzhaupt-Kleissl, M. Heck:
           Nucl. Eng. and Design (1987)

[D11-9]   L.J. Siefken et al.:
           NUREG/CR-0840 (1979)

[D11-10]   L.J. Siefken et al.:
           NUREG/CR-2148 (1981)

[D11-11]   B. Brzoska et al.:
           BMFT-FB K 79-23 (1979)

[D11-12]   B. Steinmetz, K. Fenneker:
           Internal Note, 1982

[D11-13]   R. Eberle, J. Stackmann:
           EHPG-Meeting ond "Fuel Performance Experiements and Analysis",
           Loen, Norway (1983)

[D11-14]   C.R. Kennedy et al.:
           EPRI NP-1106 (1979)

[D11-15]   D.D. Lanning et al.:
           PNL-2434/NRC-1,3 (19878)

[D11-16]   M. Oguma:
           Nucl. Eng. and Design 76 (1983), 35-45

[D11-17]   L.A. Walton, J.E. Matheson:
           Nucl. Techn. 64 (1984), 127-138

[D11-18]   E. Kolstad et al.:
           EHPG-Meeting Sandefjord Norway, HPR 188 (1974),
           EHPG-Meeting Geilo Norway, HPR 190 (1975)

a) entire pellet

b) half pellet

c) quarter pellet

d) crack → entire pellet cracked

AVERAGE STRESS
σ
PHYSICAL EXTENSION

(a) UNCRACKED BEHAVIOUR

AVERAGE STRESS
σ
PHYSICAL EXTENSION

(b) UNIAXIAL TEST

AVERAGE STRESS
σ
PHYSICAL EXTENSION

(c) ACTUAL AVERAGE STRESS

AVERAGE STRESS
σ SLOPE=E
σm
SLOPE=E/M
PHYSICAL EXTENSION

(d) MODEL USED
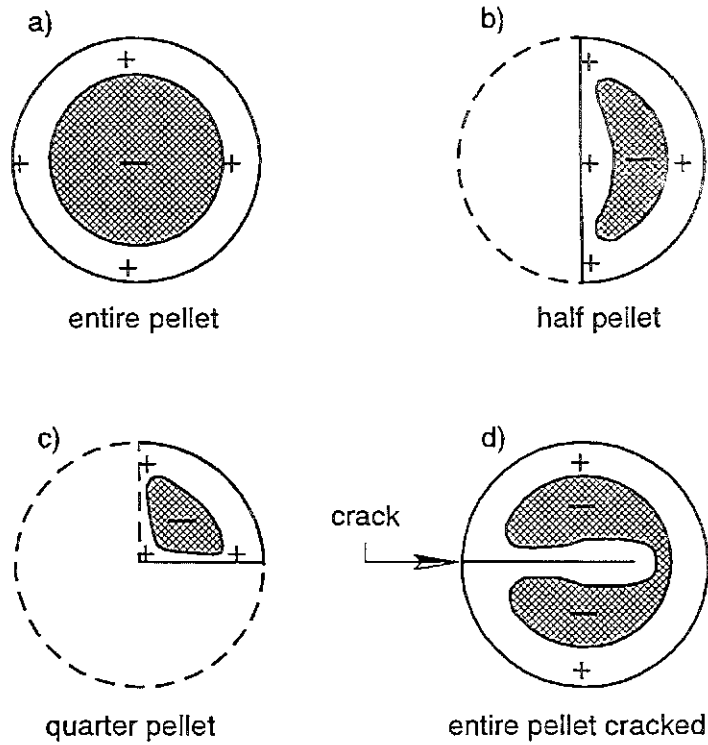
Fig.D11-1: Thermoelastic, hydrostatic stress field in different pellet geometries: the + sign represents tensile, the - sign compressive hydrostatic stress. (Acc. to G. Mezzi, adopted from Laßmann and Blank [D11-1].
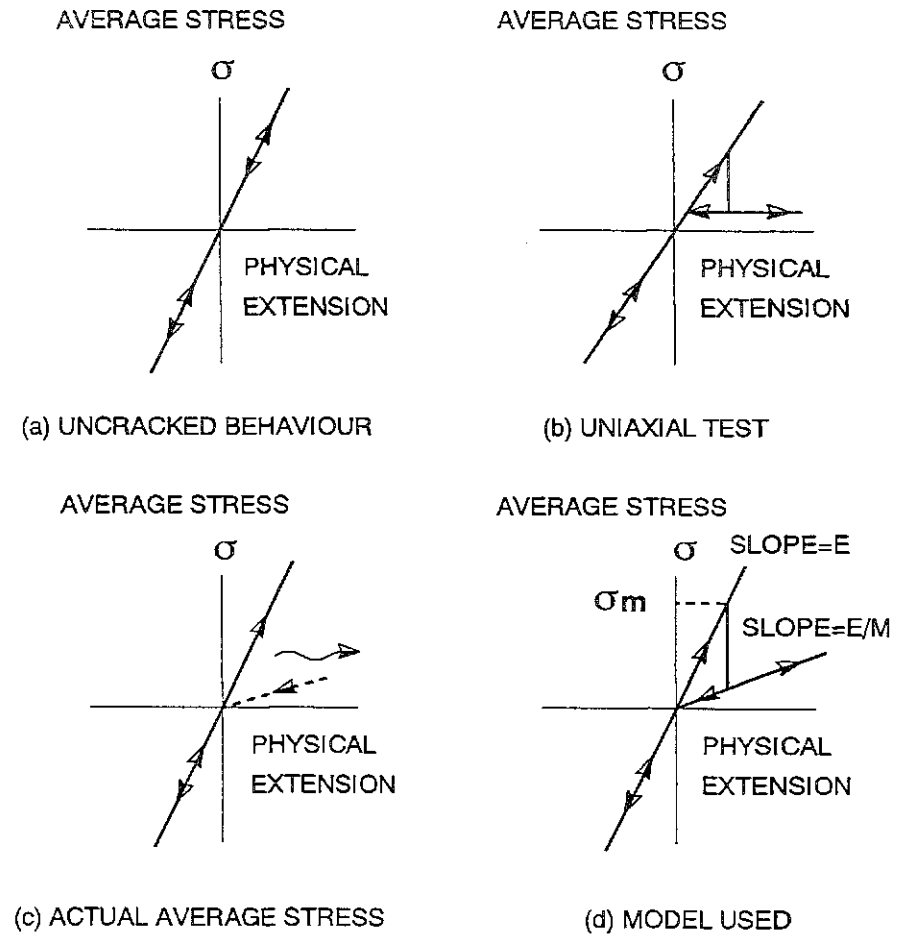
Fig.D11-2: Relation between stress and extension in a fuel pellet during cracking (The CYGRO-approach [D11-3,4,5] for the description of pellet cracking)
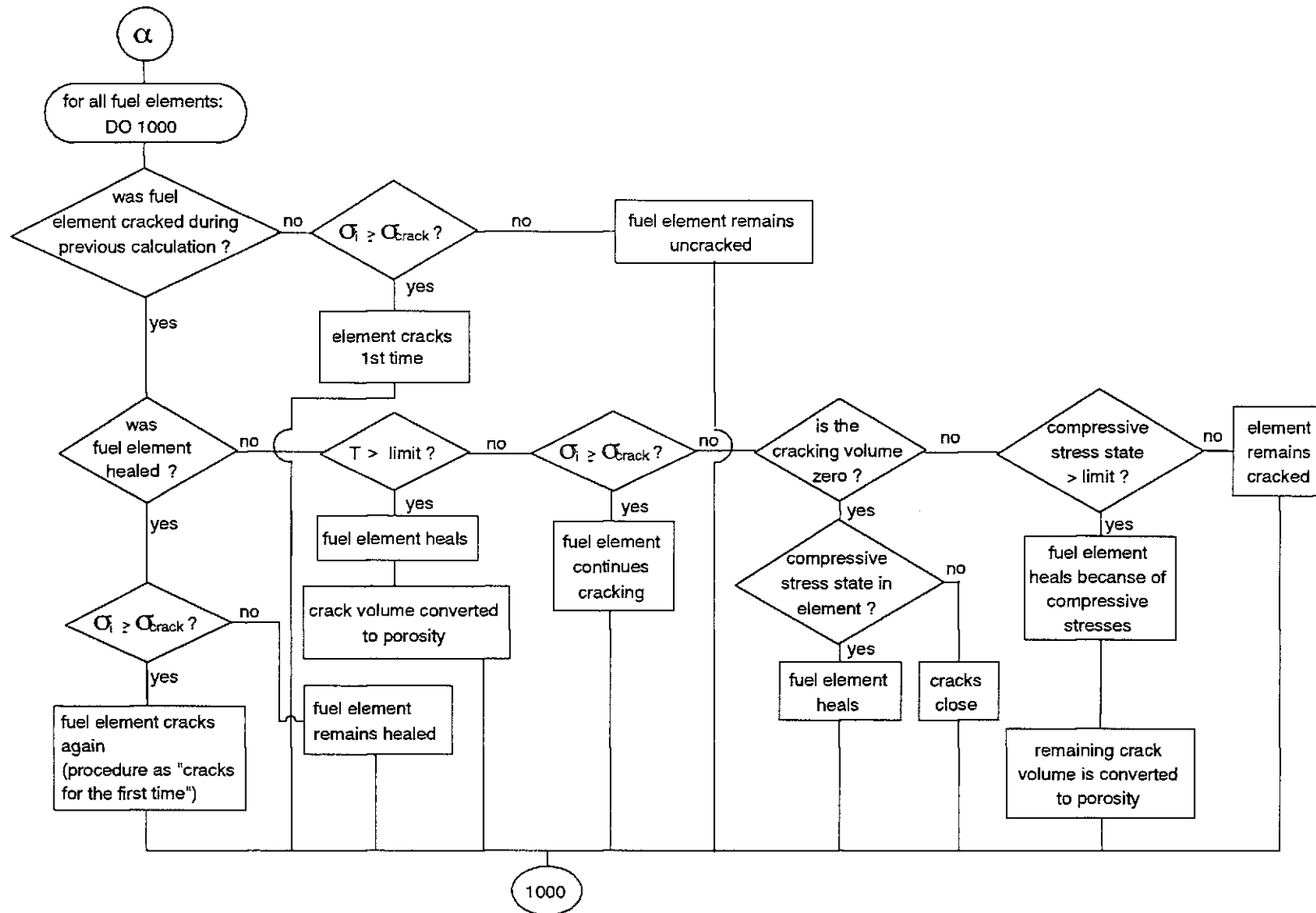
Fig.D11-3: Flow diagram of the RISS-subroutine calculating fuel cracking and healing in the SATURN FS-code

E. Thermodynamics of the Fuel Rod

E1. Heat Transfer in the Gap Between the Fuel and the Cladding

In order to describe the heat transfer in the gap between the fuel and the cladding, the GAPRS heat transfer model developed at IMF III [E1-1] is used. It is based on the familiar model by Ross & Stoute [E1-2] and it has proved valuable in the IMF III computer codes SATURN-II, PSTAT [E1-3] and TRANSIENT [E1-4].

References:

[E1-1]   M. Heck, H. Steiner:
Internal Note, September 1977

[E1-2]   A.M. Ross, R.L. Stoute:
Heat Transfer Coefficient Between UO_2 and Zircaloy-", AECL-1552, 1970

[E1-3]   H. Steiner:
PSTAT: Ein Rechencode für die mechanische Wechselwirkung Brennstoff/Hülle in Schnellbrüter-Brennstäben, KfK 3319, 1982

[E1-4]   H. Steiner:
Der Brennstabcode TRANSIENT zur Beschreibung des Brennstabverhaltens unter instationären Bedingungen
KfK 3603, 1983

E2. Pressure and Composition of the Gas Mixture in the Fuel Rod

The gas pressure directly influences the mechanical loading of the cladding. A change in gas composition effects the thermal conductivity of the gas mixture, which has consequences for the temperature distribution in the fuel rod. The effects of production and release of fission gases such as Krypton and Xenon must therefore be taken into account as part of the model.

The division of the fission gas produced into Krypton and Xenon can be modelled as follows: According to P. Hofmann [E2-1], the Xe/Kr ratios shown in Table E2-1 can be given for the produced fission gas as a function of the type of the fissile material isotope and the neutron energy:

Table E2-1:   Xe/Kr ratios of the fissile material isotopes for different neutron
               energies

| Isotope | Xe/Kr ratios for | | Fission Spectrum | 14 MeV |
	0.025 MeV	1 MeV		
U-235	6.56	6.4	6.11	4.34
U-238	0	7.2	7.28	5.25
Pu-239	16.93	12.68	14.26	12.09
Pu-241	24.32			

The data of Table E2-1 which describe thermal fission of U-235 and fast fission of Pu-239, have been confirmed in experiments to agree well with, for example, the data indicated by H. Zimmermann [E2-2].

In order to be able to determine the Xe/Kr ratio in a real fuel containing fissile material and a mixture of isotopes, the probability of fission of a given isotope must also be taken into account. This is done by weighting with the help of the respective fission cross-sections.

Table E2-2 shows the fission cross-sections of various isotopes, again as a function the neutron energies, as taken from [E2-3].

Table E2-2:   Microscopic fission cross-sections of the fissile material isotopes
               for various neutron energies

| Isotope | Fission Cross-sections (barn) for | | | | |
	0.025 MeV	Epithermal	1 MeV	Fission Spectrum	14 MeV
U-235	582	2.7	1.44	1.29	1.29
U-238	0	0	0.524	0.524	~0.005
Pu-239	741	3.0	1.76	1.76	~4.0
Pu-241	950				

Procedure in the computer program

The gas pressure in the fuel rod is computed in the FORCES and COMPL subroutines. There are two possibilities of modeling the gas pressure in each option: first, for test purposes, the gas pressure can be externally adjusted by the user as a function of time; second, the pressure and the composition of the gas mixture in the fuel rod can be computed by the program. Taking into account changes in pressure, temperature and volume in the fuel rod as well as the release of fission gases. The rate of gas release is computed in the GASREL subroutine whereas the Xe/Kr ratio of the released portion is computed in FISGAS. The composition of the gas mixture in the fuel rod is computed in the PORCOM subroutine. This gas com-

position can now be used by the GAPRS subroutine to calculate the heat transfer in the gap for the next time step.

References:

[E2-1]   P. Hofmann:
         Spaltproduktausbeuten bei der Spaltung von U-235, U-238, Pu-239 und
         Pu-241 mit Neutronen verschiedener Energien, KfK Ext. 6/70-2, 1970

[E2-2]   H. Zimmermann:
         Spaltverhalten in Oxid-Brennelementen für Schnelle Brüter, KfK 2057,
         1957

[E1-3]   J.J. Schmidt:
         Neutron Cross Sections for Fast Reactor Materials, Par I: Evaluation,
         KfK 120, 1966

E3. Restructuring of the Fuel

Modelling the restructuring of the fuel is done in connection with the analysis of the fuel void volume and of the models established to describe fuel cracking and healing ot the cracks, s. Sec. D.11.

E4. Segregation and Redistribution Processes in U, Pu Mixed Oxide

E4.1 Plutonium Redistribution

With the temperature gradients prevailing in mixed oxide fuel pellets, segregation takes place of the two components plutonium and uranium. This is associated with a change in the heat source density distribution in the fuel which, in turn, has an influence on the temperature profile which the fuel rod.

These redistributions can be described by means of two transport mechanisms:

* evaporation and condensation processes associated with the local and temporal change in the fuel void volume;

* thermal diffusion.

These phenomena have been described in detail, e.g. in (E4-1, E4-2, E4-3, E4-4, E4-5, E4-6, E4-7) as well as in a summarizing review in (E4-8).

E.4.1.1 Evaporation and Condensation Mechanism

The material transport taking place via the evaporation and condensation mechanism is associated with the segregation of these components due to the different respective vapor pressures of uranium and plutonium bearing components. The degree of segregation depends on the O/M ratio of the fuel. In fuel of low hypo-stoichiometry, the uranium bearing component evaporates preferably whereas in highly hypo-stoichiometric fuel the plutonium bearing component evaporates preferably. Preferred evaporation of uranium is equivalent to plutoniun enrichment near the central channel, and vice versa.

According to a model proposed by Lackey, Homan and Olsen [E4-3], the Pu/(U + Pu) ratio in a fuel ring at the end of a time step can be described by the following relationship; cf. also (E4-8):

$$c_{pu_1} = \frac{m \cdot c_{pu_0} + \Delta m^+ \cdot a - \Delta m^- \cdot b}{m + \Delta m^+ - \Delta m^-} \qquad \text{(E4-1)}$$

with

c_{pu_0}
c_{pu_1} Pu/U + Pu ratio in the fuel matrix of the ring element being considered, at the beginning and end, resp., of the relevant time step

m mass of heavy metal in the ring at the beginning of the time step

Δm^+ mass of heavy metal added to the ring considered during the time step as a result of pore migration

Δm^- mass of heavy metal leaving the ring considered during the time step as a result of pore migration

a Pu/U + Pu ratio of the matrix added to the ring considered via the vapor phase

b Pu/U + Pu ratio of the fuel leaving the ring considered

The variables a and b are temperature dependent and can be calculated e.g. according to (E4-3). It is assumed that the migrating pore is in equilibrium with the surrounding fuel material.

As the respective masses of the rings are kept constant in the SATURN-FS1 computer code, the mass balance for the Pu portion between neighboring rings at the end of a time step is:

$$c_{pu_1}(i) = c_{pu_0}(i) + \frac{\Delta\rho(i)}{\rho(i)} \cdot (a(i-1) - c_{pu_0}(i)) \tag{E4-2}$$

where

$\Delta\rho$	change of density in the ring considered
ρ	density of the ring being considered at the beginning of the time step
$a(i-1)$	Pu/U + Pu ratio in the vapor phase of the next innermost ring

E4.1.2 Thermal Diffusion

Plutonium re-distribution by means of thermal diffusion is a slow process compared to segregation of the plutonium and uranium bearing components of the fuel by pore migration. This process only exerts a growing influence on plutonium re-distribution at higher burnup.

As in the process of segregation, due to evaporation and condensation by pore migration, the cause of segregation due to thermal diffusion is the temperature gradient in the fuel pellet.

The mass flow of the plutonium bearing component, due to thermal diffusion in the radial temperature gradient, can be described by the following relationship (e.g. (E4-6) and (E4-7), resp.).

$$j_{Pu} = -N \cdot D_{U,Pu}(\frac{dc_{Pu}}{dr} + c_U \cdot c_{Pu} \frac{Q_{U,Pu}}{RT^2} \cdot \frac{dT}{dr}) \tag{E4-3}$$

with

j_{Pu}	(atoms/cm²/h)	Pu mass flow
N	(atoms/cm³)	total number of heavy metal atoms per volumetric element in the fuel
$D_{U,Pu}$	(cm²/s)	effective diffusion coefficient
c_U, c_{Pu}	(-)	U-and Pu-concentrations, resp., in the fuel (with $c_U + c_{Pu} = 1$)
$Q_{U,Pu}$	(J/mole)	effective heat of transport
R	(J/mole K)	universal gas constant
T	(K)	fuel temperature
r	(cm)	fuel radius

An analogous equation applies to the mass flow of the uranium component.

From the relationship describing the mass flow, the respective concentration of a component in a volumetric element can be determined as a function of time using the equation of continuity. The equation of continuity reads as follows;

$$\frac{dN_{Pu}}{dt} + \frac{1}{r}\frac{d}{dr}(r \cdot j_{Pu}) = 0 \qquad \text{(E4-4)}$$

where

$N_{Pu}(r,t)$	(atoms/cm³)	number of the plutonium atoms per unit of volume at location r and time t.

From the equation it follows by integration over the time (with $t > t_0$):

$$N_{Pu}(r,t) = N_{Pu}(r,t_0) - \int_{t_0}^{t} \left(\frac{dj_{Pu}}{dr} + \frac{j_{Pu}}{r}\right)dt. \qquad \text{(E4-5)}$$

In hypo-stoichiometric fuel, thermal diffusion as a single effect would always lead to a slow increase in plutonium concentration extending over a large space near the central channel. However, as the transport always proceeds in parallel with evaporation/condensation, excessive concentrations at the central channel are reduced by diffusion and the plutonium portion is distributed over a wide zone around the central channel.

Procedure in the computer program

U/Pu segregation due to evaporation and condensation is calculated in the PUMIX subroutine, called by the COMPL subroutine at the beginning of each time step. Segregation by evaporation and condensation is assumed to be an instantaneous effect, independant of time, and which is kept constant during the time step.

Also at the beginning of the time step, the COMPL subroutine calls the PUDIFF subroutine which describes U/Pu segregation by solid diffusion. Unlike PUMIX, PUDIFF computes a rate of change in plutonium concentration for each fuel ring.

After completion of the time step, COMPL determines the new plutonium concentration in the individual fuel rings by computing the change in concentration due to plutonium diffusion. This is done by integration of the rate of change over the time interval. Together with the plutonium profiles already computed at the beginning of the time step, this eventually gives the new radial plutonium distribution.

Oxygen redistribution is computed by the MIGOX subroutine. This subroutine, similar to PUMIX, is called by COMPL at the beginning of each new time step. As the O/M redistribution is likewise considered to be an effect independent of time, the radial O/M profile is kept constant during the time step.

References:

[E4-1]   M Bober, C. Sari, G. Schumacher:
         Redistribution of Plutonium and Uranium in Mixed (U,Pu) Oxide Fuel
         Materials in a Thermal Gradient,
         J. Nucl. Mat. 39, 265 (1971)

[E4-2]   D.R. Olander:
         The Kinetics of Actinide Redistribution by Vapor Migration in Mixed
         Oxide Fuels (II), By Pores,
         J. Nucl. Mat. 49, 35 (19713/74)

[E4-3]   W.J. Lackey, F.J. Homan, A.R. Olsen:
         Porosity and Actinide Redistribution during Irradiation of (U,Pu)O$_2$,
         Nucl. Techn . 16 (1972) 120

[E4-4]   R.O. Meyer:
         Analysis of Plutonium Segregation and Central-Void Formation in
         Mixed-Oxide Fuels,
         J. Nucl. Mat. 50, 11 (1974)

[E4-5]   M. Bober, G. Schumacher:
         Transport Phenomena in Mixed Oxide Fuel Pins,
         KfK 1987, Dez. 1973

[E4-4]   M. Bober, G. Schumacher:
         Erhöhung der Zentraltemperatur durch Uran-Plutonium-Ent-
         mischung in Mischoxid-Brennstäben schneller Reaktoren,

         KfK 1904 (1974)

[E4-7]   M. Bober, H. Kleykamp, G. Schumacher:
         Investigation of Radial Plutonium Redistribution in Mixed Oxide Fuels
         Irradiated in a Fast Flux,
         Nucl. Techn. 26 (1975) 172

[E4-8]   H. Elbel:
         Internal Note, Okt. 1979

[E4-9]   S.K. Evans, E.A. Aitken, C.N. Craig:
         Effect of a Temperature Gradient on the Stoichiometry of Urania-
         Plutonia Fuel,
         J. Nucl. Mat. 30 (1969) 57

[E4-10] M. Bober, S. Dorner, G. Schumacher:
         Kinetics of Oxygen Transport from Mixed Oxide Fuel to the Clad,
         Symposium on Fuel and Fuel Element for Fast Reactors, Brussels, July
         1973, IAEA/SM-173/III-52

E5. Depression of the Neutron Flux in the Fuel and Radial Power Distribution

The irradiation with thermal or epithermal neutrons causes a radial depression in the neutron flux within the fuel.

The computation of this radial depression should not be subject of a fuel pin performance code but is better performed by special computer codes such as MERKUR (E5-1).

It will be assumed from now on that the flux depression has alrady been calculated, or as least that the relative neutron flux in the center of the fuel is known.

If the radial neutron flux distribution is known, the values related to the undisturbed flux can be calculated for the element radii and entered as radial power shape factors $p_k(r_i)$ via the input.

However, in order to avoid lengthy computation of the values of p_k for all fuel radii, an option is available in SATURN-FS1 to have the relative radial flux development calculated by the code itself.

The radial profile of the neutron flux can be expressed by the following formula:

$$\Phi(r) = a + b\,r^2 + c\;r^4 \tag{E5-1}$$

With the known fluxes at the inner and outer edges of the fuel, Φ_i and Φ_a, the coefficients a, b and c of equation (E5-1) can be determined by reference to geometric boundary conditions:

$$b = -2\,c \cdot r_i^2 \tag{E5-2}$$

$$c = \frac{\Phi_a - \Phi_i}{(r_a^2 - r_i^2)^2} \tag{E5-3}$$

$$a = \Phi_a - b \cdot r_a^2 - c \cdot r_a^4 \tag{E5-4}$$

Now the corresponding fluxes can be computed for all fuel radii. This calculation is performed both for the thermal and, if desired, the epithermal flux portions.

The distribution of neutron flux calculated here corresponds to the radial power profile at the beginning of the computation.

Whereas the radial flux distribution is not supposed to undergo variations during the computation, the following mechanisms taking place in the fuel give rise to a change in the radial power distribution in the fuel:

- redistribution of the manufacturing porosity,
- redistribution of oxygen,
- U/Pu segregation by solid diffusion and evaporation/condensation effects.

This change in the radial power distribution in the fuel is taken into consideration by the program. Prior to starting each step of computation, the concentration of fissile isotopes present in each fuel ring is calculated. From this the respective radial power shape factors $p_k(i)$ are computed.

Procedure in the computer program:

The determination of the radial flux profile prior to the actual computation is done in the FLUXPRO subroutine. The changes in radial power distribution are determined in the QPROF and PRBDIF subroutines.

References:

[E5-1] L. Steinbock:
Das Brennstabauslegungs- und Überwachunssystem MERKUR, KfK 2163, 1975

F. Time Step Control

F1. Limitation of the Computation Interval

It is possible for the user to specifiy the expenditure of computation and hence the accuracy of the results obtained. This is done by specification of maximum tolerable increments or changes within one computational time step for:

* temperature in the cladding,
* temperature in the fuel,
* equivalent stress,
* equivalent strain.

The determination of the computation time step by limitation of the temperature increments is performed in the DTTEMP subroutine, that of the stress-strain increments in the DTIME subroutine. Another restriction follows from the pore migration model. During a computation time step, pores are not allowed to migrate further than from one ring element into the next.

The determination of the maximum tolerable computation time step due to this limitation is effected in the DTPOR subroutine.

The actual computation time step equates to the minimum of the three computed time steps. Furthermore, the internal time steps are controlled such that the end of a computation interval always matches any "external" time step specified by the user. The OUT subroutine is then called and the results are printed at that predefined point in time.

F2. Completion of the Time Step

After computation of the rates, the actual basic variables are determined. These include stresses, strains and element dimensions as well as temperatures and the new deformation rates, based on the new stresses and strains. Other variables which are to be calculated at the end of the time step include nuclear variables such as burnup and change in the radial power profile or variables concerning the entire fuel rod, such as the composition and the pressure of the fission gas.

Procedure in the computer program:

All the variables listed in this section are either computed in the COMPL subroutine or COMPL calls the corresponding subroutine.
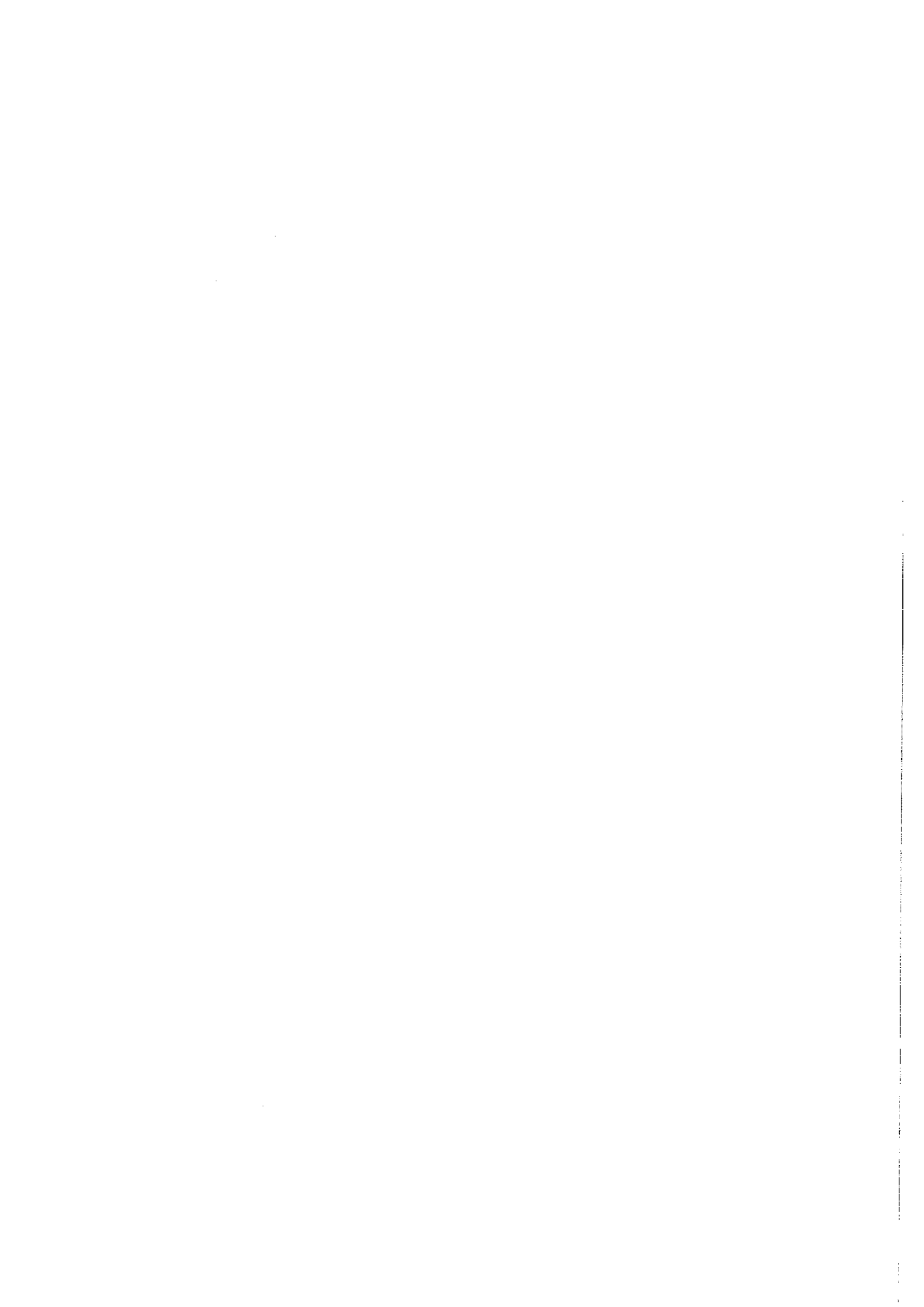
Part 2

Instructions for Use of S A T U R N - F S
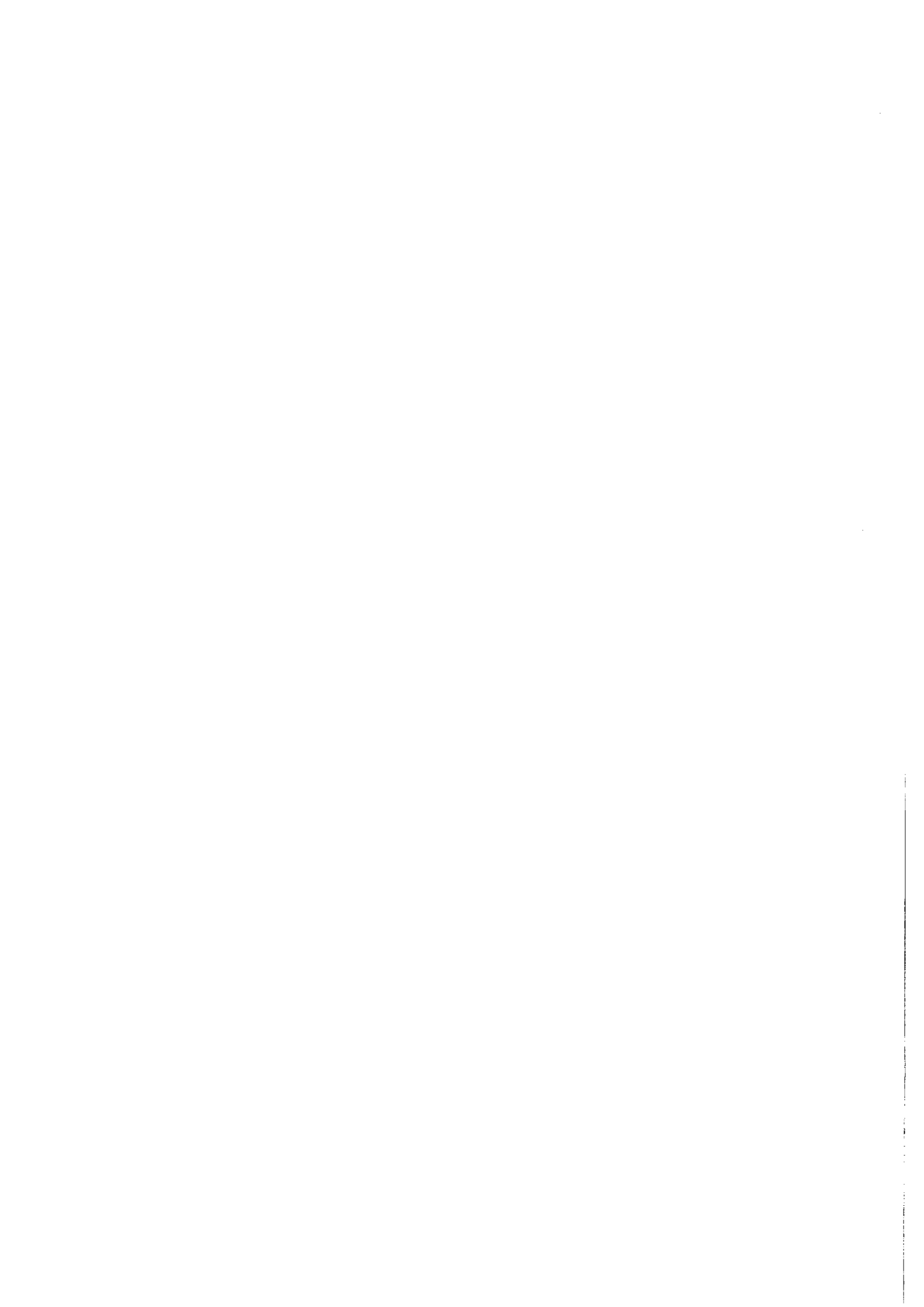
G. Material Laws, Models Used

G1. General Remarks

One of the main objectives in development of SATURN-FS1 was to establish a computer code with the widest possible field of application. This implies easy exchangeability of models or the possibility of conveniently incorporating the user's own models into existing program parts. Such program parts (which must be supplemented by the user) are available to describe, e.g., creep and gas release. In these cases, the user can enter his own model concepts in an edited version into existing tables and use them as options to the supplied models. The program then makes a linear interpolation between the tabular values supplied, either one- or two-dimensionally [G1-1]. This increases above all the flexibility of model concepts whose structures are slightly more complicated.

Simple material laws are always contained in the MATB and MATH material subroutines for the fuel and the cladding, respectively. Exceptions are the thermal conductivities of the fuel, cladding and gap, which are described in the WLAMB, WLAMH and WLGAP subroutines, resp., as well as swelling, computed in SWELLH and SWELLB, secondary fuel creep, computed in FCREEP and cladding creep, computed in CCREEP.

The IMATB and IMATH control variables set in the input are capable of taking into account different materials for the fuel and the cladding. At present, material data for UO_2 and U, Pu- mixed oxide can be called for the fuel and the stainless steel type 1.4970 and Zr-4 for the cladding. Data on other materials can also be incorporated.

G2. Fuel models

G2.1 U,Pu-mixed oxide

- Young's modulus
  c.f. MATPRO 11 TREE-NUREG/CR-0497, 1979

$$E = 2,356 \cdot 10^5 \cdot (1 - 1,3565 \cdot 10^{-4} \cdot (T-20)) \cdot (1 - 2,6 \cdot POR) \cdot (1,5 \cdot O/M - 2)$$
with

POR = relative porosity
O/M = oxygen-to-metal ratio
T = temperature in °C
E = Young's modulus in N/mm²

- **Poisson's ratio**
  c.f. IA-ITB 54.04279, 1982 and Müller-Lyda, Freund:
  unpublished report, 1980
  v = 0,32.

- **Linear thermal expansion coefficient**
  c.f. IA-ITB 54.04279, 1982

$$a_{th} = (6,8 \cdot 10^{-6} + 5,8 \cdot 10^{-9} \cdot T) \cdot (5 - 2 \cdot O/M)$$

with

T = temperature in °C
O/M = oxygen-to-metal ratio
a = linear thermal expansion coefficient in K⁻¹

- **Thermal conductivity**
  H.-J. Ritzhaupt-Kleissl, H. Elbel, M. Heck: J. Nucl. Mat. 153 (1988)
  Freund, Ernst: Unpublished report 1983, porosity correction factor acc. to
  MATPRO-11, TREE NUREG/CR-0497, 1979

$$\lambda_0 = \frac{1}{5,443 + 0,02309 \cdot T + 340 \cdot (2 - O/M)} - 7,585 \cdot 10^{-10} \cdot T^2 + 3,542 \cdot 10^{-16} \cdot T^4$$

stoichiometry correction factor for temperatures > 2273 K:

$$f_{O/M} = 0,2383 + \frac{1}{1,313 + 7,705 \cdot (2 - O/M)}$$

porosity correction factor:

$$f_{por} = 1.3048 \cdot ((1 - POR)/(1 + \beta \cdot POR))$$

whereby:

O/M ≥ 1,96: $\beta = 0,5$
1,96 < O/M < 2 : $\beta = 0,5 + 6,5 \cdot (O/M - 1,96)/0,04$
O/M ≥ 2: $\beta = 7,0$

the thermal conductivity now reads:
- for 293 K $\leq T \leq 2273$ K: $\quad \lambda = \lambda_0 \cdot f_{por}$
- for T > 2273 K: $\quad \lambda = \lambda_0 \cdot f_{por} \cdot f_{O/M}$

with

$\quad$ O/M $\quad$ = oxygen-to-metal ratio; for T > 2273 K: O/M = 2.

$\quad$ POR $\quad$ = relative porosity

$\quad$ T $\quad$ = temperature in K

$\quad$ λ $\quad$ = thermal conductivity in W/(cm·K)

- **Fuel swelling**

1st possibility:

c.f. B. Steinmetz, K. Fenneker, IA-ITB 54.04279, 1981

$$T < 1300: \qquad \frac{\delta V}{V_0} = 1{,}7 \cdot BU$$

$$1300 < T < 1650: \qquad \frac{\delta V}{V_0} = (1{,}7 - (T - 1300)/350) \cdot BU$$

$$1650 < T: \qquad \frac{\delta V}{V_0} = 0{,}7 \cdot BU$$

with

$\quad$ $\delta V/V_0$ $\quad$ = volume increase by swelling in %

$\quad$ BU $\quad$ = burnup in at %

$\quad$ T $\quad$ = temperature in °C.

In SATURN-FS, the above formulation is transferred from volume increase $(\delta V/V)$ to consideration of swelling rates $(\dot{V})$.

2nd possibility:

c.f. MATPRO-11, TREE NUREG/CR-0497, 1979:

$$\dot{V}_B = 9{,}0 \cdot 10^{-20} \, \phi$$

with

$\quad$ ϕ $\quad$ = fission rate in fiss / (cm³ · s)

$\quad$ $\dot{V}_B$ $\quad$ = swelling rate in h⁻¹

-    <u>Non elastic deformation</u>

1st possibility: see chapter D 5.1

2nd possibility:

The total nonelastic deformation can be chosen as tabulated values (Subroutine KRBMAT). Explanation of the tabulated values c.f. Ritzhaupt-Kleissl, Ernst: KfK 3145, 1981 (application not recommended, for special purpose only).

-    <u>Pore migration</u>

c.f. H. Hofmann, KfK 1863 and H. Elbel: internal note, 1979.

There are two mechanism of pore migration taken into account: surface diffusion and evaporation/condensation.

The migration velocity due to surface diffusion is:

$$v_0 = \frac{C_1}{r} \cdot \frac{1}{T^2} \cdot e^{-\frac{60500}{T}} \cdot \frac{dT}{dr}$$

with

$$C_1 \quad = \ 1{,}127 \cdot 10^7 \, mm^3 \cdot K/h$$

r = radius of the pore in mm

T = temperature in K

dT/dr = radial temperature gradient in K/mm

v_0 = pore migration velocity in mm/h

pore migration due to evaporation and condensation:

$$v_{VK} = \frac{C_2}{p_g + p_a} \cdot \frac{1}{T^{3/2}} \cdot p_0 \cdot e^{-\frac{H}{RT}} \cdot \frac{dT}{dr}$$

with

$$C_2 \quad = \ 1{,}211 \cdot 10^6 \, mm^2 \cdot K^{1/2}/h$$

p_g = gas pressure in the pore in MPa

p_a = surface tension of the pore in MPa

T = temperature in K

dT/dr = radial temperature gradient in K/mm

v_{vk} = pore migration velocity in mm/h

$p_0 \cdot e^{-H/RT}$ (MPa) is acc. to H. Elbel: unpublished note, 1979 read to:

$$\ell n(p_0 \cdot e^{-\frac{H}{RT}}) = (-212{,}275 + 65{,}842 \cdot O/M + 8{,}9453 \cdot 10^{-2} T - 2{,}55399 \cdot 10^{-2}$$

$$\cdot O/M \cdot T + 2{,}9560 \cdot (O/M)^2 - 5{,}6541 \cdot 10^{-6} T^2)$$

with

O/M = oxygen-to-metal ratio

the total pore migration velocity yields:

$$v_p(mm/h) = v_0 + v_{VK}$$

- **Fission gas release**

1 st posibility:

Fission gas release model acc. to IA-ITB 54.04279, 1982

2 nd possibility:

As for the discription of non-elastic deformation, tabulated values here also can be chosen (not recommended, for special purpose only).

- **Fuel cracking and relocation**

c.f. 7th International Seminar on the Mathematical Mechanical Modeling of Reactor Fuel Elements, La Jolla, USA, Aug. 21-22, 1989

H.-J. Ritzhaupt-Kleissl, M. Heck in K. Lassmann (Ed.): EUR 13660, 1991

G2.2 Uranium-oxide

- **Young's modulus**

c.f. MATPRO 11 TREE-NUREG/CR-0497, 1979.

$$E = 2{,}2594 \cdot 10^5 \cdot (1 - 1{,}13 \cdot 10^{-4} \cdot (T - 20)) \cdot (1 - 2{,}752 \cdot POR)$$

with

T = temperature in °C

POR = relative porosity

E = Young's modulus in N/mm²

- **Poisson's ratio**

c.f. EPRI NP 369, 1977:

if T ≤ 1700 °C: v = 0,32 - 1,791 · 10-5 · (T-25)

if T > 1700 °C: v = 0,29

with

T   = temperature in °C

- **Linear thermal expansion coefficient**

c.f. MATPRO-11, TREE NUREG/CR-0497, 1979:

$$\alpha_{th} = 7,107 \cdot 10^{-6} + 5,162 \cdot 10^{-9} \cdot T + 3,420 \cdot 10^{-13} \cdot T^2$$

with

T   = temperature in °C

α   = linear expansion coefficient in K^{-1}

- **Thermal conductivity**

c.f. Müller-Lyda, D. Freund: unpublished report 1980,

D. Freund, W. Ernst: unpublished report 1983,

porosity correction factor acc. to MATPRO-11, TREE NUREC/CR-0497, 1979

$$\lambda_0 = \frac{1}{5,443 + 0,02309 \cdot T} - 7,585 \cdot 10^{-10} \cdot T^2 + 3,542 \cdot 10^{-16} \cdot T^4$$

porosity correction factor:

$$f_{por} = \frac{1 - \beta \cdot POR}{1 - 0,05 \cdot \beta} ; \qquad \beta = 2,422 - 0,58 \cdot 10^{-3} \cdot T$$

and so the thermal conductivity reads:

$$\lambda = \lambda_0 \cdot f_{por}$$

with

T   = temperature in K

POR = relative porosity

λ   = thermal conductivity in W/(cm · K)

- **Fuel swelling**

c.f. MATPRO-11, TREE NUREG/CR-0497, 1979

$$\dot{V}_B = 9,0 \cdot 10^{-20} \cdot \Phi$$

with

Φ   = fission rate in fiss/(cm^3 · s)

$\dot{V}_B$ = matrix swelling rate in h^{-1}

- Non-elastic deformation

    1st possibility: see chapter D 5.1

    2nd possibility: see U,Pu-mixed oxide

- Pore migration

    see U,Pu-mixed oxide

- Fission gas release

    see U,Pu-mixed oxide

- Fuel cracking and relocation

    see U,Pu-mixed oxide

G3. Models describing the cladding tube material
G3.1 Stainless steel no. 1.4970

- Young's modulus

    c.f. IA-ITB 73.30, 1973:

$$E = 2,059 \cdot 10^5 - 80,8 \cdot T$$

with

    T   = temperature in °C

    E   = Young's modulus in N/mm²

- Poisson's ratio

    c.f. Nikolopoulus, Schulz, Journ.Nucl.Mat. 82, 1979:

$$v = 0,33$$

- Linear thermal expansion coefficient

    c.f. Nikolopoulus, Schulz, Journ.Nucl.Mat. 82, 1979:

$$\alpha_{th} = 1,133 \cdot 10^{-5} + 1,547 \cdot 10^{-8} \cdot T$$

with

    T   = Temperature in °C

    α   = thermal expansion coefficient in K⁻¹

- <u>Thermal conductivity</u>

c.f. IA-ITB 73.30, 1973:

$$\lambda = 0{,}1391 + 0{,}1186 \cdot 10^{-3} \cdot T$$

with

T = temperature in °C

λ = thermal conductivity in W / (cm·K)

- <u>Swelling</u>

Swelling formula for 1.4970 cw and cw, sr

according to IA-TN-543.550.3, 1980 and IA-MDB-C2, Rev 3, 1984

$$\frac{\delta V}{V_0} = \begin{cases} 0 & \text{for } DPA < D_0 \\ 0{,}15 \cdot (DPA - D_0) & \text{for } DPA \geq D_0 \end{cases}$$

with

D_0 = 70 - 0,5 · (Max(T, 480) - Max (T, 400))

and

DPA = material damage in dpa

T = cladding temperature in °C

$\delta V/V_0$ = volumetric swelling in %.

In SATURN-FS, the above formulation is transferred from volume increase ($\delta V/V$) to consideration of swelling rates ($\dot{V}$).

- <u>Non-elastic deformation</u>

1st possibility:

c.f. H.-J. Ritzhaupt-Kleissl, W. Ernst: KfK-Bericht No. 3145, 1981

H.-J. Ritzhaupt-Kleissl, M. Heck: J.Nucl.Eng. & Design 101 (1987)

M. Mayuzumi, T. Onchi: J.Nucl.Mat.171, 1990, S. 381-388

2nd possibility:

Creep table acc. fuel creep (not recommended, for special purpose only)

G3.2 Zry-4

- <u>Young's modulus</u>

$$E = 9{,}5769 \cdot 10^4 - 64{,}07086 \cdot T$$

with

T = temperature in °C

E = E-modulus in N/mm²

- <u>Poisson's ratio</u>

$$v \quad = 0,29648 - 1,217 \cdot 10^{-4} \cdot T$$

with

T = temperature in °C

- ## Linear thermal expansion coefficient

$$a_{th} = 5,699 \cdot 10^{-6} + 1,513 \cdot 10^{-9} \cdot T$$

with

T = temperature in °C

α = linear thermal expansion coefficient in K-1

- ## Thermal conductivity
c.f. MATPRO-11, TREE NUREG/CR 0497, 1979

$$\lambda = 7,51 \cdot 10^{-2} + 2,09 \cdot 10^{-4} \cdot T - 1,45 \cdot 10^{-7} \cdot T^2 + 7,67 \cdot 10^{-11} \cdot T^3$$

with

T = temperature in K

λ = thermal conductivity in W / (cm·K)

- ## Swelling
c.f. EPRI-NP 369, 1977

$$\dot{V}_{||} = 2,52 \cdot (\Phi t / 10^{21})^{-0,3} \cdot (\Phi / 10^{21})$$

with

Φt = fast neutron fluence in n/cm2; (E > 0.1 MeV)

Φ = fast neutron flux in n/(cm2 · sec); (E > 0.1 MeV)

$\dot{V}_{||}$ = Zircaloy axial elongation rate due to growth in h-1

- ## Non-elastic deformation
see chapter D 5.1

H. Explanations on the Structure of the Computer Code

H1. Structure of SATURN-FS 1

The FORTRAN-77 code includes about 70 subroutines and functions at its present state of development. The Main-program (as well as the soubroutine TNULL for time $= T_0$) are just control programs, 11 subroutines serve for input/output, data-definition and CPU-time control (the latter of which is not represented in the flow diagram).

The subroutines describing the fuel pin behaviour shall be differentiated with regard to their task using the following criteria:

(a)   Computing phenomena which are recorded either exclusively for one material (e.g. porosity of the fuel) or for which completely different models are used for the fuel and the cladding (cf. MATB-MATH subroutine, FCREEP-CCREEP, etc.).

These subroutines never include the IMAT parameter in their list of arguments so that they can be immediately distinguished from the subroutines described under (b).

(b)   Evaluation of the material behavior under the "mechanics" descriptor which is determined here by use of the Finite Element Method (same concept for cladding and fuel).

These subroutines all have an IMAT in their list of arguments (not to be changed by mistake with IMATH and IMATB). This IMAT is set in the calling routine, where 1 means fuel and 2 means cladding; extensions for arbitrary other materials are possible without any problem.

Some explanations on their structure should be added at this point:

Firstly, the global variables entered for the actual material are transferred into the available local memory. The actual computation is made in this memory space, and the variables are once again returned into the global memory. Here the results are stored.

The following two figures briefly illustrate the computing sequence.

Fig. III.1: Flow Diagram for SATURN-FS

INPUT and conversion of the input data for further use in the program

calculation of a steady state elastic solution as starting condition
t=TIMEDT=TIME(1)

start of external time step loop

TIMEDT = TIME(I+1)

start of internal time step loop

calculation of the time derivatives of temperture,pressure
and power changes

time step control acc.to max.tolerable changes in stress,nonelastic strain,
temperature and pore migration velocity (t=t+DT)

fuel cracking and relocation

solution of the thermal problem
temperature profile of fuel and cladding,heat transfer in the gap

solution of the mechanical problem for fuel and cladding

elastic and plastic/creep behaviour,swelling and densification,pore
migration and fission gas release

finite element analysis

stiffness of and forces on the whole fuel pin,stresses and displacements
of each element

completion of the time step

calculation of stresses,strains,dimensions,forces,burnup,gas pressure,
temperature,O/Me- and Pu-profile,porosity distribution,power profile,
theoretical density,diffusion velocity and of a new temperature profile

end of external time interval reached

OUTPUT

last time step

end of SATURN-FS

Fig. H1.2: Flow Chart of SATURN-FS

H2. Tasks of the Subroutines used

ANE   calculates for each element the matrix A_{nc} of the non-elastic flexibilities

ASSEM   describes the assembly of the elements and the global stiffness of cladding or fuel

ATH   calculation of the flexibility of thermal strain A_{th} for each element of fuel and cladding

CCREEP   calculates cladding creep

CMAT   determination of the matrices C_{KMI}, CE, CB and CH
with ENTRY   calculates the CEE matrices for large deformation
CMAT1   theory for each fuel and cladding element

COMPL   is called at the end of the time step, calculates the instantaneous variables such as stresses, strains, temperatures, creep rates after completion of each time step. Calls the subroutines for calculation of pellet cracking, oxygen/metal and U/Pu re-distribution, for the new determination of the radial power distribution and the new calculation of the temperature profile

CONTAC   calculates the radial and axial contact forces (friction forces) between the fuel and the cladding

CONTR   verifies the sequence of the input data blocks

DIFTAB   determination of the functional values related to given experimental data and calculation of the partial differentials of the previously defined function with respect to burnup (fuel) and neutron dose (cladding), resp. (cf. TAB)

DTIME   controls the tolerable time step due to previously defined maximum tolerable stress and strain increments - DEMAX, DSMAX, DESHM

DTPOR   controls the tolerable time step by the assumption made in the pore migration model (s. PORMIG) that within the time step the void volume is allowed to migrate only from one element into the next

DTTEMP controls the tolerable time step due to previously defined maximum tolerable temperature increments in the fuel and in the cladding - DTMAXB and DTMAXH - within one time step

ELAS builds up the flexibility matrix A_{cl} of elastic deformation for each element

EXPO function, calculates the gas extrapolation lengths for pellet/cladding heat transfer

FCREEP describes fuel creep

FISGAS calculation of fission gas production

FLUXPR radial neutron flux distribution

FORCES describes the total loads on the fuel and cladding, due to external forces (coolant pressure, gas pressure in the gap, contact pressure) and the free displacements of fuel and cladding and of the fuel/cladding assembly, resp. in case of adhesive friction. FORCES calls CONTAC

FQV calculation of the local heat transfer for mixed oxide

FSY description of the yield stress

GAPRS describes the heat transfer in the gap between the fuel and the cladding

GASREL calculates the local fission gas balance for each fuel element as the balance between the generated and released gas moles

GEOFAK calculates geometric factors for determination of the radial temperature and power distributions in the fuel. It is called by RADIAL

GSBMAT occupancy of the gas release table

INIT
INITO initialization routines
INIT1

INOUT printout of the input

INPUT controls data input

KRBMAT

KRHMAT
occupancy of the creep table for fuel and cladding

LOADCO   the residual load correction in the elements

MATB   material laws for fuel: Young's modulus,Poisson´s ratio and thermal expansion coefficient

MATH   material laws for cladding: Young's modulus, Poisson´s ratio and thermal expansion coefficient

MEYER   function for determination of the Meyer hardness of the cladding

MIGOX   modeling of the oxygen re-distribution in the fuel

NLI   function; describes the number of the pores per pore category as a function of temperature and burnup

OUT   output of the calculated values

PLAST   calculation of the element flexibilities for non-elastic deformation: $A1_{ne}$ and $A2_{ne}$

PORCOM integration of pore migration and fuel swelling over the time and determination of the gas released at the end of the time step; calculation of the inner pressure of the fission gas bubbles and the radius of each pore category

PORMEC describes gas bubble swelling and pore shinkage as a function of the external pressure and hydrostatic pressure in the pores. Calculation of the partial element flexibilities $A1_{irr}$ and $A2_{irr}$ attributable to swelling and pore effects

PORMIG procedure for calculation of pore migration in the fuel.

PRBDIF describes the influence of pore migration and plutonium diffusion on the radial power profile

PUDIFF U-Pu segregation of mixed oxide by diffusion

PUMIX   calculation of U-Pu segregation of mixed oxide by evaporation and condensation

QPROF   describes the change of the radial power profile, caused by U-Pu segregation

RADIAL
with
ENTRY
RADDT   calculation of the radial power distribution in the fuel

RATE   calculation of the rates of power, coolant temperature, and pressure

RISS   model for description of fuel pellet cracking, fuel relocation and crack healing

SHAPE   setup of the matrix of the shape functions for the elements

STDIS   calculates the total displacements of the fuel and cladding due to external forces, the displacements and strains of the individual elements and from them the stresses occurring in the elements

STIME   calculates the stiffness matrices for the individual elements

SWELLB   describes the matrix swelling rate of the fuel as a function of the burnup, of the hydrostatic pressure in the element, the temperature and of the fission rate

SWELLH   describes cladding swelling as a function of the neutron dose, of the neutron flux and of the temperature

TAB   determination of the parameters for calculation of the non-elastic, time-dependent material behavior from a user-defined table by two-dimensional linear interpolation (cf. DIFTAB)

TEMPER   temperature calculation for fuel and cladding, both on the element boundaries and in the element center

THEDI   determination of the theoretical density of fuel material

TNULL   calculation of a steady-state elastic solution for the first time step $(t = 0)$. This subroutine controls a special computation path of the MAIN program

UMRECH   calculates the relationships existing between power, fission rates, neutron flux and burnup

WANDER   calculates the pore migration rate

WGASI   function for determination of the thermal conductivity of the individual gas constituents

WLAMB   function; calculates the thermal conductivity of the fuel

WLAMH   function; calculates the thermal conductivity of the cladding

WLGAP   function; calculates the thermal conductivity of the gas mixture in the gap.

Besides using this "internal" subroutins, SATURN-FS uses some service subroutines with respect to date, time and CPU-time:

DATIM   date and time information

CPUTIME already used CPU-time since beginning of computation

TIMEL   still remaining CPU-time for this jobstep, independent on the time required for the job and the already used time in previously steps.

Caution:

  DATIM and CPUTIME conform to Industrial Real Time Fortran (IRTF) standards, TIMEL does not.

H3. COMMON Blocks

To make the program easier to handle, transmission of REALs as arguments was largely avoided (apart from some indispensable exceptions). Nevertheless to provide an exact marking of the interfaces to other subroutines with COMMON-Blocks, the input and output variables are always listed in the subroutines' heading descriptor, where the names of the program units in which the incoming values have been computed, can be found. All routines called in the subroutine are indicated here too.

A listing of all in COMMON-Blocks gathered variables and their meaning is given as Annex 1.

I. Instructions for Program Operation

General Remarks: The reference version of the SATURN-FS-code is at present operable on an IBM 3090, operating system MVS/SP 4.1, and tested with the IBM VS FORTRAN-Compiler (Rel. 5). At the present stage of development the average CPU-time is 0.02 - 0.07 sec (independent on the number of fuel-and cladding elements) required by the program per internal time increment and axial slice.

II. Program Input

The quantity of all input variables has been divided into blocks (c.f. column "DB No" in the input table) each consisting of logically connected data.

The sequence of data input is handeled according to the following scheme

        (1) control parameters,

        (2) limits, material behavior,

        (3) fuel data,

        (4) cladding data,

        (5) operating conditions.

For a standard routine all data needed are specified in a BLOCK DATA subroutine (cf. column "BD" in the following table). This means that only those blocks containing any variables different from those in the BLOCK DATA must be read in. So the number of data written into the input file by the user is only a part of the total amount of all input variables actually used by the program. The data blocks need not be read in according to a special order, only within a data block a predetermined sequence is requested.
For a detailed instruction see the following table.

Format Specification:

The input of SATURN-FS 1 is designed list directed (* - format) with the exception of the first card (TEXT (CH * 72) is read in by A-format).
Caution: the input file must not be a numbered dataset (columns 72-80).

Unit-identifier:
Instead of an external unit reference number the * - identifier is used to select the default value which was estabished at the time of FORTRAN-system generation. But it´s also possible to exchange it for an explicit unit reference number (represented by the parameter IW in the subroutine INPUT).

for special purpose only

DB No.	Line No.	FORTRAN-Name	Standard (recom.) Value	Unit	Explanation
	1	Text		--	optional text consisting of max. 72 characters (will be printed as headline of the input data)
					Caution: The line, mentioned above, is also necessary for the standard case. If no further data block shall be read in, NRDATB must be set to zero (NRDATB = 0). This is also valid for the standard case.
1	1	NRDATB			number of the actual DB ('1' for this case)
	2	MCEEB	0	-	{= 1: matrix CEE is used for calculation of the fuel elements' stiffness {= 0: CEE is neglected
		MCRPB	2		{= 1: *fuel creep and plasticity are treated according to the creep table (KRBMAT) now only valid for IMATB = 2 (UO$_2$) {= 2: fuel creep and plasticity according to FCREEP; now valid for IMATB = 1 ((U,Pu)O$_2$) and IMATB = 2 (UO$_2$)
		ISWELB	2		(U,Pu)O$_2$: {= 2: fuel swelling acc. to IA-ITB 54.04279, 1981 {= 3: fuel swelling acc. to MATPRO-11, 1979 UO$_2$: = 3: fuel swelling acc. to MATPRO 11, 1979
		IGASB	2	-	{= 1: *fission gas release acc. to table (GSBMAT); only for IMATB = 2 (UO$_2$) {= 2: Interatom fission gas release model
	3	MCEEH	1		{= 1: matrix CEE is used for the calculation of the cladding elements stiffness {= 0: CEE is neglected
		MDRI	0		{= 1: internal pin pressure is an input value at every external time step (DRI(1:IANZZP)) {= 0: internal pin pressure is calculated by the code, only input of a start value is necessary (DRI (1))
		MCRPH	2		{= 1: *cladding creep and plasticity are treated acc. to the creep table (KRHMAT) {= 2: cladding creep according to built in models (CCREEP)
		ISWELH	2	-	= 2: { IMATH = 1 (ZRY 4): Swelling acc. to EPRI-N369, 1977 IMATH = 2 (SS 1.4970): Swelling acc. to IA-MDB C2, Rev3, 1984

	4	IPTTRA	1	-	{=0: HGAP is a constant value, given by input (HGFIX) {=1: gas bonding in the fuel-cladding gap {=2: sodium bonding (= 1+2: HGAP is calculated internally)
		IPTGAP	0	-	{=0: fuel column is concentric within cladding tube {=1: fuel column is not concentric within cladding tube
2	1	NRDATB	-	-	no. of actual DB (here '2')
	2	NRB	21	-	no. of fuel radii (2≤NRB≤IRB)
		IMATB	1	-	{=1: mixed oxide fuel {=2: UO₂-fuel
	3	ZLB(1)	12	cm	length of the axial fuel column node, resp. of the fuel elements
		RAUBR	3.0E-04	cm	fuel surface roughness
		OMV0	1.93	-	oxygen to metal ratio in the fuel (start-value)
		FKORN	1.0E-03	cm	grain diameter
	4	CPU0	0.28		Pu-concentration (Pu/(U + Pu)) in the fuel (start-value)
		U35	0.73	-	
		PU38	0.01	-	
		PU39	0.67	-	Isotope distribution in the fuel (start-value)
		PU40	0.26		(U₃₅/(U₃₅ + U₃₈) bzw. Puₓ/Pu total)
		PU41	0.05	-	
		PU42	0.01	-	
	5	POR0	0.05		fuel porosity (start-value, c.f. VLLKGO in DB No. 6)
		PORMAX	0.15		max. tolerable porosity in a fuel ring
	6	RABR	0.3235	cm	fuel outer radius (≐RB(NRB))
		RIBR	0.0	cm	fuel inner radius (≐RB(1))
3	1	NRDATB		-	no. of the actual DB (here: '3')
	2	EFISS	203.0	MeV/fiss	fission energy
		SIGFAK	0.0218		factor for converting neutronflux to fission rate
		PHIDT0	0.	fiss/cm³	time-integrated fission rate (≐ burnup)
	3	TMAX	2800.	°C	max. tolerable fuel centerline temperature
		DELTB	20.	°C	max. tolerable temperature mismatch within two succeeding iteration steps during the calculation of the fuel temperature profile
		DTMAXB	50.	°C	max. tolerable change of a fuel element's temperature from one internal time step to the next
	4	TZERO	20.	°C	reference temperature (start-value)
		DEMAX	5.0E-04		max. tolerable change of the non-elastic strain during an internal time step
		DESHM	0.5		max. tolerable change of strain hardening strain related to the non-elastic strain change (DESHM ≤ 0.5 * DEMAX)

		DSMAX	500.	N/cm	max. tolerable change of equivalent stress during an internal time step
	5	GAMMA	3.0E-03	N/cm	surface tension of the pores
		RGRZ	5.0E-05	cm	minimum radius for migrating pores
		RSC	10.	-	factor describing the pore migration velocity
		RSP	1.	-	factor describing the plastic stress limit in the pore region
		BREL	1.	-	factor for gas release modelling
4	1	NRDATB	-	-	no. of the actual DB
	2 +	SIGVB (1,1:NEB)	20*0.	N/cm²	radial stress in the fuel element
	3 +	SIGVB (2,1:NEB)	20*0.	N/cm²	tangential stress in the fuel element
	4 +	SIGVB (3,1:NEB)	20*0.	N/cm²	axial stress in the fuel element
	5	FCONR	0.	N	radial contact force between fuel and cladding
		FCONZ	0.	N	axial contact force between fuel and cladding
	6 +	EVB (1:NEB)	20* 0.1E-06		non elastic equivalent strain in the fuel element
	7 +	ESHB (1:NEB)	20* 0.1E-06		strain hardening strain in the fuel element
	8	SIGMCR	5000.	N/cm²	cracking stress for the fuel
		CRAFAK	0.6	-	E-modulus in the fuel element is divided by this factor in the cracked state
		FMUE	3.0E-03	-	friction coefficient for friction between fuel and cladding
5	1	NRDATB	-	-	no. of actual DB
	2	RMAB PMAB	1. 1.	-	{factors for modelling the mechanical anisotropy in the fuel
	3	RALFAB (1:3)	1., 1., 1.	-	thermal anisotropy-factors for the fuel
	4	RIRRB (1:3)	0.33,0.33, 0.33		factors for modelling an irradiation induced fuel anisotropy
6	1	NRDATB	-		no. of actual DB
	2	NP	2	-	no. of void volume classes
	3	NPROD (1:NP)	1,1	-	{= 0: void volume class represents fabrication porosity {= 1: void volume class represents gas bubbles
	4	MNLKG (1:NP)	1, -1		{= -1: no. of voids of the i'th class of void volume will decrease {= 0: no. of voids of the i'th class of void volume is constant {= 1: no. of voids of the i'th class of void volume will increase

	5	XNLKG0 (1:NP)	1.6E06, 1.0E23	cm^{-3}	no. of voids of the i'th class of void volume (start-value)
	6	TGRZKG (1:NP)	1200., 1200.	°C	temperature limit for each class of voids. Void migration takes place at higher temperatures
	7	BPORKG (1:NP)	-1.0E-03, -1.0E-03	-	coefficient describing the number of voids dependent on temperature
	8	VLKG0 (1:NP)	0.9, 0.1		"region of influence" (gross volume) of each class of voids $$\sum_{i=1}^{NP} VLKG0(i) = 1., \quad VLKG0(i) > 0.$$
	9	VLLKG0 (1:NP)	0.0499999, 1.0E-7		real volume of each class of voids, related to total porosity in the ring element $$\sum_{i=1}^{NP} VLLKG0(i) = PORO., \quad VLLKG0(i) > 0.$$
7					This DB is omitted. When called an error message is given and the calculation is ended.
8	1	NRDATB	-	-	No. of the actual DB
	2	FKB	5.0		strain hardening characteristic
9 to 11					These DB's are omitted. When called, an error is given and the calculation is ended.
12	1	NRDATB	-		no. of the actual DB
	2	NRH	6	-	no. of cladding radii
		IMATH	2		{ = 1: Zry-cladding { = 2: SS-1.4970 cladding { = 3: not active
	3	ZLH(1)	33.	cm	length of the actual cladding node, resp. of the cladding elements
		RAUHU	3.0E-04	cm	cladding surface roughness
	4	DOSDT	0.	n/cm^2	neutron dose
	5	RAHU	0.38	cm	cladding outer radius
		RIHU	0.33	cm	cladding inner radius
	6	HCOOLH	13.	W/cm^{2}K	heat transfer coefficient cladding to coolant
13	1	NRDATB			no. of actual DB
	2	DELTH	0.5	°C	max. tolerable temperature mismatch within two succeeding iteration steps during the calculation of the cladding temperature profile
		DTMAXH	10.	°C	max. tolerable of a cladding element's temperature from one internal time step to the next

14	1	NRDTAB		-	no. of the actual DB
	2+	SIGVH (1, 1:NEH)	5*0.	N/cm	radial stress in the cladding element
	3+	SIGVH (2, 1:NEH)	5*0.	N/cm	tangential stress in the cladding element
	4+	SIGVH (3, 1:NEH)	5*0.	N/cm	axial stress in the cladding element
	5+	EVH (1:NEH)	5* 1.0E-07	-	non-elastic equivalent strain in the cladding element
	6+	ESHH (1:NEH)	5* 1.0E-07		strain hardening strain in the cladding element
15	1	NRDATB			no. of the actual DB
	2	RMAH PMAH	1. 1.	- -	factors for modelling the mechanical anisotropy of the cladding
	3	RALFAH (1:3)	1.,1.,1.		thermal anisotropy-factors for the cladding
	4	RIRRH (1:3)	0.0, 0.67 0.33	-	factors for modelling an irradiation induced cladding anisotropy
16 to 17					These DBs are omitted. When called an error message is given and the calculation is ended.
18	1 2	NRDATB FKH	- 8.5		no. of the actual DB strain hardening characteristic
19					This DB is omitted. When called an error message is given and the calculation is ended.
20	1	NRDATB	-	-	no of actual DB
	2	ZBR	12.	cm	length of fuel column (total)
		ZBRU	7.6	cm	length of blanket column
		RABRU	0.315	cm	outer radius of blanket material
		RIBRU	0.	cm	inner radius of blanket material
	3	ZHU	33.	cm	total length of cladding tube
		VSTRUK	0.475	cm³	volume of internal structure parts
21	1	NRDTAB	-	-	no. of actual DB
	2	IANZZP	see list		number of time steps within the irradiation history (external time steps) limitation: 2 ≤ IANZZP ≤ IZEIT
	3+	TIMEH (1:IANZZP)	of standard	h	setpoints of time during irradiation, externally given by user
	4+	TPLEN (1:IANZZP)	input	°C	plenum temperature at time setpoints

	5 +	TCOOL (1:IANZZP)	see	°C	coolant temperature at time setpoints
	6 +	DRA (1:IANZZP)	list of	N/cm²	system pressure at time setpoints
IF(MDRI-EQ.1):	7a +	DRI (1:IANZZP)	Standard Input	N/cm²	internal pressure at time setpoints
IF (MDRI-EQ.0):	7b	DRI (1)	(Annex 2)	N/cm²	internal pressure (starting value) corresponding to temperature T (1)
	8 +	Q (1:IANZZP)		W/cm	linear power at time setpoints
22	1	NRDATB	-		no. of the actual DB
	2	FLUXSA	0.17E16	n/cm²-sec	non-disturbed fast neutron flux
		FLUXEA	0.	n/cm²sec	non-disturbed epithermal neutron flux
		FLUXTA	0.	n/cm²-sec	non-disturbed thermal neutron flux
	3	FLUXEI	1.	-	flux depression (resp. minimum of the relative flux) for epithermal flux
		FLUXTI	1.	-	flux depression for thermal flux
23	1	NRDATB	-		no. of the actual DB
IF (IPTTRA-EQ.0):	2a	HGFIX	1.5	W/cm²·k	fuel-cladding heat transfer coefficient, if it is chosen as constant value
IF (IPTTRA-EQ.1):	2b	CON (1:IGAS) (He,Ar,Kr, Xe,N₂)	0.5, 0.5, 0.,0.,0.	-	gas mixture in the gap
		EPST	10	°C	upper limit for the fuel surface temperature mismatch during two succeeding iteration steps when calculating the fuel-cladding heat transfer
IF (IPTTRA-EQ.2):	2c	WLAMNA	0.5	W/cm²·k	thermal conductivity of sodium (or of another liquid metal)
24 to 30					These DBs are not active. When called an error message is given and the calculation is ended.

I1.1 Tolerances and Limits

The values related to tolerances and limits can be subdivided into three groups:

Group 1: Control of the validity region of the single models

Group 2: Limitation of the number of calculational steps, iterations and similar numerical procedures

Group 3: Specification of array dimensions.

They have been specified via the subroutine INPUT or as PARAMETERs in the respective subroutines (in this case details are given below). The values in brackets correspond to the established and recommended values.

Group 1:

The tolerances and limits described below control the range of validity of the respective models. The requirement of accuracy is however limited by both the inaccuracy of computation itself and systematic errors which are due to the numerical procedures and model assumptions used in the individual models.

DELTB($20°C$): maximum tolerable temperature difference of two successive iteration steps during calculation of the temperature distribution in the fuel

DELTH($0.5°C$): idem for the cladding

EPST($10°C$): upper limit for the difference of two successive fuel surface temperatures during iterative determination of the heat transfer in the gap

DTMAXB($50°C$): maximum tolerable temperature jump in the fuel elements from time i to i + 1

DTMAXH($10°C$) idem for the cladding

DEMAX(5.E-4): maximum tolerable change of non-elastic strain from time i until i + 1

DESHM(0.5): maximum tolerable change of strain hardening strain, related to the change of non-elastic strain from time i until i + 1

DSMAX: maximum tolerable change of equivalent stress
(500 N/mm^2) from time i until i + 1

ICMAX(20):   maximum permissible number of cracks in a fuel ring
in RISS

KRIMAX(1900°C): upper limit of the fuel temperature up to which creep is taken
in DTTEMP   into account in calculation of the internal time interval DT

OMEPS(0.001):   maximum tolerable error limit during iteration in MIGOX
in MIGOX

PORMAX(0.15):   maximum porosity in the fuel; a higher pore fraction than
PORMAX is attributed to the central channel

PORMIN(0.01):
in PORCOM   minimum permissible porosity in the fuel rings
PORMIG

TMAX(2800 °C):   maximum tolerable fuel temperature (prints out message).

Group 2:

When these internal numerical counting limits are exceeded, the calculation is stopped. Program interruptions may be avoided by reviewing the finite element geometry, and/or the allowable tolerances and accuracies of the models which describe the materials´ behaviour.

EXPMAX(140):   maximum possible exponent of the exponential function for
in FCREEP   avoiding underflow and overflow, resp. in the FCREEP sub-
routine

ITEMAX(10):   maximum permissible number of iterations during calculation
in GAPRS   of the fuel surface temperature (causes program interruption)

ITM(50):   maximum permissible number of iterations in the MIGOX
in MIGOX   subroutine (causes program interruption)

ITMAX(7000):   maximum permissible number of internal computer time
in MAIN   intervals per external time interval (causes program interrup-
tion)

TEPS(1.E-10-h):	is necessary for the determination of the <u>last internal</u> time
in DTIME	increment each of an <u>external</u> time interval so that the end of
DTTEMP	the respective internal intervals exactly coincides with the end
DTPOR	of the external interval. This implies that in this special case it
MAIN	is also the shortest possible computer time interval or internal time increment resp.

Group 3:

The following symbolic constants are used to simulate variable dimensioning. They facilitate any necessary increase in dimensions and only the respective parameter must be modified in the concerning program units.

IRB = 50	lengths of "<u>radius</u>-dependent" fields
IRH = 10	(B $\triangleq$ fuel , H $\triangleq$ cladding)

IEB = 49	lengths of fields relating to the <u>elements</u>
IEH = 9	(IEB = IRB-1 and H, resp.)

IGAS = 5	lengths of the fields which concern the number of gas components in the fuel rod (must not be modified without corresponding modifications in the respective subroutines! cf. GAPRS)

IKF = 10	parameters for specifying the dimensions of the gas release
IKT = 20	and creep tables (identical for B and H);
IKZ = 5	

IZEIT = 100	available maximum number of <u>external</u> time intervals given by user or the length of the corresponding arrays resp.

11.2 Instructions for the use of the interpolation tables

As has already been mentioned previously, certain material phenomena (cf. G2., Fuel Creep and Fission Gas Release; G3., Cladding Creep) can be calculated either by models provided in the program or for special purpose by a table specified by the user (by two-dimensional interpolation). To avoid difficulties arising in use of this table, some explanations are now given as to its use.

General form of the table

F_1	T_1	$y_1(F_1T_1)$	$y_2(F_1T_1)$	$y_z(F_1T_1)$
	T_2	$y_1(F_1T_2)$	$y_2(F_1T_2)$	$y_z(F_1T_2)$
	⋮	⋮	⋮	⋮
	T_n	$y_1(F_1T_n)$	$y_2(F_1T_n)$	$y_z(F_1T_n)$
F_2	T_1	$y_1(F_2T_1)$	$y_2(F_2T_1)$	$y_z(F_2T_1)$
	T_2	$y_1(F_2T_2)$	$y_2(F_2T_2)$	$y_z(F_2T_2)$
	⋮	⋮	⋮	⋮
	T_n	$y_1(F_2T_n)$	$y_2(F_2T_n)$	$y_z(F_2T_n)$
F_3	T_1	$y_1(F_3T_1)$	$y_2(F_3,T_1)$	$y_z(F_3T_1)$
	⋮	⋮	⋮	⋮
F_x	T_1	$y_1(F_xT_1)$	$y_2(F_xT_1)$	$y_z(F_xT_1)$
	⋮	⋮	⋮	⋮
	T_n	$y_1(F_xT_n)$	$y_2(F_xT_n)$	$y_z(F_xT_n)$

In the program the vectors FB and FH, resp., are provided for $F_1...F_x$ whose length is IKF; for $T_1...T_n$ the fields TB and TH, resp., of the length IKT. For the rest of the table, namely $y_1(F_1F_1)...y_z(F_xT_n)$, the FTMB-H memory with the dimensions (IKT, IKF, IKZ) is provided. Filling up this three-dimensional field is done by the subroutine KRBMAT for Fuel Creep, KRHMAT for Cladding Creep and GSBMAT for Fission Gas Release. (Available dimensions cf. I.1.1)

If the user wishes to change tables, the procedure for "columnar storage of multi-dimensional fields" in FORTRAN should be kept in mind.

I2. Program Output

The output list generated by the program consists of two parts:

• output of the input data,

• output of all results of the computation.

Output of the input data

The first output generated by the program is a list of the input data used. Also those variables are output which in the INIT subroutine are calculated directly from input data (c.f. Annex 2).

Output of all results of computation

At the appropriate times as specified by the input, the variables are output which characterize the materials´ state as calculated by the code (additional outputs are produced just before and after fuel cracking and in case of errors).

The first line of the list generated at each time-step contains the number of the time interval just terminated, when it began and when it ended. The end of the time interval is the "instantaneous" point in time at which the actual calculation was made.

The denotations KM, KR, KE at the beginning of each line mean:

KM: material designation: 1 for fuel, 2 for cladding

KR: numbering by radii

KE: numbering by elements (rings)

KG: numbering by void volume classes

IC: = 0 : fuel ring uncracked

> 0 : fuel ring cracked, indication of the number of cracks in the fuel ring

At the end of the list an information is given about the total number of internal time steps and used CPU-time.

Control of the SATURN-FS 1 Output:

The output generated can be written into one (PARAMETER IW = 6: standard unit reference number) ore more external output files. If desired any part of the output can be directed into a special output file. For that purpose some more unit reference numbers (IW1-IW5) are available in the PARAMETER-list of the sub-programs OUT and INOUT. For its activation the exchange in the standard unit reference number IW for one of the parameters IW1-IW5 is required in the corresponding WRITEs. In that case additional DD-cards are needed in the Job Control.

An illustration of a print-out is given as Annex 3. The output data can be interpreted using the following table.

I2.1 Meaning of the Output Variables

FORTRAN SYMBOL	Dimension	Meaning
BU	MWd/kg Me	burnup
CPROB	--	approach to tolerable cladding load
CPU	--	Pu-concentration in the fuel ring KE
DOSDT	n/cm^2	total neutron dose
DOSP	$n/cm^2 \cdot s$	neutron flux
DPA	--	neutron damage (displacement per atom)
DRADT	N/cm^2	system coolant pressure
DRIDT	N/cm^2	internal gas pressure
EPSNE (1)	--	rad. nonelastic strain in the element KE of the material KM
EPSNE (2)	--	tang. nonelastic strain in the element KE of the material KM
EPSVB 3	--	axial total strain of fuel
EPSVH 3	--	axial total strain of cladding
ESH	--	strain hardening strain in the element KE of material KM
EV	--	nonelastic equivalent strain in the element KE of material KM
FCONR	N	radial contact force
FCONZ	N	axial contact force
FESH	1/h	rate of strain hardening strain in the element KE of material KM
FEV	1/h	total nonelastic deformation rate of the element KE and material KM
FIMA	--	burnup
FPGKG	N/cm^2	gas pressure in the pores of void volume class KG in the element KE
FRISS	cm^2	cracked area in the fuel element KE
GMFREI	Moles	total number of released gas moles
GMKG	Moles	no. of gas moles in the void volume class KG of the element KE
HGAP	$W/cm^2 \cdot K$	heat transfer between fuel and cladding
HE, AR, KR, XE, N2	--	gas mixture in the gap
IC	--	no. of cracks in the element KE ($\triangleq$ ICRACK)
IT	--	no. of internal computation steps in the instantaneous external time interval
IZP	--	no. of the instantaneous external time interval

FORTRAN SYMBOL	Dimension	Meaning
KE	--	numbering by elements (rings)
KG	--	numbering by void volume classes
KM	--	material designation: 1 for fuel, 2 for cladding
KR	--	numbering by radii
O/M	--	oxygen-to-metal ratio
PHIDTQ	fiss/cm^3	radial average of the time integrated fission rate
PHIP	fiss/cm$^3 \cdot$ sec	local fission rate in the fuel element KE
PHIPQ	fiss/cm$^3 \cdot$ sec	radial averaged fission rate
POR	--	porosity in the fuel element KE
PRA	cm	radius of the pores of the void volume class KG in the fuel element KE
PRB	--	relative flux distribution at the fuel radius KR
QDT	W/cm	linear power
RAD	cm	radii of the rings or resp. elements of the material KM
SFRISS	cm^2	crack volume per unit length
SIG (1) SIG (2) SIG (3)	N/cm^2 N/cm^2 N/cm^2	radial tangential } stress in the element KE of material KM axial
SKDT	W/cm	thermal conductivity integral
SV	N/cm^2	equivalent stress of the element KE of the material KM
TCOLDT	°C	coolant temperature
TIME (IZP)	h	start of the time interval IZP
TIMEDT	h	end of the time unterval IZP or instantaneous time setpoint
TEDTR	°C	temperature at the radius KR of the material KM
TPLEDT	°C	plenum temperature
VLLKG	--	"effective" pore volume of the void volume class KG in the element KE
VPLEN	cm^3	void volume in the fuel rod
XNLKG	cm^{-3}	no. of pores of the void volume class KG in the fuel element KE
ZL	cm	axial length of the element KE at the radius KR of the material KM

I2.2 Program Interruptions

Program interruption occurs, e.g. if input errors are made or if specified boundary limits have been reached (cf. I1.1, Group 2). Should such a termination take place, reasons are given in the output list which also indicates the program unit where the interruption was initiated.

A defined stop also occurs if the predetermined CPU-time limit will probably be exceeded (controlled in MAIN by Subroutines CPUTIME and TIMEL). In this case an output list is given, which contains all results up to the last computed internal time step. The allowed remaining CPU-time is 0.1 sec. If it falls short of 0.2 sec a warning is given that computation will be interrupted. (These values are related to an IBM 3090 and have to be occasionally adjusted).

Part 3

Code Verification and Examples of Application

K .Verification

K1. General

During the test and verification phase experiments are recalculated with the code in order to compare the analytical results with experimental data or with the results of other codes. The experiments selected for recalculation with SATURN-FS 1 are chosen so that it is possible to compare single effects such as fuel temperatures, fuel structure and redistribution effects or fuel rod mechanical behaviour.

K2. Cladding Creep Test

As a first step the mechanical behaviour of internal pressurized Zry cladding tubes was recalculated. Thus the description of the complete elastic and nonelastic mechanics could be tested, especially as the experiments were performed not only under constant internal pressure but also under varying pressure levels.

* Material data

Material :	Zry-4
Dimensions :	
outer diameter	10.922 ± 0.055 mm
inner diameter	9.576 ± 0.05 mm
wall thickness	0.610 mm
last annealing	2 h at 485 °C
Mechanical properties at room temperature:	
ultimate tensile strength	$R_m = 783$ N/mm^2
yield strength	$R_{p\,0,2} = 583$ N/mm^2
max. uniform elongation	$A_g = 20 \%$
at 343 °C	
ultimate tensile strength	$R_m = 487$ N/mm^2
yield strength	$R_{p\,0,2} = 382$ N/mm^2
max. uniform elongation	$A_g = 21 \%$

* Experimental conditons

Temperature (°C)	Internal pressure (MPa)			
316			18.04	22.55
343		13.53	18.04	22.55
370	9.02	13.53	18.04	22.55
400	9.02	13.53	18.04	

Furthermore, at a temperature level of 343 ºC transient tests were performed:

- after 300 hours the internal pressure was raised from 18.04 MPa to 22.55 MPa and

- also after 300 hours the internal pin pressure was decreased from 22.55 MPa to 18.04 MPa.

● Results

Comparisons between experimental data and calculational results are given in Figs. K2-1 to K2-5. These figures show that the SATURN-FS code is capable to describe the mechanical behaviour of cladding tubes under steady state and under transient pressure with good accuracy.

Fig. K2-1:   Comparison between measured and calculated circumferential creep strain at 316 °C and different internal pressure

Fig. K2-2:   Comparison between measured and calculated circumferential creep
strain at 343 °C and different internal pressure
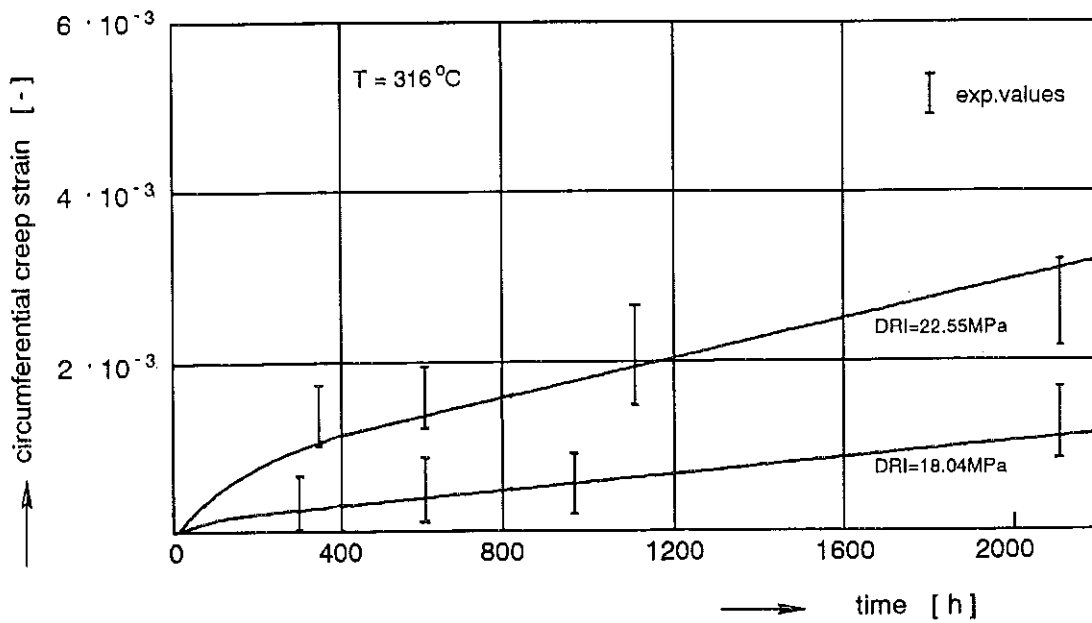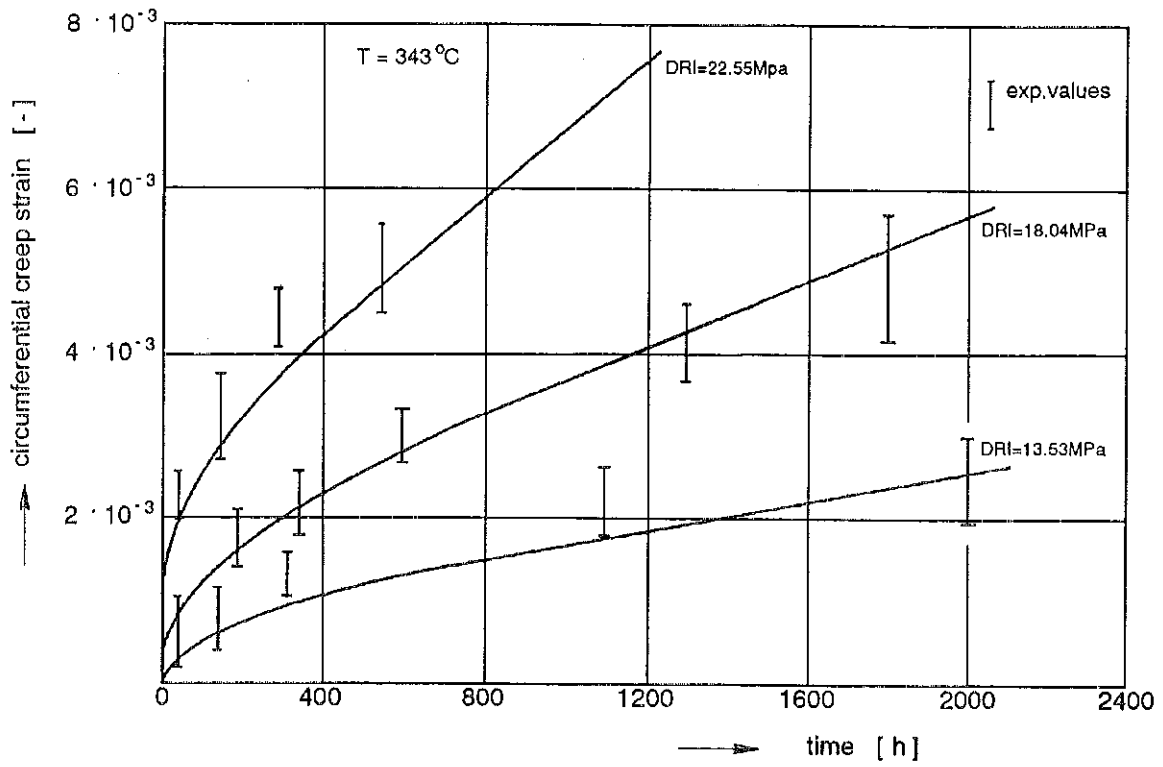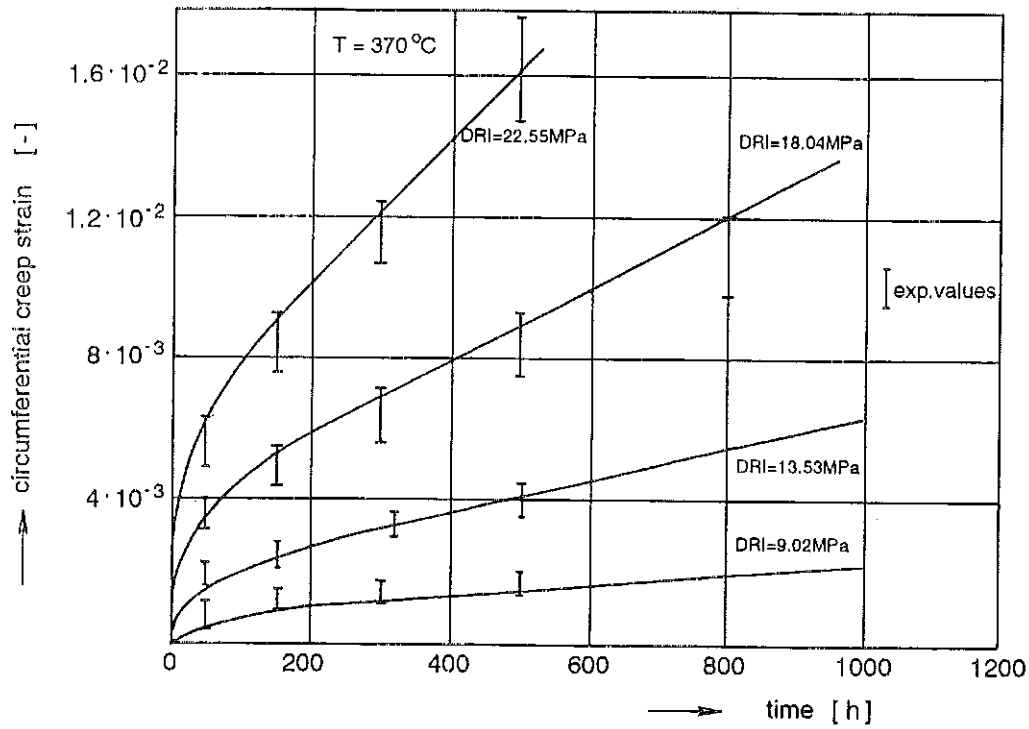

Fig. K2-3:   Comparison between measured and calculated circumferential creep
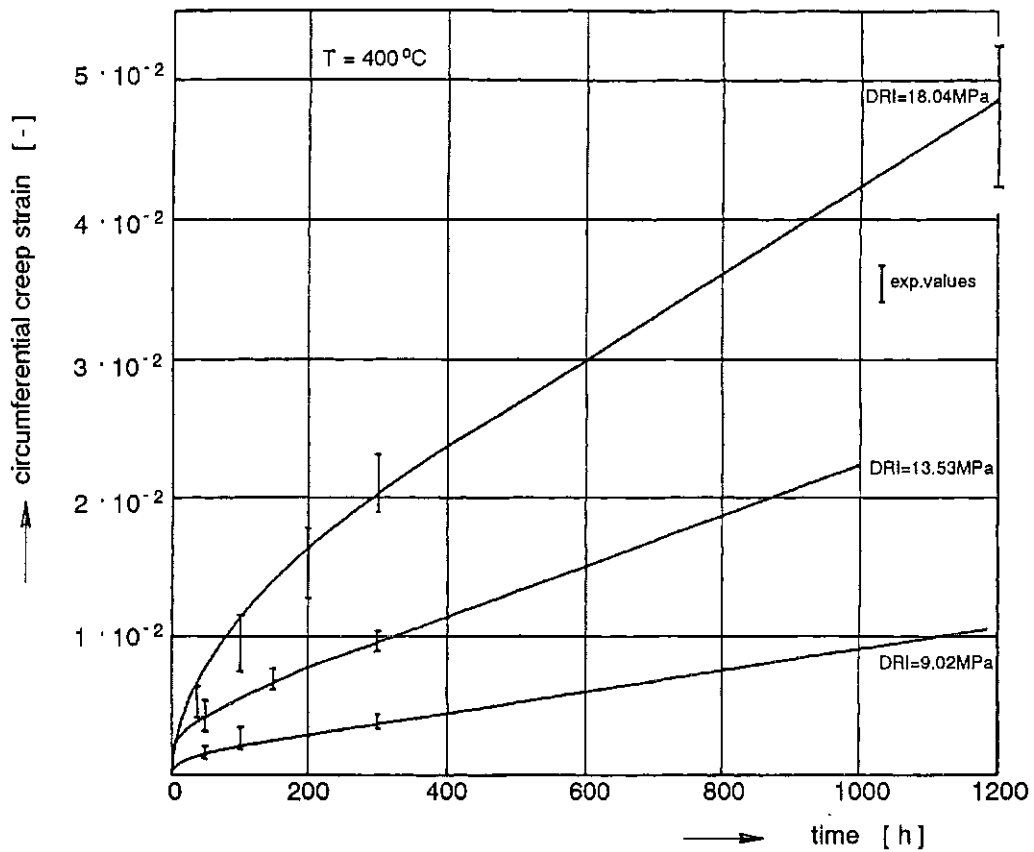strain at 370 °C and different internal pressure

Fig. K2-4: Comparison between measured and calculated circumferential creep strain at 400 °C and different internal pressure
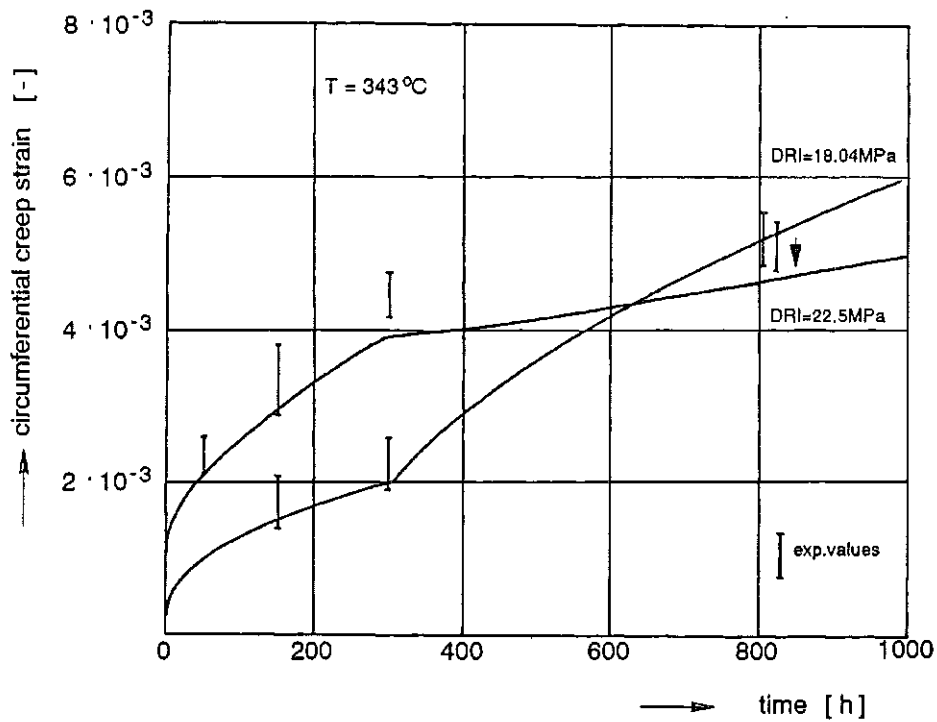

Fig. K2-5: Comparison between measured and calculated circumferential creep strain at 343 °C with variable internal pressure

K3. The IFA-404[1] Irradiation Test

The IFA-404 test was performed in the Halden Reactor in Halden, Norway. Fig. K3-1 shows a drawing of the "Instrumented Fuel Assembly" IFA 404. With this test rig it was possible to measure the diameter and length changes of three fuel pins during irradiation.

⊛ Test objective

Objective of the IFA-404[1] test was to measure the diameter increase, ridging and length changes of fuel pins with different gaps between fuel and cladding. Furthermore this test series should investigate the influence of lubricating or protecting layers on the fuel and on the inside of the cladding.

⊛ Fuel pin data

Recalculation was done for the pin no. 403 with no lubrication layer. The data of the fuel pin are given in Fig. K3-2.

⊛ Test conditions

The first power cycle of the pin no. 403 was recalculated. During this cycle the linear power was increased from zero to 535 W/cm, kept at about this level for nearly 24 h and then slowly reduced, see Fig. K3-3.

⊛ Recalculation

Objective of the recalculation of this experiment was to do a complete thermomechanical modeling of a fuel pin and to compare the calculational results with the experimental data. Especially the mechanical parts of the models could be tested by recalculating this experiment.

The most important of them are

- fuel cracking and relocation

- the onset of contact after gap closure

- contact forces and friction forces

- combination of fuel and cladding thermomechanical behaviour resulting in creep and plastic deformation of the cladding.

⊛ Results

Fig. K3-4 shows the power history of the first power cycle, and the resulting circumferential stresses and strains in the cladding as they were calculated by the SATURN-FS code. The calculated circumferential cladding strains are compared

to the experimental values. The agreement between experiment and calculation is quite good.

Quite more informative, not only with respect to the modeling of the gap closure, but also for a more general judgement whether the model can sufficiently describe fuel pin mechanics and especially PCI and friction effects is the presentation in Fig. K3-5. Here, the calculated and the experimental values for axial and circumferential cladding strains are drawn versus the linear heat rate during the first power cycle. With respect to the circumferential cladding strains, the results of two kinds of calculations are shown besides the experimental values: at first the results of a calculation without a crack/relocation model, as it was used in earlier code version [K3-1]. As can be clearly seen from this curve, a sudden hard contact, at about 250 W/cm is predicted, which is in contrary to the experimental result. This deficiency was already mentioned in [K3-1]. Looking at the results of the calculation when the new crack/relocation model is implemented into the code, the agreement has improved. Especially, the modeling of the soft onset of the contact forces between fuel and cladding tube seems to be very satisfactory. The only slight discrepancy between experiment and calculation exists after ramp down at zero power. Here, the model obviously overpredicts the circumferential strain by about $5 \cdot 10^{-4}$ or 0.05 %.

But keeping in mind the rather complicated conditions in the fuel pin, this discrepancy seems to be acceptable. Perhaps, a better agreement would have been reached, if more detailed data for the cladding material were available, e.g. creep data or information on the mechanical anisotropy of this special material.

The lower part of Fig. K3-5 gives an impression of the axial cladding strain - measured and recalculated. Besides a slight overprediction during ramp up at linear heat rates above 400 W/cm the agreement is very good.

References

[K3-1]   H.-J. Ritzhaupt-Kleissl. M. Heck
         Nuclear Eng. and Design, 101 (1987) 219

3 PIN DIAMETER RIG

Shroud

Failure detector (steam sampler)

D₂O hydraulic drive cylinders (2 up, 1 down)

Inlet thermocouples

He-3 tubular coil for local neutron flux control

Neutron sensors (5)

Fuel rods (3)

Fuel rod diameter sensors (3)

Cladding extensometers (3)

Inlet thermocouples (2)

Inlet flowmeter

Electromagnetic three-way valve (forced/natural circulation)

Forced circulation subcooled inlet flow

FUEL LOADING:

Three 50 cm long fuel rods (replaceable).

TEST CAPABILITIES:

Measure diameter profile and length of 3 fuel rods at power.

Change power in range 60 - 100% of FP at max. rate 5% of FP/min.

TEST OBJECTIVES:.

Clad cracking by localized strains over pellet interfaces (ridges) and fuel cracks constitute a major problem for power reactor operation.

The localized strains (ridges) are affected by fuel design parameters and by type of power manipulations.

This rig with its special instrumentation and He^3 power depression system is specially well suited to study the influence of both these effects.

The example below is from a study of the influence of interface lubrication.

Graphite on pellets   Siloxane on clad.   No lubrication
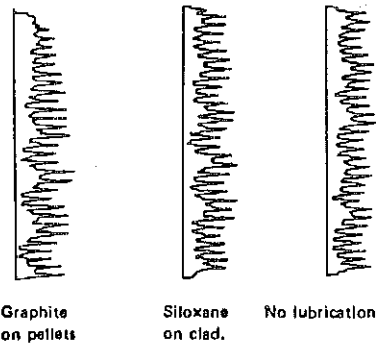
The three diameter profiles show that there is no significant influence of interface lubrication on the ridging.

Fig. K3-1:   Instrumented fuel assembly IFA-404 for in-pile diameter measurement of fuel pins

	DATA SHEET	ISSUE NO. 2	PAGE: 2
		SIGN: *E.W*	DATE: 22 5-73

IFA- 404^I

TEST ASSEMBLY DATA

DESCRIPTION				
Fuel Form	Sintered and ground UO_2 pellets			
Pin No.	401¹⁾	402²⁾	403	Total
Fuel Weight kg	0.604	0.599	0.605	1.808
End Pellets	.033	.033	.034	0.100
Fuel Density g/cm³	10.40 (95% of T.D.)			
Fuel Diameter mm	12.63	12.60	12.64	
Enrichment	7 ^W/o U-235			
EC No.	1	2	3	
Diam. Clearance, µm	0.060	0.100	0.060	
End Pellets	One at each end, depleted UO_2. Length = 12 mm			
Pellet Length mm	15			
Dishing	Dished one end (spherically)			
Dishing Depth mm	1.0 (Dish volume = 2.4%)			
Land Width mm	1.0			
Cladding	Zr-2			
Cladding State	ASTM B 353-64T. Fully annealed			
	R.T.: UTS = 58.4 (kp/mm²) YS = 43.5 EL = 28 (%)			
	300°C: " = 29.4 " " = 17.9 " - 45 (")			
Welding	TIG			
Filler Gas	Helium			
Clad. Int. Diam. mm	12.70			
Clad. Thickness mm	0.80			
No. Pins /Cluster	3			
Pitch Distance mm	46 (P.C.D.)			
Spacers	Two end plates			
Fuel Length/Pin mm	500 active fuel length			
Plenum				
Shroud Material	Al X 8001			
Shroud Int. Diam. mm	70.5			
No. Of Clusters	1			

1) Pellets coated with graphite, ~5 µm thick.

2) Cladding coated inside with siloxane, ~ 5 µm thick.

Moisture content < 5 ppm.

Fig. K3-2: Design data of the IFA 404I irradiation test

3-rod diameter rig IFA-404I (HP)
Total irradiation time: 22/6 - 29/9-73.
No. of shutdowns (zero power) : 19.

O   Diam. runs during the 1st power cycle
⊙   Selected for use in this report
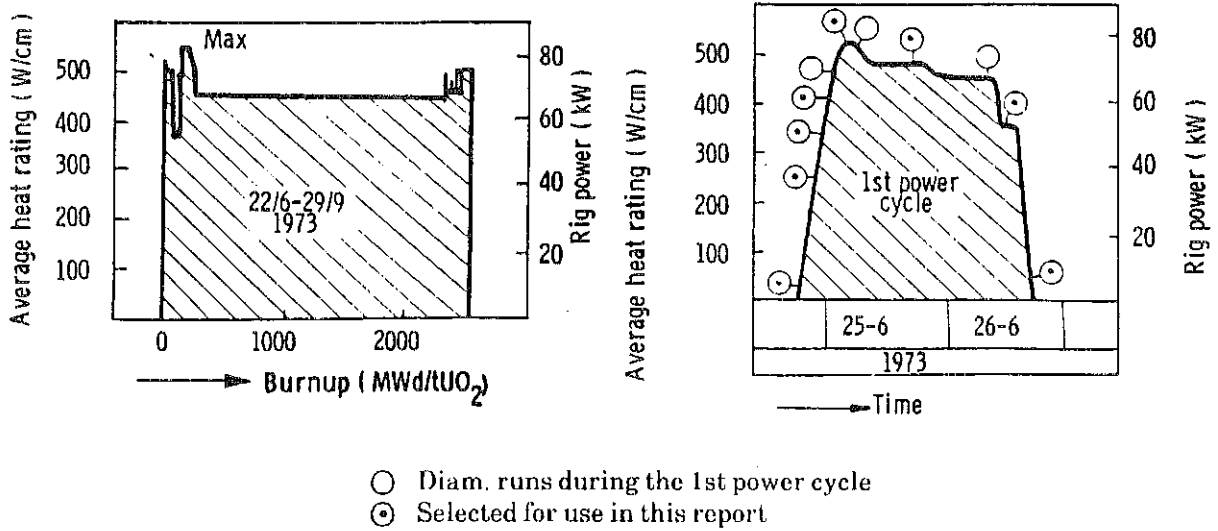
Fig. K3-3:   Power history of the IFA-404I irradiation (left)and of the
recalculated first cycle (right)
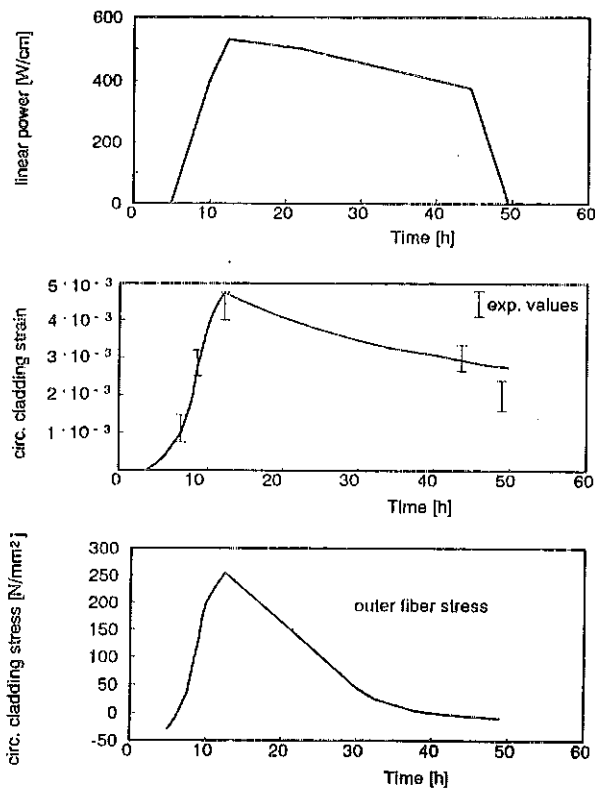
Fig. K3-4:   (top) Power history of the IFA-404 first power cycle;
(middle) comparison between measured and calculated cladding
circumferential strain, plotted vs. time;
(bottom) calculated cladding circumferential stress vs. time
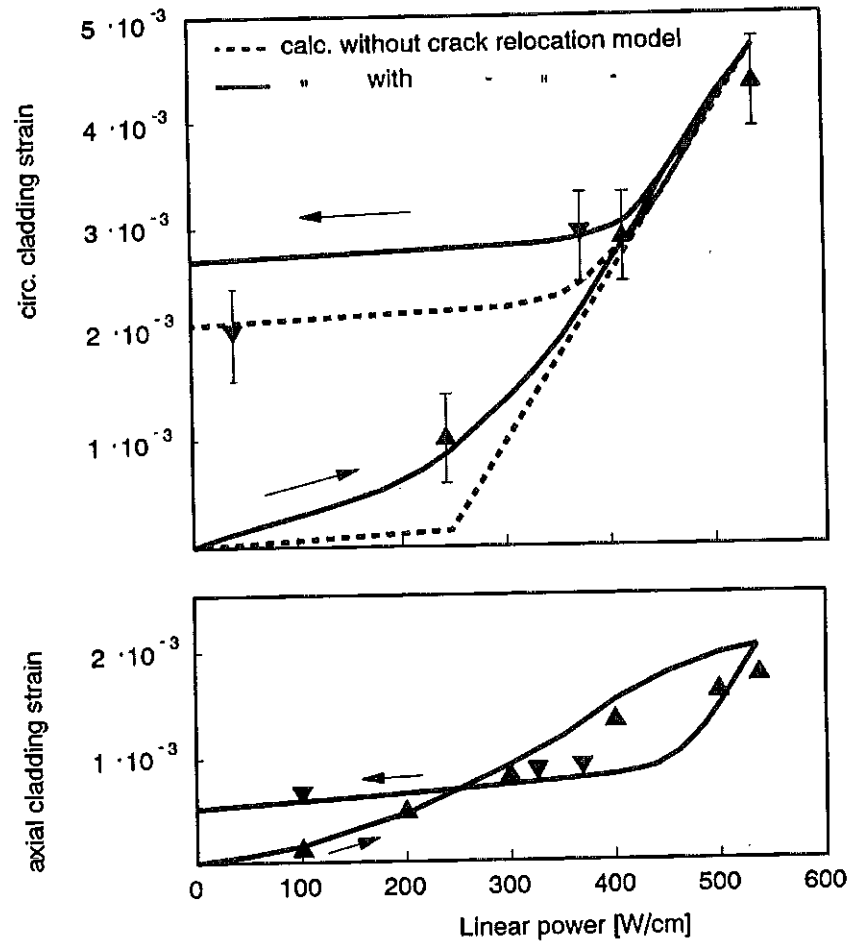
Fig. K3-5: Comparison between experimental values and SATURN-FS results of cladding circumferential and axial strain vs. the linear power during the first power cycle of the Halden test IFA 404, pin 403. Calculations were performed with and without the new developed crack model RISS

K4. The IFA-405[1] Fast Power-Ramp-to-Failure Tests

As the IFA-404 test IFA-405 test was performed in the Norwegian Halden Reactor. But, supported by an internal He-3 system in the fast power transients could be verified in the IFA-405 rig.

● Test objective

The objective of the first test series IFA 405[1] was to study the influence of power transients with different rates on the failure behaviour of preirradiated pins. During the experiment the axial cladding strains could be measured.

● Fuel pin data

The materials and dimensions of the IFA 405[1] pins are the same as for the IFA 404[1] test pin no. 403, mentioned in section K3. The pins were preirradiated for about 0.8 % FIMA.

● Test conditions

The test conditions and results are schematically represented in Fig. K4-1. As can be seen, pin no.101 was first ramped very slowly up to 660 W/cm, then rated down and again ramped up with a ramp-rate of 27 W/(cm · min) up to 670 W/cm and kept at this power for 10 hours. Pin no.103 was ramped up with 26 W/(cm·min) up to 660 W/cm. After a short time at the maximum power level the test was interrupted by a reactor scram. After the scram the test was continued. Pin no. 104 was ramped up to 700 W/cm with a ramp rate of 30 W/(cm · min).

● Test results

While the pin no. 101, which was conditioned by the first slow power increase, remained unfailed, the pins no. 103 and 104 failed.

● Recalculation

The objective of the recalculation was to test the capabilities of the SATURN-FS code to describe the effect of fuel pin conditioning; i.e. the influence of creep and stress relaxation especially with respect to the prediction of PCI fuel pin failures.

● Results

The results of the calculations are depicted in Figs. K4-2 to K4-8. Fig. K4-2 shows the power history of the preirradiation of all three pins as well as their circumferential and equivalent stresses and their circumferential and axial strains during preirradiation. As can be seen, no permanent strains are generated. The power history, circumferential and equivalent stress as well as total and plastic circum-

ferential strain of pin no. 101 during the slow power increase - the conditioning phase - is given in Fig. K4-3. Here the calculated maximum circumferential stress at 660 W/cm is about 240 N/mm^2 and the equivalent stress is 170 N/mm^2. The maximum total circumferential strain is $7 \cdot 10^{-3}$, the maximum plastic strain at the end of the conditioning phase is $4 \cdot 10^{-3}$. Fig. K4-4 represents the results for the fast power ramp of pin no. 101. As can be seen, in spite of the 10 W/cm higher linear power (670 W/cm) the stresses are lower than the maximum values during conditioning. The plastic portion of the circumferential strain shows a small increase to $4.2 \cdot 10^{-3}$, the total circumferential strain is $7.4 \cdot 10^{-3}$.

The calculated stresses and strains for the pin no. 103 are given in Fig. K4-5. The maximum circumferential stress for this pin is 300 N/mm^2, the maximum equivalent stress exceeds 200 N/mm^2. The plastic portion of the circumferential strain at the time of the first power maximum is $3.4 \cdot 10^{-3}$, the total circumferential strain reaches nearly $7 \cdot 10^{-3}$. The stresses and strains for the cladding of pin no. 104 are still higher than those of pin 103 (see Fig. K4-6). But in this figure also the creep induced stress reduction can be seen. After reaching maximum power, there is a plastic circumferential cladding strain of $3.7 \cdot 10^{-3}$, correlated to a circumferential stress of 330 N/mm^2. During the holding time of 12 hours at the maximum power level the plastic part of the circumferential strain is increased to $4.9 \cdot 10^{-3}$, whereas the circumferential stress decreases to 270 N/mm^2.

An impression of the quality of the performed analyses can be given by the comparison of the calculated vs. measured axial cladding strains as given in Figs. K4-7 and in K4-8. As can be seen, the agreements are good.

With respect to the failed and not failed fuel pins, the calculated results can well represent the experimental facts. Table K4-1 shows the cladding stresses of the pins 103 and 104 normalized to those of no. 101.

Table K4-1: Cladding stresses of pins no. 103 and 104 normalized to the stresses of pin no. 101

pin no.	$\sigma_t/\sigma_{t,101}$	$\sigma_v/\sigma_{v,101}$
103	1.25	1.18
104	1.38	1.35

As Table K4-1 shows, the circumferential stress of pin no. 103 is 25 % higher and the equivalent stress is 18 % higher than that of pin no. 101. The corresponding values for pin no. 104 are even higher - 38 % and 35 %.

For unirradiated material the ultimate tensile strength in the considered temperature region is about 290 N/mm². Taking into .account stress peaks at the pellet-pellet interfaces - a stress intensity factor of 1.5 is not unrealistic - and considering the influence of the chemical inventory, the calculated failure stresses, which at the first moment seem to be rather low, lie within realistic limits. The confidence in the calculated stresses is further supported by the good agreement of the calculated axial cladding strains with the experimental data.
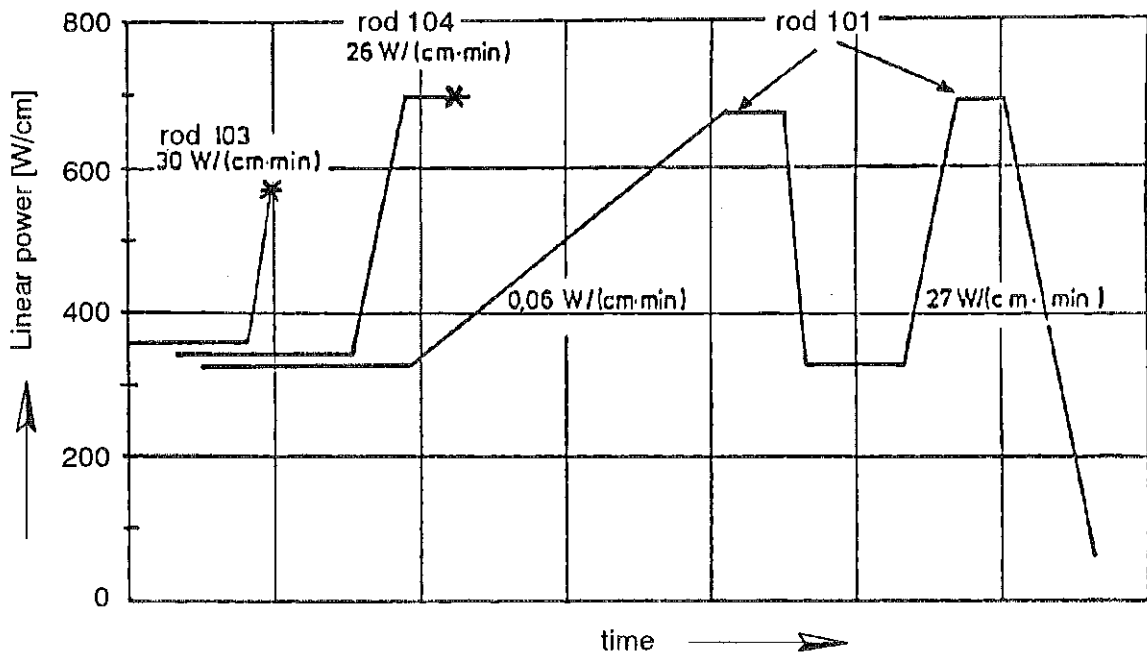
Fig. K4-1: Schematic representation of the test conditions and the results of the IFA 405 power ramp test
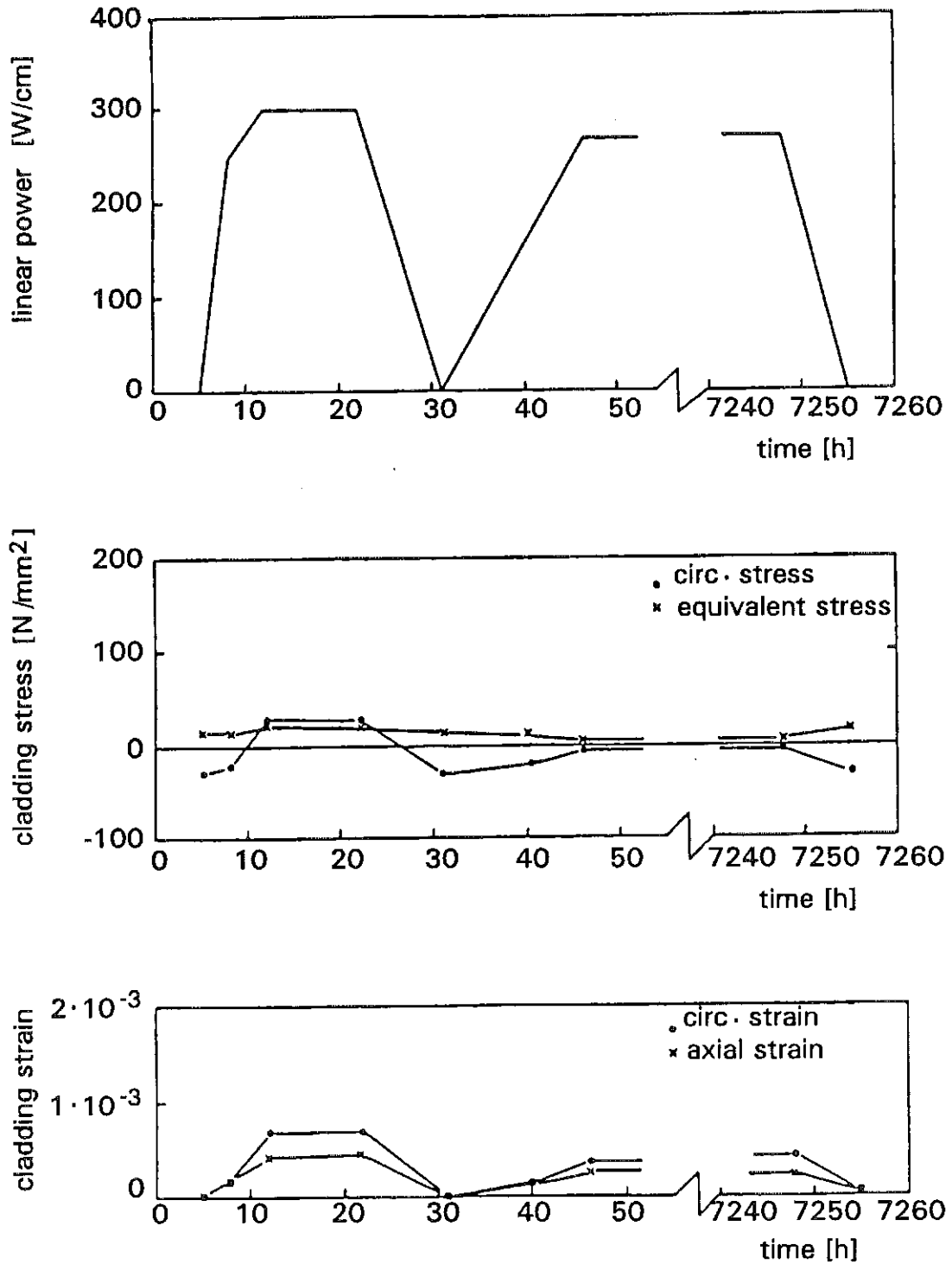
Fig. K4-2: Power history and with SATURN FS calculated cladding stresses and strains of the IFA 405 test pins during pre irradiation
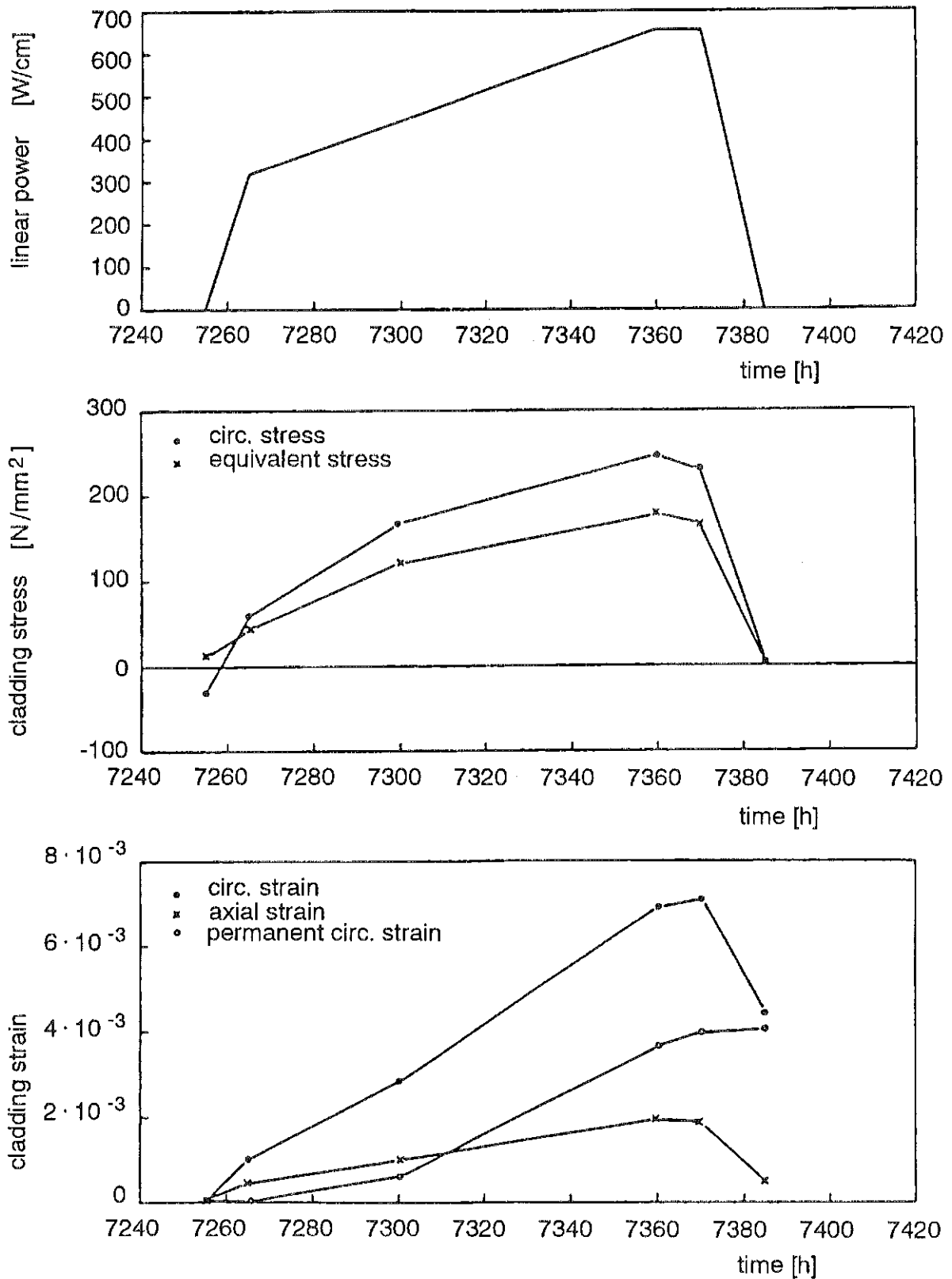
Fig. K4-3: Power history and with SATURN FS calculated cladding stresses and strains of pin no. 101 during conditioning
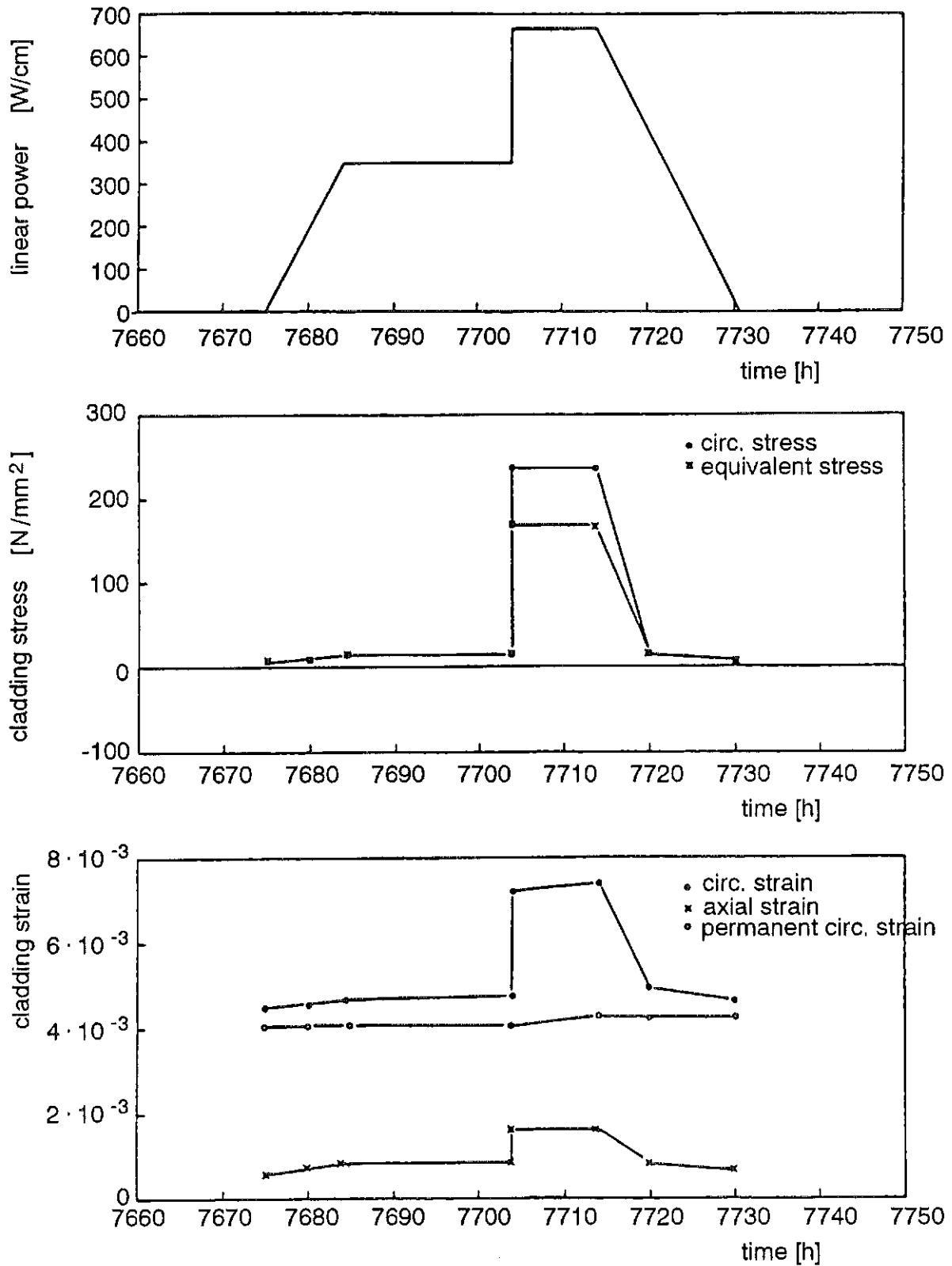
Fig. K4-4: Power history and with SATURN FS calculated cladding stresses and strains of pin no. 101 during the fast power ramp
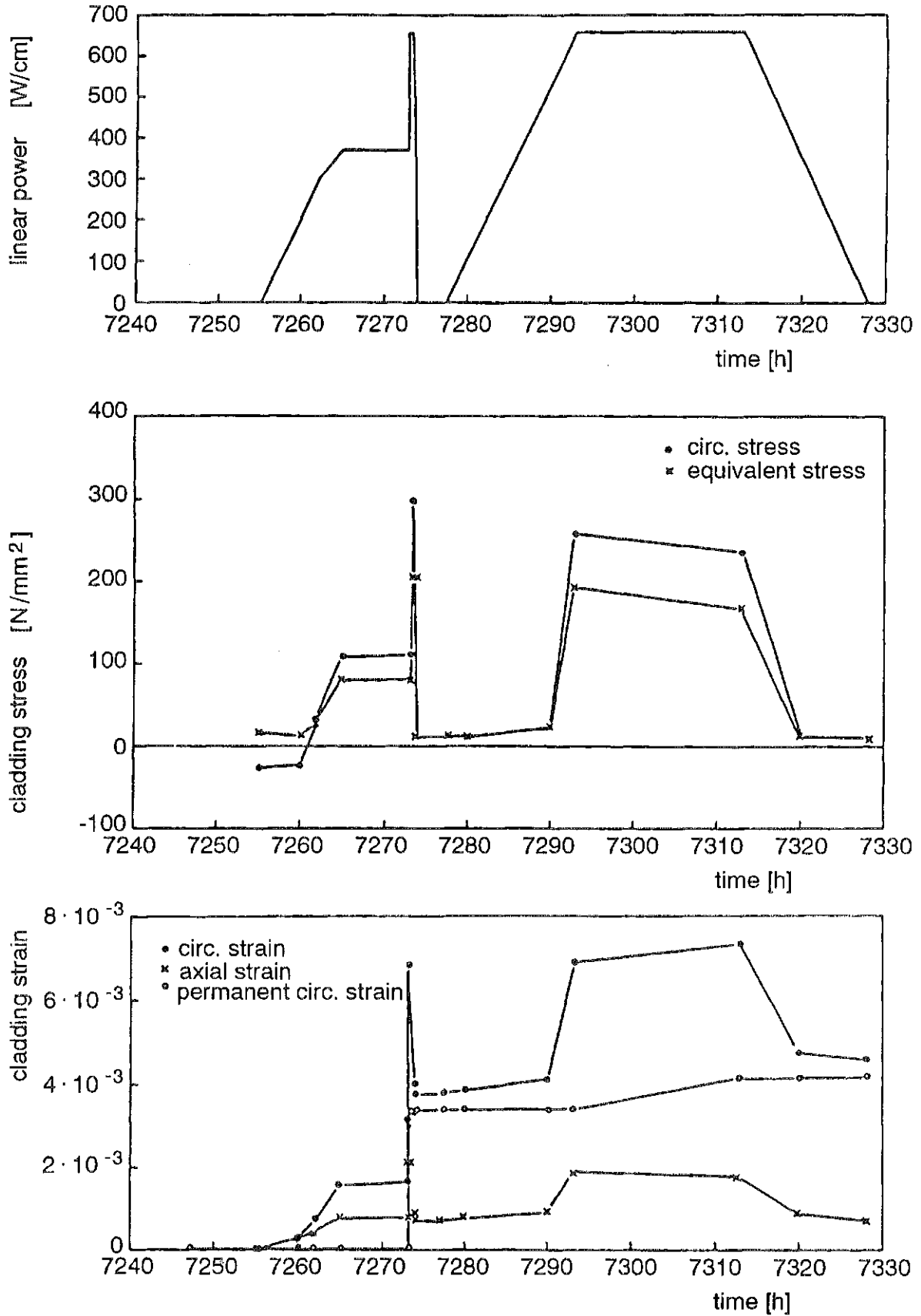
Fig. K4-5: Power history and with SATURN FS calculated cladding stresses and strains of pin no. 103
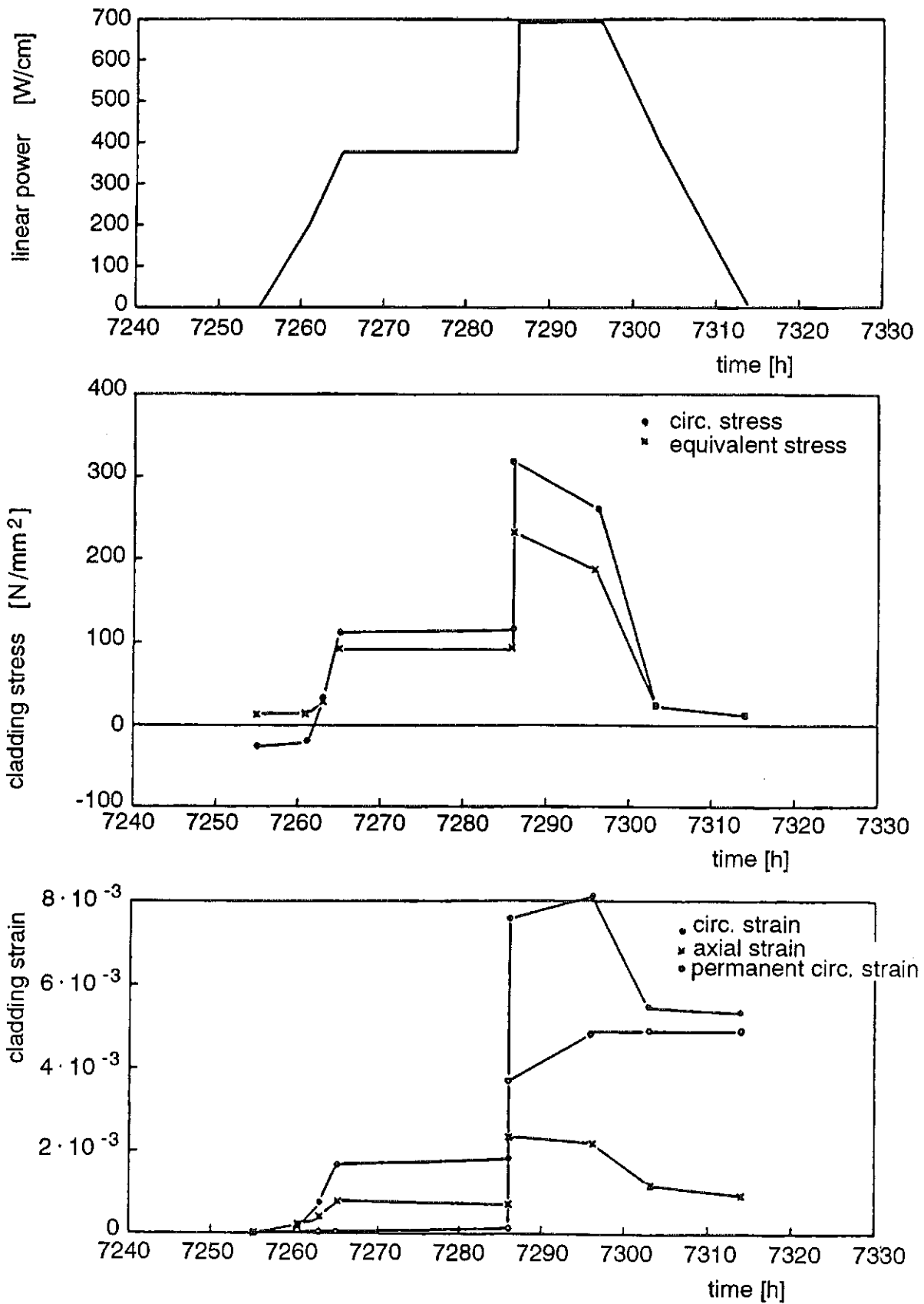
Fig. K4-6: Power history and with SATURN FS calculated cladding stresses and strains of pin no. 104
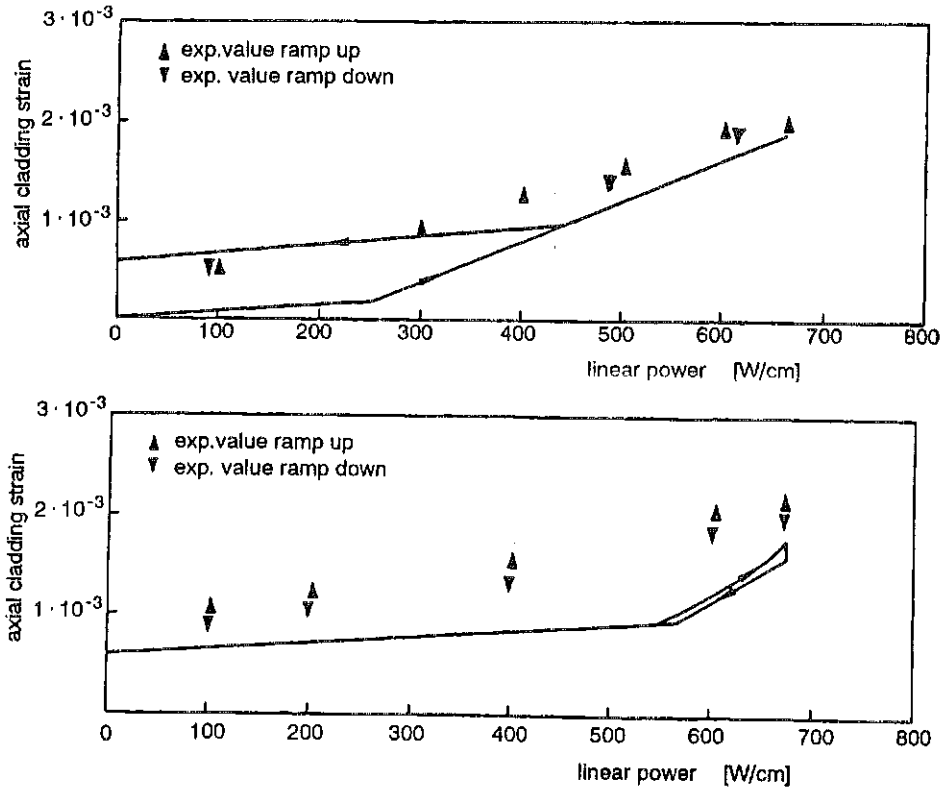
Fig. K4-7: Comparison of experimental data with SATURN FS results for the axial cladding strain of pin no. 101 during conditioning (top) and during the fast power ramp (bottom)
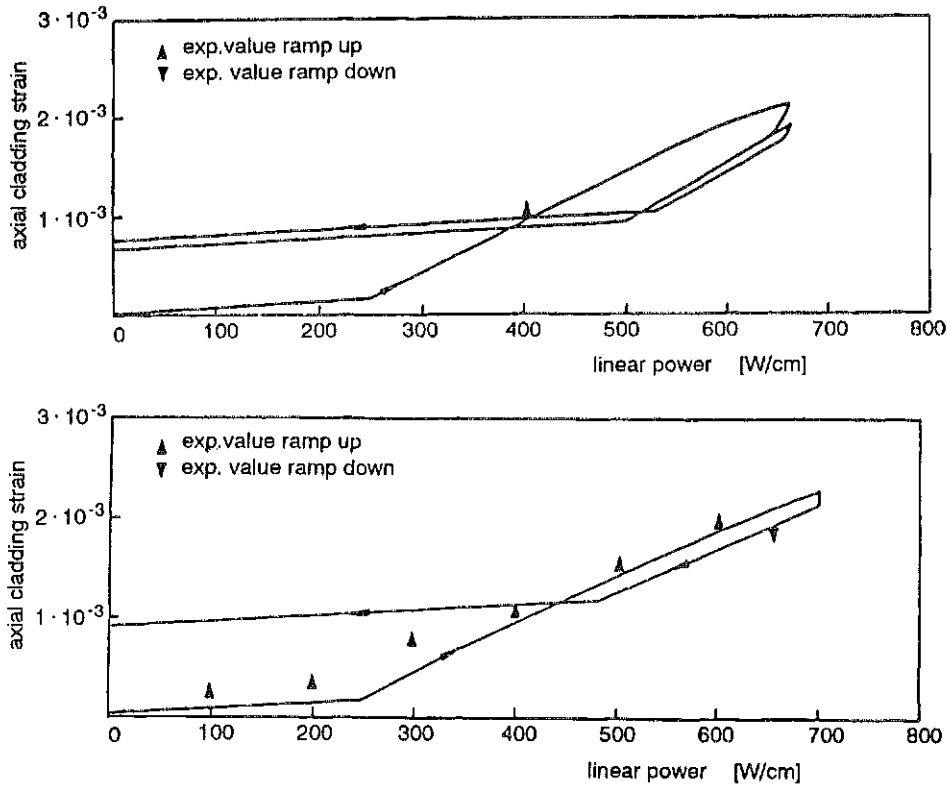
Fig. K4-8: Comparison of experimental data with SATURN FS results for the axial cladding strain of pin no. 103 (top) and 104 (bottom)

K5. An FR2-Vg 7 Irradiation

The Vg 7 irradiation test series was performed in the Karlruhe FR2 test reactor in order to develop new types of Fast Breeder Reactor fuel. The fuels inserted in these tests can be characterized as follows:

- U/Pu-mixed oxide fuel
- 95 % density
- O/M-ratio of about 1.96
- 25 % Pu-enrichment.

The objectives of recalculating this irradiation experiment were to test the agreement between experiment and the calculation with respect to

- temperature profile in the fuel
- dimensions of the central void
- gap closing
- porosity profile in the fuel.

The comparison between experimental data - gained by post-irradiation examination (PIE) - and modeling results are given in Figs. K5-1 to K5-4.

Fig. K5-1 shows the calculated radial temperature profile of the pin at maximum power compared to the structure radii evaluated by PIE in the hot cells. The outer radius of the zone of equiaxed grain growth can be correlated to a temperature range between 1300 °C and 1400 °C. Also the outer radius of the columnar grain zone is correlated to a temperature range between 1600 °C and 1700 °C. So, if the modeling prediction is good, vertical lines starting from the radii, measured by PIE and horizontal lines starting from the boundary temperatures must match together on the calculated radial temperature profil as it is shown in Fig. K5-1. As the fuel restructuring is an irreversible process always the maximum thermal load conditions must be compared with the PIE structure information.

The predicted development of the structure and geometry changes of the fuel during irradiation is shown in Fig. K5-2. As can be seen from this figure, there is a very early gap closure and a continuous increase of the central void. The isotherms at 1300 °C, 1400 °C, 1600 °C and 1700 °C generally show a decrease of the thermal load in the fuel during the irradiation. Again the calculated isotherms, representing the structure radii, are compared to the PIE-values and furthermore there is a comparison between the calculated radii of the central void and the measured data. The overall good agreement of the SATURN-FS predictions can be seen.

The calculated radial distribution of pores and cracks are compared with the hot cell data in Fig. K5-3. There seems to be some discrepancies with respect to the pore profile between prediction and experiment, which need to be discussed. The

hot cell measurement was performed with image analysis on a radial trace of the fuel. This trace was selected so that the amount of cracks was as small as possible. But, as can be seen from the metallographic cross section (Fig. K5-4), it seems to be impossible to find a radial trace where only pores can be measured, without any partizipation of cracks. So, if the calculated crack area is added to the calculated porosity, the agreement between analysis and experiment is much better. Curve no. 1 in Fig. K5-3 shows the calculated porosity only, curve no. 2 porosity plus cracks. The peak in curve no. 2 at a relative fuel radius of about 0.75 is related to a maximum of the crack portion in the fuel and may perhaps in a very rough estimate be related to the cracking during cool-down, which in reality shows cracks perpendicular to the radial direction.

The metallographic cross section in Fig. K5-4 shows this crack formation at a relative radius of about 0.6 - 0.7.
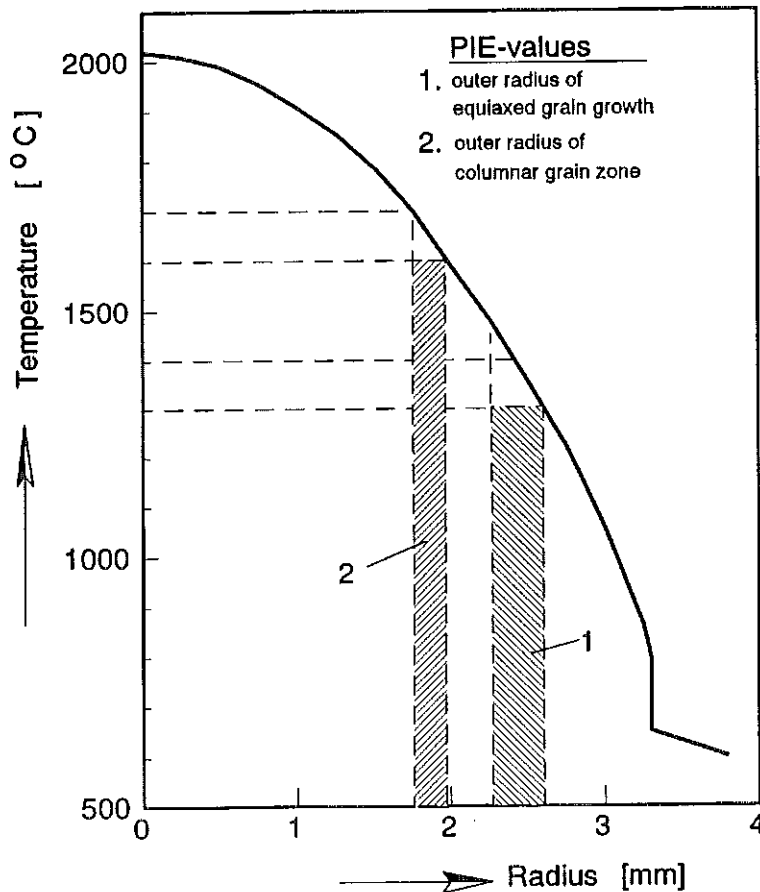
Fig. K5-1: Analysis of fuel temperatures and structure radii of the mixed oxide experiment Vg 7/KVE 165. Comparison with PIE-data
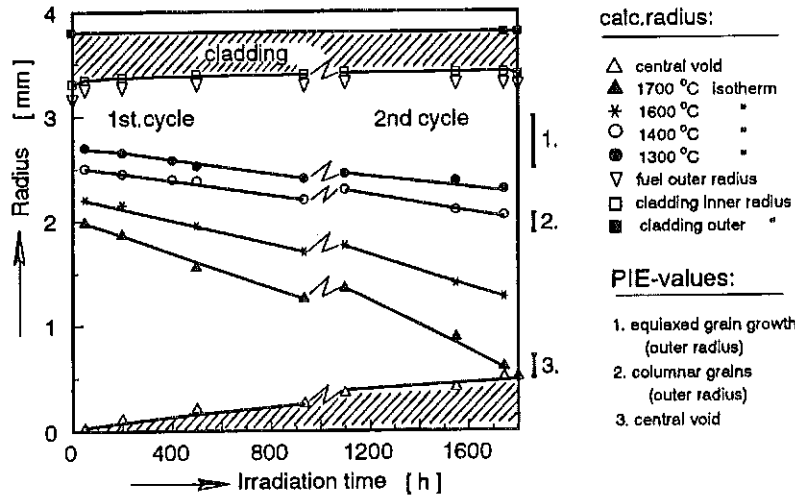
Fig. K5-2: Analysis of fuel geometry and structure radii of the mixed oxide experiment Vg 7/KVE 165. Comparison with PIE-data
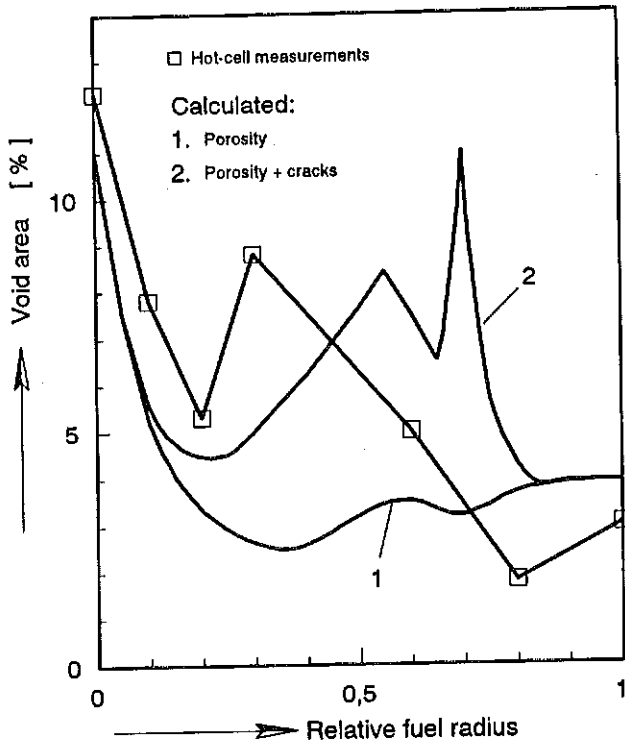
Fig. K5-3: Analysis of the radial profiles of porosity and cracks in the Vg 7/KVE 165-fuel. Comparison with PIE data
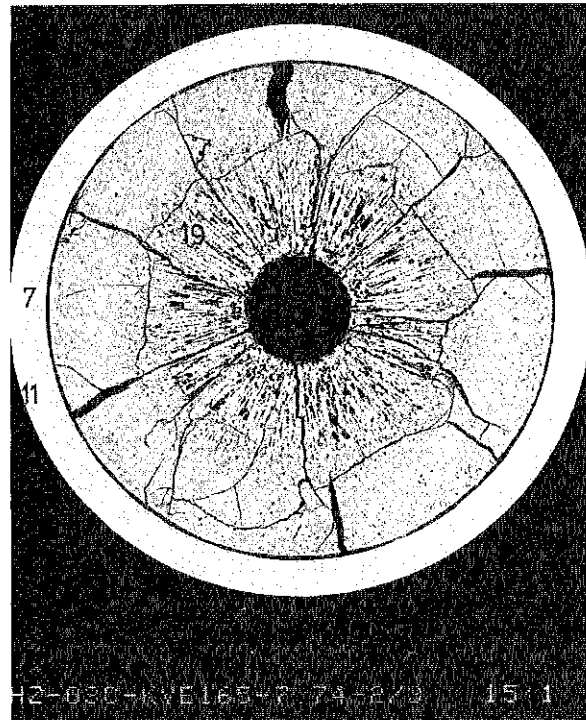
Fig. K5-4: Metallographic cross section of the Vg 7/KVE 165 fuel pin.

L. Application

L1. Design Calculations for Test Pin with LWR-Geometry

L1.1 Introduction

As a part of the cooperation between an external partner and KfK, an irradiation experiment with an LWR-type fuel pin has been planned.

As a first step of design considerations for the test fuel pin, studies on the anticipated behaviour of test fuel pins were performed.

L1.2 Design of the Test Pin

As the final construction of the test pin is not yet completed, an estimated design was taken as a basis for the behaviour analysis. This design was chosen rather similar to standard PWR fuel and fuel pin dimensions. The fuel pin length was accomodated to existing of the irradiation device data.

The test pin data are as follows:

* Fuel rod
  - length: 366 mm
  - plenum volume: 1.44 cm^3
  - backfill gas: 90 % He, 10 % Ar

* Cladding
  - material: Zry 4
  - outer diameter: 10.75 mm
  - inner diameter: 9.30 mm
  - surface roughness: 0.7 µm

* Fuel
  - material: UO$_2$
  - diameter: 9.08 mm
  - density: 94 % TD
  - enrichment: 3 % U-235
  - grain size: 10 µm
  - surface roughness: 2 µm
  - stack length: 321 mm

* Irradiation facility
  - neutron flux 1.2·10^{11} n/cm^2·s)
  - heat transfer

coefficient

coolant to cladding: 6 W/(cm^2·K)

L1.3 Fuel Pin Performance Calculations

To study the operational behaviour of the test fuel pins, fuel modelling calculations were done, using the SATURN-FS 1 computer code.

To take into account the influence of different environmental conditions, the analyses were performed for different coolant temperatures, coolant pressures and pressures of the backfill gas.

So the following variations have been studied:

Fuel rod type	1	2	3
coolant temperature (°C)	160	310	310
coolant pressure (bar)	5	130	130
backfill gas pressure (bar)	1	1	20

The power history, which was chosen for the analyses, consists of the following parts:

-       startup ramp
-       steady state operation at 350 W/cm for 2000 h
-       load reduction to 100 W/cm,
-       low power operation for 30 days, followed by a ramp up to 350 W/cm again,
-       overpower ramp to 450 W/cm with a ramp rate of 10 W/(cm·s).

L1.4 Results of the Analyses

The results of the calculations are shown in Figs. L1-1 to L1-5.

Fig. L1-1 shows the radial temperature distribution of the typ 1 fuel pin at several linear power levels. As can be seen, the fuel centerline temperature reaches a maximum of 1220 °C at 350 W/cm.

Due to this low thermal load, there is no contact between pellet and cladding.

The radial temperature distribution as shown in Fig. L1-2 is derived by the type 2 fuel pin. The maximum fuel centerline temperature is here about 1450 °C. The difference to the type 1 pin is mainly caused by the higher coolant temperature.

As there is no difference between the temperature profiles of the pressurized and the non pressurized fuel pin, the temperature profiles for the prepressurized pin, case 3, are just the same as those shown in Fig. L1-2 for the non pressurized.

Fig. L1-3 shows the calculated power history of the type 1 fuel rod and the resulting cladding inside radii and stresses. As can be seen there is no cladding diameter change during full power operation. Furthermore, the cladding stresses are low and are also nearly constant.

This is quite different with the type 2 fuel rod which is operated under 130 bar coolant pressure, 310 °C coolant temperature and with a backfill gas pressure of 1 bar.

Fig. L1-4 shows the results of the analysis of this case. In the bottom part of the figure, the power history is given, the top part shows the generalized cladding stress and the middle part the inner radius of the cladding during the operational time.

As can be seen, there is a strong cladding creepdown with a hard contact between pellet and cladding after about 1000 h. After this contact the cladding radius remains constant as long as the power is not changed. After the power reduction at 2000 h the cladding is freestanding again and shows further creepdown. During the following power increase the gap is closed again and, after reaching the 350 W/cm level, the cladding tube shows a creep in outward direction until the start of the strong diameter increase caused by the overpower ramp.

Looking at the generalized cladding stress, it can be seen, that, after a slight increase during the period before hard contact occurs, the stress is slightly reduced after the hard contact point by a support of the cladding by the fuel and by stress relaxation.

This is just more illustrated by the stress increase after power reduction, when again there is a freestanding cladding. At the following gap closure there is a stress reduction again, and the stress is still further reduced by cladding creep and stress relaxation effects as mentioned before. The overpower ramp gives a stress peak with a height of about 50 N/mm^2 and with an absolute value of about 86 N/mm^2.

Creepdown of the cladding during low power operation for longer times may sometimes lead to high cladding stresses when the power is increased again.

Peak stresses may also occur at power ramps, as shown in Fig. L1-4, especially late-in-life after some cladding embrittlement, then perhaps leading to fuel rod

failures. To avoid these failures or to reduce the probability of the occurrence of these failures, modern PWR fuel rods are prepressurized up to about 20 bar as a standard fabrication step, but this is not so necessary with short-time, low power test irradiations.

Fig. L1-5 shows the advantage of a pre-pressurized rod in comparison with the behaviour of the non-pressurized rod in Fig. L1-4. As can be seen from this figure, the creepdown is more slowly than with the non-pressurized rod and "hard" contact occurs only at the power ramp up to 450 W/cm. The stress increase during the low power operation is here caused by the decrease of the internal gas pressure, thus increasing the pressure difference across the cladding tube.

L1.5 Conclusion

Design calculations were run for a test fuel pin, in oder to model the operational behaviour of this pin at typical PWR conditions.

It can be shown that a test fuel pin, if irradiated at these or some similar conditions, will not show any unexpected results.
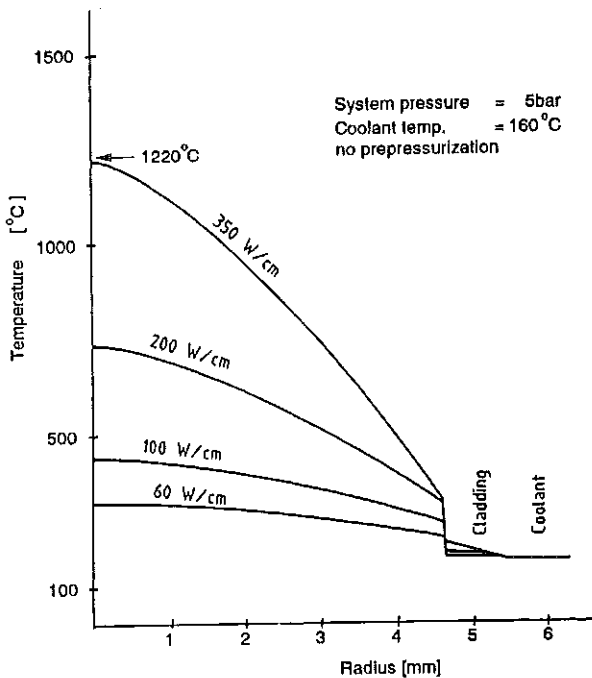
Fig. L1-1:   Radial temperature
distribution in fuel rod of
type 1
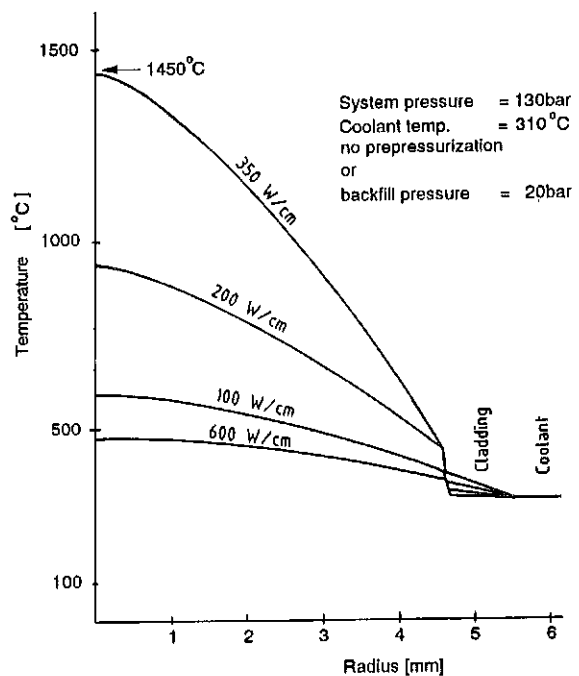
Fig. L1-2:   Radial temperature
distribution in fuel rods
of type 2 and type 3
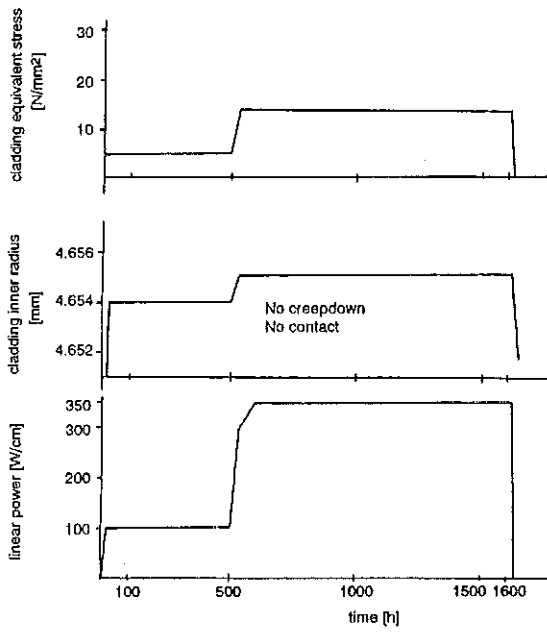
Fig. I.1-3: Power history, cladding stress and inner radius of the type 1 fuel rod
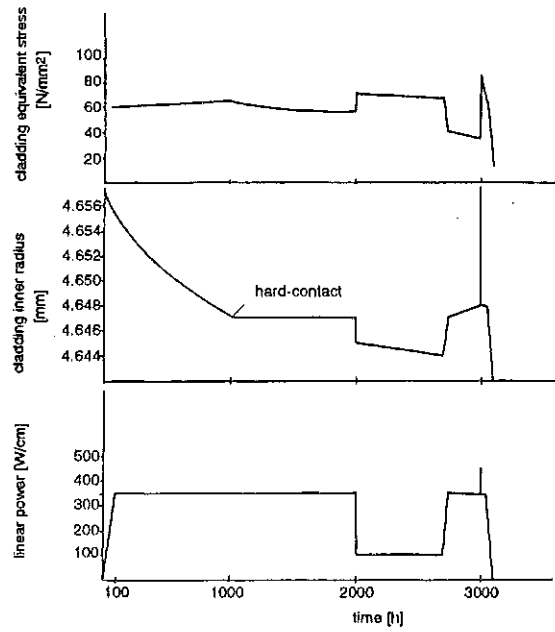
Fig. I.1-4: Non pressurized fuel rod, type 2
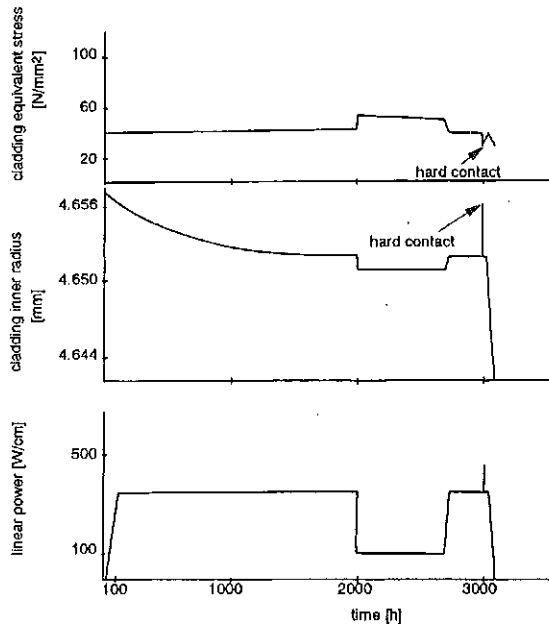
Fig. I.1-5: Pressurized fuel rod, type 3

L2. Considering the Influence of Microcracks on the Thermal Behaviour of Mixed Oxide Fuel [L2-1]

L2.1 Experimental Evidence

The thermal conductivity of the fuel is one of the most important features in fuel pin design, because the maximum heat generation in the fuel is limited by its thermal conductivity via maximum tolerable temperatures. For this reason, the thermal conductivity of various FBR fuel types was experimentally determined. The results were correlated to effective fuel structure parameters [L2-2].

The thermal conductivity was deduced from thermal diffusivity measurements in the temperature range from 750 to 1450 °C which were made in the Karlsruhe European Institute of Transuranium Elements. Two extreme results are shown in Figs. L2-1 and L2-2. The data of the fuel type given in Fig. L2-1 are about 20% worse than the data [L2-3] commonly used as standard or reference data in the data base for design calculations, whereas those of the fuel type shown in Fig. L2-2 are better by about the same percentage than these reference data.

The two fuel types differed by the following parameters:

- The fuel type of Fig. L2-1 had an oxygen-to-metal (O/M) ratio 1.962 just after fabrication and of 1.997 at the time of the determination of the thermal conductivity. The amount of open porosity related to the total porosity was about 92% at the same time.

- The values for the fuel type shown in Fig. L2-2 are 1.958, 1.960 and 7%, respectively.

As also observed with other fuel types, the fraction of open porosity increased with increasing O/M shift, particularly in the range of small channel diameters less than 100 nm which can be attributed to microcracks. Fig. L2-3 shows an example for this effect.

The investigation of the thermal conductivity of the new FBR fuel types yielded the following results:

- Pellets without open porosity (microcracks) seem to have a significantly better thermal conductivity than expected from the reference data.

- Although the increase of the O/M ratio leads to an improvement of the thermal conductivity of the fuel material itself [L2-3], the effective thermal conductivity decreases slightly with increasing O/M shift as consequence of the formation of microcracks.

L2.2 Consequences for the Thermal Behaviour at Begin of Operation

An increase of the O/M ratio is found in the outer part of hypostoichiometric fuel pellets under operation conditions. The radial temperature gradient is the reason, why the O/M ratio falls below the initial value in the inner hot region, whereas it goes up to values near 2.00 in the outher cold region [L2-4].

It must be expected that the formation of microcracks accompanies this increase of the O/M ratio in the same way as observed out-of-pile. The influence of this phenomenon on the thermal behaviour of the fuel pellets at begin of operation was analyzed by means of modeling calculations using the SATURN-FS 1 computer code.

The operational data chosen for this purpose are typical for the irradiation test to be considered in the following chapters.

The radial temperature profile after restructuring as it is expected according to the reference data is shown in Fig. L2-4 (case 1). A global fit to the experimental values leads to the second profile in Fig. L2-4 (case 2).

A more detailed consideration was carried out using the so-called Maxwell-Eucken equation [L2-5].

$$\lambda/\lambda_0 = \beta(1-P)/(1+P) \tag{L2-1}$$

with

λ = thermal conductivity of the porous fuel,

λ_0 = thermal conductivity of the 100% dense fuel, and

P = volume fraction of porosity.

This equation takes into account pore structure and thermal conductivity through the pores by means of the pore shape factor β [L2-6].

This factor β was correlated in the analysis to the local O/M ratio according to
$0.5 \leq \beta \leq 7.0$
with

$\beta = 0.5$ for the initial fuel structure with original O/M ratio, without cracks-sand with, approximately, spherical pores, and

$\beta = 0.7$ for the fuel structure resulting from the increase of the O/M ratio up to 2.00 (according to ref. [L2-2].

The temperature profile calculated under these asssumptions (case 4) is compared in Fig. L2-5 with two profiles which were calculated assuming constant values for β, 5.0 an 0.5 respectively (case 3 and 5). Table L2-1 summarizes geometric and

Table L2-1: Thermal fuel analysis dependent on different conductivity data and pore shape factors

Case No.	Thermal conductivity	Fuel radius (mm)		Fuel temperature (°C)		
		inner r_j	Outer r_s	Centerline T_i	Surface T_s	T_j - T_s
1	λ_{ref}	0.599	3.301	2230	715	1515
2	λ^*_{exp}	0.627	3.296	2150	750	1400
3	$\lambda^*(\beta=5.0)$	0.613	3.296	2200	750	1450
4	$\lambda^*(\beta=0.5\text{-}7.0)$	0.622	3.288	2170	800	1370
5	$\lambda^*(\beta=0.5)$	0.619	3.279	2140	850	1290

thermal data of the analysis of the five cases.

The results of the five cases, presented in Figs. L2-4 and L2-5 as well as in table L2-1 mainly differ from each other by their radial temperature gradient across the different fuel regions and by their total temperature increase from fuel surface to mid pellet. Case 1, representing the reference data of the thermal conductivity λ_{ref}, shows the largest temperature difference. Assuming spherical pores and a corrected thermal conductivity λ^*, as done in case 5, results in the smallest temperature difference, as expected. The same tendency is also valid for the fuel centerline temperatures, whereas the fuel surface temperatures show just the inverse effect. Caused by the higher expansion the outher pellet radius for case 1 exceeds that of case 5, resulting in a smaller temperature jump across the fuel-cladding gap. The other cases, 2 to 4, just lie between these extreme cases 1 and 5.

References

[L2-1]   H.-J. Ritzhaupt-Kleissl, H. Elbel, M. Heck
J. Nuclear Mat. 153 (1988) 221

[L2-2]   H. Elbel, D. Vollath
J. Nuclear Mat. 153 (1988) 50

[L2-3]   H.-E. Schmidt
High Temp.-High Press. 3 (1971)345

[L2-4]   C. Sari and G. Schumacher
J. Nuclear Mat. 61 (1976) 192

[L2-5]   A. Eucken, VDI Forschungsheft 353, 1932
Ed. B., Vol. 3 (VDI Verlag, Berlin, 1932)

[L2-6]   G.P. Marino
J. Nuclear Mat. 38 (1971) 178
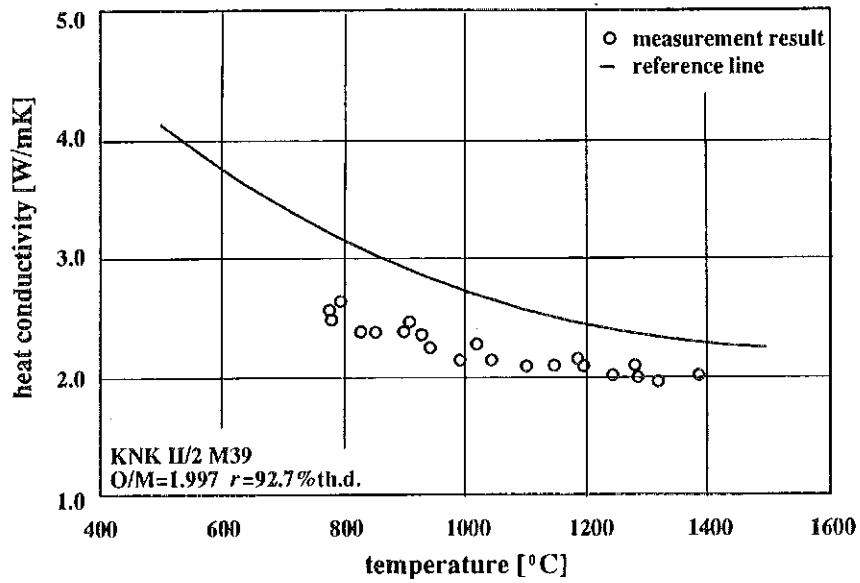
Fig. L2-1: Thermal conductivity of the KNK II/2, M39 fuel, reference line according to ref. [L2-3]
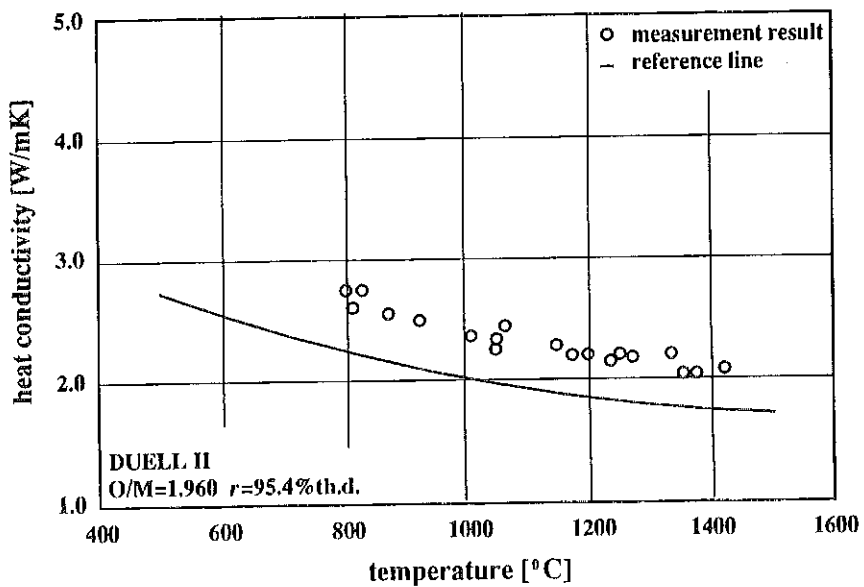
Fig. L2-2: Thermal conductivity of the DUELL-II fuel, reference line according to ref. [L2-3]
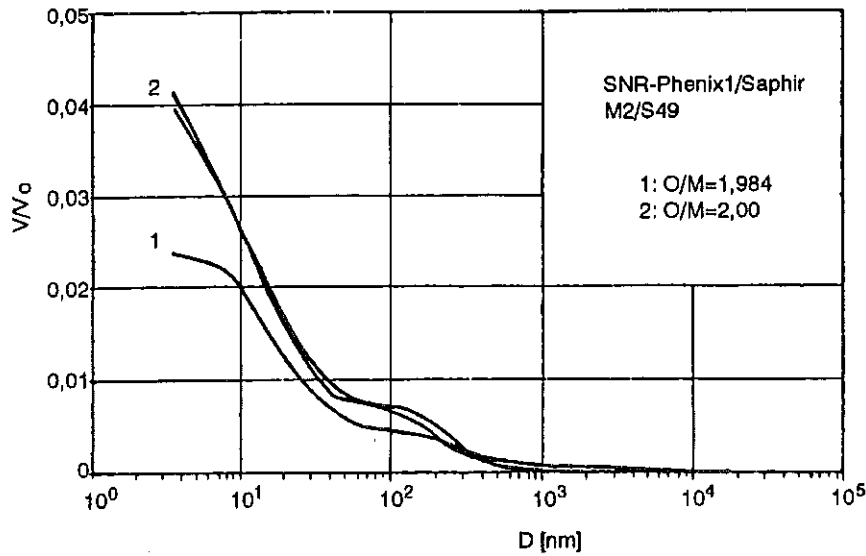
Fig. L2-3: Cumulative open porosity versus intrusion channel diameter of the SNR-Phenix 1/Saphir fuel.
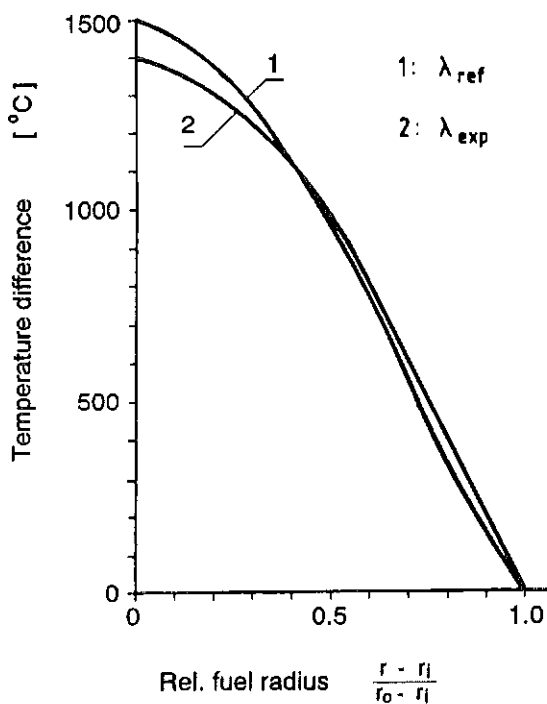
Fig. L2-4: Radial fuel temperature profiles according to the reference data for thermal conductivity (case 1) and based on experimental values (case 2)
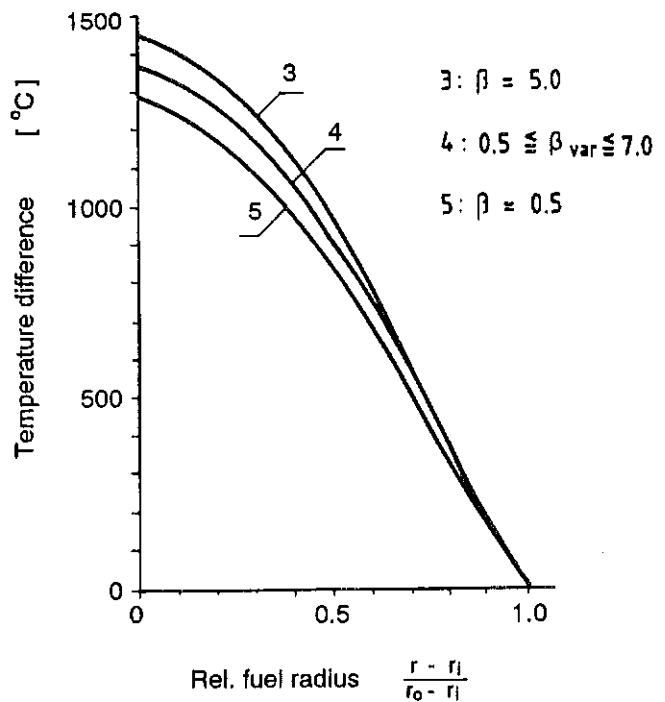
Fig. L2-5: Radial fuel temperature profiles based on the Maxwell-Eucken porosity correction with several pore shape factors

L3. Thermal analysis of a high-burnup LWR-fuel pin

L3.1 Objective

A thermal analysis of a high-burnup LWR fuel pin was performed with the SATURN-FS code in order to support the interpretation of the PIE results [L3-1].

L3.2 Fuel Pin and Irradiation Data

● Nominal data BOL

  - Fuel data
    Material   : $UO_{2.003}$
    Enrichment   : 3.2% U-235
    Pellet diameter   : 9.2 mm
    Pellet density   : 10.35 g/cm^3 = 94% TD

  - Cladding data
    Material   : Zry-4
    Outer diameter   : 10.75 mm
    Wall thickness   : 0.70 mm

  - Fuel pin data
    Prepressurization : 2.8 MPa He
    System pressure   : 15.5 MPa
    Coolant temperature : 320 ºC

● Irradiation data
    Local burnup   : 55900 MWd/t heavy metal (= 5.9% FIMA)
    Time averaged linear power : 210 W/cm

● Nominal fuel pin data EOL
  - Radial cold gap   : 10 µm
  - Radial EOL porosity
    distribution: $r/r_o \leq 0.9$: 5% porosity
                         $r/r_o > 0.9$: 20% porosity

  - Enrichment   : 1.38% PuO_2 (PuO_2 / (UO_2 + PuO_2 + fiss. prod.)
                         0.56% U-235/U_{tot}

  - Fission gas release : 2% integral
  - Thickness of Zirconia layer on
    the cladding surface : 40 µm.

L3.3 Generation of Input Data for the Analysis

● Calculation of the internal gas pressure and the gas mixture

The burnup of 55900 MWd/t is equivalent to about $5.0 \cdot 10^{21}$ fiss/cm^3. Assuming that the average burnup in the fuel pin is about 2/3 of the peak burnup and considering a fission gas production coefficient of 0.3 atoms per fission and a fuel inventory of 260 cm^3 UO$_2$ in the pin, the volume of the fission gas produced can be calculated to about 104 cm^3. So the 2% released fission gas amounts to 200 cm^3. Assuming a plenum volume of 20 cm^3, the internal pin pressure is thus increased for 10 bar to 38 bar, related to room temperature. Under operating conditions this pressure will increase to about 80 bar.
Considering thermal neutron flux conditions the Kr/Xe ratio of the fission gas is 1 : 7. So the following gas mixture will exist in the fuel pin:

> 73% He + Ar
> 24% Xe
> 3% Kr.

● Calculation of the radial power profile in the fuel

The radial power profile (acc. to the flux depression) for the fuel is calculated in the SATURN-FS code as follows:

$$\phi(r) = a + br^2 + cr^4 \tag{L3-1}$$

This formulation, describing the fresh fuel conditions could not be used for the analysis of the high-burnup pin. As PIE shows [L3-1], in the high burnup state power is mainly generated by the fission of the plutonium, which was generated by the U-238/Pu-239 conversion. The profile of the radial Pu-concentration typically shows a very steep gradient in a narrow outer region of the fuel pellet (r ≥ 0.9550). The maximum Pu-concentration at the pellet surface is 3.8% PuO$_2$, the pellet average value is 1.38%.

The relevant radial power profile in the fuel at EOL is shown in Fig. L3-1. The relative average power, according to the experimental data, is 40% of the maximum value.

In order to describe this actual radial power profile, the following approach was chosen:

$$\phi(r) = a + b \cdot r^{12} + c \cdot r^{24} \tag{L3-2}$$

with the boundary conditions:

$$\phi(r_i) = \phi_i \qquad \text{(L3-3)}$$

$$\phi(r_0) = \phi_0 \qquad \text{(L3-4)}$$

$$\frac{d\phi}{dr}(r_i) = 0 \qquad \text{(L3-5)}$$

The agreement between the average power in the real irradiation and in the calculation demands for:

$$\overline{\phi} = \frac{1}{r_0 - r_i} \cdot \int_{r_i}^{r_0} \phi(r)\,dr = 0{,}4 \qquad \text{(L3-6)}$$

Equation [L3-2] can be rearranged with the help of the boundary conditions:

$$\frac{\phi(r) - \phi_i}{\phi_0 - \phi_i} = \left(\frac{r^{12} - r_i^{12}}{r_a^{12} - r_i^{12}} \right)^2 \qquad \text{(L3-7)}$$

Equations [L3-6] and [L3-7] give the relative power at the fuel center related to the maximum value at the fuel surface:

$$\phi_i = 0{,}375 \qquad \text{(L3-8)}$$

This is a SATURN-FS input value. Fig. L3-1 shows, that the radial power profile curve, as it is taken for the analysis is in good agreement with the measured values.

* Determination of the temperature increase on the cladding surface by the zirconia layer

Taking into consideration a zirconia layer with a thickness of 40 µm and a thermal conductivity of zirconia of 2 W/(cm · K), the following values are generated:

The temperature increase by thermal conductance is generally:

$$\Delta T = \frac{Q}{2\pi \cdot \lambda} \cdot \ell n\left(\frac{r_0}{r_i} \right) \qquad \text{(L3-9)}$$

with

Q	$=$	Linear power in W/m
λ	$=$	Thermal conductivity in /(W/m·K)
r_0	$=$	Outer radius of the layer
r_i	$=$	Inner ″ ″ ″ ″

The temperature increase was determined for several power levels. So, at 20 kW/m there was a temperature increase on the cladding surface of 12 K, 28 kW/m generated an increase of 16.5 K. These rather small increases in temperature shall be treated as a ficticious increase of the coolant temperature. So the calculations will be performed with a coolant temperature of 334 °C.

● Radial porosity profile

In order to take into account a radial porosity profile even as a starting condition of a computer analysis, the input routine for the as-fabricated pellet porosity was changed for this special purpose. The porosity profile, as it is used for the actual analysis is shown in Fig. L3-2.

● Burnup influence on the thermal conductivity of the fuel

It is known that solid fission products in the fuel matrix decrease the thermal conductivity [L3-2], [L3-3]. These facts can be quantified as follows:

For 10% burnup and 1000 K there is a decrease in fuel temperature conductivity of 28%.

For 10% burnup and 2000 K the decrease in fuel thermal conductivity is 19%.

Based on these data a linear interpolation was done so that the influence of the solid fission products on the thermal conductivity of the fuel can be described as follows:

$$\lambda_{Bu} = \lambda \cdot [1.0 - FIMA \cdot (3.456 - 9.02 \cdot 10^{-4} \cdot T)] \tag{L3-10}$$

with

λ_{Bu}	= thermal conductivity with burnup correction
λ	= thermal conductivity without burnup correction
$FIMA$	= burnup
T	= fuel temperature [°C].

The relation (L3-10) shall be valid for temperatures ≤ 2000 °C. At higher temperatures the fission products more and more go into solution in the fuel matrix.

The above equation (L3-10) is implemented into the SATURN-FS code and here into the subroutine WLAMB, describing the thermal conductivity of the fuel. The expression is treated as an additional correction term.

$$f_{bu} = 1.0 - FIMA \cdot (3.456 - 9.02 \cdot 10^{-4} \cdot T)$$ (L3-11)

for $20\,°C \leq T \leq 2000\,°C : \lambda = \lambda_o \cdot f_{bu}$ (L3-12)

for $T > 2000\,°C: \lambda = \lambda_o$ (L3-13)

To show the effect of the burnup correction of the fuel thermal conductivity, Fig. L3-3 shows the fuel centerline temperatures for a typical FBR fuel pin with and without the correction term of the thermal conductivity. As anticipated, the temperature difference increases with increasing burnup and at about 7% burnup it amounts up to about 130 K.

L3.4   Results of Thermal Analysis

The results of the thermal analysis of the high-burnup LWR fuel pin are given as radial temperature profiles in Fig. L3-4. Besides the analysis for a linear power of 21 kW/m two more analyses were performed for higher (25 kW/m) and lower (15 kW/m) linear powers (see Fig. L3-4). So it is possible to estimate the influence of the power level on the actual temperature profile. Obviously, an increase in linear power for about 5 KW/m results in an increase of the centerline fuel temperature for about 200 K for the high-burnup pin considered here. For the average power level of 21 kW/m a fuel centerline temperature of 1175 °C was calculated. The 15 kW/m resulted in 910 °C and the 25 kW/m in 1389 °C. Table L3-2 lists the contributions of temperature raises which finally result in the fuel centerline temperature.

The lower temperature increase between cladding and fuel for 21 kW/m compared to 15 kW/m and 25 kW/m is caused by an improved heat transfer by reduction of the fuel-cladding gap.

The radial profiles of the fuel temperature show steep gradients in an outer ring with $r \geq 0.8 \cdot r_o$ (see Fig. L3-4). This is caused by the radial profiles of the porosity and of the power. While the high porosity in the outer ring (see Fig. L3-2) reduces

Table L3-2: Contributions of temperature raises resulting in the fuel centerline temperature

Linear power	[kW/m]	15	21	25
ΔT by heat transfer coolant-cladding	[K]	7	10	12
ΔT by zirconia layer	[K]	14	14	14
ΔT by heat conductance in the cladding	[K]	20	28	33
ΔT by heat transfer cladding-fuel	[K]	50	36	47
ΔT in the fuel	[K]	499	767	963

markedly the fuel thermal conductivity, it can be seen from the radial power distribution (see Fig. L3-1) that about 50% of the heat production also takes place in the outer fuel region.

L3.5 Summary and Conclusions

The analyses performed here with high burnup LWR pin fit well within the PIE-results [L3-1]. Furthermore the flexibility of the SATURN-FS code could be shown. As it was demonstrated, with SATURN-FS also problems can be analyzed, which are besides main field of application of this code.

References

[L3-1]   H. Kleykamp et al.
         Internal KfK-Report (1988)

[L3-2]   H. Kleykamp
         KfK Report No. 1245 (1970)

[L3-3]   H. Kleykamp
         J. Nucl. Mat. 131 (1985)221
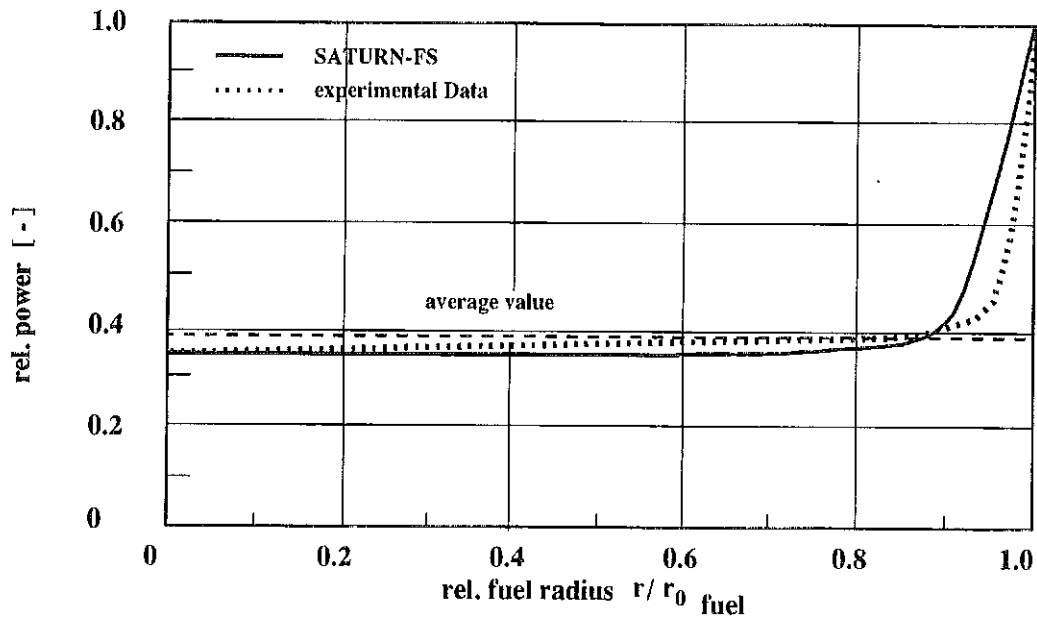
Fig. L3-1: Radial power profile in the fuel after 5,9 % burnup, experimentally determined by the Nd-distribution and calculated
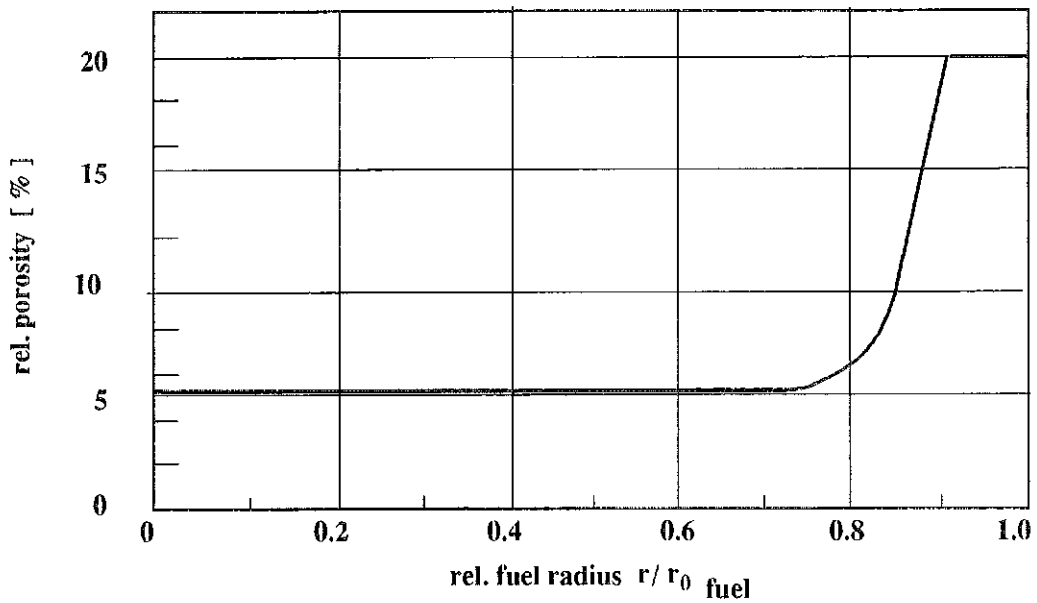
Fig. L3-2: Radial porosity profile in the fuel
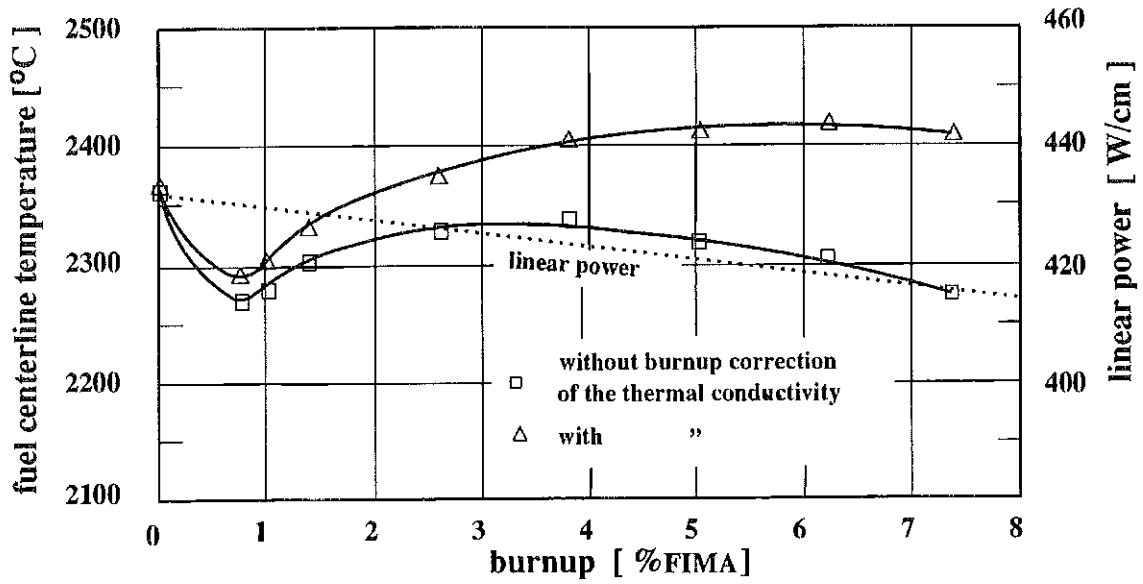
Fig. L3-3: Change of the fuel centerline temperature in an FBR pin by the influence of the thermal conductivity (Q = 430 W/cm)
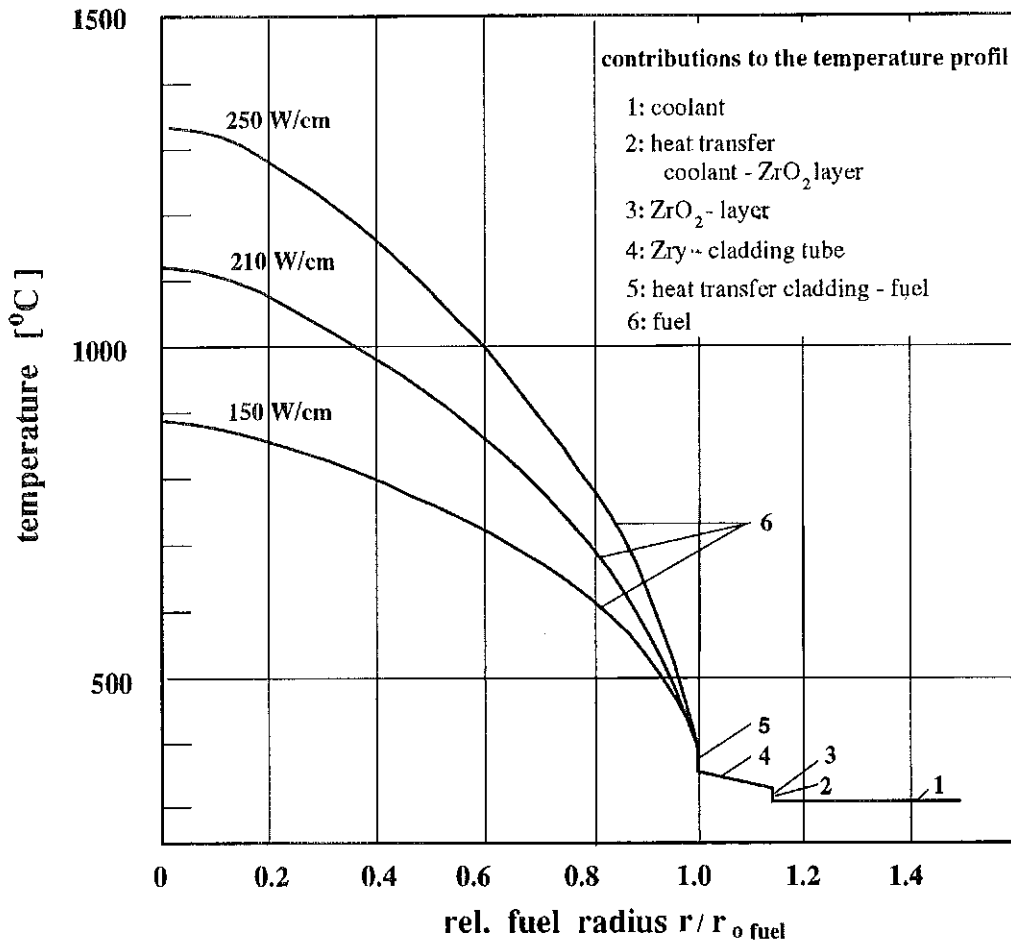
Fig. L3-4: Radial temperature profile in a high burnup LWR fuel pin at different linear power levels

L4. Designing the KNK II-TOAST Irradiation Experiment

L4.1 Introduction

The development of hypostoichiometric (U,Pu) mixed oxide fuels for Fast Breeder Reactors (FBRs) proceeded to the new fuel types of high density and - with respect to reprocessing - of good solubility [L4-1] - [L4-4]. During the last recent years investigations on structure and properties of these fuel types as well as modelling calculations of their operational behaviour have been performed.

In order to optimize the fabrication process of the fuel pins, aiming at a high quality product and reasonable fabrication efforts and, furthermore, to investigate the influence of extreme values of some important fuel pin design parameters, such as

-   fuel stoichiometry,
-   pellet diameter,
-   purity of the backfill gas, and
-   sintering atmosphere,

and their combinations on the operational behaviour of fuel pins, the TOAST irradiation experiment will be performed in the Karlsruhe KNK II reactor. The TOAST experiment - TOlerance Augmentation STudy - has the following main objectives:

-   To study the existing fuel specifications with respect to tolerable fabrication tolerances under the aspect of fabrication cost reduction.

-   To have an experimental proof of acceptable fabrication tolerances.

-   To reduce the effort of fabrication and quality control.

Furthermore, from a fuel modelling point of view, the design calculations, which had to be performed for the TOAST experiment, gave a nearly unique opportunity to get the computer code, which is used for the calculations, thoroughly tested. An analysis for a series of fuel pins with a field of different design parameters is carried out. This analysis has to prove that not only the result of one single modelled fuel pin type, but also the results of all calculated cases must be acceptable, and fit into a pattern, which can be interpreted considering the influence of the single parameters and their combinations.

L4.2   Design Aspects for the Irradiation Test

L4.2.1 Definition of the Test Parameters

The objective of the irradiation test is to show, that there may be allowable increase in the tolerances of certain fabrication parameters as compared with those which must be met due to current specifications.

The verification of this increase in production tolerances will lead to a reduction of the efforts needed in fabrication and in quality control procedures.

The parameters, taken into account in the irradiation experiment, are as follows:

- Pellet diameter
  Net shape sintering will claim for an enlargement of diameter tolerances. So there will be an investigation of two pellet versions, one with a 100 µm smaller and one with a 100 µm larger diameter compared with the nominal value of the current standard FBR pellet. This tolerance will sufficiently enclose the possible dimensional variations of the sintered pellets.

- Purity of the backfill gas
  The heat transport across the gap between fuel pellets and cladding is determined by the composition of the filling gas. In order to investigate the influence of the amount of impurities in the backfill gas, normally consisting of nearly pure He, the He-contents will be reduced from values $> 95\%$, as used as a standard, to a composition of 50 % He/50 % Ar in one of the experimental versions.

- Fuel stoichiometry
  Due to the fabrication process low-stoichiometry fuel can be fabricated, with O/M ratios markedly below the reference value of 1.97. So it will make sense to fabricate and to investigate an experimental fuel version with a very low O/M-ratio of 1.93. This will result in a clear reduction of the fuel thermal conductivity.

Out of all possible combinations of the above mentioned parameters those combinations were selected, which are anticipated to give the most interesting results regarding the thermal fuel pin behaviour, i.e. fuel temperatures and structures, as well as the mechanical behaviour, e.g. cladding stresses and strains. The test matrix of the irradiation experiment is shown in Table L4-1.

Table L4-1: Irradiation test matrix

Pin type	Fuel diameter	O/M-ratio	Backfill gas
P1 S1 F1	d - 100 µm	1.93	> 95 % He
P1 S1 F2	"	1.93	50 % He/50 % Ar
P1 S2 F1	"	1.97	> 95 % He
P1 S2 F2	"	1.97	50 % He/50 % Ar
P2 S1 F1	d + 100 µm	1.93	> 95 % He
P2 S1 F2	"	1.93	50 % He/50 % Ar
P2 S2 F1	"	1.97	> 95 % He
P2 S2 F2	"	1.97	50 % He/50 % Ar

d = 6.37 mm

The names of the pin types, as given in Table L4-1 and as used further in the report, refer to their characteristics as follows: the letter P characterizes the pellet, P1 is the small-diameter, P2 is the large-diameter pellet. S means Sintering, S1 is sintering to low, S2 is sintering to the higher oxygen-to-metal ratio. F describes the Fill gas in the pin, F1 is the low fill gas contamination (i.e. 10 % Ar, 90 % He) and F2 the high fill gas contamination (50 % Ar, 50 % He).

L4.2.2 Experimental Description

The TOAST experiment was planned to be performed in the 3rd core of the KNK II-reactor. A special ring fuel assembly [L4-5] should be mounted into the reactor core, see Fig. L4-1, carrying a 19-pin reloadable subassembly in its center, as it is shown in Fig. L4-2, making it possible to perform the TOAST-irradiation as a two-step experiment. The first 19-pin subassembly was to be inserted to study the fuel pin behaviour at the beginning of irradiation (BOL). The irradiation time for this "BOL-bundle" was planned to be about 70 equivalent full power days (EFPDs).

After the removal of the BOL-bundle, the second part of the experiment should be run. Plannesd as a long-time irradiation, another 19-pin subassembly, the "EOL-bundle", should stay in the reactor for 650 EFPDs or up to about 6 - 7 % burnup, so giving information on the behaviour of the test fuel pins during medium to high burnups.

L4.2.3 Design Criteria

The design and licensing procedure of the irradiation experiment was done according to the general licensing path as used for normal power reactor fuel elements. Regarding the fuel pin, it must be shown by the design calculations that several criteria concerning the operational safety are met. The most important criteria are:

- It must be shown that no fuel melting will occur during operation, The melting temperature of U,Pu-mixed oxides depends on Pu-content, O/M-ratio and on the content of soluble fission product phases in the fuel matrix [L4-6] - [L4-10]. The latter effect is mainly governed by burnup. It is required that the highest possible fuel temperature is sufficiently lower than the solidus temperature. Concerning, for example, the fuel with an O/M-ratio of 1.93, the solidus temperature for fresh fuel is about 2660 °C, which is reduced during irradiation down to about 2600 °C.

- It has to be shown that no cladding failure will occur during irradiation. This means that safety margins concerning cladding stresses and strains have to be met, for steady state irradiation as well as for defined instationary states, such as startup ramps, cyclic loading, overpower ramps etc. as they are anticipated during normal operation.

L4.3 Operation Conditions

L4.3.1 Steady State Operation

The axial power profile for the TOAST-pins as well as the axial coolant profile under reactor nominal conditions are shown in Fig. L4-3. Maximum linear powers, burnups and temperatures for the fuel pins in the BOL- and EOL-bundle are given in Table L4-2. Due to reactor core characteristics, the linear power values are somewhat higher when the BOL bundle is replaced after 70 EFPDs by the EOL-bundle. Furthermore, the fuel pins containing the large diameter pellets show an about 6 % higher linear power than the pins with the small diameter fuel, the values of the latter are given in brackets in Table L4-2. During irradiation the power decreases slightly. The power values representing the end of the irradiation for each bundle are also given in Table L4-2. As can be seen there is nearly no decrease of power for the BOL-bundle, whereas in the EOL-bundle the linear power decreases for about 4 % during operation.

Table L4-2: Operation conditions (nominal)

	BOL-bundle		EOL-bundle	
	0 EFPDs	70 EFPDs	0 EFPDs	650 EFPDs
Max. Linear Power (W/cm) Burnup (MWd/kgM) Neutron Dose (dpa)	426 (400) 0 0	425 (399) 10 5	432 (406) 0 0	414 (390) 86 (84) 41
Coolant - Inlet Temperature (°C) - Outlet-Temperature (°C)	360 606	360 606	360 606	360 607
Cladding Midwall Temperature (°C)	620	620	623	621

Taking into account the statistical analysis of uncertainty with respect to local linear power and coolant temperature, power and coolant temperature values can be calculated, which represent the "worst case" or "design" conditions. It has to be shown by the design calculations that even under these assumptions the fuel pins would not fail. The characteristic data for the power history under design conditions are shown in Table L4-3 for the fuel pins in the EOL-bundle, having the

Table L4-3: Operation conditions (worst case) for EOL-bundle

Pellet Diameter		6.27 mm		6.47 mm	
Irradiation time (EFPDs) Max. linear power (W/cm) Burnup (MWd/kgM)		0 448 0	650 432 94	0 476 0	650 460 96
Coolant -Inlet temperature (°C) - Outlet temperature (°C)		360 666	360 666	360 666	360 666
Cladding Midwall temperature (°C)		685	685	685	685

higher power of the two bundles. Also, the different data are shown for the pin types with different fuel diameters. It can be seen that the maximum linear power for the types with large diameter fuel is 476 W/cm. This is a 10 % higher power than under nominal conditions and represents a margin of 2.6 σ. (σ is the standard deviation for the uncertainty of local power.)

The design condition for the coolant temperature profile is defined by assuming that the maximum tolerable cladding midwall temperatures of 685 °C will be reached at the upper end of the fissile column. This assumption represents a margin of more than 4 σ (σ is the standard deviation for the uncertainty of the coolant temperature.)

L4.3.2 Operational Transients

Besides the steady state operation, power ramps and overpower transients have to be taken into account within the frame of the design calculations. It has to be shown that the fuel pins would not fail during these design transients.

In detail, the following transient operation conditions have to be analyzed:

- The startup ramp

    During startup the fuel pin is ramped slowly to nominal power with several conditioning steps, in order to get a reduction of early stress peaks, the growth of the central void and fuel restructuring.

- Ramp after low power operation at EOL

    At EOL a low power operation period of 30 days at 30 % power has to be taken into consideration, followed by a stepwise ramp up to nominal power. The ramp rate is 10 % per minute up to 60 % power, then 1 % per minute up to 85 %, followed by a conditioning step at this power level. Then the fuel pin is ramped up to nominal power with a ramp rate of 1 % per minute.

- Overpower ramp

    At BOL and at EOL a 100 % to 112 % overpower ramp has to be modelled with a ramp rate of 1 % per second.

L4.4   Results of the Analyses

L4.4.1 Thermal Analysis

- Thermal behaviour under nominal conditions

The nominal power history, including the steady state operation and the 12 % overpower ramps at BOL and EOL, is given in Fig. L4-4. This power history represents the peak power nodes of the fuel pins. In the following, the presentation of the influence of the design parameters on fuel pin behaviour and the comparison

of the different fuel types will mainly be limited to the consideration of the peak power nodes as this is generally the most interesting part of the fuel pin.

Influence of the fuel diameter

The influence of the different pellet diameters on fuel centerline and surface temperatures can be seen by comparing Figs. L4-5 and L4-6. So, the pin types, which have initially the smaller pellet diameter, have generally lower temperatures than the other ones. This is caused mainly by the facts that the larger diameter leads to a higher linear power and may show less radial relocation, a smaller central void and so higher centerline temperatures. The comparison of the fuel surface temperatures for the pins with small-diameter (P1-types) and large-diameter fuel (P2-types) (see Figs. L4-5 and L4-6), demonstrates that at BOL the fuel with the larger diameter shows lower surface temperatures. This is because of the smaller gap between fuel and cladding which leads to an increased gap conductance.

Referring to the gap conductance, it can clearly be seen from Fig. L4-7 that in the first part of the irradiation time there is an increase of the gap conductance for the pin types containing the fuel with small diameter (P1-types), whereas the versions with the large-diameter fuel (P2-types) start at high gap conductance values, but they show a fast decrease.

Influence of the backfill gas

The reduction of the He-amount in the backfill gas from 90 % to 50 % results in an increase of the fuel surface temperature of about 6 %, see Figs. L4-5 and L4-6. For longer irradiation times the different amount of He in the backfill gas is the only reason for the differences between all the 8 versions investigated in the current study, concerning the gap conductance (Fig. L4-7).

And, as can also be seen from Fig. L4-7, the influence of the initial backfill gas composition on the gap conductance clearly diminishes up to the end of irradiation.

The comparison of the curves in Figs. L4-5 and L4-6 demonstrates, that there is generally no major influence of the backfill gas composition on the fuel centerline temperatures for the P1-versions at irradiation times longer than about 100 EFPDs. But a major influence exists for the P2-versions, containing the pellets with the large diameter.

Influence of the fabrication stoichiometry

The influence of the fabrication stoichiometry on the fuel centerline temperature is shown in Fig. L4-5 for the P1 pins with small-diameter fuel and in Fig. L4-6 for the P2 types with large-diameter fuel. These figures show that the low O/M ratio results in an increase of the fuel centerline temperature of about 8 %. The shift of the radial O/M profiles for both cases during operation is given, for example, in Fig. L4-8 for the P1 types with small-diameter fuel. The general increase of the O/M ratio during irradiation can clearly be seen as well as some saturation effects in the cold outer fuel zones of the S2 pins with high-O/M fuel at late-in-life operation.

There is also an influence of the initial O/M ratio on the radial Pu-profile. Presumably this could be a more indirect effect, which is controlled by different radial temperature profiles. In Fig. L4-9 two radial Pu-profiles, for fuel with high and low initial stoichiometry are plotted versus the irradiation time.

As expected, the fuel with low initial stoichiometry, which has higher temperatures and higher temperature gradients, also shows the steeper gradients in the radial Pu-profile and the higher enrichment at the central void.

● Thermal behaviour under design conditions

The power history at the peak power nodes for the design or "worst case" conditions is given in Fig. L4-10 for the pins with the two different fuel diameters. Only the pin versions P1S1F2 and P2S1F2 will be considered unter the design conditions. They both represent the fuel with low stoichiometry and the pins with only 50 % He in the backfill gas and differ only by the pellet diameter. For nominal conditions these versions showed the highest temperatures for their diameter class.

The results of the analyses of the fuel centerline and surface temperatures during the irradiation time of these two cases are shown in Fig. L4-11. It can clearly be seen, that, similar as for nominal conditions, the pin type which contains the large diameter fuel has the higher temperatures. The difference in the centerline temperature is about 8 %. Whereas a steep temperature drop appears after completion of the startup ramp at BOL for the P1-version with the small-diameter fuel, the P2-version, containing the large diameter fuel, does nearly not show this effect. As the gap is already closed during the startup ramp for the P2-version, the

temperature tends to increase from the beginning of the full power operation. For the pin type with the large fuel diameter the highest centerline temperature, about 2500 °C is calculated at EOL. A comparison with the fuel solidus temperature for the same burnup, which lies at about 2600 °C, shows that the analyzed maximum fuel temperature is well below the melting region.

The radial temperature profiles of the fuel pins at BOL (Fig. L4-12) and at EOL after 650 EFPDs (Fig. L4-13) demonstrate that at BOL the surface temperature of the P1-version is higher than that of the P2-version, because the gap is not yet closed for the P1-version. In spite of this effect the centerline temperature of the P1-version is lower than that of the P2-type, caused by a larger central void and a lower linear power. At EOL, the fuel surface conditions are nearly the same for both cases, caused by gap closure for the small diameter fuel as well as by Xe- and Kr-poisoning of the gas mixture in the gap. And as the difference of the central voids of the two versions is less pronounced at EOL than at BOL, the generally higher fuel temperature of the P2-version can be related to the higher power and the different O/M- and U/Pu-redistribution effects, as already mentioned, when considering nominal irradiation conditions.

L.4.4.2 Mechanical Analysis

● Mechanical behaviour under nominal conditions

Contact pressure and generalized cladding stress

Mainly, two representative fuel pin types will be presented and discussed here, the type P1S1F2 for the pins with small-diameter fuel, and the type P2S1F2 for those with large-diameter fuel.

They both show the highest thermal loads for their diameter class, see Figs. L4-5 and L4-6. The mechanical loads on the cladding are rather similar within each diameter class. It is obvious, and the calculations show, that the large-diameter version causes higher stresses than the small-diameter version. During irradiation, there is a change in the axial location of the maximum generealized cladding stress, see Fig. L4-14. At BOL the stress peaks coincide roughly with peak power, but at EOL there is a clear stress maximum at the lower end of the fuel column, where stresses cannot be reduced due to the rather low cladding temperature.

It should be mentioned that the axial stress profiles, shown in Fig. L4-14, are calculated without running the 12 %-overpower ramp after 5 EFPDs.

The change of generalized cladding stress during the irradiation will be discussed for the peak power position, allowing comparison to the thermal analysis.

The greatest difference in the mechanical behaviour of the two pin versions considered is the onset and the amount of the contact pressure. Fig. L4-15 represents the calculated values for the contact pressure between fuel and cladding for the pin versions P1S1F2 and P2S1F2 for nominal operation conditions with and without the 12 %-overpower ramp after 5 EFPDs. Referring to the power history without the overpower ramp, the pin type with the small-diameter fuel has no contact pressure before about 250 EFPDs, whereas the maximum contact pressure for the large-diameter fuel occurs just after the startup ramp. This value is reduced within short time because of creep effects. After reaching the minimum, the contact pressure increases again caused by fuel swelling effects. The increase rates are nearly the same for both diameter types.

Concerning the overpower ramp early in life irreversible mechanisms occur (Fig. L4-15) in the small-diameter and the large-diameter fuel. They lead for the P1S1F2 fuel pin type to an earlier onset of contact and for the P2S1F2 version to a contact pressure which is about twice as high as without the overpower ramp. Similar to the contact pressure is the development of the generalized cladding stress during irradiation time, see Fig. L4-16. Apparently, the large-diameter types have the higher stresses, the slopes of which after the minimum at about 100 EFPDs are parallel to that for the small-diameter versions. The general result is that the highest cladding stresses are generated in the P2S1F2-pin version, which also undergoes the highest thermal loads.

The increase of the cladding stress during operation is caused by fuel swelling and the buildup of fission gas pressure. The peak stresses for all fuel pin types occur during the 12 %-overpower ramp at EOL, but the calculated stress values lie well below tolerable values. The yield stress for the cladding material at the present conditions is about 500 MPa.

Tangential cladding stress

Interesting aspects follow from the evaluation of the cladding tangential stress distribution across the wall thickness and its change during irradiation, as given in Figs. L4-17 and L4-18. Fig. L4-17 shows the stress distribution for the first 50 days at full power. During this time, the tangential stress distribution is deter-

mined by thermal stresses, negative at the cladding inner surface and positive at the outer surface. For the large-diameter (P2) version, a contact stress component is added to the symmetric stress pattern with the neutral zone in the mid of the cladding, as it was calculated for the small-diameter (P1) version. Further development of the tangential stress pattern at higher irradiation time reveals a transition from the thermal stress configuration to a pressure vessel stress distribution, with tangential stresses all positive, the maximum values being at the inner cladding surface. This development is made visible in Fig. L4-18. The change in the stress distribution is caused by the reduction of initially existent thermal stresses by creep effects and later on by the buildup of fission gas and contact pressure. Comparing the radial profiles of the tangential stresses for all 8 fuel pin types just after completion of the startup ramp, it can be demonstrated (see Fig. L4-19) that 7 of the 8 versions exhibit nearly similar profiles. Only the version P2S1F2 has remarkably higher stresses. Nevertheless, the slopes of the stress profiles are nearly the same for all 8 pin types.

Stresses induced during ramp-up at EOL

After a 30 day operation at a 30 % power level at EOL an increased mechanical interaction between fuel and cladding (PCI) occurs during ramp-up to nominal power. For short times peak stresses of about 150 MPa for the P1S1F2 version and of 250 MPa for the P2S1F2 version (see Fig. L4-20) are reached. But even these values, representing the highest stress loads calculated during the whole analysis, lie well below tolerable values.

●   Mechanical behaviour under design conditions

The axial profiles of the generalized cladding stresses under design conditions at BOL just after completion of the startup ramp and after 5 EFPDs as well as at EOL after 650 EFPDs are shown in Figs. L4-21 and L4-22. The stresses at BOL do not differ significantly from those calculated for nominal conditions. Also, the axial locations for the peak stresses coincide again with the peak power node. Significantly different stresses have been calculated for EOL conditions. Not only the absolute stress values are lower for design conditions than for nominal conditions, but also the shapes of the axial profiles are different. Under design conditions the stress maximum coincides with the power maximum in contrast to nominal conditions. The reason for this and the generally lower stress values is the fact, that at the higher coolant temperatures as they exist under design conditions, thermally

activated processes, such as creep and stress relaxation, can proceed faster result-ing in stress reduction.

L4.5   Considering the Reliability of the Calculated Results

Based on irradiation experience and literature data, the linear power, which causes fuel melting, can be determined by evaluation of the fuel conductivity inte-gral up to melting [L4-11, L4-12].

$$Q_{melt} = \frac{4\pi}{F} \cdot \int k dT \tag{L4-1}$$

with

$\int k dT$ $=$ conductivity integral up to melting in W/cm

$F =$ geometry factor, depending on pellet inner and outer radius

$Q_{melt} =$ power-to-melt in W/cm.

The $\int$kdT-values are hereby known from the material data base, see e.g. [L4-13, L4-14].

Using this method, the power-to-melt values for the P1S1F2 version have been de-termined for BOL and EOL (Table L4-4). They are 633 W/cm at BOL and 559

Table L4-4:   Fuel melting criterion and max. tolerable power

		P1 S1 F2		P2 S1 F2	
		BOL	EOL	BOL	EOL
Power to melt	(W/cm)	633	559	590	521
Max. tolerable power	(W/cm)	565	499	527	465
Max. linear power	(W/cm)	406	390	432	414
3 σ-confidence of uncertainty		1.13	1.14	1.13	1.14
Confidence level		> 8 σ	> 6 σ	4.9 σ	2.7 σ
Confidence level	(%)	> 99.9	> 99.9	> 99.9	99.65

W/cm at EOL. The P2S1F2 type values are 590 W/cm at BOL and 521 W/cm at EOL. In Table 4 also the maximum tolerable power levels, which are set 12 % be-low the melt limit, are presented. The comparison of these levels with the maxi-mum nominal linear power levels demonstrates, based on the results of the statis-tical analysis of the uncertainty of the linear power, that melting of the TOAST pins is excluded with a high confidence level.

In order to test the results of the design calculations done so far with the SATURN-FS code, a "fuel melt" calculation was performed for the two pin types mentioned above. For this analysis the following conditions were used: after the normal TOAST startup ramp an additional very slow ramp was run. The ramp rate was as slow as 10 W/(cm·h) up to high power levels. Comparison with the solidus temperatures from the materials data base showed, that the P1S1F2 pin type reached the solidus temperature at 630 W/cm and the P2S1F2 type at 590 W/cm (see Fig. L4-23). Comparing these results to those of the ∫kdT-method gives a very good agreement (see also Table L4-4).

In addition several characteristic events can be identified from Fig. L4-23. The holding time during the startup ramp is accompanied by a temperature decrease of the pin type with the small-diameter fuel, but not with that containing the large-diameter fuel, as this has already closed the gap at a lower power level. After completion of the startup ramp, the temperature decreases slightly for the P1S1F2 version, also caused by gap closure. Hard contact between fuel and cladding occurs already during the startup ramp for the P2S1F2 pin type, but not before about 600 W/cm for he P1S1F2 pin version.

L4.6 Conclusions

A fuel modelling study was performed as part of the designing and licensing phase of an irradiation experiment. The objectives of this experiment are to investigate the influence of extended tolerances of certain fabrication parameters on the operational behaviour of FBR fuel pins. The investigated parameters are the pellet diameter, the O/M-ratio of the fuel, and the composition of the backfill gas.

The calculations yielded the following results:
The thermal performance of the fuel pin is influenced by the composition of the backfill gas via the gap conductance. The reduction of the He-content in the backfill gas from 95 % down to 50 % results in an about 12 % reduction of the gap conductance. The difference in gap conductance between high- and low-He-containing pins becomes smaller during irradiation by fission gas release.

The reduction of the O/M-ratio from the 1.97 standard value down to 1.93 will cause a deterioration of the fuel thermal conductivity and, so, lead to higher fuel centerline temperatures. In the analyzed case the temperature increase was about 8 %. Another parameter, which causes higher fuel centerline temperature is the increase of the pellet diameter. Although there is an early gap closure and an im-

proved heat transfer from the pellet to the cladding, leading to a temperature decrease, this effect is more than counterbalanced by the following mechanisms:

- Early gap closure results in a cold outer pellet ring, hindering pore migration and crack healing. Radial fuel relocation is also less than for "large gap" pins. This results in a smaller central void accompanied by higher centerline temperatures.

- Larger pellet diameters result in higher linear power provided that the neutron flux is unchanged.

The combination of the parameter variations can partially lead to the compensation or even an inversion of the single effects. This fact, e.g., exists when the small diameter is combined with high O/M (= good thermal conductivity) and 95 % He in the gap (= good gap conductance). In this case, at start of operation, fuel restructuring and relocation will not take place to the same amount as for the "hotter" fuel of other combinations. The fuel temperatures in this case will, for a certain time, exceed those of the others, until the restructuring and relocation phase will be completed. Generally, the highest fuel centerline temperature is reached with the combination of fuel with low O/M-ratio, large diameter and only 50 % He in the backfill gas. However, the maximum fuel temperature lies well below the melting region.

The mechanical performance of the fuel pin variations studied here is mainly influenced by the pellet diameter. The pin type with large-diameter fuel has considerably higher cladding stresses. Peak stresses occurring at the start of steady-state operation, just after completion of the startup ramp, are quickly reduced. A stress increase occurring at higher burnups can be related to contact and fission gas pressure buildup. The pin version with "large diameter/low O/M-" fuel and 50 % He in the backfill gas has the highest cladding stresses, but even these are still far below any safety limits.

Regarding the influence of the combination of all the investigated fabrication parameters and their changes, the conclusion can be drawn that the fabrication standards for FBR fuel pins may be reduced within the limits treated in the modelling study without a deterioration of the operational behaviour.

The following statements, concerning the application of the SATURN-FS code can be made:

- The results, which were gained for the analyzed fuel pin versions are consistent.

- The calculated power-to-melt is in good agreement with the values deduced by the $\int kdT$-method.

References:

[L4-1]   P. Funke, H. Roepenack, W. Stoll:
          Atomenergie-Kerntechnik 36 (1980) 253

[L4-2]   H. Roepenack:
          Jahrestagung Kerntechnik 1981, Berichtsband zur Fachsitzung
          "Brennelemente und Brennelementwerkstoffe"

[L4-3]   D. Hanus, J. Krellmann, R. Löb:
          Jahrestagung Kerntechnik 1982, 377

[L4-4]   H. Roepenack:
          Atomwirtschaft, März 1983, 143

[L4-5]   H.E. Häfner, E. Bojarsky:
          KfK-Report No. 4141 (1986)

[L4-6]   M.F. Lyons et al.:
          Nuclear Eng. and Design, 21 (1972) 167

[L4-7]   W. L. Lyon and W.E. Baily:
          J. Nucl. Mat., 22, (1967) 332

[L4-8]   E.A. Aitken, S.K. Evans:
          GEAP-5672 /1968)

[L4-9]   J.L. Krankota, C.N. Craig:
          Trans. Am. Nucl. Soc. 11 (1968), 132

[L4-10]   H. Kleykamp:
          J. Nucl. Mat. 131 (1985) 221

[L4-11]   J.A.L. Robertson:
          AECL-807, 1959

[L4-12]   M.F. Lyons et al.:
          GEAP-5591, 1968

[L4-13]   M.F. Lyons et al.:
          Nucl. Eng. & Design 21 (1972) 16

[L4-14]   D.L. Hagrman, G.A. Reyman Eds.:
          NUREG/CR-0497, TREE 1280,1979

Ring element head

Coolant mixing device

Test bundle head

Test bundle

Ring element

Ring element foot

Test bundle foot

Ring fuel element:

outer width across flats, outer wrapper	122.75 mm
inner width across flats, inner wrapper	62.45 mm
number of fuel pins, Dia. 7.6 mm	102

Test bundle:

outer width across flats of wrapper	44.24 mm
number of fuel pins, Dia. 7.6 mm	19

Fig. I.4-1: KNK II fuel element
with reloadable subassembly

Fig. I.4-2: Ring fuel element with
TOAST test bundle for
KNK II
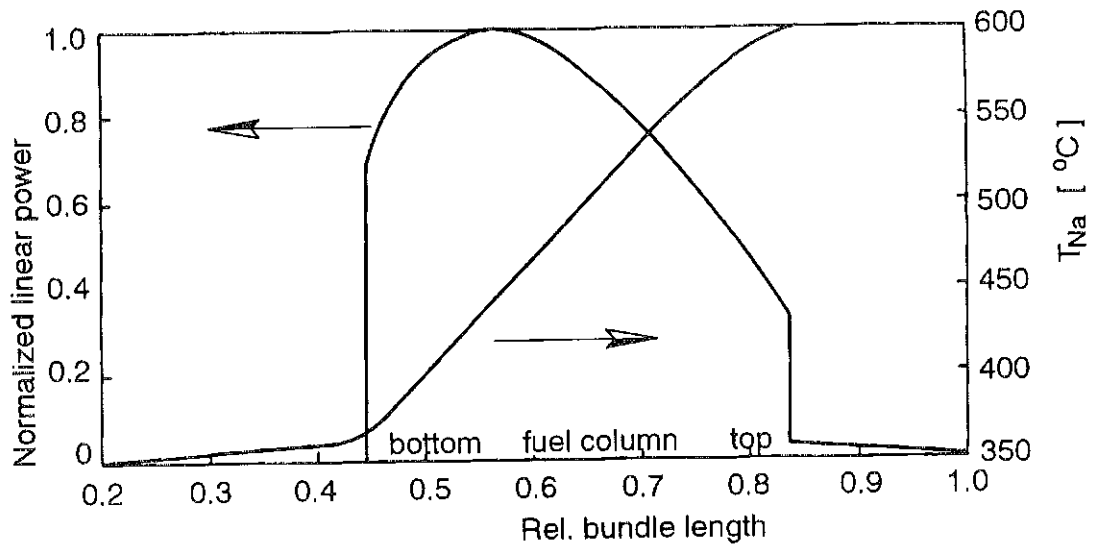
Fig. I.4-3: Relative axial power profile and coolant heatup rate for nominal
operation conditions for the TOAST element in the KNK II reactor
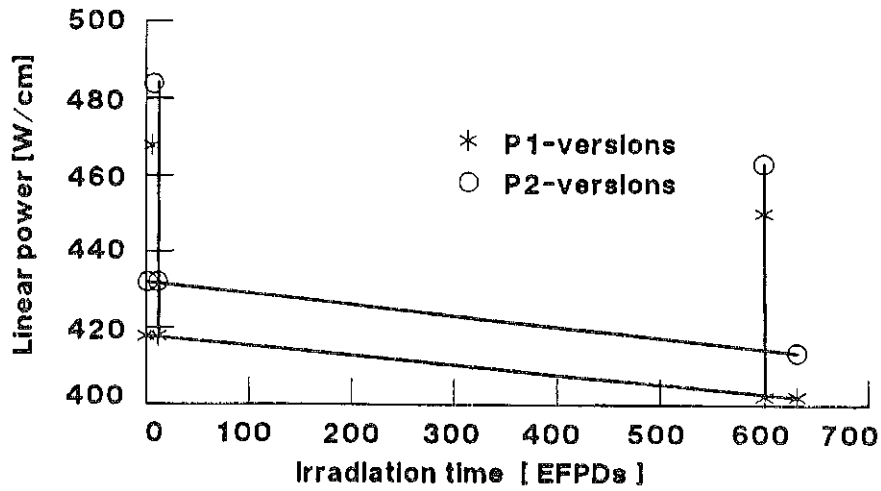
Fig. I.4-4:   Power history for the TOAST fuel pins under nominal conditions
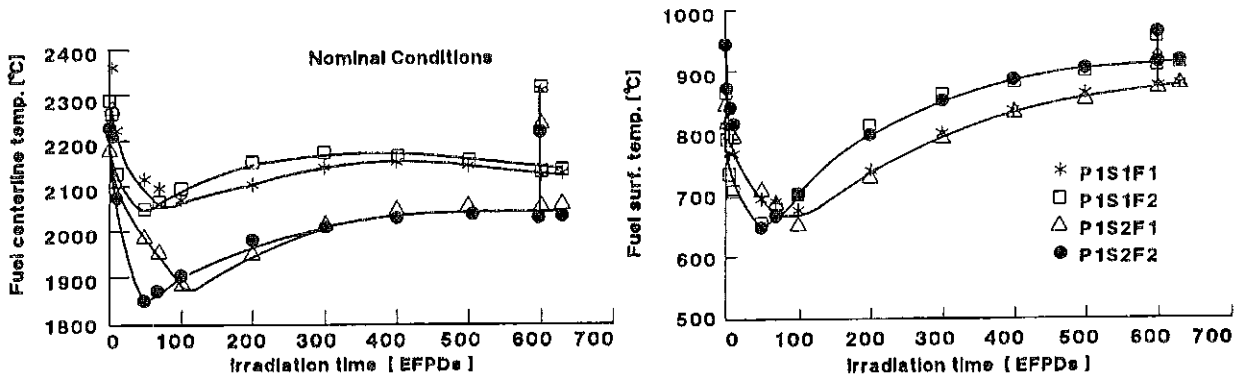
Fig. I.4-5:   Fuel centerline and surface temperatures vs. irradiation time in
              equivalent full power days (EFPDs) for the pin types with small
              diameter pellets (P1-types) under nominal conditions
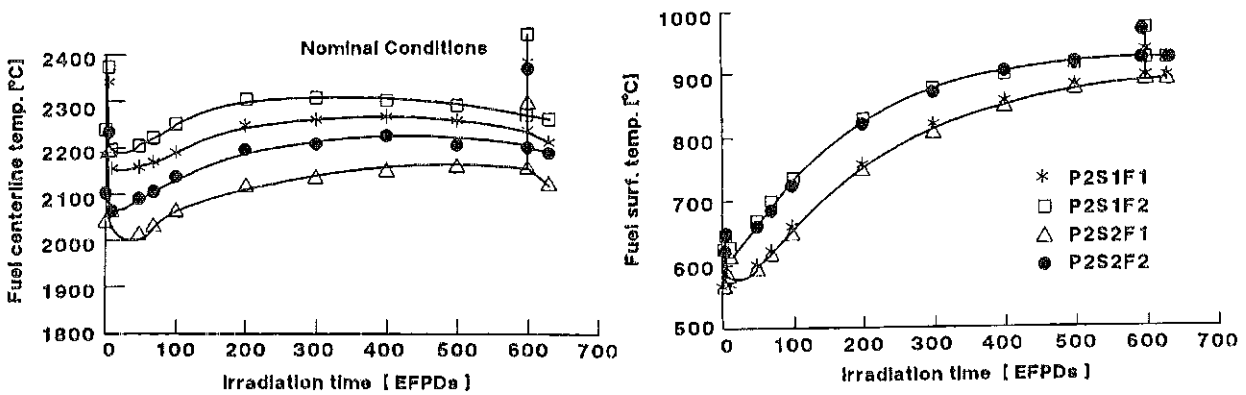
Fig. I.4-6:   Fuel centerline and surface temperatures vs. irradiation time in
              equivalent full power days (EFPDs) for the pin types with large
              diameter pellets (P2-types) under nominal conditions
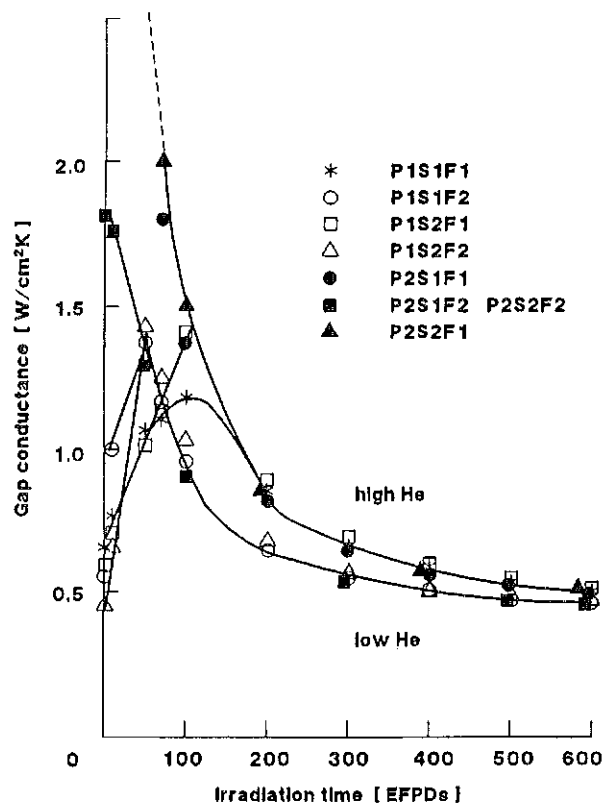
Fig. I.4-7: Gap conductance for the various test pins vs. irradiation time in equivalent full power days (EFPDs)
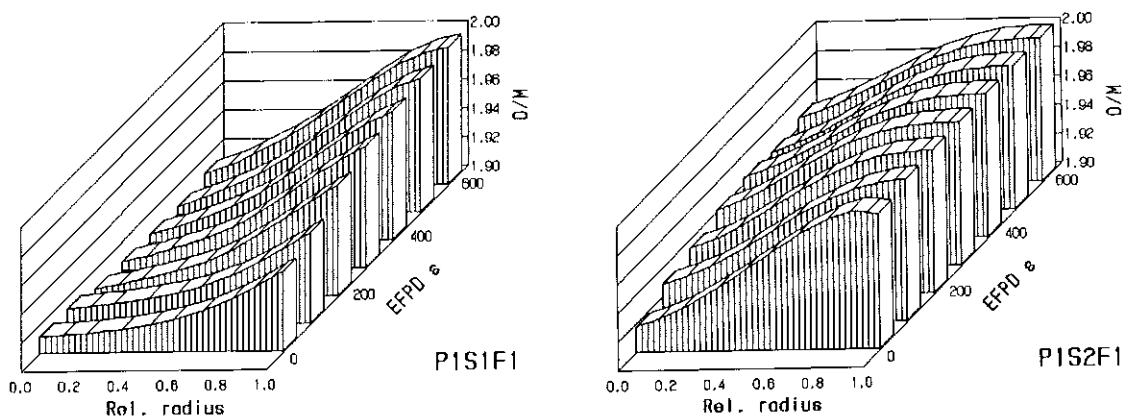
Fig. I.4-8: Shift of radial oxygen-to-metal (O/M)-profiles for fuel pellets with low (S1, top) and high (S2, bottom) initial O/M ratio vs. irradiation time in equivalent full power days (EFPDs)
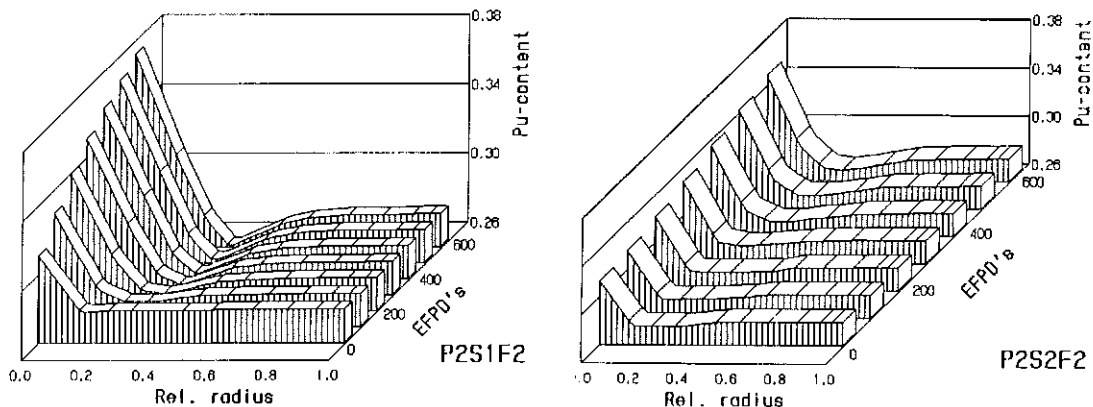
Fig. L4-9: Shift of radial Pu-content for fuel pellets with low (S1, top) and high (S2, bottom) initial O/M ratio vs. irradiation time in equivalent full power days (EFPDs)
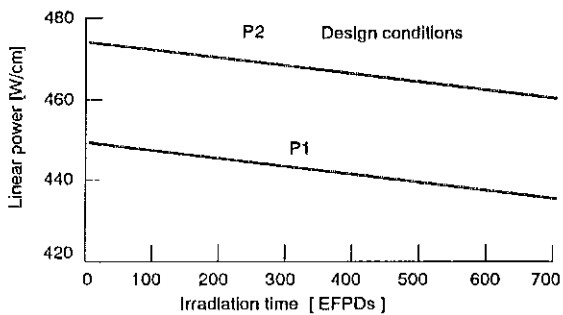
Fig. L4-10: Power history for the TOAST fuel pins under design conditions
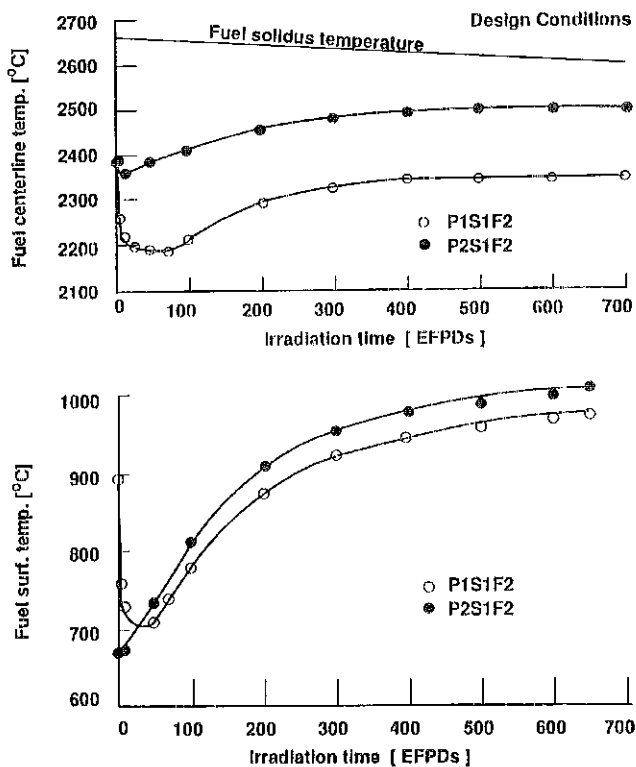
Fig. L4-11: Fuel centerline and surface temperatures vs. irradiation time in equivalent full power days (EPDs) for the P1S1F2 and P2S1F2 pin versions under design conditions
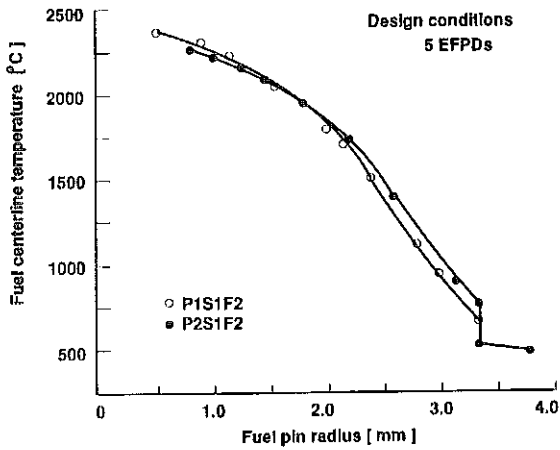
Fig. I.4-12: Radial temperature profiles for the pin versions P1S1F2 and P2S1F2 at BOL after 5 EFPDs under design conditions
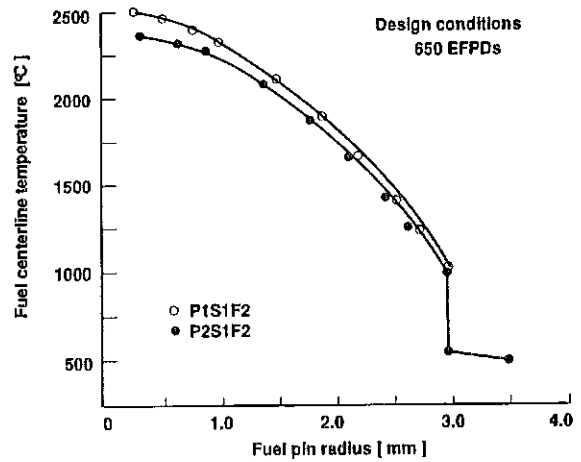
Fig. I.4-13: Radial temperature profiles for the pin versions P1S1F2 and P2S1F2 at EOL after 650 EFPDs under design conditions
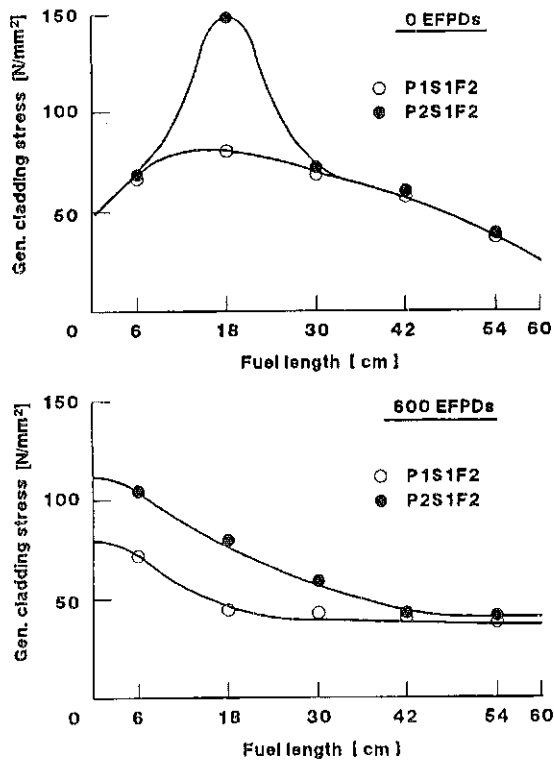
Fig. I.4-14: Axial profiles of generalized cladding stress at beginning of life (BOL) and end of life (EOL) for the "small and large fuel diameter" versions under nominal conditions
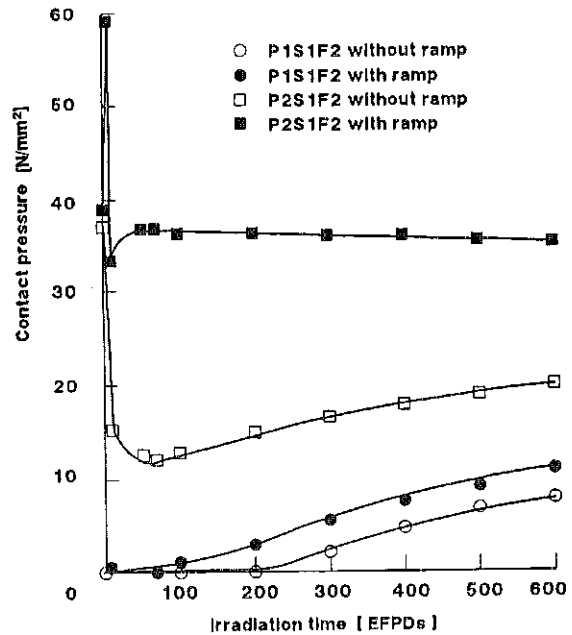
Fig. I.4-15: Contact pressure between fuel and cladding vs. irradiation time in equivalent full power days (EFPDs) with and without the BOL overpower ramp under nominal conditions
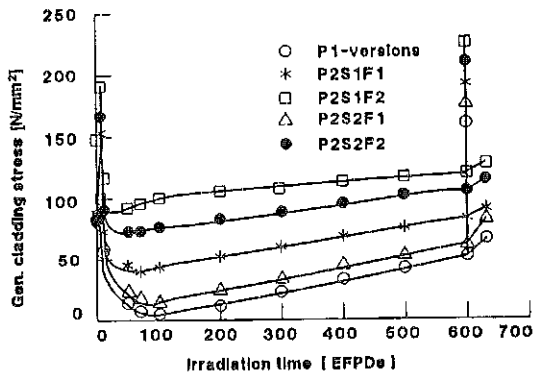
Fig. L4-16: Generalized cladding
stresses for pins with small
and large diameter fuel vs.
irradiation time in equivalent
full power days (EFPDs) under
nominal conditions
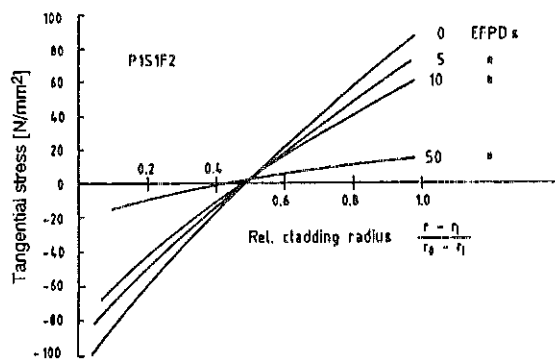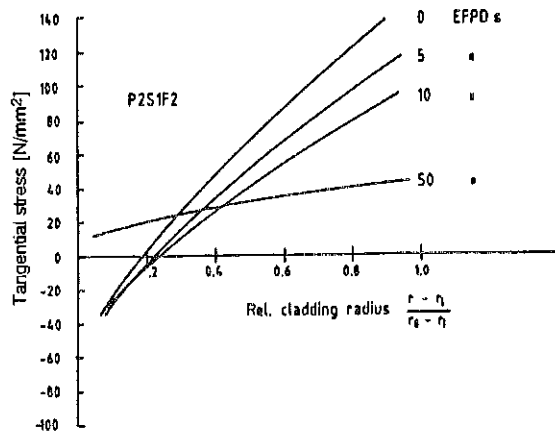
Fig. L4-17: Distribution of tangential
stress across the cladding
wall thickness for the first
50 days at full power for the
P1S1F2 (top) and P2S1F2
pin version (bottom)
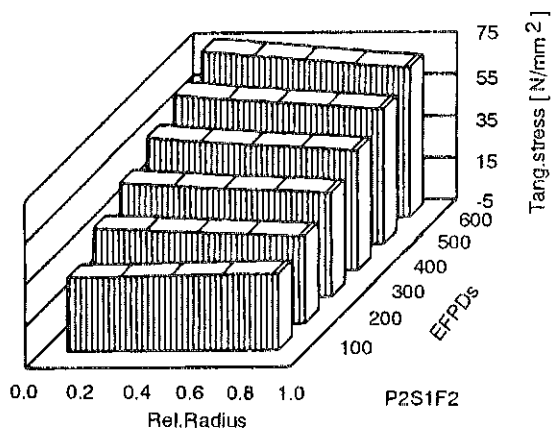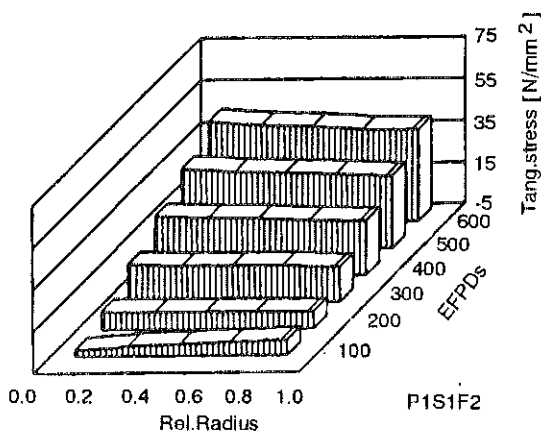
Fig. L4-18: Tangential stress pattern across the cladding wall thickness vs.
irradiation time in equivalent full power days (EFPDs) for the
P1S1F2(left) and P2S1F2 pin version (right)
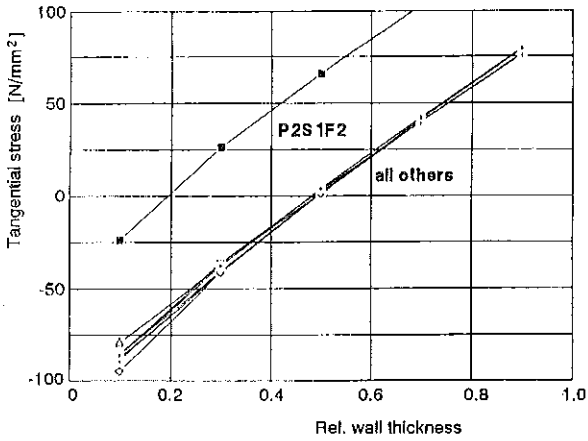
Fig. L4-19: Tangential stress pattern across the cladding wall thickness after completion of the startup ramp for the P2S1F2 pin version (top curve) and all other TOAST pin versions (lower curve), calculated for nominal conditions
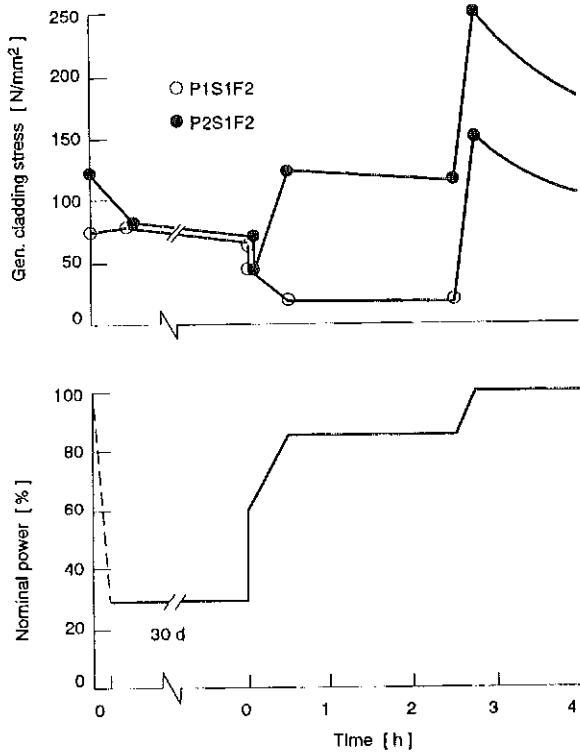
Fig. L4-20: Generalized cladding stresses and power ramp design for the P1S1F2 and P2S1F2 pin versions, calculated for an EOL ramp up after a 30 day low power operation
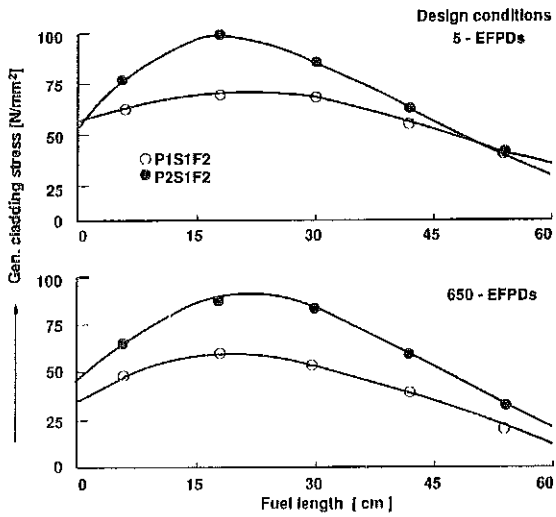
Fig. L4-22: Axial profiles of generalized cladding stress at BOL after 5 equivalent full power days (EFPDs) (top) and at EOL after 650 EFPDs (bottom) for the P1S1F2 and P2S1F2 pin versions under design conditions
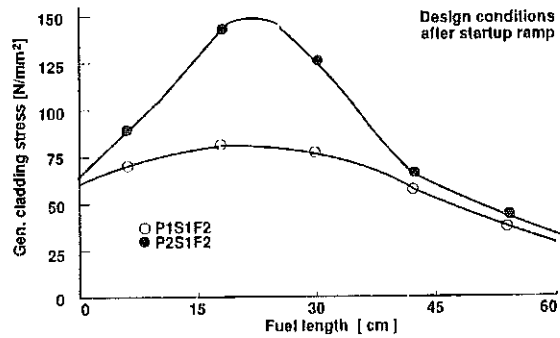
Fig. L4-21: Axial profiles of generalized cladding stress after completion of the startup ramp for the P1S1F2 and P2S1F2 pin versions under design conditions
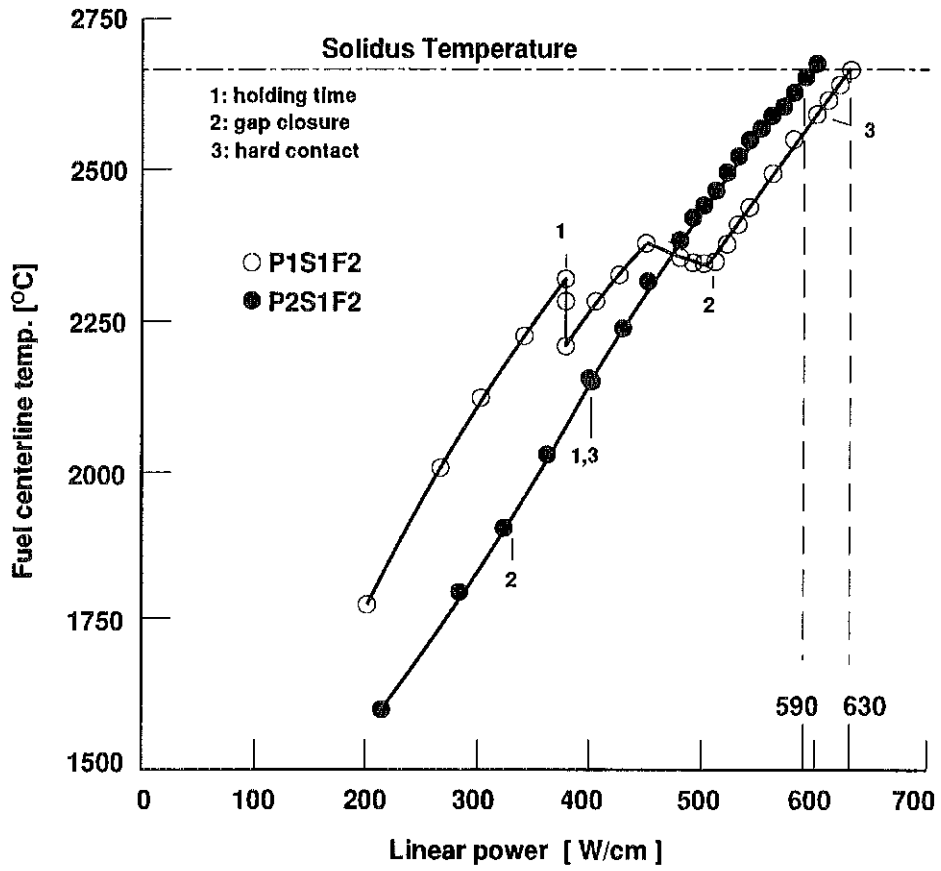
Fig. I.4-23: Modelling the power-to-melt for the P1S1F2 and P2S1F2 pin versions

ANNEX 1:

Description of all COMMON-Variables

FORTRAN-Name	COMMON-Name	Description	Dimension	Mathematical notation
A1IRVB (3, IEB) A1IRVH (3, IEH)	PORMA3 PORMA3	part of the elements flexibility due to swelling-effects of fuel part of the elements flexibility due to swelling-effects of cladding	--	$\{A1_{irr}\}^k$
A1NEVB (3, IEB) A1NEVH (3, IEH)	PLASA1 PLASA1	vector of non-elastic flexibilities of the fuel-elements vector of non-elastic flexibilities of the cladding-elements	--	$\{A1_{ne}\}^k$
A2IRMB (3,3,IEB) A2IRMH (3,3,IEH)	PORMA3 PORMA3	fuel partial flexibility due to irradiation and porosity influence (in case of cladding = 0)	--	$[A2_{irr}]^k$
A2NEMB (3,3,IEB) A2NEMH (3,3,IEH)	PLASA1 PLASA1	matrix of stress-induced non-elastic fuel-flexibilities matrix of stress-induced non-elastic cladding-flexibilities	--	$[A2_{ne}]^k$
AFISSS (IEB)	FISGA1	fission gas production coefficient	moles/fiss	A
AGF (IRB)	GEOFA1	geometric factor for fuel temperature and power distribution (cf. BGF, DGF)	--	A_k
AKR (IEB) AXE (IEB)	FISGA1	Kr-portion of produced fission gas Xe-portion of produced fission gas	--	--
ALFA1 (IGAS) ALFA2 (IGAS)	XIN1A4 XIN1A4	accomodation coefficients gas /fuel (INIT1) accomodation coefficients gas /cladding (INIT1)	--	$a1_i$ $a2_i$
ALFAB (IEB) ALFAH (IEH)	MATBA1 MATHA1	linear thermal expansion coefficient of fuel linear thermal expansion coefficient of cladding	1/K 1/K	a_{th} a_{th}
AMB (3,3) AMH (3,3)	ASSA1 ASSA1	Matrix of the total stress induced flexibility fuel Matrix of the total stress induced flexibility cladding	--	$[A_{BB}]$ $[A_{HH}]$
AMMETO AMOXO	THEDA2 THEDA2	mole mass of the fuel metal portions mole mass of the fuel oxide portions	g/Mol	M_{met} M_{ox}
AMPU0 AMPU1 AMPU2 AMPU8 AMPU9	XIN1A1 XIN1A1 XIN1A1 XIN1A1 XIN1A1	isotopic mass Pu-240 (INIT1) isotopic mass Pu-241 (INIT1) isotopic mass Pu-242 (INIT1) isotopic mass Pu-238 (INIT1) isotopic mass Pu-239 (INIT1)	g/Mol	--
AMU5 AMU8	XIN1A1 XIN1A1	isotopic mass U-235 (INIT1) isotopic mass U-238 (INIT1)	g/Mol	--
ANEVB (3, IEB) ANEVH (3, IEH)	ANEA1 ANEA1	flexibility matrix of the non-elastic strain fuel flexibility matrix of the non elastic strain cladding	--	$\{A_{ne}\}^k$
ANVTMB(3,3,IEB) ANVTMH(3,3,IEH)	PLASA2 PLASA2	} auxiliary value: product of $\{A_{ne}\} \cdot \{A_{ne}\}^T$	--	--
ATHVB (3, IEB) ATHVH (3, IEH)	ATHA1 ATHA1	flexibility vector of the thermal expansion fuel flexibility vector of the thermal expansion cladding	--	$\{A_{th}\}^k$
ATUVB (4, IEB) ATUVH (4, IEH)	ASSA2 ASSA2	auxiliary value: thermal flexibility of the structure when adding the k-th element to the element k-1	--	$\{A_{(k-1)kt}\}$
ATVB (3) ATVH (3)	ASSA1 ASSA1	vector of the total thermal flexibility of fuel vector of the total thermal flexibility of cladding	--	$\{A_{kt}\}$
AUMB (4,4, IEB) AUMH (4,4, IEH)	ASSA2 ASSA2	auxiliary value: stress-induced flexibility of the structure when adding the k-th element to the element k-1	--	$[A_{(k-1)k}]$

FORTRAN-Name	COMMON-Name	Description	Dimension	Mathematical notation
AVOL (IEB)	THEDA1	atomic volume	cm^3/Atom	V
B1VB (3,IEB) B1VH (3,IEH)	STIMA1 STIMA1	auxiliary value for the calculation of thermal element stiffness for fuel and cladding	--	$\{B_1\}$
B2MB (3,3,IEB) B2MH (3,2,IEH)	STIMA2 STIMA2	auxiliary value for the calculation of the stress induced element stiffness for fuel and cladding	--	$\lvert B_2 \rvert$
BESMB (3,3,IEB) BESMH (3,3,IEH)	STIMA2 STIMA2	matrix of stress-induced fuel-elements stiffness matrix of stress-induced cladding-elements stiffness	--	$\lvert B_{es} \rvert^k$
BETVB (3, IEB) BETVH (3, IEH)	STIMA1 STIMA1	vector of stress-induced fuel-element stiffness vector of stress-induced cladding-element stiffness	--	$\{B_{et}\}^k$
BGF (IRB)	GEOFA1	geometric factor for the analysis of fuel temperature- and power distribuion (cf. AGF, DGF)	--	B_k
BMB (3,3) BMH (3,3)	ASSA1 ASSA1	matrix of total stress-induced fuel stiffness matrix of total stress-induced cladding stiffness	--	$\lvert B_{BB} \rvert$ $\lvert B_{HH} \rvert$
BPORKG (KG)	XXX117	coefficient describing the relation between amount of pores and temperature (INPUT)	--	b_{Por}
BREL	XXX115	factor for gas release description (INPUT)	--	B
BTVB (3) BTVH (3)	ASSA1 ASSA1	vector of the total thermal fuel-stiffness vector of the total thermal cladding-stiffness	-- --	$\{B_{Bt}\}$ $\{B_{Ht}\}$
BU	UMRA1	burnup at the end of a computing interval or at "TIMEDT" respectively (OUTPUT)	MWd/kg M	Bu
BUFAK	UMRA2	conversion factor for burnup calculation	$\dfrac{MWd \cdot g}{\text{fiss kg}}$	--
CB (3,3) CH (3,3)	CMA1 CMA1	transfer matrix for calculation of external forces	--	$\lvert C_B \rvert$ $\lvert C_H \rvert$
CDIFIS (IEB)	PDA11	concentration of fissile fuel-isotopes (Pu + U) (INIT)	--	--
CE (3,4)	CMA1	matrix for the calculation of the element displacment rate	--	$\lvert C_e \rvert$
CEEB (3,3,IEB) CEEH (3,3,IEH)	CM1A1 CM1A1	matrix to calculate fuel element displacements (large deflection theory) matrix to calculate cladding element displacements (large deflection theory)	--	$\lvert C_{ee} \rvert^k$
CKM1 (3,4)	CMA1	coefficient matrix for assembling the structure	--	$\lvert C_{k-1} \rvert$
CON (IGAS)	PCOA3	gas mixture in the gap (see INPUT) (OUTPUT:HE, AR, KR, XE, N2)	--	--
CP (IGAS)	XIN1A5	specific heat of the particular gas-components (INIT)	J / (g · K)	C_{p_i}
CPROB (IEH) CPROBP (IEH)	COMPA9 CCRPA1	approach to tolerable cladding load (OUTPUT) rate of approach to tolerable cladding load	-- 1/h	-- --
CPU (IEB) CU (IEB)	PUPDA1 PUPDA1	fuel elements Pu-concentration (INIT, OUTPUT) fuel elements U-concentration (INIT)	-- --	C_{pu} C_u
CPUFIS (IEB) CUFIS (IEB)	PUMA11 PUMA11	portion of fissile Pu-isotopes in total Pu (INIT) portion of fissile U-isotopes in total U (INIT)	--	$C_{pu\,fiss}$ $C_{u\,fiss}$

FORTRAN-Name	COMMON-Name	Description	Dimension	Mathematical notation
CPUO	PUPDAI	Pu-concentration(Pu/(U-Pu)) in the fuel (start-value: INPUT)	--	C_{pu_0}
CPUP (IEB)	PUDA1	modification-rate of fuel elemtents Pu-concentration	1/h	$\dot{C}_{Pu}$
CUP (IEB)	PUDA1	modification-rate of fuel elemtents U-concentration		$\dot{C}_u$
CRAF (IEB)	RISSA5	reduction factor	--	CRAF
CRAFAK	XXX15	empirical factor for fuel cracking description (INPUT)	--	--
CVP (IGAS)	XIN1A5	coefficient for calculating the heat transfer in the gap between fuel and cladding (INIT1)	--	Cv_i / Cp_i
DCPUMX (IEB)	PUMA1	change of Pu-concentration based on evaporation and condensation	--	$\Delta C_{pu,VK}$
DELTB	XXX16		K	$\Delta T_{B\,max}$
DELTH	XXX16	boundary conditions and tolerances (see INPUT)	K	$\Delta T_{H\,max}$
DEMAX	XXX11		--	$\Delta \varepsilon_{max}$
DESHM	XXX11		--	$\Delta \varepsilon_{SH\,max}$
DEVSHB (IEB)	COMPA1	partial derivative of the nonelastic deformation rate with respect to strain hardening strain of fuel cladding		$\dfrac{\partial \dot{\varepsilon}_v}{\partial \varepsilon_{SH}}$
DEVSHH (IEH)	COMPA1			
DEVSVB (IEB)	COFCA1	partial derivative of the nonelastic deformation rate with respect to the equivalent strain of fuel cladding	--	$\dfrac{\partial \dot{\varepsilon}_v}{\partial \sigma_v}$
DEVSVH (IEH)	COCCA1			
DFERB (IEB)	COMPA7	partial derivative of the nonelastic deformation rate with respect to the recovery strain of fuel and cladding	--	$\dfrac{\partial \dot{\varepsilon}_v}{\partial \varepsilon_R}$
DFERH (IEH)	COMPA7			
DFESHB (IEB)	COMPA7	partial derivative of the strain hardening strain rate with respect to the strain hardening strain of fuel and cladding	--	$\dfrac{\partial \dot{\varepsilon}_{SH}}{\partial \varepsilon_{SH}}$
DFESHH (IEH)	COMPA7			
DGF (IEB)	GEOFA1	geometric factor for analysis of fuel temperature - and power distribution (cf. AGF, BGF)	--	D_k
DMXFIS (IEB)	PUMA1	change of amount of fissile isotopes due to vaporization and condensation	--	--
DOSDT	UMRA1	total neutron dose (INPUT, OUTPUT)	n/cm^2	F
DOSDTE	UMRA3	epithermal neutron dose	n/cm^2	F_e
DOSDTS	UMRA3	fast neutron dose	n/cm^2	F_s
DOSDTT	UMRA3	thermal neutron dose	n/cm^2	F_t
DOSP	UMRA1	neutron flux (OUTPUT)	$n/(cm^2 \cdot s)$	$\dot{F}$
DP2	FORA2	auxiliary value: rate of change of the gap fuel-cladding	cm/h	$\dot{D}$
DPA	UMRA1	material damage (OUTPUT)	--	--
DPAP	UMRA1	material damage rate	1/h	--
DRA (IZEIT)	XXX11	system pressure at external time setpoints (INPUT)	N/cm^2	$Pa_i, P_{kühl}$
DRADT	COMPA5	instantaneous system pressure (OUTPUT)	N/cm^2	$Pa, P_{kühl}$
DRAP	RATEA1	coolant or system pressure rate respectively	$N/(cm^2 \cdot h)$	$\dot{Pa}$
DRI (IZEIT)	XXX11	internal pressure at the external timpe setpoint (see INPUT)	N/cm^2	Pi_i, P_{gas}

FORTRAN-Name	COMMON-Name	Description	Dimension	Mathematical notation
DRIDT	COMPA5	instantaneous internal pressure (OUTPUT)	N/cm^2	P_i, P_{gas}
DRIP	RATEA1	internal pressure rate	$N/(cm^2 \cdot h)$	$\dot{P}_i$
DSMAX	XXXI1	max. tolerable change of equivalent stress during a computing interval (INPUT)	N/cm^2	$\Delta\sigma_{max}$
DSVLL (IEB)	PCOMA1	change of void volume in the fuel ring during a computing interval	--	ΔSV_{LL}
DT	DTIMA1	length of the instantaneous computing time interval	h	Δ_t
DTMAXB DTMAXH	XXXI9 XXXI9	max. tolerable change of a fuel or cladding element´s temperature from one internal timestep to the next (INPUT)	^0C	--
DVMIN (IEB) DVPLU (IEB)	PCOMA5 PCOMA5	incoming void volume per fuel ring by pore migration outgoing void volume per fuel ring by pore migration	-- --	ΔV_i^- ΔV_i^+
DVMKGP (IEB, KG) DVPKGP (IEB, KG)	PMIGA1 PMIGA1	as DVMIN, DVPLU, but additionally related to pore classes	-- --	ΔV^- ΔV^+
EFISS	XXXI4	fission energy (INPUT)	MEV/fiss	E_{fiss}
EMODB (IEB) EMODH (IEH)	MATBA1 MATHA1	Youngs´s modulus of the fuel Youngs´s modulus of the cladding	N/cm^2	E
EPELVB (3, IEB) EPELVH (3, IEH)	STDA2 STDA2	portion of the elastic strain rate related to the total strain rate of fuel and cladding (in the order: rad., ax., tang.)	1/h	$\{\dot{\varepsilon}_{el}\}^k$
EPIRVB (3, IEB) EPIRVH (3, IEH)	STDA2 STDA2	strain rate based on swelling, condenstation of fission gas bubbles and fission gas release for fuel and cladding	1/h	$\{\dot{\varepsilon}_{irr}\}^k$
EPNELB (3, IEB) EPNELH (3, IEH)	STDA2 STDA2	portion of the non-elastic strain rate related to total strain rate of fuel and cladding elements	1/h	$\{\dot{\varepsilon}_{ne}\}^k$
EPSEVB (3, IEB) EPSEVH (3, IEH)	COMPA2 COMPA2	elastic strain of each fuel and cladding element	--	$\{\varepsilon_{el}\}^k$
EPSNEB (3, IEB) EPSNEH (3, IEH)	COMPA3 COMPA3	non-elastic strain of the fuel and cladding elements (OUTPUT)	--	$\{\varepsilon_{ne}\}^k$
EPSPVB (3, IEB) EPSPVH (3, IEH)	STDA2 STDA2	total strain rate of fuel and cladding elements	1/h	$\{\dot{\varepsilon}\}^k$
EPST	XXXI12	convergence limit for iteration of fuel surface temperature (see INPUT)	^0C	$\varepsilon_{max T}$
EPSVB (3,IEB) EPSVH (3,IEH)	COMPA2 COMPA2	total strain of fuel and cladding elements (OUTPUT: EPSVB 3, EPSVH 3)	--	$\{\varepsilon\}^k$
EQ	XXXI4	average fast neutron energy	Mev	
ERB (IEB) ERH (IEH)	COMA3 COMA3	recovery strain of the fuel and cladding elements (INIT)	--	ε_R^k
ESHB (IEB) ESHH (IEH)	COMA3 COMA3	strain hardening strain of fuel and cladding elements (INPUT, OUTPUT)	--	ε_{SH}^k
EVB (IEB) EVH (IEH)	COMA3 COMA3	non-elastic equivalent strain of fuel and cladding elements (INPUT, OUTPUT)	--	ε_v^k

FORTRAN-Name	COMMON-Name	Description	Dimension	Mathematical notation
FB (IKF) FH (IKF)	KRITH1 KRITH1	vector of x-values for the creep table for fuel (KRBMAT) vector of x-values for the creep table for cladding (KRHMAT)	fiss/cm^3·h)/ n/cm^2	--
FCONR FCONZ	FORAH1 FORAH1	radial contact force between fuel and cladding (INPUT,OUTPUT) axial contact force between fuel and cladding (INPUT, OUTPUT)	N	F_r F_z
FERB (IEB) FERH (IEH)	COMPA1 COMPA1	recovery strain rate of fuel and cladding elements	1/h	$\dot{\varepsilon}_R$
FESHB (IEB) FESHH (IEH)	COMPA1 COMPA1	rate of strain hardening strain of fuel and cladding elements (OUTPUT)	1/h	$\dot{\varepsilon}_{SH}$
FEVB (IEB) FEVH (IEH)	COFCA1 COCCA1	total nonelastic deformation rate of fuel and cladding elements ($\dot{\varepsilon}_v = \dot{\varepsilon}_R + \dot{\varepsilon}_{SH}$) (OUTPUT)	1/h	$\dot{\varepsilon}_v^k$
FGFR (IKF)	GASTH1	vector of x-values for the fission gas release table (GSBMAT)	fiss/cm^3	--
FIMA	UMRA1	burnup at time setpoint TIMEDT (OUTPUT)	--	FIMA
FKB FKH	INP11 INP11	fuel strain hardening characteristic cladding strain hardening characteristic	--	$\dot{\varepsilon}_v$ $\dot{\varepsilon}_s$
FKORN	XXXI13	grain diameter (INPUT)	cm	d
FLUXEA	XXXI20	undisturbed epithermal neutron flux (INPUT)	n/(cm^2·s)	Φ_{epi}^0
FLUXEI	XXXI20	flux depression (resp. minimum of the relative flux) for epithermal flux (INPUT)	--	--
FLUXEM (IEB)	FLXPA1	absolute epithermal neutron flux in the elements	n/(cm^2·s)	Φ_{epi}
FLUXSA	XXXI20	undisturbed fast neutron flux (INPUT)	n/(cm^2·s)	Φ_s
FLUXTA	XXXI20	undisturbed thermal neutron flux (INPUT)	n/(cm^2·s)	Φ_{th}^0
FLUXTI	XXXI20	flux depression for thermal flux (INPUT)	--	--
FLUXTM (IEB)	FLXPA1	absolute thermal neutron flux in the elements	n/(cm^2·s)	Φ_{th}
FMUE	XXXI2	friction coefficient for friction between fuel and cladding (INPUT)	--	μ
FORB (3) FORH (3)	FORA3 FORA3	total contact force fuel total contact force cladding	N N	$\{F_B\}$ $\{F_H\}$
FPAKG (IEB, KG)	PCOMA2	sum of gas pressure and surface tension of each void volume class in the elements	N/cm^2	f_{pa}
FPB (3) FPH (3)	FORA1 FORA1	total force-rates for fuel and cladding	N/h	$\{\dot{F}_B\}, \{\dot{F}_H\}$
FPCON (3)	CONA1	friction forces	N	$\{F_{con}\}$
FPGKG (IEB, KG)	PCOMA2	gas pressure of each void volume class in the elements (OUTPUT)	N/cm^2	f_{pg}
FPPB (3) FPPH (3)	FORA1 FORA1	pressure force rate fuel pressure force rate cladding	N/h N/h	$\{\dot{F}_{PB}\}$ $\{\dot{F}_{PH}\}$
FPVB (3, IEB) FPVH (3, IEH)	STDA1 STDA1	total force-rates for each fuel element total force-rates for each cladding element	N/h N/h	$\{\dot{F}_{Be}\}^k$ $\{\dot{F}_{He}\}^k$
FRISS (IEB)	RISSA1	cracked area in the fuel ring (OUTPUT)	cm^2	--
FSYB (IEB)	COFCA2	creep rate at the yield strength of fuel	1/h	$\dot{\varepsilon}_y$

FORTRAN-Name	COMMON-Name	Description	Dimension	Mathematical notation
FTMB (IKF,IKT,IKZ)	KRITI1	creep table for fuel (KRBMAT)		
FTMH (IKF,IKT,IKZ)	KRITI1	creep table for cladding (KRHMAT)	--	--
FTX (2) FTY (IKZ)	KRITA1 KRITA1	auxiliary values for creep table application		
FVPKGP (IEB, KG)	PORMA1	rate of pressure induced volume change for each void volume class in the element during the computing interval	1/h	f_{vp}
FVTKGP (IEB, KG)	PORMA1	rate of thermal volume change for each void volume class during the computing intervall	1/h	f_{vt}
FWL (IGAS)	XIN1A4	mean free path of gas molecules at 0^0C und 1 bar (INIT1)	cm	ℓ_m
GAMMA	XXX114	surface tension of the pores (INPUT)	N/cm	γ
GMARO, GMHEO, GMKRO, GMN2O, GMXEO	XIN1A2	number of gas moles of each backfill gas component in the order: Ar, He, Kr, N_2, Xe (see INPUT: CON ( )) (INIT 1)	Mole	$M_{He}, M_{Kr..}$
GMFDT	PCOMA4	total number of all released gas moles in a computing interval DT	Mole	$M_{g\,frei}$
GMFKG (IEB, KG)	PCOMA3	number of released gas moles per void volume class and ring all over the computing intervals	Mole	$M_{g\,frei}(i, kg)$
GMFKGP (IEB, KG)	GASRA1	rate of fission gas release per void volume class and ring	Mole/h	$\dot{M}_{g\,frei}(i, kg)$
GMFREI	PCOMA4	total number of released gas moles (OUTPUT)	Mole	$M_{g\,frei}$
GMFRKR GMFRXE	PCOMA4 PCOMA4	total number of the released Kr- or Xe moles resp.	Mole	--
GMKG (IEB, KG)	PCOMA3	no. of gas moles per void class at "TIMEDT" (OUTPUT)	Mole	$M_{g_i}(t)$
GMKGP (IEB, KG)	GASRA1	rate of fission gas balance	Mole/h	$\dot{M}_{g\,abs}$
GMKGPR (IEB,KG)	GASRA1	fission gas balance related to the ring volume	1/h	$\dot{M}_{g_i}$
GMTOTO	XIN1A2	number of moles of the backfill gas	Mole	$M_{g\,tot}$
H2B (IEB) H2H (IEH)	PLASA2 PLASA2	auxiliary values	--	--
HCOOLH	XXX17	heat transfer coefficient cladding to coolant (INPUT)	$W/(cm^2 \cdot K)$	$h_{cool}H$
HGAP	GAPA1	heat transfer between fuel and cladding (OUTPUT)	$W/(cm^2 \cdot K)$	h_{gap}
HGFIX	XXX112	fuel-cladding heat transfer coefficient (see INPUT)	$W/(cm^2 \cdot K)$	h_{gap}
IANZZP	INP6	number of time steps within the irradiation history (INPUT)	--	--
ICR0 ICRN	RISSA5 RISSA5	total number of the cracked elements	--	--
ICRACK (IEB)	RISSA2	= 0: fuel element not cracked (OUTPUT: IC) > 0: fuel element cracked	--	--
IGASB	INP1	option for fission gas release model (see INPUT)	--	--

FORTRAN-Name	COMMON-Name	Description	Dimension	Mathematical notation
IMATB IMATH	INP42 INP42	options for fuel and cladding materials (see INPUT)	--	--
INP	CH2	vector for the identification of the data blocks to be read in (INPUT)	--	--
IPTGAP	INP7	option for gap type (see INPUT)	--	--
IPTTRA	INP7	option for gas- or sodium bonding in the fuel-cladding gap (see INPUT)	--	--
IQ	MACOA1	control variable for fuel cracking	--	--
ISWELB ISWELH	INP1 INP2	options for fuel- and cladding swelling (see INPUT)	--	--
IVRIS0 (IEB)	RISSA2	control variable for fuel cracking	--	
IZKRB IZKRH	INP5 INP5	dimension of the creep table fuel and cladding	--	--
MCEEB MCEEH	INP1 INP2	options for calculation acc. to large deflection theory (see INPUT)	--	
MCRPB MCRPH	INP1 INP2	options for calculation of fuel and cladding creep and plasticity (see INPUT)	--	
MDRI	INP2	option for internal pin pressure (see INPUT)	--	--
MGFR	INP10	dimension of the fission gas release table	--	--
MNLKG (KG)	INP8	option for void volume classes (see INPUT)	--	M_{NL}
MTB MTH	INP5 INP5	dimension of the creep table fuel and cladding	--	--
NEB NEH	INP3 INP3	number of fuel and cladding elements (see. INPUT: NEB,H = NRB,H-1, INIT)	--	--
NFB NFH	INP5 INP5	dimension of the creep table fuel and cladding	--	--
NGFR	INP10	dimension of the fission gas release table	--	--
NP	INP8	no. of void volume classes (INPUT)	--	N_p
NPROD (KG)	INP8	option for void volume classes (see INPUT)	--	--
NRB NRH	INP3 INP3	no. of fuel radii (INPUT) no. of cladding radii (INPUT)	--	--
OMV (IRB)	MIGAH	oxygen - to - metal ratio in the fuel elements (INIT, OUTPUT)	--	O/M
OMVO	XXXI3	initial value for oxygen -to- metal ratio in the fuel (INPUT)	--	O/M
PEB (IEB)	QPRAFP	relative flux distribution in the fuel elements	--	--
PHDT (IEB)	UMRAH	time integrated fission rate of each fuel element (INIT)	fiss/cm³	ϕ
PHDTO	UMRAH	initial value of time-integrated fission rate (INPUT)	fiss/cm³	ϕ_0
PHDTQ	UMRAH	radial average of the ime-integrated fission rate (INIT, OUTPUT)	fiss/cm³	ϕ
PHP (IEB)	UMRA1	local fuel elements ´fission rate (OUTPUT)	fiss/(cm³ · s)	$\dot{\phi}$

FORTRAN-Name	COMMON-Name	Description	Dimension	Mathematical notation
PHIPQ	UMRA1	radial averaged integrated fission rate (OUTPUT)	fiss/(cm$^3 \cdot$ s)	$\overline{\dot{\phi}}$
PMAB PMAH	XXXI7 XXXI7	factors for modelling the mechanical anisotropy in fuel and cladding (INPUT)	--	P_B P_H
POR (IEB)	PCOAI2	porosity in the fuel rings (INIT, OUTPUT)		por
PORMAX	XXXI6	max. tolerable void volume in a fuel ring (INPUT)	--	por_{max}
PORO	XXXI3	initial value of fuel porosity (INPUT)	--	por_0
PRAKG (IEB, KG)	PCOMA3	radii of pores of the different void volume classes in the fuel rings (OUTPUT : PRA)	cm	R_{ai}
PRB (IRB)	QPRAFP	relative flux distribution at the fuel radii (OUTPUT)	--	--
PU38 PU39 PU40 PU41 PU42	XXXI18 XXXI18 XXXI18 XXXI18 XXXI18	isotope distribution in the fuel (INPUT) $(U_{35}/(U_{35} + U_{38}), Pu_x/Pu_{total})$	--	--
PUFISS	XIN1A3	Pu 39 + Pu 41 (INIT 1)	--	Pu_{fiss}
PVT	COMPA8	auxiliary value: $p \cdot V / T_{abs}$	N $\cdot$ cm / K	--
Q (IZEIT)	XXXI11	linear power at the external time setpoints (INPUT)	W/cm	χ
QDT	COMPA5	linear power at the end of a computing interval (OUTPUT)	W/cm	χ
QDTE (IEB)	RADA1	linear power in the fuel elements at the end of a computing interval	W/cm	χ
QFAK	UMRA2	conversion factor: fission energy from MeV in J	J / fiss	--
QP	RATEA1	linear power rate	W / (cm $\cdot$ h)	$\dot{\chi}$
QUOTB (IEB) QUOTH (IEH)	STIMA3 STIMA3	auxiliary internal variables	--	--
QVDT	RADA1	volumetric averaged heat production rate in the fuel	W / cm^3	Q_v
QVDTE (IEB)	RADA1	volumetric averaged heat production rate in the fuel rings	W / cm^3	Q_v
QVLDTE (IEB)	RADA1	volumetric averarged linear power in the fuel rings	W / cm^3	--
RAB (IEB) RAH (IEH)	COMAI1 COMAI1	inner radii of the fuel elements (INIT) inner radii of the cladding elements (INIT)	cm	r_1, r_a
RABR RIBR	COMAI2 COMAI2	fuel outer radius (INPUT) fuel inner radius (INPUT)	cm	r_{Ba} r_{Bi}
RABRO	XIN1A7	fuel outer radius at the time setpoint T_0 (INIT1)	cm	$r_{Ba,0}$
RABRU RIBRU	XXXI10 XXXI10	outer radius of blanket material (INPUT) inner radius of blanket material (INPUT)	cm	ra_{Br} ri_{Br}
RAHU RIHU	COMAI2 COMAI2	cladding outer radius (INPUT) cladding inner radius (INPUT)	cm	r_{Ha} r_{Hi}
RALFAB (3) RALFAH (3)	XXXI8 XXXI8	thermal anisotropy-factors for the fuel (INPUT) thermal anisotropy-factors for the cladding (INPUT)	cm	$R_{ar}, R_{at},$ R_{az}

FORTRAN-Name	COMMON-Name	Description	Dimension	Mathematical notation
RAUBR	XXXI3	fuel surface roughness (INPUT)	cm	δ rau $_B$
RAUHU	XXXI3	cladding surface roughness (INPUT)		δ rau $_H$
RB (IRB)	COMAI1	radii of fuel rings or elements resp. (INIT, OUTPUT)	cm	r_B
RH (IRH)	COMAI1	radii of cladding rings or elements resp. (INIT, OUTPUT)		r_H
RBB (IEB)	COMAI1	outer radii of the fuel elements (INIT, OUTPUT)	cm	$r_{2,}r_B$
RBH (IEH)	COMAI1	outer radii of the cladding elements (INIT, OUTPUT)		
RGRZ	XXXI14	minimum radius for migrating pores (INPUT)	cm	r_{grz}
RHOO	THEDA2	theoretical density of the fuel at the start of calculation $T = TIME(1)$	g/cm^3	ρ_0
RHOTH (IEB)	THEDA1	theoretical density of the fuel ring material	g/cm^3	ρ_{th}
RHHUO	XINIA7	cladding inner radius at the time setpoint T_0 (INIT1)	cm	$r_{Hi,0}$
RIRRB (3)	XXXI14	factors for modelling the irradiation induced anisotropy of fuel	--	$\{R_{irr}\}_B$
RIRRH (3)	XXXI14	and cladding (INPUT)		$\{R_{irr}\}_H$
RMAB	XXXI7	factors for modelling the mechanical anosotrpoy of fuel and	--	R_B
RMAH	XXXI7	cladding (INPUT)		R_H
RPUNB (IRB)	STDA1	radial displacement rate of the fuel and cladding element radii	cm/h	$\dot{r}_B$
RPUNH (IRH)	STDA1			$\dot{r}_H$
RSC	XXXI19	factors describing the pore migration velocity or the plastic stress	--	R_{sc}
RSP	XXXI19	limit respectively in the pore region (INPUT)		R_{sp}
SCKG (IEB, KG)	COMPA4	slope of the creep curve for the fuel elements and in the different void volume classes	N/(cm^2·h)	S_c
SFPVLB (3)	STDA4	total force rates of all fuel elements (rad., ax., tang.)	N/h	--
SFPVLH (3)	STDA4	total force rates of all cladding elements (rad., ax., tang.)	N/h	
SFRISS	RISSA1	crack-volume per unit length (OUTPUT)	cm^2	--
SIGFAK	XXX14	conversion factor neutron flux vs. fission rate (INPUT)	--	--
SIGMCR	XXXI5	cracking stress of the fuel (INPUT)	N/cm^2	σ_{cr}
SIGPVB (3, IEB)	STDA3	stress rate vector of the fuel elements	N/(cm^2·h)	$\{\dot{\sigma}\}^k$
SIGPVH (3, IEH)	STDA3	stress rate vector of the cladding elements		
SIGVB (3, IEB)	COMAI5	radial, tangential and axial stress of the fuel or cladding elements	N/cm^2	$\{\sigma\}^k$
SIGVH (3, IEH)	COMAI5	respectively (INPUT, OUTPUT)		
SIPVEB (IEB)	STDA3	equivalent stress rate of the fuel elements	N/(cm^2·h)	$\dot{\sigma}_v{}^k$
SIPVEH (IEH)	STDA3	equivalent stress rate of the cladding elements		
SKDT	TEMPA2	thermal conductivity integral (OUTPUT)	W/cm	--
SP (IEB)	COMPA4	plastic stress limit in the fuel elements	N/cm^2	σ_p
SUTH (IGAS)	XINIA4	Sutherland-constant of the backfill gas components (INIT1)	K	S
SVB (IEB)	COMPA6	equivalent stress of the fuel elements (OUTPUT)	N/cm^2	$\sigma_v{}^k$
SVH (IEH)	COMPA6	equivalent stress of the cladding elements (OUTPUT)		
SVLFAK (IEB)	RISSA4	remaining crack volume, converted to pore volume	--	--

FORTRAN-Name	COMMON-Name	Description	Dimension	Mathematical notation
SVLL (IEB)	PCOAI2	absolute void volume in the fuel rings at the end of a computing interval or at "TIMEDT" respectively (INIT)	cm^3	SVLL
SYB (IEB)	FSYA1	yield stress of fuel elements	N/cm^2	σ_y
TABGFR (IKF, IKT)	GASTI1	gas release table (GSBMAT)	--	--
TB (IKT) TH (IKT)	KRITI1 KRITI1	vector of y-values for the creep table fuel (KRBMAT) vector of y-values for the creep table cladding (KRHMAT)	^0C	--
TCOLDT	COMPA5	coolant temperature at the end of a computing interval or at "TIMEDT" respectively (OUTPUT)	^0C	T_{cool}
TCOOL (IZEIT)	XXXI11	coolant temperature at the external time setpoints (INPUT)	^0C	T_i
TCOOLP	RATEA1	rate of the coolant temperature change	K/h	$\dot{T}_i$
TEDTEB (IEB) TEDTEH (IEH)	TEMPA1 TEMPA1	temperature in the fuel and cladding elements during or resp. at the end (TIMEDT) of a computing interval	^0C	T
TEDTRB (IRB) TEDTRH (IRH)	TEMPA1 TEMPA1	temperature at the fuel and cladding radii at "TIMEDT" (OUTPUT)	^0C	T
TEMPPB (IEB) TEMPPH (IEH)	DTEMA1 DTEMA1	temperature rate in fuel and cladding elements	K/h	$\dot{T}$
TEXT	CI11	headline of output (see INPUT)	--	--
TGFR (IKT)	GASTI1	vector of y-value of the gas release table (GSBMAT)	^0C	--
TGRZKG (KG)	XXXI17	lower temperature limit for pore migration of each void volume class (see INPUT)	^0C	T_{grz}
TIMEH (IZEIT)	XXXI11	user option: externally given setpoints of time during irradiation (INPUT, OUTPUT)	h	t_i
TIMEDT	MAINA1	instantaneous computing time or end of the computing interval resp. (OUTPUT)	h	t
TMAX	XXXI6	max. tolerable fuel centerline temperature (INPUT)	^0C	T_{max}
TPLEDT	COMPA5	plenum temperature at the instantaneous "TIMEDT" (OUTPUT)	^0C	T_{plen}
TPLEN (IZEIT)	XXXI11	plenum temperature at the time setpoints (INPUT)	^0C	T_{plen}
TPLENP	RATEA1	plenum temperature rate	K/h	$\dot{T}_{plen}$
TZERO	XXXI0	reference temperature (start-value: INPUT)	^0C	T_0
U35	XXXI18	isotope distribution in the fuel (see INPUT)	--	U 235
UFISS	XIN1A3	fissile portion of U in the fuel	--	U_{fiss}
UPB (3) UPH (3)	FORA3 FORA3	vector of free thermal displacement rates of fuel or cladding resp.	cm/h	$\{\dot{u}\}$
VEB (IEB)	RISSA3	volume of the fuel elements	cm^3	$V_{element}$
VELOKG (IEB, KG)	WANDA1	pore migration velocity in the fuel rings for the different void classes	cm/h	ρ
VLKG (IEB, KG)	XIN1A6	relative volume of pore class region (INIT)	--	V_{Li}
VLKGO (KG)	XXXI16	$\triangle$ VLKG (IEB, KG), initial value (see INPUT)	--	V_{Li}^0

FORTRAN-Name	COMMON-Name	Description	Dimension	Mathematical notation
VLKGP (IEB, KG)	PORMA2	total volume change rate for each pore class in the fuel element during a computing interval	h^{-1}	$\dot{V}_{Li}$
VLLKG (IEB, KG)	PCOA1	"effective" pore volume of each class of voids, related to total porosity in the ring elements (OUTPUT)	--	V_{LLi}
VLLKGO (KG)	XXXI16	$\triangleq$ VLLKG (IEB, KG), initial value (see INPUT)	--	V_{LLi}^{0}
VMBP (IEB) VMHP (IEH)	SWBA1 SWHA1	swelling rate in the fuel element swelling rate in the cladding element	h^{-1}	$\dot{V}, \dot{\varepsilon}_{VS}$
VOELB (IEB) VOELH (IEH)	COMPA7 COMPA7	volume of the fuel rings (INIT) volume of the cladding rings (INIT)	cm^3	$V_{element}$
VPLEN	COMA16	void volume in the fuel rod (INIT, OUTPUT)	cm^3	V_{plen}
VPLENP	PLEVA1	rate of void volume change in the fuel rod	cm^3/h	$\dot{V}_{plen}$
VPU (IEB)	MIGA1	Pu-valency in the fuel rings	--	V_{pm}
VRB (IEB) VRBO (IEB)	RISSA3 RISSA3	crack volume in the fuel elements	cm^3 cm^3	V_{crack} $V_{crack,O}$
VSTRUK	XXXI10	volume of internal structure parts in the fuel rod (INPUT)	cm^3	V_{Struk}
VTOT (IEB)	PCOMA1	auxiliary value: relative fuel element volume	--	V_{TOT}
WA (IGAS) WB (IGAS)	XIN1A5 XIN1A5	coefficients for calculating the thermal conductivity of the gas components in the gap: $\lambda_i = a_i + b_i \cdot T$ (INIT1)	$W/(cm \cdot K)$ W/cm	a b
WGAP	WGAPA1	thermal concuctivity of the gas mixture in the fuel cladding gap	$W/(cm \cdot K)$	λ_{gas}
WLAMNA	XXXI12	thermal conductivity of Na (see INPUT)	$W/(cm \cdot K)$	λ_{Na}
XMB	XXXI4	molecular mass of the fuel (INIT)	g/Mol	M_B
XMGG (IGAS)	XIN1A4	molecular mass of each gas component of the gas mixture in the gap (INIT1)	g/Mol	M_i
XMMET	XXXI4	molecular mass of heavy metal (INIT)	g/Mol	M_{met}
XNLKG (IEB,KG)	NLIA1	no. of voids of the different void volume classes in the fuel elements (OUTPUT)	$1/cm^3$	N_{Li}
XNLKGO (KG)	XXXI16	$\triangleq$ XNLKG (IEB, KG), initial value (see INPUT)	$1/cm^3$	N_{Li}^{0}
XNSM	UMRA1	no. of heavy metal atoms per unit volume	$Atome/cm^3$	N_{SM}
XNUEB (IEB) XNUEH (IEH)	MATBA1 MATHA1	poisson´s ratio for the fuel poisson´s ratio for the cladding	--	ν
ZBR ZBRU ZHU	COMA12 XXXI10 COMA12	total length of fuel column (INPUT) total length of blanket (INPUT) total length of cladding (INPUT)	cm	ℓ_{ZB} ℓ_{ZBr} ℓ_{ZH}
ZLB (IEB) ZLH (IEH)	COMA11 COMA11	length of the fuel or resp. of cladding elements in an axial column section (INPUT, INIT, OUTPUT)	cm	ℓ_z
ZLBO	XIN1A7	length of the axial fuel column section (node) at the time setpoint T_0 (INIT 1)	cm	$\ell_{z,0}$
ZLPB (IEB) ZLPH (IEH)	STDA1 STDA1	axial displacement rate of the fuel elements axial displacement rate of the cladding elements	cm/h	$\dot{\ell}_z$

ANNEX 2:

Output of the Input Data

LIST OF INPUT DATA
==================

FUEL MATERIAL (U,PU)O2 :
========================

OPTIONS AND LIMITS

CALCULATION WITHOUT MATRIX CEE	MCEEB	= 0	
FUEL CREEP A. PLASTICITY ACC TO FCREEP MODEL	MCRPB	= 2	
FUEL SWELLING ACC. TO SWELLB-MODEL	ISWELB	= 2	
FISSION GAS RELEASE ACC TO GASREL-MODEL	IGASB	= 2	
MAX TOLERERABLE FUEL CENTERLINE TEMPERATURE	TMAX	= 2800.	GRD.C
MAX TOLERABLE POROSITY IN A FUEL RING	PORMAX	= 0.150	-
CRACKING STRESS FOR THE FUEL	SIGMCR	= 5000.0	N/CM**2
EMPIRICAL FACTOR FOR E-MOD IN CRACKED STATE	CRAFAK	= 0.600E+00	-
REFERENCE TEMPERATURE	TZERO	= 20.	GRD.C
MAX TOL.TEMPERATURE MISMATCH DURING ITERATION	DELTB	= 20.	GRD.C
MAX TOL. CHANGE OF ELEM-TEMP. FROM TIME I TO I+1	DTMAXB	= 50.	GRD.C
MAX TOL. CHANGE OF NON-ELASTIC STRAIN	DEMAX	= 0.50E-03	-
MAX TOL. CHANGE OF STRAIN HARDENING STRAIN	DESHN	= 0.5	-
MAX TOL. CHANGE OF EQUIVALENT STRESS	DSMAX	= 500.	-

GEOMETRY

RABR = 0.32350 CM   RIBR = 0.00000 CM   ZBR = 12.00000 CM   NRB =21 NEB =20

KE	RB (CM)	RAB (CM)	RBB (CM)	ZLB (CM)
1	0.000	0.000	0.072	12.00
2	0.072	0.072	0.102	12.00
3	0.102	0.102	0.125	12.00
4	0.125	0.125	0.145	12.00
5	0.145	0.145	0.162	12.00
6	0.162	0.162	0.177	12.00
7	0.177	0.177	0.191	12.00
8	0.191	0.191	0.205	12.00
9	0.205	0.205	0.217	12.00
10	0.217	0.217	0.229	12.00
11	0.229	0.229	0.240	12.00
12	0.240	0.240	0.251	12.00
13	0.251	0.251	0.261	12.00
14	0.261	0.261	0.271	12.00
15	0.271	0.271	0.280	12.00
16	0.280	0.280	0.289	12.00
17	0.289	0.289	0.298	12.00
18	0.298	0.298	0.307	12.00
19	0.307	0.307	0.315	12.00
20	0.315	0.315	0.323	12.00
21	0.323			

MATERIALS CHARACTERISTIC

FUEL SURFACE ROUGHNESS	RAUBR	= 0.300E-03	CM
GRAIN DIAMETER	FKORN	= 0.100E-02	CM
START VALUE FOR FUEL POROSITY	PORO	= 0.0500	-
SURFACE TENSION OF THE PORES	GAMMA	= 0.300E-02	N/CM
MINIMUM RADIUS OF MIGRATING PORES	RGRZ	= 0.500E-04	CM
FACTOR DESCRIBING PORE MIGRATION VELOCITY	RSC	= 10.0	-
FAC. DESCR. PLASTIC STRESS LIMIT IN PORE REGION	RSP	= 1.0	-
FACTOR FOR GAS RELEASE MODELLING	BREL	= 1.0	-
PU-CONCENTRATION IN THE FUEL	CPU0	= 0.2800	-
ISOTOPE DISTRIBUTION IN THE FUEL	PU38	= 0.0100	-
	PU39	= 0.6700	-
	PU40	= 0.2600	-
	PU41	= 0.0500	-
	PU42	= 0.0100	-
U235-CONCENTRATION IN THE URANIUM	U35	= 0.7300	-
OXYGEN-TO METAL RATIO	OMVO	= 1.930	-

```
FISSION ENERGY                              EFISS  = 203.0     MEV/FISS
TIME-INTEGRATED FISSION RATE                PHIDTO = 0.000E+00 FISS/CM**3
MECHANICAL ANISOTROPY FACTORS               RMAB   = 1.00      -
                                            PMAB   = 1.00      -
THERMAL ANISOTROPY FACTORS                  RALFAB = 1.00
                                                     1.00
                                                     1.00      -
STRAIN HARDENING CHARACTERISTIC             FKB    = 5.00      -
FRICTION COEFFICIENT                        FHUE   = 0.003     -
RADIAL CONTACT FORCE FUEL-CLADDING          FCONR  =    0.     N
AXIAL CONTACT FORCE FUEL-CLADDING           FCONZ  =    0.     N
```

STRAINS AND STRESSES

KE	SIGVB(1) (N/CM**2)	SIGVB(2) (N/CM**2)	SIGVB(3) (N/CM**2)	EVB -	ESHB -	ERB -
1	0.00000E+00	0.00000E+00	0.00000E+00	0.10000E-06	0.10000E-06	0.00000E+00
2	0.00000E+00	0.00000E+00	0.00000E+00	0.10000E-06	0.10000E-06	0.00000E+00
3	0.00000E+00	0.00000E+00	0.00000E+00	0.10000E-06	0.10000E-06	0.00000E+00
4	0.00000E+00	0.00000E+00	0.00000E+00	0.10000E-06	0.10000E-06	0.00000E+00
5	0.00000E+00	0.00000E+00	0.00000E+00	0.10000E-06	0.10000E-06	0.00000E+00
6	0.00000E+00	0.00000E+00	0.00000E+00	0.10000E-06	0.10000E-06	0.00000E+00
7	0.00000E+00	0.00000E+00	0.00000E+00	0.10000E-06	0.10000E-06	0.00000E+00
8	0.00000E+00	0.00000E+00	0.00000E+00	0.10000E-06	0.10000E-06	0.00000E+00
9	0.00000E+00	0.00000E+00	0.00000E+00	0.10000E-06	0.10000E-06	0.00000E+00
10	0.00000E+00	0.00000E+00	0.00000E+00	0.10000E-06	0.10000E-06	0.00000E+00
11	0.00000E+00	0.00000E+00	0.00000E+00	0.10000E-06	0.10000E-06	0.00000E+00
12	0.00000E+00	0.00000E+00	0.00000E+00	0.10000E-06	0.10000E-06	0.00000E+00
13	0.00000E+00	0.00000E+00	0.00000E+00	0.10000E-06	0.10000E-06	0.00000E+00
14	0.00000E+00	0.00000E+00	0.00000E+00	0.10000E-06	0.10000E-06	0.00000E+00
15	0.00000E+00	0.00000E+00	0.00000E+00	0.10000E-06	0.10000E-06	0.00000E+00
16	0.00000E+00	0.00000E+00	0.00000E+00	0.10000E-06	0.10000E-06	0.00000E+00
17	0.00000E+00	0.00000E+00	0.00000E+00	0.10000E-06	0.10000E-06	0.00000E+00
18	0.00000E+00	0.00000E+00	0.00000E+00	0.10000E-06	0.10000E-06	0.00000E+00
19	0.00000E+00	0.00000E+00	0.00000E+00	0.10000E-06	0.10000E-06	0.00000E+00
20	0.00000E+00	0.00000E+00	0.00000E+00	0.10000E-06	0.10000E-06	0.00000E+00

FUEL SWELLING

```
IRRADIATION-INDUCED ANISOTROPY FACTORS              RIRRB  = 0.33
                                                             0.33
                                                             0.33      -
```

CHARACTERISATION OF THE VOID VOLUME CLASSES

```
NUMBER OF VOID VOLUME CLASSES                       NP     = 2
```

KL	NPROD -	VLKG0 -	VLLKG0 -	XNLKG0 (CM**-3)	HNLKG -	TGRZKG -	BPORKG -
1	1	0.9000	0.500E-01	0.160E+07	-1	1200.	-0.001
2	1	0.1000	0.100E-06	0.100E+24	-1	1200.	-0.001

CLADDING MATERIAL 1.4970 :
==============================

OPTIONS AND LIMITS

```
CALCULATION WITH MATRIX CEE                         MCEEH  = 1
INTERNAL PIN PRESSURE IS CALCULATED BY THE CODE     MDRI   = 0
CLADDING CREEP A. PLAST. ACC TO CCREEP MODEL        MCRPH  = 2
CLADDING SWELLING ACC TO SWELLH MODEL               ISWELH = 2
MAX TOL.TEMPERATURE MISMATCH DURING ITERATION       DELTH  = 0.50     GRD.C
MAX TOL. CHANGE OF  ELEM-TEMP. FROM TIME I TO I+1   DTMAXH = 10.      GRD.C
```

GEOMETRY

```
RAHU =  0.38000 CM   RIHU =  0.33000 CM   ZHU = 33.00000 CM    NRH = 6  NEH = 5
```

KE	RH (CM)	RAH (CM)	RBH (CM)	ZLH (CM)
1	0.330	0.330	0.340	33.00
2	0.340	0.340	0.350	33.00
3	0.350	0.350	0.360	33.00
4	0.360	0.360	0.370	33.00
5	0.370	0.370	0.380	33.00
6	0.380			

MATERIALS CHARACTERISTIC

CLADDING SURFACE ROUGHNESS	RAUHU = 0.300E-03	CM
STRAIN HARDENING CHARACTERISTIC	FKH = 8.50	-
NEUTRON DOSE	DOSDT = 0.000E+00	NEU/CM**2
NEUTRON DOSE TO FISS RATE CONVERT. FACTOR	SIGFAK = 0.0218	-
MECHANICAL ANISOTROPY FACTORS	RMAH = 1.00	-
	PMAH = 1.00	-
THERMAL ANISOTROPY FACTORS	RALFAH = 1.00	
	1.00	
	1.00	-
HEAT TRANSFER COEFFICIENT CLADD. TO COOLANT	HCOOLH = 0.130E+02	W/CM**2*K
VOLUME OF INTERNAL STRUCTURE PARTS	VSTRUK = 0.475	CM**3
PIN VOID VOLUME	VPLEN = 4.501	CM**3

STRAINS AND STRESSES

KE	SIGVH(1) (N/CM**2)	SIGVH(2) (N/CM**2)	SIGVH(3) (N/CM**2)	EVH -	ESHH -	ERH -
1	0.00000E+00	0.00000E+00	0.00000E+00	0.10000E-06	0.10000E-06	0.00000E+00
2	0.00000E+00	0.00000E+00	0.00000E+00	0.10000E-06	0.10000E-06	0.00000E+00
3	0.00000E+00	0.00000E+00	0.00000E+00	0.10000E-06	0.10000E-06	0.00000E+00
4	0.00000E+00	0.00000E+00	0.00000E+00	0.10000E-06	0.10000E-06	0.00000E+00
5	0.00000E+00	0.00000E+00	0.00000E+00	0.10000E-06	0.10000E-06	0.00000E+00

CLADDING SWELLING

IRRADIATION-INDUCED ANISOTROPY FACTORS	RIRRH = 0.00	
	0.67	
	0.33	-

BLANKET :
=========

GEOMETRY

OUTER RADIUS	RABRU	= 0.31500	CM
INNER RADIUS	RIBRU	= 0.00000	CM
BLANKET COLUMN LENGTH	ZBRU	= 7.60000	CM

GAP :
=====

OPTIONS AND LIMITS

FUEL COLUMN IS CONCENTRIC WITHIN CLADD. TUBE	IPTGAP = 0	
GAS BONDING IN THE FUEL-CLADDING GAP	IPTTRA = 1	
UPPER LIMIT FUEL SURF. TEMPERATURE MISMATCH		
DURING ITERATION FUEL-CLADDING HEAT TRANSFER	EPST = 10.0	GRD.C

MATERIALS CHARACTERISTIC

GASMIXTURE IN THE GAP	HE = 0.500	-
	AR = 0.500	
	KR = 0.000	
	XE = 0.000	
	N2 = 0.000	

NEUTRON FLUX CHARACTERISTIC

UNDISTURBED FAST NEUTRON FLUX	FLUXSA = 0.170E+16	NEU/(CM**2*S)
UNDISTURBED EPITHERMAL NEUTRON FLUX	FLUXEA = 0.000E+00	NEU/(CM**2*S)
UNDISTURBED THERMAL NEUTRON FLUX	FLUXTA = 0.000E+00	NEU/(CM**2*S)
EPITHERMAL FLUX DEPRESSION	FLUXEI = 0.100E+01	-
THERMAL FLUX DEPRESSION	FLUXTI = 0.100E+01	-

POWER HISTORY

I	TIME H	TPLEN GRD.C	TCOOL GRD.C	DRA N/CM**2	DRI N/CM**2	Q W/CH
1	0.00	20.	20.	10.0	10.0	0.0
2	1.00	383.	445.	10.0	-	15.0
3	5.00	383.	445.	10.0	-	77.0
4	8.00	383.	445.	10.0	-	128.0
5	8.25	383.	445.	10.0	-	192.0
6	8.50	383.	445.	10.0	-	256.0
7	9.50	383.	445.	10.0	-	292.0
8	10.50	383.	445.	10.0	-	327.0
9	11.50	383.	445.	10.0	-	363.0
10	108.00	383.	445.	10.0	-	363.0
11	109.00	383.	445.	10.0	-	388.0
12	111.00	383.	445.	10.0	-	432.0
13	135.00	383.	445.	10.0	-	432.0
14	231.00	383.	445.	10.0	-	432.0
15	351.00	383.	445.	10.0	-	432.0
16	1311.00	383.	445.	10.0	-	429.0
17	2511.00	383.	445.	10.0	-	429.0
18	14511.00	383.	445.	10.0	-	414.0
19	14511.05	383.	445.	10.0	-	463.0
20	14511.10	383.	445.	10.0	-	463.0
21	14511.20	383.	445.	10.0	-	414.0
22	15231.00	383.	445.	10.0	-	414.0
23	15255.00	383.	445.	10.0	-	124.0
24	15975.00	383.	445.	10.0	-	124.0
25	15975.50	383.	445.	10.0	-	248.0
26	15976.00	383.	445.	10.0	-	352.0
27	15978.00	383.	445.	10.0	-	352.0
28	15978.25	383.	445.	10.0	-	414.0
29	16191.00	383.	445.	10.0	-	414.0
30	16191.17	383.	445.	10.0	-	0.0
31	16192.00	20.	20.	10.0	-	0.0

ANNEX 3:

Example of a Print-out

KM	KE	KG	VLLKG (-)	XNLKG (CM**-3)	PRA (CM)	GMKG (-)	FPGKG (N/CM**2)
1	1	1	0.479E-01	0.100E+04	0.225E-01	0.191E-06	0.959E+02
		2	0.894E-07	0.100E+14	0.129E-06	0.358E-12	0.102E+03
1	2	1	0.275E-01	0.403E+05	0.546E-02	0.195E-06	0.160E+03
		2	0.501E-07	0.252E+22	0.168E-09	0.356E-12	0.175E+03
1	3	1	0.281E-01	0.184E+06	0.331E-02	0.198E-06	0.151E+03
		2	0.510E-07	0.115E+23	0.102E-09	0.359E-12	0.166E+03
1	4	1	0.342E-01	0.327E+06	0.292E-02	0.199E-06	0.119E+03
		2	0.619E-07	0.204E+23	0.100E-09	0.361E-12	0.131E+03
1	5	1	0.422E-01	0.473E+06	0.277E-02	0.201E-06	0.929E+02
		2	0.762E-07	0.295E+23	0.100E-09	0.362E-12	0.102E+03
1	6	1	0.493E-01	0.625E+06	0.266E-02	0.202E-06	0.761E+02
		2	0.887E-07	0.391E+23	0.100E-09	0.364E-12	0.842E+02
1	7	1	0.532E-01	0.782E+06	0.253E-02	0.203E-06	0.672E+02
		2	0.955E-07	0.489E+23	0.100E-09	0.365E-12	0.745E+02
1	8	1	0.548E-01	0.941E+06	0.241E-02	0.204E-06	0.620E+02
		2	0.980E-07	0.588E+23	0.100E-09	0.366E-12	0.689E+02
1	9	1	0.552E-01	0.110E+07	0.229E-02	0.199E-06	0.583E+02
		2	0.988E-07	0.687E+23	0.100E-09	0.374E-12	0.649E+02
1	10	1	0.532E-01	0.125E+07	0.216E-02	0.197E-06	0.573E+02
		2	0.989E-07	0.783E+23	0.100E-09	0.378E-12	0.615E+02
1	11	1	0.495E-01	0.140E+07	0.204E-02	0.193E-06	0.583E+02
		2	0.990E-07	0.875E+23	0.100E-09	0.386E-12	0.583E+02
1	12	1	0.495E-01	0.154E+07	0.197E-02	0.194E-06	0.550E+02
		2	0.990E-07	0.965E+23	0.100E-09	0.388E-12	0.551E+02
1	13	1	0.495E-01	0.160E+07	0.195E-02	0.195E-06	0.519E+02
		2	0.990E-07	0.100E+24	0.100E-09	0.389E-12	0.519E+02
1	14	1	0.495E-01	0.160E+07	0.195E-02	0.195E-06	0.489E+02
		2	0.990E-07	0.100E+24	0.100E-09	0.390E-12	0.489E+02
1	15	1	0.536E-01	0.160E+07	0.200E-02	0.196E-06	0.424E+02
		2	0.990E-07	0.100E+24	0.100E-09	0.390E-12	0.459E+02
1	16	1	0.535E-01	0.160E+07	0.200E-02	0.197E-06	0.399E+02
		2	0.990E-07	0.100E+24	0.100E-09	0.388E-12	0.432E+02
1	17	1	0.535E-01	0.160E+07	0.200E-02	0.198E-06	0.376E+02
		2	0.990E-07	0.100E+24	0.100E-09	0.387E-12	0.406E+02
1	18	1	0.535E-01	0.160E+07	0.200E-02	0.199E-06	0.354E+02
		2	0.990E-07	0.100E+24	0.100E-09	0.385E-12	0.382E+02
1	19	1	0.535E-01	0.160E+07	0.200E-02	0.200E-06	0.333E+02
		2	0.990E-07	0.100E+24	0.100E-09	0.384E-12	0.359E+02
1	20	1	0.535E-01	0.160E+07	0.200E-02	0.201E-06	0.313E+02
		2	0.990E-07	0.100E+24	0.100E-09	0.383E-12	0.337E+02

KM	KR	RAD (CM)	TEDTR (GRD.C)
2	1	0.3324	506.
2	2	0.3425	496.
2	3	0.3526	486.
2	4	0.3626	477.
2	5	0.3727	468.
2	6	0.3828	458.

KM	KE	ZL (CM)	ESH (-)	EV (-)	FESH (1/H)	FEV (1/H)	EPSNE(1) (-)	EPSNE(2) (-)
2	1	33.225	0.26514E-03	0.32936E-03	0.00000E+00	0.36198E-06	0.26588E-03	0.19690E-04
2	2	33.225	0.19705E-03	0.23142E-03	0.00000E+00	0.20353E-06	0.46797E-04	0.16029E-03
2	3	33.225	0.27316E-03	0.30880E-03	0.00000E+00	0.23833E-06	-0.20466E-03	0.30150E-03
2	4	33.225	0.45634E-03	0.50540E-03	0.00000E+00	0.34297E-06	-0.44895E-03	0.42207E-03
2	5	33.225	0.67398E-03	0.73239E-03	0.18347E-06	0.59036E-06	-0.69436E-03	0.54000E-03

KM	KE	CPROB (-)	SV (N/CM**2)	SIG(1) (N/CM**2)	SIG(2) (N/CM**2)	SIG(3) (N/CM**2)
2	1	0.32051E-12	3027.	-283.	-968.	-3594.
2	2	0.10115E-13	1702.	-276.	872.	-1084.
2	3	0.15354E-13	1993.	-227.	2038.	551.
2	4	0.59288E-13	2868.	-150.	3135.	1858.
2	5	0.99008E-12	3583.	-52.	3928.	2918.

```
LINEAR POWER            QDT   = 0.43200E+03  W/CM          FUEL DAMAGE              DPA   = 0.74907E+00  -
BURNUP                  BU    = 0.11528E+01  MWD/KG HE      SYSTEM PRESSURE          DRADT = 0.10000E+02  N*CM**2
BURNUP                  FIMA  = 0.10660E-02  -             INTERNAL PRESSURE        DRIDT = 0.22862E+02  N*CM**2
TOTAL NEUTRON DOSE      DOSDT = 0.13130E+22  NEU/CM**2      COOLANT TEMPERATURE      TCOLDT = 0.44500E+03  GRD.C
NEUTRON FLUX            DOSP  = 0.17642E+16  NEU/CM**2*SEC  PLENUM  TEMPERATURE      TPLEDT = 0.38300E+03  GRD.C
RAD.AV.TIME-INT.FISSR,  PHIDTQ = 0.28609E+20  FISS/CM**3    RAD. CONT.FORCE FU-CLAD  FCONR = 0.67181E+04  N
RAD.AVERAGED FISSIONRATE PHIPQ = 0.38461E+14  FISS/CM**3*SEC AX.  CONT.FORCE FU-CLAD  FCONZ = 0.20199E+02  N
VOID VOLUME             VPLEN = 0.44559E+01  CM**3          TOTAL STRAIN OF FUEL     EPSVB3 = 0.31612E-01  -
CRACK VOL.P.UNIT LENGTH SFRISS = 0.35052E-02  CM**3         TOTAL STRAIN OF CLAD.    EPSVH3 = 0.69182E-02  -
VALUE P*V/TABS          PVT   = 0.15360E+00  N/CM*K         THERM. CONDUCT. INTEGRAL SKDT  = 0.36106E+02  W/CM
TOT.NUMB. REL.GAS MOLES GMFREI = 0.20310E-05  MOLE          HEAT TRANSFER FUEL-CLAD. HGAP  = 0.17917E+01  W/CM**2*K
GAS MIXTURE             HE = 0.4946
                        AR = 0.4946
                        KR = 0.0012
                        XE = 0.0097
                        N2 = 0.0000
```